An Engineering Analysis Method for Deep Geothermal Energy

Xiaoyu Lu

Department of Engineering

University of Cambridge

This thesis is submitted for the degree of

Doctor of Philosophy

Clare Hall June 2019

Declaration

This thesis is the result of my own work and includes nothing which is the outcome of work done in collaboration except as declared in the Preface and specified in the text. It is not substantially the same as any that I have submitted, or, is being concurrently submitted for a degree or diploma or other qualification at the University of Cambridge or any other University or similar institution except as declared in the Preface and specified in the text. I further state that no substantial part of my thesis has already been submitted, or, is being concurrently submitted for any such degree, diploma or other qualification at the University of Cambridge or any other University or similar institution except as declared in the Preface and specified in the text. This thesis contains less than 65,000 words including appendices, bibliography, footnotes, tables and equations and has less than 150 figures.

Xiaoyu Lu

June 2019

An Engineering Analysis Method for Deep Geothermal Energy

Xiaoyu Lu

Abstract:

At present there are already many deep geothermal projects allowing us to have a better understanding of deep geothermal energy. However, there are still many issues to be solved for more reliable use of deep geothermal energy. This thesis proposes an engineering analysis method to assess the performance of a typical deep geothermal system, which is a doublet system with one injection well and one extraction well.

A convective heat transfer boundary between the aquifer and overburden layers is applied for the axisymmetric problem based on the Lauwerier model for the first time. A new analytical solution is deduced using a series of Laplace transforms. The interaction between the injection well and extraction well is first neglected. Compared with other relevant analytical solutions, this new analytical solution comprehensively includes both heat conduction and heat advection in the aquifer and the heat flux between the aquifer and overburden layer. As long as the relevant parameters are obtained, the new analytical solution can intuitively illustrate the temporal and spatial temperature distribution within the aquifer. It can be used to determine the location of the extraction well and to evaluate the extracted geothermal power of the hot water aquifer.

The convective heat transfer boundary at the interface does not only reflect the actual heat transfer process at the interface, but also models the heat transfer process in the overburden layer. It is shown that the dimensionless equivalent heat transfer coefficient is expressed as a function of the dimensionless injection rate and the dimensionless thermal conductivity of the overburden layer so the new analytical solution effectively incorporates the properties of the overburden layer. A series of FE simulations are conducted, and the analytical model is curve fitted to the FE results to evaluate the values of the dimensionless equivalent heat transfer coefficient. Based on the results of the curve fitting exercise, two empirical equations are proposed for typical cases. Applying the analytical solution coupled with these empirical equations and along with proper error estimates, it is possible to conduct a simple and rapid evaluation of the geothermal potential of a particular site.

The revised analytical solution in this thesis is novel as there is no other analytical or semi analytical solution for the doublet system considering the heat conduction and heat advection in the aquifer and the heat flux between the aquifer and overburden layer. The revised analytical solution extended the analytical solution for a single injection well to a doublet scheme by considering the interaction effect between the injection well and the extraction well. The expression of the critical distance between two wells is obtained so that the best location of the extraction well in a doublet system can be determined. The spatial and temporal temperature distribution in the aquifer for a doublet scheme can be given by the revised analytical solution when the well distance is greater than the critical distance. It is found that it is valid to use a single well model to simplify a doublet scheme when the extraction well is far away from the injection well. The temperature of the extracted water against different time, injection rates and well distances can be obtained via the revised analytical solution. The revised analytical solution is compared with the experimental data and the numerical solutions and it is found that they match with each other well.

The effect of a natural fault/fracture that exists in the aquifer on the performance of a doublet system, namely the temperature distribution and extracted temperature, is evaluated. By comparing the line model with the domain model, it is found that the line model is valid and computationally efficient. It is found that the acceleration effect of the fracture on thermal movement is the greatest when the fracture is located at the midpoint of the two wells. When the fracture is shifted towards the injection (extraction) well, the acceleration effect decreases and then becomes the deceleration effect. The deceleration effect of the fracture is the greatest when the fracture is located at the injection (extraction) well. The expressions of the critical angle for any position of the fracture in the doublet system are obtained. Equipped with these expressions, it is possible to decide whether the doublet system is still efficient during its life span once the cold water injection rate and the geometry and properties of the fracture are given.

Acknowledgements

I am particularly grateful to my supervisor, Professor Kenichi Soga, for his encouragement, support, patience, and guidance throughout my PhD study. I have been learning a lot from him, getting a better understanding of academia and life. It is my fortune and honour to have worked with him.

I am grateful to BP for providing financial support for my work.

I would like to thank Professor Jon Gluyas and Dr. Santo Bains for their great support.

I would like to express my gratitude to Yi Rui, Yi Zhang, Xiaomin Xu, He Qi, Denis Garber and to all former and current members of this research group for their friendship.

I wish to express my heartiest appreciation to my parents for their support and encouragement.

Abstract

At present there are already many deep geothermal projects allowing us to have a better understanding of deep geothermal energy. However, there are still many issues to be solved for more reliable use of deep geothermal energy. This thesis proposes an engineering analysis method to assess the performance of a typical deep geothermal system, which is a doublet system with one injection well and one extraction well.

A convective heat transfer boundary between the aquifer and overburden layers is applied for the axisymmetric problem based on the Lauwerier model for the first time. A new analytical solution is deduced using a series of Laplace transforms. The interaction between the injection well and extraction well is first neglected. Compared with other relevant analytical solutions, this new analytical solution comprehensively includes both heat conduction and heat advection in the aquifer and the heat flux between the aquifer and overburden layer. As long as the relevant parameters are obtained, the new analytical solution can intuitively illustrate the temporal and spatial temperature distribution within the aquifer. It can be used to determine the location of the extraction well and to evaluate the extracted geothermal power of the hot water aquifer.

The convective heat transfer boundary at the interface does not only reflect the actual heat transfer process at the interface, but also models the heat transfer process in the overburden layer. It is shown that the dimensionless equivalent heat transfer coefficient is expressed as a function of the dimensionless injection rate and the dimensionless thermal conductivity of the overburden layer so the new analytical solution effectively incorporates the properties of the overburden layer. A series of FE simulations are conducted, and the analytical model is curve fitted to the FE results to evaluate the values of the dimensionless equivalent heat transfer coefficient. Based on the results of the curve fitting exercise, two empirical equations are proposed for typical cases. Applying the analytical solution coupled with these empirical equations and along with proper error estimates, it is possible to conduct a simple and rapid evaluation of the geothermal potential of a particular site.

The revised analytical solution in this thesis is novel as there is no other analytical or semi analytical solution for the doublet system considering the heat conduction and heat advection in the aquifer and the heat flux between the aquifer and overburden layer. The revised analytical solution extended the analytical solution for a single injection well to a doublet scheme by considering the interaction effect between the injection well and the extraction well. The expression of the critical distance between two wells is obtained so that the best location of the extraction well in a doublet system can be determined. The spatial and temporal temperature distribution in the aquifer for a doublet scheme can be given by the revised analytical solution when the well distance is greater than the critical distance. It is found that it is valid to use a single well model to simplify a doublet scheme when the extraction well is far away from the injection well. The temperature of the extracted water against different time, injection rates and well distances can be obtained via the revised analytical solution. The revised analytical solution is compared with the experimental data and the numerical solutions and it is found that they match with each other well.

The effect of a natural fault/fracture that exists in the aquifer on the performance of a doublet system, namely the temperature distribution and extracted temperature, is evaluated. By comparing the line model with the domain model, it is found that the line model is valid and computationally efficient. It is found that the acceleration effect of the fracture on thermal movement is the greatest when the fracture is located at the midpoint of the two wells. When the fracture is shifted towards the injection (extraction) well, the acceleration effect decreases and then becomes the deceleration effect. The deceleration effect of the fracture is the greatest when the fracture is located at the injection (extraction) well. The expressions of the critical angle for any position of the fracture in the doublet system are obtained. Equipped with these expressions, it is possible to decide whether the doublet system is still efficient during its life span once the cold water injection rate and the geometry and properties of the fracture are given.

Contents

List of Figures

List of Tables

Nomenclature

α	Dimensionless injection rate
α'	Revised dimensionless injection rate
$\Gamma(\alpha)$	Gamma function
γ	Reduction factor
θ	Critical angle of fracture
λ	Thermal conductivity of aquifer
λ_2	Thermal conductivity of overburden layer
λ_f	Thermal conductivity of fracture
λ_s	Thermal conductivity of porous media
λ^*	Dimensionless thermal conductivity of overburden layer
ρc	Volumetric heat capacity of aquifer
$(\rho c)_2$	Volumetric heat capacity of overburden layer
$(\rho c)_f$	Volumetric heat capacity of water
$(\rho c)_s$	Volumetric heat capacity of soil
A	Angle of fracture
D	Thermal diffusivity

d	Thickness of fracture
H	Thickness of aquifer
H_2	Thickness of overburden layer
H^*	Dimensionless thickness of overburden layer
h	Convective heat transfer coefficient
h^*	Dimensionless heat transfer coefficient
I_α	Modified Bessel function of the first kind
K_α	Modified Bessel function of the second kind
k_f	Permeability of fracture
k_s	Permeability of porous media
L	Well distance
L^*	Dimensionless well distance
L_b	Heat breakthrough distance
L_b^*	Dimensionless heat breakthrough distance
L_c	Critical distance
L_c^*	Dimensionless critical distance
n	Porosity
n_f	Porosity of fracture
n_s	Porosity of porous media
P	Power

Q	Injection rate
Q'	Revised injection rate
q	Darcy velocity
R	Delay factor
r	Radius
$r*$	Dimensionless radius
T	Temperature of aquifer
T_0	Initial temperature
T_1	Temperature of ground surface
T_e	Temperature of extracted water
$T*$	Dimensionless temperature
T_w	Temperature of water
t	Time
$t*$	Dimensionless time
v	Advection rate
w_0	Heat flux

Chapter 1 Introduction

1.1 Background

With the rapid development of industry and society around the world, the consumption of energy is much larger than ever before. A majority of the energy consumed nowadays is fossil fuels. It is apparent that the amount of fossil fuels stored in the Earth is limited and will be eventually exhausted some day in the future. What is worse, CO_2 emissions during the process of using fossil fuels can significantly aggravate the climate change and global warming of the Earth, which is one of the severest social, economic and environmental challenges that the world is facing. Take the UK for example, half of the UK energy consumption is for heating, which accounts for nearly 50% of the UK emissions (EC, 2009). UK has a long-term objective to reduce the greenhouse gas emissions to 80% below 1990 levels by 2050 (UK Climate Change Act 2008). Therefore, both governments and individuals must explore some effective ways to dramatically reduce the carbon footprint. One good and promising option is the utilisation of renewable energy.

Geothermal energy is considered to be one of the important renewable energies in the current world. It utilizes the thermal energy generated and stored in the Earth; the volume of storage is very huge and can be used to heat buildings and to generate electricity. As geothermal energy is not affected by temperature changes, it can be used all year round and 24 hours a day. Geothermal energy is reliable, sustainable and environmentally friendly. Globally, over the next ten years, the investment in the geothermal industry is about 40 billion dollars (Global Data, 2012). The Department of Energy and Climate Change (DECC), which is now part of the Department for Business, Energy and Industrial Strategy, is considering the merits of installing the longest electricity cable in the world to use the geothermal energy in Iceland

(DECC, 2010a). Currently, geothermal energy provides only 0.3% of global power production (Gluyas et al., 2018). There are four potential applications of geothermal energy in the UK: (1) Electricity generation; (2) Combined heat and power (CHP); (3) Direct heat utilization; and (4) Heat pump.

In general, geothermal energy can be divided into two categories: (i) shallow geothermal energy and (ii) deep geothermal energy.

1.2 Shallow Geothermal Energy

Shallow geothermal energy is the energy stored in the upper layer of soils or rocks that is up to 200 - 300 metres beneath the earth surface. The energy comes from the heating process of solar radiation. Generally speaking, at a depth of around 15 metres, the ground temperature is not affected by seasonal air temperature changes. As a result, the temperature below that depth remains stable all year around at the mean annual temperature which is typically 9 – 13 ℃ in the UK (Rybach and Sanner, 2000). In other words, the ground temperature is lower than the air temperature in summer and higher than the air temperature in winter. Such a temperature difference can be exploited effectively by Ground Source Heat Pumps (GSHP) to heat or cool buildings.

There are generally two types of GSHP systems: Open-loop Ground Source Heat Pumps and Closed-loop Ground Source Heat Pumps. Open-loop systems exchange heat with ground water so that an aquifer within an appropriate distance from the surface is necessary in such systems. The layout of a typical open-loop system is shown in Figure 1.1. Closed-loop systems extract the heat from the ground by heat exchangers that are installed in boreholes. The layout of a typical closed-loop system is shown in Figure 1.2.

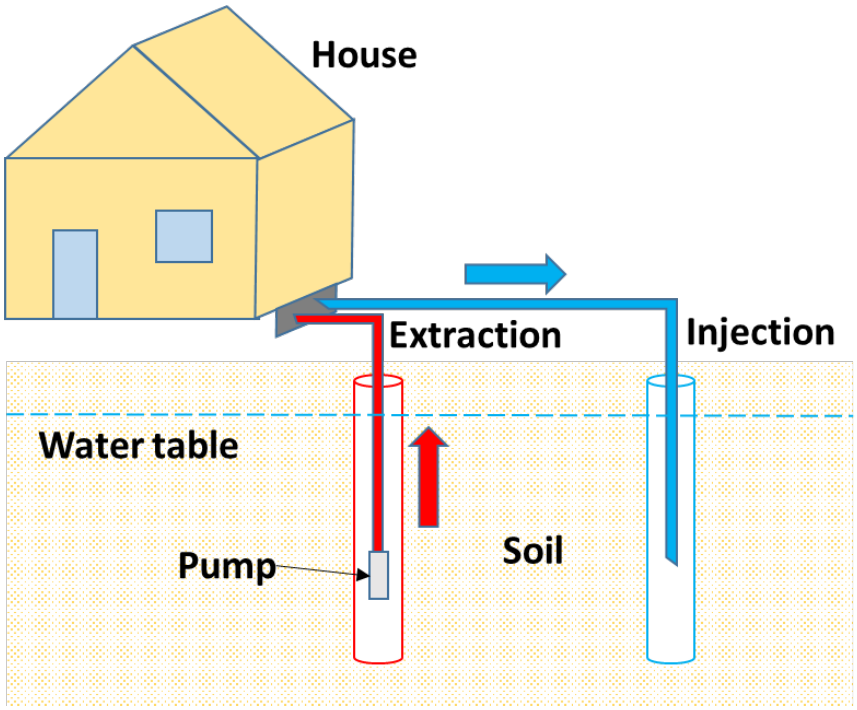

Figure 1.1: Open-loop Ground Source Heat Pump

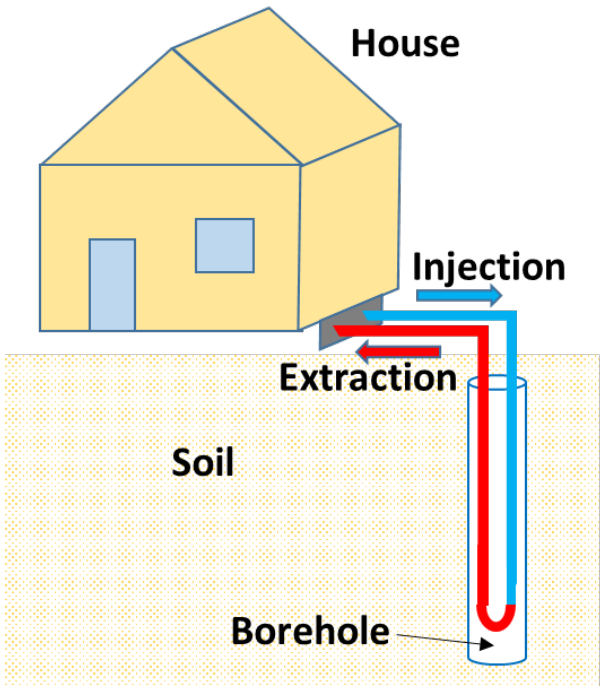

(a)

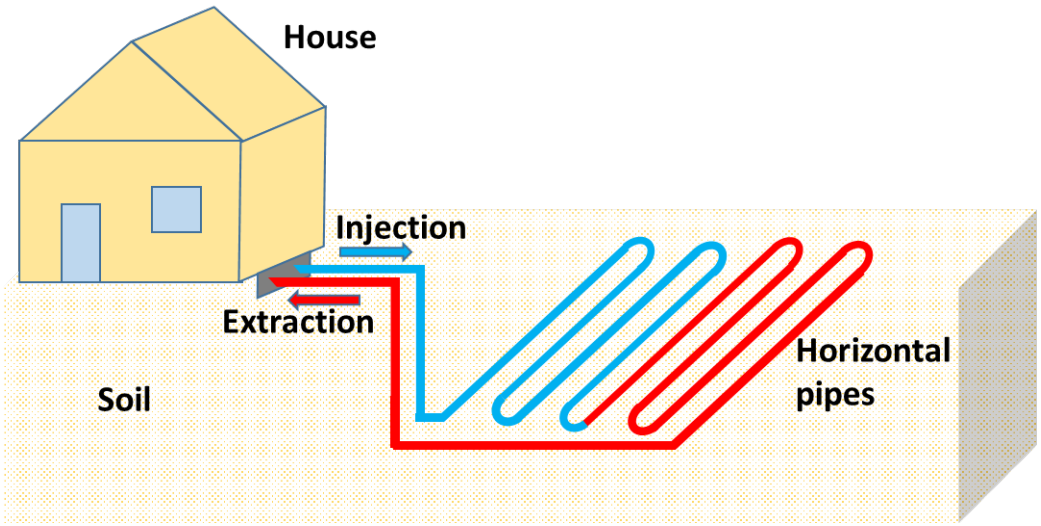

(b)

Figure 1.2: (a) Vertical Closed-loop Ground Source Heat Pump; (b) Horizontal Closed-loop Ground Source Heat Pump

1.3 Deep Geothermal Energy

Unlike shallow geothermal energy, in terms of deep geothermal energy, the ground temperature is mainly influenced by the geothermal heat flow that is conducted upwards from the Earth's core and mantle so that the ground temperature increases with depth. The deep geothermal energy comes from the geothermal gradient of the ground. In the UK, the average geothermal gradient is 26 ℃ per kilometre (Busby, 2010). The heat flow map of the UK is shown in Figure 1.3. It can be found in the figure that the overall heat flow of the UK is relatively low and the heat flow in the middle and south-west is much larger than that of other districts in the UK.

This thesis focuses on deep geothermal energy. We are most interested in the heat resources up to 5 kilometres deep in the ground, because at this depth, the heat resources are sufficient and drilling costs are economically feasible. In most cases, the ground temperature greater than 100 ℃ can be used to generate electricity and the one greater than 60 ℃ is used to directly heat buildings (Lund et al., 2011). With the technology advancement in the offshore oil and gas industries, it is possible to extract geothermal energy from rocks or aquifers up to 5 kilometres deep in the ground, providing 9.5 GW of baseload renewable electricity and 100

GW of heat. That is equal to 20% of the UK annual electricity generation capacity requirement and the equivalent to the total annual heat consumption in the UK (SKM, 2012).

In general, there are two categories of deep geothermal systems. One category is Hot Sedimentary Aquifer (HSA) systems in which the heat stored in hot water aquifers is extracted. The other is Engineered Geothermal Systems (EGS) in which the heat stored in hot rocks is extracted by stimulating a reservoir.

Between the late 1970s and mid-1990s, the UK government funded the "Geothermal Energy Program" which investigated the following issues: (1) evaluation of the heat flow; (2) potential of hot brines from deep HSA for direct heat; and (3) potential of EGS in granites. The summary of these studies can be found in Barker et al. (2000) as follows: (1) low temperature resources ranging from 40 ℃ to 100 ℃, are found in Permo-Triassic sandstones in a few deep sedimentary basins, which are estimated at 69.1×10^{18} J in total; (2) such resources also occur in Upper Palaeozoic aquifers but it is difficult to exploit as the permeability of these aquifers depends upon fissures; (3) the potential of EGS in the Carnmenellis granite in Cornwall has been investigated and three boreholes drilled in the granite to depths of over 2 km have been connected by developing natural fractures.

There are a number of very promising locations in the UK for deep geothermal system. Two areas in the UK, the Wessex Basin and Cheshire Basin, have the potential for HSA electricity generation (GT Energy, 2011 and Cheshire East Council, 2013). But due to lack of well information, based on the Australian Geothermal Reporting Code (AGEA and AGEG, 2010), which is an internationally recognised code, these two areas are classified as Inferred Resources. An Inferred Resource is a part of a geothermal resource in which thermal energy is estimated with a low level of confidence mainly from geological, geochemical and geophysical data without (or with very limited) information from drilling and well testing. In fact, most geothermal resources in the UK are relevant to the "inferred" category. A geothermal resource can be classified as "indicated" if drilling into the area can determine the quality, nature, amount and distribution of data so that the geological framework can be interpreted, continuity of the geothermal distribution can be assumed and the extent of the resource can be estimated.

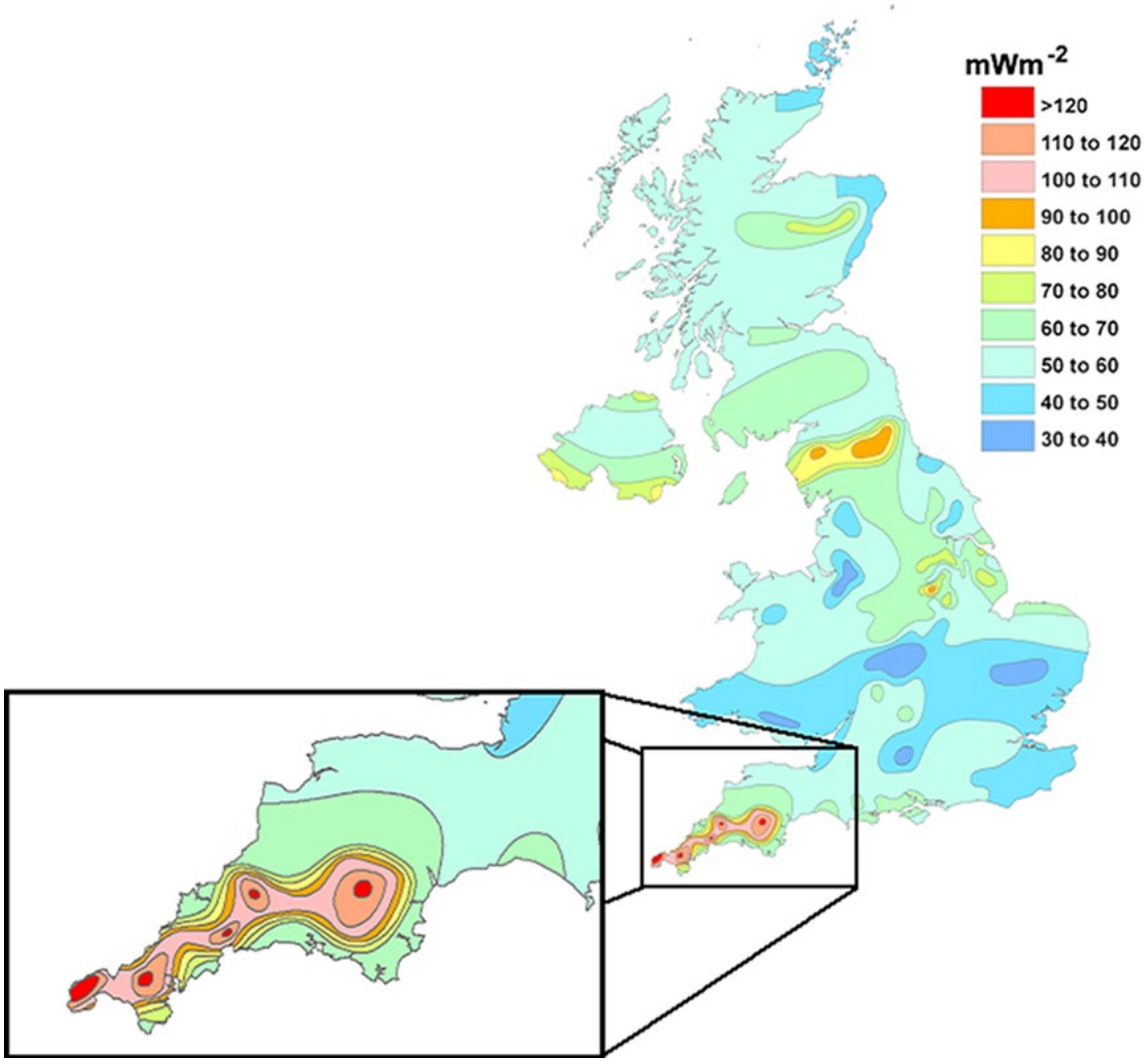

Figure 1.3: Heat flow map of UK (British Geological Survey website)

1.3.1 Hot Sedimentary Aquifer (HSA) Systems

According to the fluid temperatures, Hot Sedimentary Aquifer (HSA) resources can be classified as: (1) Low temperature which is less than 90 ℃; (2) Medium temperature which is between 90 – 160 ℃; (3) High temperature which is greater than 160 ℃. In the UK, a majority of the HSA resources are in the low and medium temperature categories. The schematic of an HSA project is shown in Figure 1.4. For medium temperature resources, such as the Cheshire Basin in the UK, the heat can be converted to electricity by binary cycle power plant. This technology is well established and has been applied to relatively low grade heat recovery from

geothermal, solar and biomass. High temperature resources, which are usually known as magmatic resources, are associated with volcanic heat resources in most cases. Such resources have higher temperatures and are located at relatively shallow grounds. They are often found in Iceland, Italy, Greece, Turkey, Indonesia, New Zealand, etc.

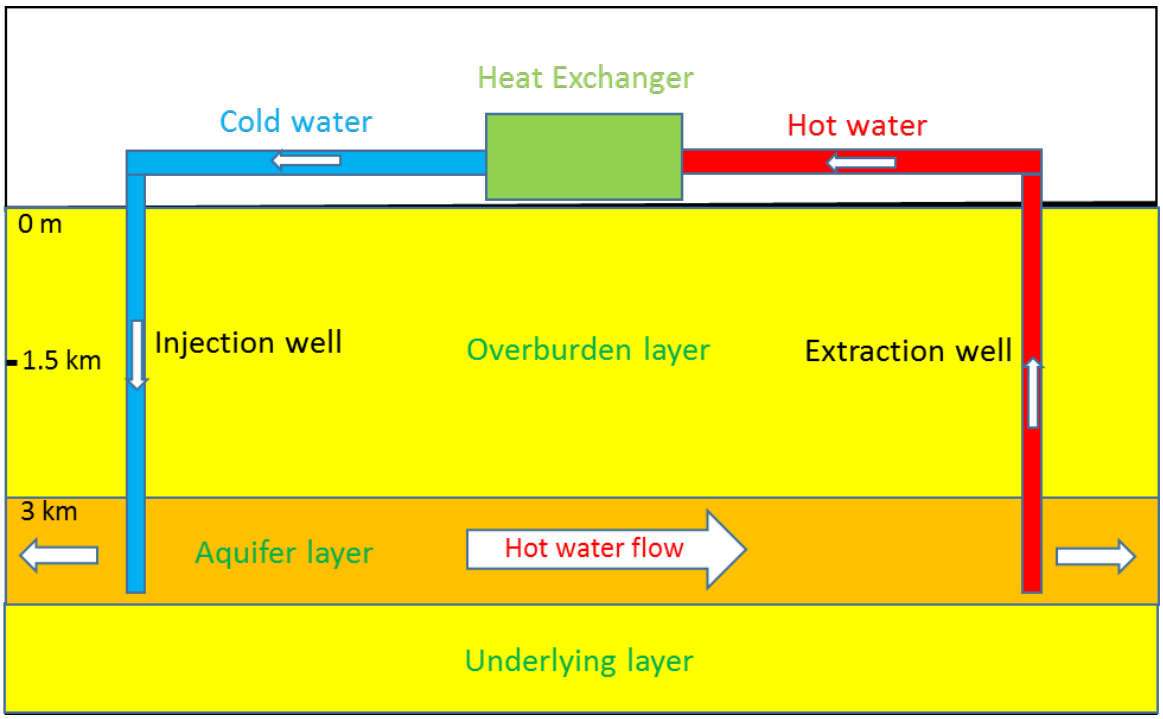

Figure 1.4: Schematic of an HSA project

Generally, HSA resources exist in sedimentary basins where there is a high flow rate of ground water with high temperature. Sedimentary basins have not only thermal insulation to hold heat flow but also have reservoir formations with storage capacity. Due to these properties, a large amount of geothermal potential can be harvested from low and medium temperature sedimentary aquifers at economically drillable depths. In addition, as sedimentary aquifers are permeable, geothermal energy can be extracted without complex stimulation or permeability enhancement.

There are a number of HSA projects in the UK which have been completed, under way or planned, such as the Isle of Wight project, Keele University Staffordshire project and GT Energy Ballymena project. Direct heat use from HSA can be achieved with the existing

technology and avoids poor conversion efficiency when converted to electricity. Hence, direct heat use from HSA can be the easiest gains for securing renewable energy in the UK.

1.3.2 Engineered Geothermal Systems (EGS)

For Engineered Geothermal Systems (EGS), natural hot temperature aquifers are not needed, while in HSA systems there must exist at least one natural hot temperature aquifer. EGS extracts the energy stored in hot rocks by injecting water as a working fluid. When it is impossible to retrieve economically viable flow rates, hydraulic stimulation is required to obtain ideal water circulation rates. This also explains why such systems are referred as Enhanced or Engineered Geothermal Systems (EGS). The schematic of an EGS project is shown in Figure 1.5. When an EGS is set up, injected water flowing through the reservoir is heated by the surrounding hot rocks, then runs through a heat exchanger system or power station and is finally re-injected into the ground.

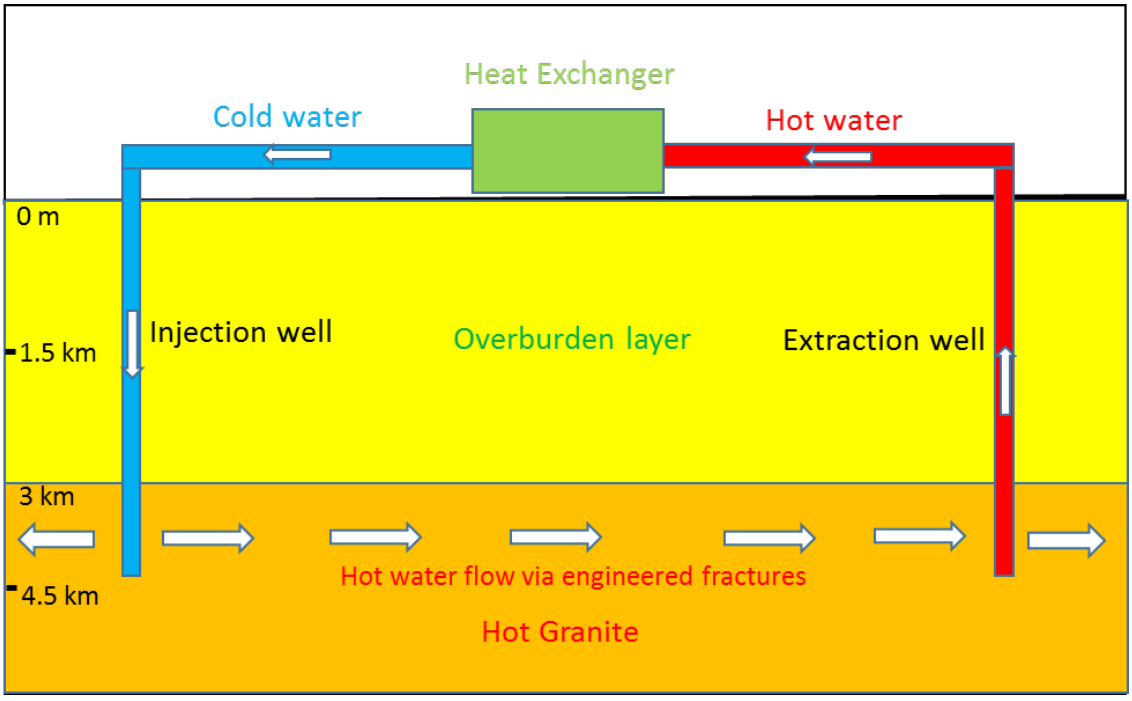

Figure 1.5: Schematic of an EGS project

The concept of EGS is to improve the permeability of rocks (small fractures and porosity between mineral grains). Water is pumped through injection wells into hot crystalline rocks

with very high pressures. By implementing this process (called hydro-stimulation), it is possible to open naturally occurring joints or even produce new fractures in the reservoir. Similar techniques have been proved to be effective for oil/gas recovery in the oil and gas industry. For example, it has dramatically enhanced the production of gas in impermeable shale reservoirs. A successful stimulation must aim to: (1) produce new permeability; (2) stimulate some zones to get sufficient contact areas; (3) avoid preferential pathways; and (4) maintain the conductive fractures in a variety of stress, temperature and geochemical regimes (Rose et al., 2012). The size of a created reservoir is directly related to the amount of water pumped into rocks and local stress regime. In order to increase near-well permeability, a chemical stimulation, which is achieved by injecting acid into the reservoir, is usually a useful approach to dissolve scale on any sealed fractures. It is noted that local geologic conditions also contribute to the orientation, shape and internal structure of the stimulated reservoir. Once the stimulation is successful, it is critical to keep the stimulation on a fine scale to keep the flow paths created so that heat can be extracted from the hot rocks.

However, the processes of enhancing the permeability of natural fractures are not fully understood. Research and projects have shown that hydraulic stimulation can achieve an increase in-rock mass permeability. But the progress so far is very limited in demonstrating the required procedures to stimulate large naturally fractured rocks at a required scale to create a commercial reservoir. Although a large fractured rock mass has been created in full-scale and in-situ experiments, circulating fluid through these fractures at a commercial rate of 50 kg/s has not been achieved yet. Although hydraulic stimulation can enhance the permeability of rocks, creation of sufficiently uniform or low injection impedance flow paths has not yet been demonstrated (Zimmermann, 2010).

EGS resources are mainly found in very hot granites. Such resources are buried deep with very high temperature (often higher than 200 ℃ at 5.5 kilometres) (MIT, 2006). Therefore, in order to have a suitable reservoir for geothermal, a stimulation is required to create sufficient connected permeability. Such buried granites often have higher heat flows than the surrounding rock formations. High heat flow can be found over granites characterized by: (1) high concentration of primary radiogenic elements; and (2) large gravity anomalies implying

radiogenic, low density crystalline rocks, which extend to a few kilometres depth (MIT, 2006). In other words, large granite bodies imply greater heat generation.

The key criteria for an economically viable EGS are: (1) an underlying radiogenic granite with suitable mineralization to produce heat; (2) an inferred geothermal gradient that will achieve a temperature of greater than 160 ℃ at a depth of around 4 kilometres; (3) a thick sedimentary sequence overlying a reservoir acts as heat insulation so that a higher temperature can be found at an economically viable depth; and (4) an appropriate rock fabric and stress regime to achieve a good permeability enhancement during stimulation (Barker et al., 2000). (1) and (2) are the most critical ones among these key criteria.

There is only one EGS exploration project completed in the UK, which is the Rosemanowes (near Redruth) experiment for hydraulic stimulation. Deep and hot granitic formations with temperature 175-200 ℃ at 5 kilometres are limited to Southwest England and considerable developments in technology are required to extract heat (Batchelor et al., 2010). There are some EGS potentials in the East Grampian batholiths in Scotland if deeper drilling is implemented (Busby, 2010). The significant problem for deep geothermal in the UK is the lack of knowledge concerning the thermal properties of rocks at various depths and temperatures. Drilling investigation can improve this understanding.

Compared with HSA systems, development of EGS is more economically risky because of its uncertainty whether sufficient permeability can be achieved or not to obtain the required flow rates at reasonable levels of pumping parasitic load.

1.4 Concerns about Deep Geothermal Energy

At present, there are already several deep geothermal projects around the world allowing us to have a better understanding of deep geothermal energy. However, there are still many issues to be solved for more reliable use of deep geothermal energy.

(1) How can we obtain the temperature distribution in the ground accurately and efficiently? The temperature distribution in the ground is fundamentally important in the utilization of deep

geothermal energy. However, experimental data about temperature distribution of a given site is rare. This is because the scale of a geothermal site is usually so large that it is difficult, laborious and expensive to measure the temperature of different locations at different times. Therefore, estimating the temperature distribution with aid of analytical and numerical methods is attractive.

(2) How can we evaluate the temperature of extracted water against time? The amount and rate of geothermal energy extracted during the life span of a deep geothermal system need to be predicted to assess the feasibility of geothermal to satisfy the demand.

(3) How can we evaluate the effect of neighbouring geological layers on the production from a given aquifer layer? There is often heat exchange between a targeted aquifer layer and the surrounding layers. Such effect needs to be assessed for predicting the amount and rate of energy extracted.

(4) How can we deal with the interaction between injection wells and extraction wells? The interaction effects of injection and extraction wells which make the spatial and temporal distribution of fluid flow movements complicated, causing the temperature distribution and extracted temperature complex.

(5) How can we evaluate the influence of natural fractures or faults on the temperature of a deep geothermal system? Existence of fractures or faults changes the distribution of fluid flow and temperature.

(6) How can we determine the optimum locations of both injection and extraction wells? If an extraction well is too close to an injection well, the extracted temperature will decrease during the life span of the system. If an extraction well is too far away from an injection well, longer pipelines and surface facilities are required, which in turn will increase the cost of the system.

1.5 Research Aim and Objectives

The overall research aim of the study presented in this dissertation is to propose an engineering analysis method to examine the performance of a typical deep geothermal system, which is a

doublet system with one injection well and one extraction well. The measurable research objectives are as follows:

(1) Develop an analytical solution that gives the temperature distribution around an injection well considering the effect of the overburden layer on the temperature distribution inside the aquifer layer. The interaction between the injection well and extraction well is first neglected.
(2) Evaluate an equivalent heat transfer coefficient, which is used to characterize the effect of the overburden layer on the aquifer layer in the analytical solution, from a series of finite element simulations for various geological conditions. An empirical expression that links the heat transfer coefficient to various physical and geometric properties of the aquifer is developed.
(3) Develop a revised analytical solution of temperature distribution and extracted temperature of a geothermal system that takes into consideration the interaction between injection well and extraction well. The revised analytical solution is compared with the experimental data and numerical solutions to check its validity.
(4) Evaluate the effect of a natural fault/fracture that exists in the aquifer on the performance of a doublet system, namely the temperature distribution and extracted temperature. The position and angle of the fault/fracture are varied.

1.6 Structure of the Thesis

This thesis includes seven chapters. They focus on the analytical and numerical methods that evaluate the performance of a doublet system for geothermal energy recovery from a deep high temperature aquifer.

Chapter 1 summarises the background of geothermal energy, shallow geothermal, HSA and EGS, highlights issues in conducting engineering analysis of deep geothermal energy system and lists the research aim and objectives of the study presented in this dissertation.

Chapter 2 reviews the literature of analytical solutions for a single well system, analytical solutions for a doublet system, findings from the past numerical studies, and findings from the past field experiments on a doublet system and fracture flow.

Chapter 3 describes the development of an analytical solution using the convective heat transfer boundary condition, neglecting the interaction between injection well and extraction well.

Chapter 4 gives the results of a study that combines the analytical solution with numerical simulation results to develop an expression that can give the equivalent heat transfer coefficient used in the analytical solution for a given set of aquifer physical properties and geometry. The equivalent coefficient is used to take into consideration the effect of overburden layer on the temperature variation within the aquifer layer.

Chapter 5 describes a revised analytical solution for the temperature distribution and extracted temperature of a doublet system, which considers the interaction between the injection well and extraction well. The interaction effect is quantified by a series of finite element simulations and the analytical solution derived in Chapter 3 is revised to incorporate the effect. Then the revised analytical solution is compared with the experimental data and numerical solutions.

Chapter 6 shows the study that evaluates the effect of a natural fault/fracture in the aquifer on the performance of a doublet system. The position and angle of the fault/fracture are varied and an expression of the critical angle, at which the fracture will not affect the extracted temperature, is proposed.

Chapter 7 provides the conclusions made from the findings of this study. Recommendations for future research are also given.

Chapter 2 Literature Review

This literature review chapter is divided into four sections. The first section reviews the analytical solutions available for a single well system. The second section reviews the analytical solutions for a typical doublet system, namely the geothermal system with one injection well and one extraction well. The third section reviews some results on fracture flow. The fourth section reviews some experimental data and analysis of deep geothermal systems.

2.1 Analytical Solutions for a Single Well System

2.1.1 Line Source Model (LSM)

The Line Source Model (LSM) was first put forward by Kelvin in 1882 (also known as Kelvin line source model). In this model, a single well or an underground line-shaped heat exchanger is considered to be an infinitely long line heat source in an infinite solid, as shown in Figure 2.1(a). Given the fact that the length of the borehole is much greater than its diameter, the borehole can be regarded as a one dimensional model.

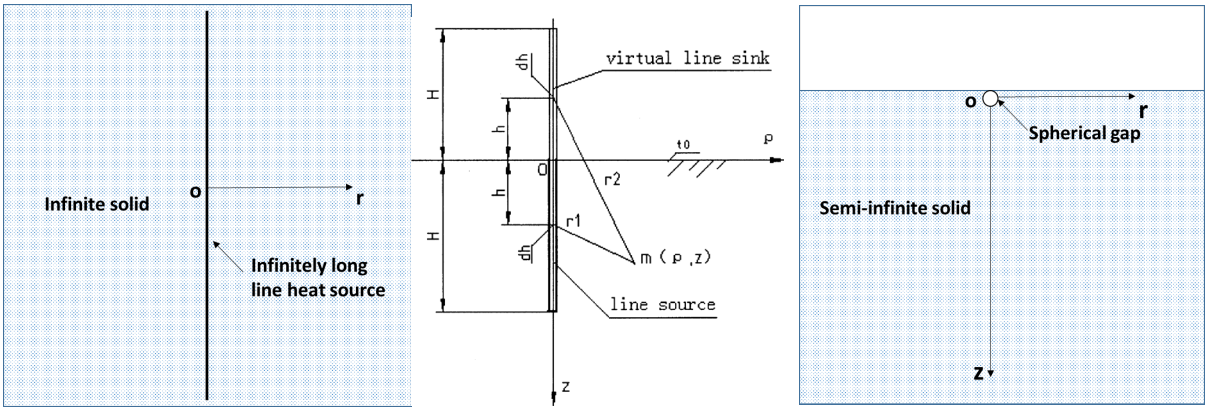

(a) Kelvin line source model (b) Zeng model (Zeng et al., 2002) (c) semi-infinite body

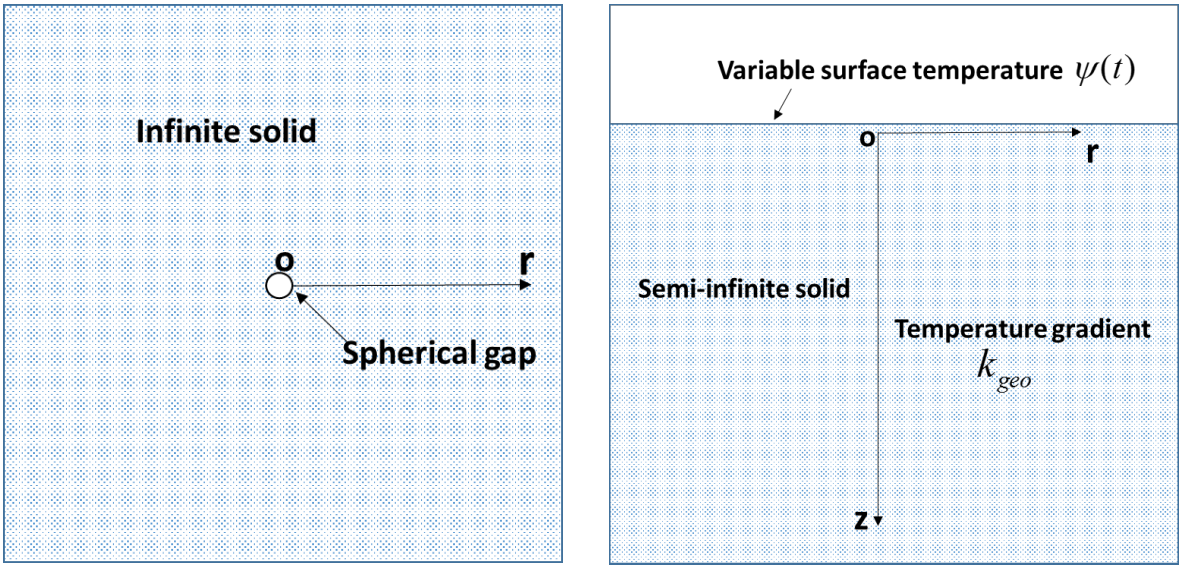

(d) infinite body with spherical gap (e) Bandos model

Figure 2.1: Line source model

Ingersoll et al. (1954) further developed the Kelvin Line Source Model. In their line source model, heat transfer from a single well is considered to be a line heat source with constant heat flux *q'* in an infinite medium. The initial temperature of the medium is assumed to be uniform T_0. The temperature distribution in the medium is expressed as follows:

$$T - T_0 = \frac{q'}{2\pi\lambda}\int_{\eta}^{\infty}\frac{e^{-\beta^2}}{\beta}d\beta = \frac{q'}{2\pi\lambda}E_1(\eta) \tag{2.1}$$

where q' is the constant heat flux of line source, T_0 is the undisturbed ground temperature, and λ is the ground thermal conductivity, E_1 is the exponential integral, η is a dimensionless parameter defined as:

$$\eta = \frac{r}{2\sqrt{Dt}} \tag{2.2}$$

where r is the radius coordinate, D is the ground thermal diffusivity, and t is the time.

Hart and Couvillion (1986) defined the far-field radius of the ground as the range which is influenced by a single well. The ground temperature change beyond the far-field radius is negligible. The line source equation is similar to that of Ingersoll's model as follows:

$$T - T_0 = \frac{q'}{4\pi\lambda}\int_{\eta^2}^{\infty}\frac{\mathrm{e}^{-\beta}}{\beta}\mathrm{d}\beta = \frac{q'}{4\pi\lambda}E_1(\eta^2) \tag{2.3}$$

where λ is the ground thermal conductivity.

Zeng et al. (2002) gave an axisymmetric analytical solution for the temperature distribution under a boundary condition of constant heat flux (i.e., a Cauchy boundary condition) perpendicular to the finite line source, which represented the geothermal heat exchanger installed in boreholes with a length of *H*, as shown in Figure 2.1(b).The expression of the temperature distribution is as follows:

$$\Delta T(r,z,t) = \frac{q'}{4\pi\lambda}\int_0^H \left(\frac{erfc\left(\frac{\sqrt{r^2+(z-h)^2}}{2\sqrt{Dt}}\right)}{\sqrt{r^2+(z-h)^2}} - \frac{erfc\left(\frac{\sqrt{r^2+(z+h)^2}}{2\sqrt{Dt}}\right)}{\sqrt{r^2+(z+h)^2}}\right)\mathrm{d}h \tag{2.4}$$

where ΔT is the temperature excess, q' is the heat flux of the line source, λ is the thermal conductivity of soil, D is the thermal diffusivity of the soil, H is the length of line-source, r is the radius, z is the coordinate along the depth direction, and *erfc* is the complementary error function.

Brandl (2006) derived analytical solutions for heat conduction in a semi-infinite body and an infinite body with spherical gap under a sudden temperature change at the boundary or centre, i.e. a Dirichlet boundary condition, as shown in Figure 2.1(c) and (d). The expressions of the temperature distribution are as follows:

$$\Delta T(z,t) = \Delta T(0,0)\cdot erfc\left(\frac{z}{2\sqrt{Dt}}\right) \tag{2.5}$$

$$\Delta T(r,t) = \Delta T(a,0) \cdot \frac{a}{r} \cdot erfc(\frac{r-a}{2\sqrt{Dt}}) \tag{2.6}$$

where ΔT is the temperature rise at the boundary, D is the thermal diffusivity of the aquifer, a is the radius of the spherical gap and z is the coordinate along the depth direction.

Bandos (2009) proposed an axisymmetric analytical solution to the finite line-source (FLS) model for borehole heat exchangers (BHEs) that considers geothermal gradient and allows arbitrary ground surface temperature changes, as shown in Figure 2.1(e). The analytical expressions for the average ground temperature is derived by integrating the exact analytical solutions over the line-source depth as follows:

$$\begin{aligned} T &= T_0 + k_{geo}\frac{H}{2} + T_s \frac{2\sqrt{2d_p}}{H}\sin(\omega t - \frac{\pi}{4}) \\ &+ \frac{q'}{4\pi\lambda}\int_{r/\sqrt{4Dt}}^{+\infty} \{4erf(\frac{Hu}{r}) - 2erf(\frac{2Hu}{r}) - (3 + \mathrm{e}^{-4H^2u^2/r^2} - 4\mathrm{e}^{-H^2u^2/r^2})\frac{r}{\sqrt{\pi}Hu}\}\frac{\mathrm{e}^{-u^2}}{u}\mathrm{d}u \end{aligned} \tag{2.7}$$

where T_0 is the undisturbed ground temperature, k_{geo} is the geothermal gradient, H is the depth of the borehole heat exchanger, T_s is the amplitude of the ground temperature oscillations, d_p ($=\sqrt{2D/\omega}$) is the depth of thermal penetration, ω is the frequency of ambient temperature change, D is the ground thermal diffusivity, q' is the heat flux of the line source, and λ is the thermal conductivity of soil.

2.1.2 Cylindrical-Source Model (CSM)

The Cylindrical-Source Model (CSM) was first proposed by Carslaw and Jaeger in 1947. The heat exchanger is assumed to be an infinitely long column heat source with a diameter or a geometry, as shown in Figure 2.2(a). In this sense, the Line Source Model is a simplification of the Cylindrical-Source Model.

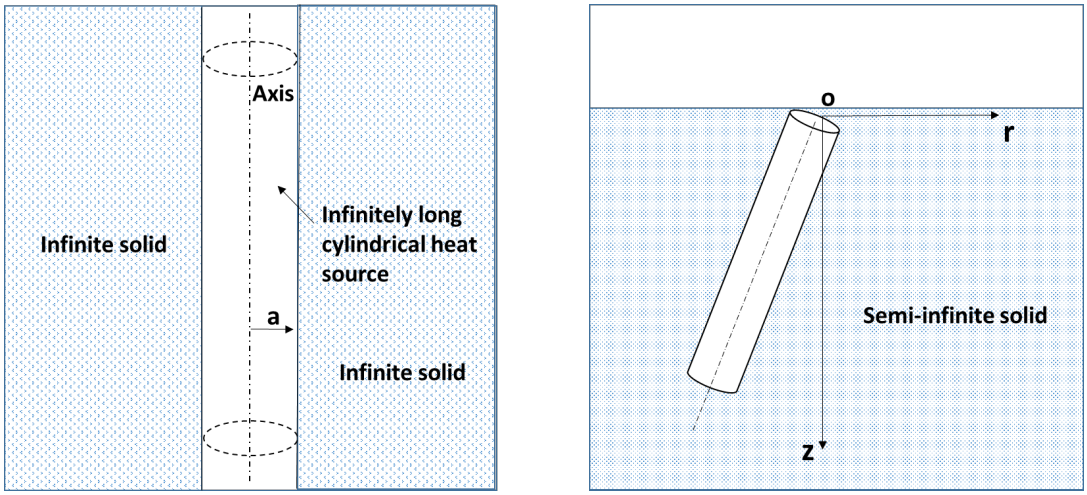

(a) infinite Cylindrical-Source Model (b) inclined finite Cylindrical-Source Model

Figure 2.2: Cylindrical-Source Model

Carslaw and Jaeger (1959) derived the temperature distribution for a Cylindrical-Source Model in the cylindrical coordinate system:

$$T = \frac{2q'\lambda t}{Da} + \frac{q'a}{D}\left(\frac{r^2}{2a^2} - \frac{1}{4} \cdot 2\sum_{n=1}^{\infty} e^{\frac{\lambda\alpha_n^2 t}{a^2}} \frac{J_0\left(\frac{r\alpha_n}{a}\right)}{\alpha_n^2 J_0(\alpha_n)}\right) \tag{2.8}$$

where q' is the constant heat flux, λ is the thermal conductivity, t is the time, D is the thermal diffusivity, J_0 is the zero order term of Bessel function, and r is the radial distance from the borehole centreline, a is the radius of the cylinder, α_n (n=1, 2, 3…) are the positive roots of $J_1(\alpha) = 0$ ($J_1(\alpha)$ is the first order term of Bessel function).

In practice, a majority of the heat exchangers are U-shaped pipes. Therefore, such U-shaped pipes systems are simplified as a single pipe and then modelled using the Cylindrical-Source Model, as shown in Figure 2.3. After such simplification, the problem becomes how to determine the equivalent pipe diameter $D_{eq} = CD_0$, where C is a coefficient and D_0 is the outer diameter of the pipe. Claesson and Dunand (1983) proposed $D_{eq} = \sqrt{2}D_0$, whereas Mei and Baxter (1986) found that the range of the coefficient C is 1.0 ~ 1.662 with an average value of 1.279.

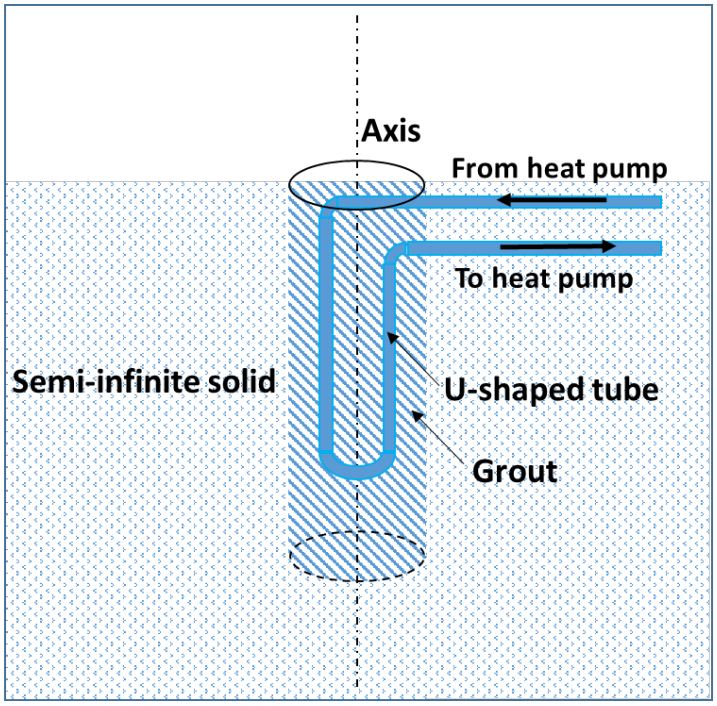

Figure 2.3: Schematic of a borehole ground heat exchanger with a single U-shaped tube

Deermman and Kavanaugh (1991) derived the following expression of the temperature distribution for a U-shaped cylindrical-source model with $D_{eq} = \sqrt{2} D_0$. The temperature distribution T can be written in the following forms:

$$\Delta T = \frac{q'}{\lambda} \cdot G(r, z, t) \tag{2.9}$$

$$T = T_0 - \Delta T \tag{2.10}$$

where T is the temperature at radius r, ΔT is the difference between the temperature at radius r and the initial ground temperature T_0, $G(r, z, t)$ defined here is the temperature response to a unit-step heat flux and has various expression depending on the specific case considered.

Kavanaugh (1985) further developed Carslaw's cylindrical source model. A correction term is included to take into account the non-uniform heat flow rate in the zones closest to the pipes and the number of U-tubes in the borehole. The average water temperature is as follows:

$$T_{ave,w} - T_0 = \frac{q'}{\lambda} G(r,z,t)_{ave} + \frac{q'}{2\pi a C N h_{eq}} \tag{2.11}$$

when $N = 2$, $C = 0.85$ and when $N = 4$, $C = 0.6 \sim 0.7$.

Bandyopadhyay (2008) obtained the Laplace domain solutions for the equivalent single core of a U-tube in grouted boreholes. The Laplace domain solutions take into account the thermal capacity of the aggregate fluid mass in the system representing the U-tubes as an equivalent single core. As it is difficult to do the Laplace inversion analytically, a numerical Laplace inversion algorithm (Gaver-Stehfest) is used to obtain the borehole temperature and the fluid temperature numerically. The temperature values obtained match the results of finite element models of the actual U-tube geometry of the grouted boreholes.

Lamarche (2011) modified the classical expression of the finite source method for inclined boreholes by Marcotte and Pasquier (2009) to improve its efficiency for a practical design approach, as shown in Figure 2.2(b). A generalized g-function can be calculated for inclined boreholes as follows:

$$T_{ave}(t) - T_0 = \frac{q'}{2\pi\lambda_s} \tilde{g}_i(a,t) \tag{2.12}$$

$$\tilde{g}_i(a,t) = \text{mean}(g_{i,n}) \tag{2.13}$$

$$g_{i,n} = g_{n,n} + 2\pi\lambda_s \sum_{\substack{m=1 \\ m \neq n}}^{N_b} \frac{\Delta T_{b,m \to n}}{q'} \tag{2.14}$$

where T_{ave} is the mean borehole temperature, T_0 is the far-field ground temperature, q' is the heat flux per unit length, g is the g-function, λ_s is the thermal conductivity of soil, and a is the borehole radius.

2.1.3 Lauwerier Model

The solutions given in the previous two sections are used when thermal flux is applied along the heat source boundary (i.e. thermal conduction). Lauwerier Model (1955) is a mathematical model for the injection of hot water into an oil bearing layer (i.e. thermal advection), which is shown in Figure 2.4. In the model, hot water of temperature T_w (the reservoir temperature T_0 being taken as zero) is pumped at a constant rate v into an injection well placed in a straight line. Water and oil are extracted by an extraction well, positioned in a straight line parallel to and at a distance L from the first. The flow of water is assumed to be linear so that the problem can be treated as a two-dimensional one by considering a strip of unit width. As a first simplification, water flows in only one layer of constant thickness $2b$, the temperature T of which is constant in any cross section. Thus the temperature only depends on the distance x from the injection well.

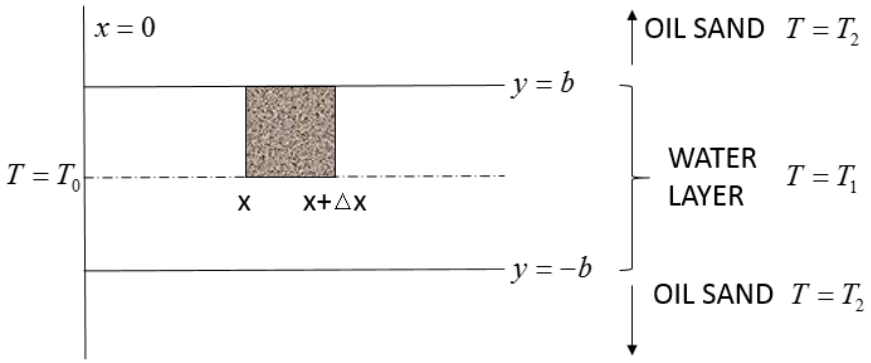

Figure 2.4: Lauwerier Model

A horizontal water layer

$$x > 0,\ -b < y < b \tag{2.15}$$

is situated in an oil sand of initial temperature $T_2 = 0$. The temperature T of the water layer is initially also zero. From the time $t = 0$ onwards the boundary

$$x = 0,\ -b < y < b \tag{2.16}$$

is kept at a constant temperature

$$T_w > T \tag{2.17}$$

by injection of water of temperature T_w at a rate q m/s so as to result in a convective heat transport in the *x*-direction. Heat is carried off at the oil/water interface

$$x > 0,\ y = b \tag{2.18}$$

by conduction through the oil-saturated part of the sand. A second simplification is introduced by neglecting heat conduction in the horizontal direction inside the water- and the oil-layers. Further, it is assumed that the establishment of the temperature equilibrium water/sand grain is instantaneous. The temperatures T and T_2 can now be calculated as functions of x, y and the time t.

During the derivation of the equations, the following constants are used:

$(\rho c)_f$ = volumetric heat capacity of water, J/(m^{3}K)

q = linear water velocity, m/s

λ_2 = thermal conductivity of the oil-saturated sand and surrounding rock, W/(mK)

n = porosity of sand

$(\rho c)_s$ = volumetric heat capacity of sand grain, J/(m^{3}K)

$(\rho c)_0$ = volumetric heat capacity of oil, J/(m^{3}K)

s_0 = residual oil saturation of the water layer

s_c = connate-water saturation of the oil layer

Applying the balance of heat to the hatched region of Figure 2.4, we find:

$$b\rho c\frac{\partial T}{\partial t}+b(\rho c)_f q\frac{\partial T}{\partial x}-\lambda_2(\frac{\partial T_2}{\partial y})_{y=b}=0 \tag{2.19}$$

where $\rho c=(1-n)(\rho c)_s+n(1-s_0)(\rho c)_f+ns_0(\rho c)_0$ is the volumetric heat capacity of the water layer. In the oil sand, the normal equation for heat conduction holds:

$$\lambda_2\frac{\partial^2 T_2}{\partial y^2}=(\rho c)_2\frac{\partial T_2}{\partial t} \tag{2.20}$$

where $(\rho c)_2=(1-n)(\rho c)_s+n(1-s_c)(\rho c)_0+ns_c(\rho c)_f$ is the volumetric heat capacity of the oil-saturated sand which is assumed to be equal to that of the surrounding rock.

After applying the Laplace transformation, the temperature in the water layer can be obtained from the above equations:

$$T=T_w erfc(\frac{\xi}{2\sqrt{(\tau-\xi)/h_2}})U(\tau-\xi) \tag{2.21}$$

where $\xi=\frac{\lambda_2}{b^2(\rho c)_f q}x$, $\tau=\frac{\lambda_2}{b^2(\rho c)}t$, $h_2=\frac{(\rho c)_2}{(\rho c)}$ and $U(\xi)$ stands for the unit function: 0 for $\xi<0$ and 1 for $\xi>0$.

Ogata and Banks (1961) proposed an analytical solution of the concentration of solute in the porous media based on the Lauwerier Model. As the differential equations and boundary conditions for concentration and temperature are equivalent, the corresponding temperature distribution in the aquifer is as follows:

$$T=T_0+\frac{T_w-T_0}{2}(erfc(\frac{x-vt}{2\sqrt{Dt}})+\mathrm{e}^{\frac{xv}{D}}erfc(\frac{x+vt}{2\sqrt{Dt}})) \tag{2.22}$$

where T_0 is the initial temperature of the aquifer; D is the thermal diffusivity of the aquifer with $D=\frac{\lambda}{(\rho c)}$; λ is the thermal conductivity of the aquifer; $v=q\frac{(\rho c)_f}{(\rho c)}$ is the thermal

advection velocity, q is the water velocity. This analytical solution is a planar solution that considers both heat advection and conduction in the aquifer, but neglects the heat exchange at the interface between the aquifer and overburden layer.

Barends (2010) improved Lauwerier's planar analytical solution by taking into account both heat advection and heat conduction in the aquifer, as well as the heat exchange at the interface between the aquifer and overburden layer. The Barends' planar analytical solution is also derived with Laplace transformation, which is as follows:

$$T_2 = T_0 + \frac{2(T_w - T_0)}{\sqrt{\pi}} \mathrm{e}^{\frac{xv}{2D}} \int_{\frac{x}{2\sqrt{Dt}}}^{\infty} \mathrm{e}^{-\sigma^2 - (\frac{xv}{4D\sigma})^2} erfc((\frac{x^2 h_2 \sqrt{D_2}}{8DH\sigma^2} + \frac{y}{2\sqrt{D_2}})(t - \frac{x^2}{4D\sigma^2})^{-0.5}) \mathrm{d}\sigma \quad (2.23)$$

where T_2 is the temperature of the overburden layer and the temperature of the aquifer layer when $y = 0$; $h_2 = \frac{(\rho c)_2}{\rho c}$, $(\rho c)_2$ is the heat capacity of the overburden layer; H is the thickness of the aquifer layer; D_2 is the thermal diffusivity of the overburden layer; $v = q\frac{(\rho c)_f}{(\rho c)}$ is the thermal advection velocity, q is the water velocity.

Barends (2010) also proposed an axis-symmetric analytical solution of radial convective-diffusive heat transport for a single injection well, taking into account the heat exchange at the interface between the aquifer and overburden layer. However, because of the mathematical difficulties, this analytical solution is actually an approximate solution by considering in two steps: (1) without thermal conduction in the aquifer and (2) without the heat exchange at the interface. The piece-wise solutions are as follows:

$$T = T_0 + (T_w - T_0) erfc[\frac{h_2 \vartheta \sqrt{D_2}}{2H\sqrt{t - \vartheta}}],\ r < \sqrt{a^2 + 4\alpha D(t - t_0)} \quad (2.24)$$

$$T = T_0 + (T_w - T_0)\frac{\Gamma[\alpha, \eta^2]}{\Gamma[\alpha]},\ \sqrt{a^2 + 4\alpha D(t - t_0)} < r < \sqrt{a^2 + 4\alpha Dt / R} \quad (2.25)$$

where a is the radius of the injection well; t_0 is the time required to heat or cool the soil within the radius a; α is the dimensionless injection rate; R is the delay factor; $\vartheta = \frac{r^2 - a^2}{4D_r}$, $D_r = \frac{QR}{4\pi nH}$, Q is the volumetric injection rate; $\eta = \frac{r}{2\sqrt{Dt}}$; $\Gamma(\alpha)$ is the Gamma Function and $\Gamma(\alpha, \eta^2)$ is the Incomplete Gamma Function.

Tan et al. (2012) proposed a planar analytical solution that includes both heat advection and conduction in the aquifer, with a convective heat transfer boundary condition ($w_0 = h(T - T_0)$, h is the heat transfer coefficient, T_0 is the reference temperature) at the interface between the aquifer and overburden layer, which is shown in Figure 2.5.

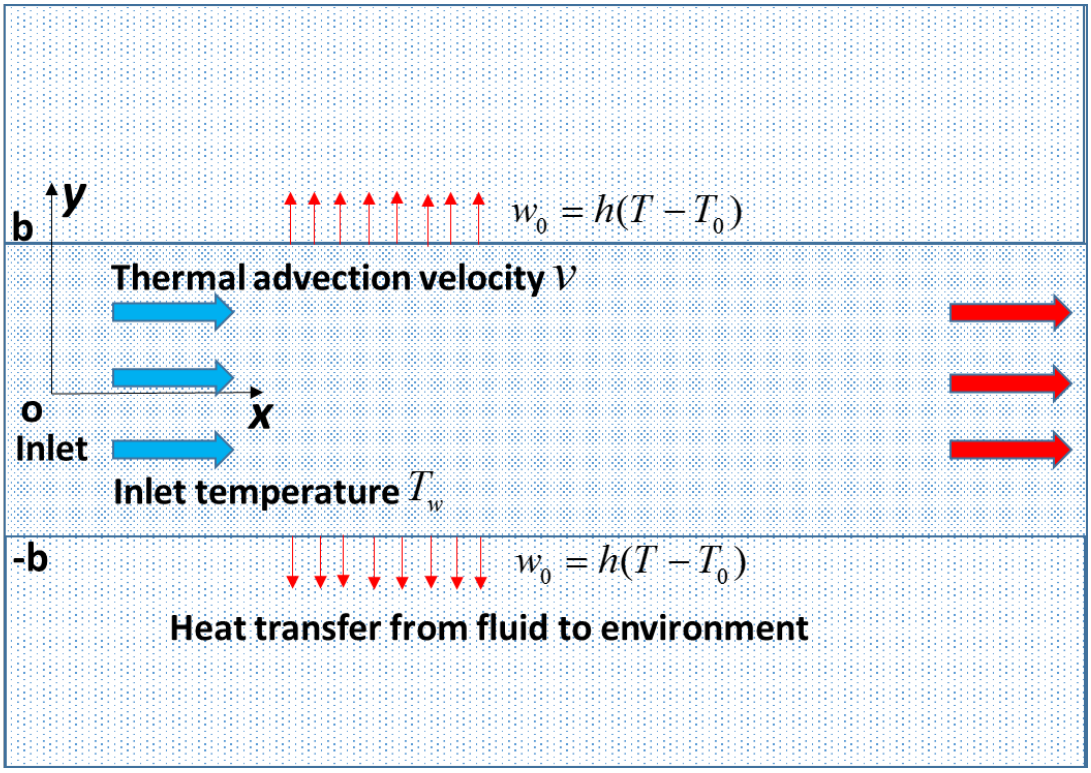

Figure 2.5: A planar model under convective heat transfer boundary condition

After a series of Laplace transformation, the analytical solution can be derived as follows:

$$T = T_0 + \frac{(T_w - T_0)}{2} \cdot \mathrm{e}^{\frac{vx}{2D}} \left(\mathrm{e}^{-\frac{x\sqrt{\frac{v^2\rho cb+8hD}{\rho cb}}}{2D}} \cdot erfc\left(\frac{x}{2\sqrt{Dt}} + \frac{\sqrt{\frac{v^2\rho cb+8hD}{\rho cb}} \cdot \sqrt{Dt}}{2D}\right) \right.$$
$$\left. + \mathrm{e}^{\frac{x\sqrt{\frac{v^2\rho cb+8hD}{\rho cb}}}{2D}} \cdot erfc\left(\frac{x}{2\sqrt{Dt}} - \frac{\sqrt{\frac{v^2\rho cb+8hD}{\rho cb}} \cdot \sqrt{Dt}}{2D}\right) \right) \tag{2.26}$$

where T_w is the temperature of the injected water.

2.1.4 Discussion

The advantages of the Line Source Models and the Cylindrical-Source Models are that they can solve a lot of problems concerning heat conduction. However, both models cannot include the process of heat advection, which is very important in the application of deep geothermal energy as the heat has to be extracted and used via the medium of water. On the other hand, Lauwerier Model is capable of solving the problems concerning heat conduction, heat advection and hydro-thermal coupling. Therefore, the application of Lauwerier-type models is preferable when it comes to the study of the deep geothermal energy.

A list of the advantages and limitations of different analytical solutions based on Lauwerier Model is given in Table 2.1. In this study, an improved axis-symmetric Lauwerier model is proposed and introduced in Chapter 3.

Table 2.1: Comparison between different analytical solutions based on Lauwerier Model

Model	**Advantages**	**Limitations**
Lauwerier (1955)	It takes into account the advection in the aquifer and heat exchange at the interface between the aquifer layer and overburden layer. The	It neglects the heat conduction in the aquifer layer which can affect the temperature of the extracted water. Besides, it is a planar model where the fluid

	expression is concise and easy to use.	velocity is constant but in most practical cases it is not constant.
Ogata and Banks (1961)	It considers both the heat conduction and heat advection in the aquifer layer. The expression is easy to calculate.	It neglects the heat exchange between the aquifer layer and overburden layer which can affect the temperature of the extracted water. Besides, it is a planar model where the fluid velocity is constant but in most practical cases it is not constant.
Barends (2010) planar	It considers more factors than other solutions: the heat conduction and heat advection in the aquifer and heat exchange at the interface between the aquifer and overburden layer.	It is a planar model where the fluid velocity is constant but in most practical cases it is not constant. The expressions are complicated and it is even difficult to draw the figure using the computer.
Barends (2010) axi-symmetric	It is an axi-symmetric model considering the fluid velocity around a well which is closer to the practical cases than the constant velocity planar model.	Its expression is piece-wise and neglects the heat exchange at the interface in the first section and heat conduction in the aquifer in the second section which will make the solution less accurate.

Tan et al. (2012)	It considers more factors than other solutions: both the heat conduction and advection in the aquifer and the heat exchange at the interface using the heat transfer boundary condition.	It is a planar model where the fluid velocity is constant but in most practical cases it is not constant. The expressions are complicated.

2.2 Analytical Solutions for a Doublet System

A typical geothermal doublet system includes one injection well and one extraction well. Generally hot water is extracted via the extraction well then reinjected into the injection well after the hot water is used for heating buildings or generating electricity and eventually becomes cold again. The injected cold water is usually pumped via the injection well to a very deep aquifer layer in the ground, with a depth ranging from 3 kilometres to 5 kilometres. The cold water then flows outwards radially from the injection well through the voids or fractures of the aquifer layer and is heated up by the hot soils or rocks. The heated water will finally reach the extraction well again and will be pumped upwards to the ground surface. By this means, it forms a cycled and sustainable system.

2.2.1 Analytical Solutions without Interaction between Two Wells

Bodvarsson and Tsang (1982) considered the problem of cold water injection into a fractured geothermal reservoir. During injection, the cold water advances along the fractures, gradually extracts heat from the adjacent rock matrix, and eventually arrives at the production well. If the injected water has not fully been heated by then, detrimental effects on energy production from decreasing fluid enthalpies may result. They used an analytical solution in the design of injection/production systems, mainly for determining the appropriate locations and the flow rates of the injection wells, and to estimate the amount of recoverable energy from the

geothermal system based on a given injection/production scheme once temperature contour maps are given.

The analytical model they used is an axis-symmetric model neglecting the influence of the extraction well, therefore it is actually a single well model similar to the Lauwerier's model in Section 2.1.3 with nearly the same assumptions, as shown in Figure 2.6.

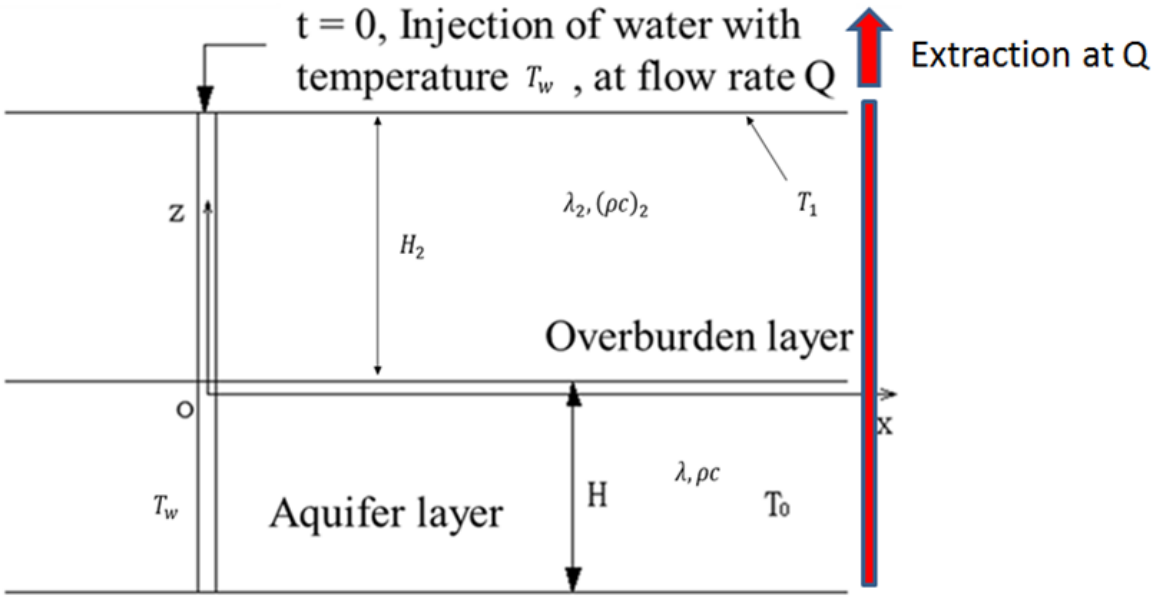

Figure 2.6: An axis-symmetric model without the interaction between two wells

The governing differential equations are as follows:

$$\rho c \frac{\partial T}{\partial t} + \frac{1}{2\pi r} \frac{(\rho c)_f Q}{H} \frac{\partial T}{\partial r} - \frac{\lambda_2}{H} \left(\frac{\partial T_2}{\partial z}\right)_{z=0} = 0 \tag{2.27}$$

$$\frac{\partial^2 T_2}{\partial z^2} = \frac{(\rho c)_2}{\lambda_2} \frac{\partial T_2}{\partial t} \tag{2.28}$$

where T is the temperature of the aquifer layer and T_2 is the temperature of the overburden layer; ρc is the heat capacity of the aquifer layer; $(\rho c)_f$ is the heat capacity of water; $(\rho c)_2$ is the heat capacity of the overburden layer; H is the thickness of the aquifer layer; Q is the volumetric injection rate; λ_2 is the thermal conductivity of the overburden layer.

It can also be seen from Equation (2.27) that the model is axis-symmetric without the influence of the extraction well as it assumes the flow rate in the aquifer layer is $q = \frac{Q}{2\pi rH}$, which will not be the case if the influence of the extraction well is considered. Besides, the analytical model neglects the thermal conductivity of the aquifer layer.

After a series of Laplace transformation, the solutions in the Laplace domain can be obtained. However, they could not invert the solutions analytically from the Laplace domain so that a numerical inverter was used. In other words, the solution for their model is a numerical solution instead of an analytical solution.

2.2.2 Analytical Solutions with Interaction between Two Wells

Gringarten and Sauty (1975) gave a solution of the temperature at the extraction well by considering a stream channel between the injection well and the extraction well, as shown in Figure 2.7.

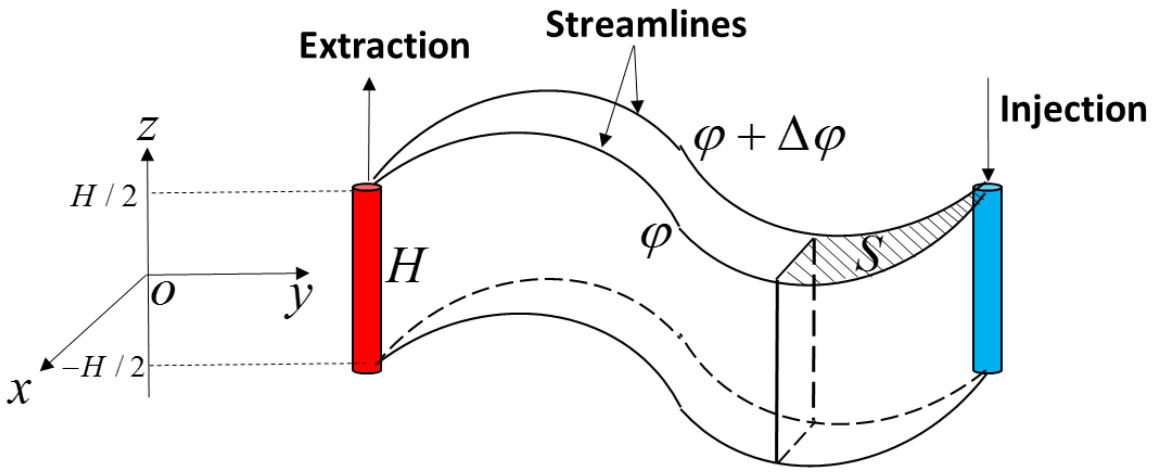

Figure 2.7: Visualization of a stream channel

The differential equation governing the water temperature T within a stream channel is obtained by heat balance on an element of stream channel from the injection well, which is as follows:

$$\frac{H}{2}(\rho c)\frac{\partial T(S,t)}{\partial t}+\frac{q}{2}(\rho c)_f\frac{\partial T(S,t)}{\partial S}=\lambda_2\frac{\partial T(S,z,t)}{\partial z}_{z=H/2} \tag{2.29}$$

where q is the rate of flow within the stream channel, $(\rho c)_f$ is the water heat capacity, (ρc) is the aquifer heat capacity, and λ_2 is the cap rock thermal conductivity.

If the streamlines leaving an injection well reach an extraction well, the water temperature at that extraction well within an elementary stream channel is obtained by substituting the total stream channel area between the two wells, $S_{\max}$ (Except in a few simple cases, $S_{\max}$ must be calculated numerically). The result can be written in terms of dimensionless parameters as:

$$\frac{T-T_0}{T_w-T_0}=erfc\{\frac{d(S_{\max}/L_D{}^2)}{d(\varphi/Q)}[\lambda_D(t_D-\frac{d(S_{\max}/L_D{}^2)}{d(\varphi/Q)})]^{-1/2}\} \tag{2.30}$$

where $\lambda_D=[(\rho c)_f(\rho c)/\lambda_2(\rho c)_2](QH/L_D{}^2)$, $t_D=[(\rho c)_f/(\rho c)](Qt/L_D{}^2H)$, L_D is some characteristic length, and $d(S_{\max}/L_D{}^2)/d(\varphi/Q)$ is the dimensionless derivative of the total stream channel area with respect to the stream function. Heat transfer between the aquifer and the cap rock or bedrock is negligible for $\lambda_D\geq 10^4$.

Clyde and Madabhushi (1983) discussed the risk of failure of thermal well-doublet systems where naturally cold groundwater is extracted and warmed water is reinjected to the aquifer. Ideally (Figure 2.8), the injection well would be located down the hydraulic gradient from the extraction well, in the hope that natural groundwater flow would carry the reinjected warm water away from the scheme in a "thermal plume". The neat scenario in Figure 2.8 will only happen if L (the well separation) is relatively large and if Q (volumetric injection rate) is relatively small. In fact, the thermal plume will only fully disappear down-gradient if:

$$L>\frac{2Q}{\pi i T_T} \tag{2.31}$$

where T_T = aquifer transmissivity and i = regional natural hydraulic gradient.

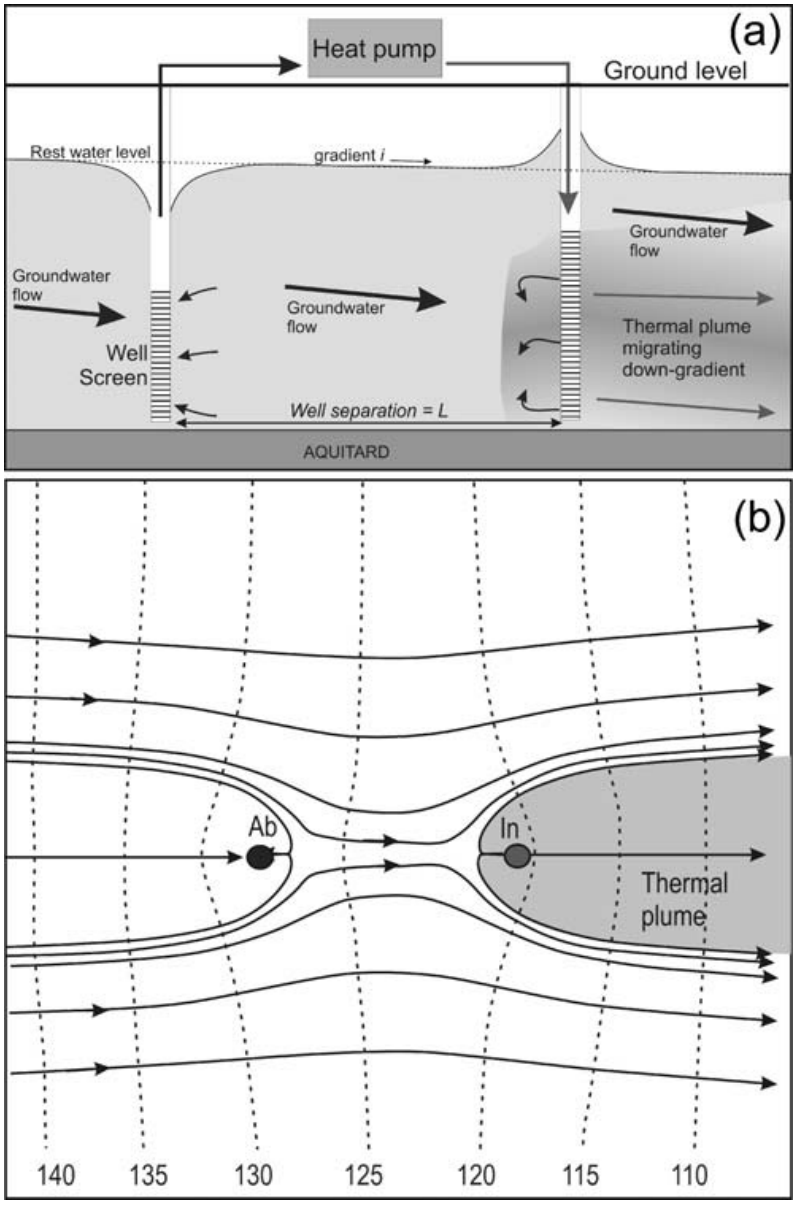

Figure 2.8: (a) Section view and (b) Plan view of a well-doublet system for cooling where no hydraulic feedback occurs (Clyde and Madabhushi, 1983)

Banks (2012) discussed the thermal breakthrough time in detail. The formulae for one-dimensional advective/dispersive transport of a sorbed chemical solute (Equation (2.32); Domenico and Schwartz, 1990) and of heat (Equation (2.33); De Marily, 1986) are as follows:

$$\frac{D_x}{R_f}\frac{d^2C_C}{dx^2} - \frac{1}{R_f}\frac{d(q_xC_C)}{dx} = \frac{dC_C}{dt} \tag{2.32}$$

where D_x is a dispersion coefficient, q_x is the linear velocity of groundwater flow and C_C is solute concentration, R_f is the solute retardation factor.

$$\frac{\lambda_e}{(\rho c)}\frac{d^2T}{dx^2}-\frac{n(\rho c)_f}{(\rho c)}\frac{d(q_xT)}{dx}=\frac{dT}{dt} \tag{2.33}$$

λ_e is an effective thermal conductivity that also takes into account a hydrodynamic dispersion effect, (ρc) is the volumetric heat capacity of the saturated aquifer. The parameter $\frac{(\rho c)}{n(\rho c)_f}$ is thus analogous to R_f and a thermal retardation factor R (Bodvarsson, 1972) can be defined:

$$R=\frac{q_{hyd}}{v}=\frac{(\rho c)}{n(\rho c)_f} \tag{2.34}$$

where v is the velocity of a thermal front and q_{hyd} is the hydraulic velocity of a water molecule. Therefore, the thermal breakthrough time t_{the} can be deducted as follows (Gringarten, 1978; Clyde and Madabhushi, 1983; Banks, 2008):

$$t_{the}=\pi H\frac{(\rho c)L^2}{3(\rho c)_f Q}\ for\ i=0 \tag{2.35}$$

$$t_{the}=\frac{(\rho c)L}{(\rho c)_f Ki}[1+\frac{4\alpha_1}{\sqrt{-1-4\alpha_1}}\tan^{-1}(\frac{1}{\sqrt{-1-4\alpha_1}})]\ for\ i<0 \tag{2.36}$$

where $\alpha_1=\frac{Q}{2\pi KHiL}$, H is the aquifer thickness, K is the hydraulic conductivity.

Barker (2010) developed a model to investigate heat transport between an injection well and an extraction well both pumping at the same rate in a fractured porous rock, as shown in Figure 2.9. The figure shows direct and indirect flow paths between two wells. The angle of entry of the path into the extraction well is used to characterize a flow path. For direct flow between two wells, $\tau(0)=1$, the flow leaving one well in the opposite direction to the other well is, in

principle, passing along a circle of infinite diameter and hence the travel time is infinite, and thus $\tau(\pm\pi) = \infty$. Barker also stated that the flow leaving one well perpendicular to the line between two wells takes three times the direct flow time, $\tau(\pi / 2) = 3$, which is identical to the time required for a flow if only one well were pumping.

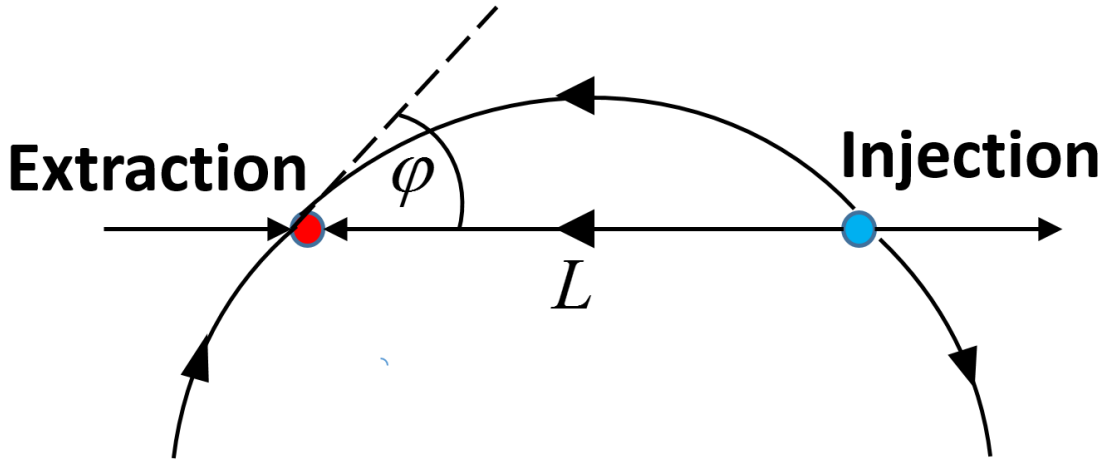

Figure 2.9: The flow lines across a doublet are circles through the well centres. Direct flow is along a circle of infinite radius

Using a series of numerical simulation of the problem, Lipmann and Tsang (2010) provided an empirical formula for predicting how the temperature of the extracted water T will evolve, following thermal breakthrough (for time $t > t_{the}$):

$$\frac{T - T_w}{T_0 - T_w} = 0.34\exp(-0.0023\frac{t}{t_{the}}) + 0.34\exp(-0.109\frac{t}{t_{the}}) + 1.37\exp(-1.33\frac{t}{t_{the}}) \qquad (2.37)$$

where T_w is the temperature of the injected water (which is assumed to be constant, although in a real operation it may increase as the temperature of the extracted water increases), T_0 is the initial ambient groundwater temperature, t is time following commencement of extraction/injection and t_{the} is the thermal breakthrough time.

2.2.3 Discussion

The analytical solutions without the interaction between injection well and extraction well are actually a single well model so that analytical solutions based on Lauwerier Model can be directly used to give the expressions of the temperature distribution, the optimal location of the extraction well and the amount of extracted energy. However, if the distance between the two wells is small, the interaction between the two wells will be very intense so that the associated errors will be very large.

Generally, there is no analytical solution that gives the temperature distribution in the aquifer, the temperature at the extraction well or the optimal location of the extraction well if the interaction between two wells is considered. At the moment, there are only some expressions for the temperature at the extraction well that are obtained by numerical methods. In this study, we propose to develop a new set of analytical solutions for the problem.

2.3 Fracture Flow

2.3.1 Introduction

In deep geothermal energy utilization, water mainly flows through the fractures of the rocks. Therefore, it is significant to study the properties and modelling of the fracture flow. Fracture flow is usually idealized as flow through the space bounded by two parallel plates (Ranjith and Viete, 2011). The total area for the free flow is given as follows:

$$S = wd \tag{2.38}$$

where w is the width of the fracture joint and d is the hydraulic aperture.

For such a parallel plate model, Witherspoon et al. (1979) gave an expression of permeability of Darcian incompressible flow through a fracture:

$$k_f = \frac{d^2 \rho \mathrm{g}}{12} \tag{2.39}$$

where ρ is the fluid density; and g is gravity acceleration.

The Darcy's Law for flow of an incompressible fluid through a fracture is as follows:

$$\frac{\mathrm{d}p}{\mathrm{d}x} = Q \frac{12\mu}{d^3 w \rho g} \tag{2.40}$$

and

$$d = \left(\frac{12Q\mu}{w\rho g} \frac{\mathrm{d}x}{\mathrm{d}p}\right)^{\frac{1}{3}} \tag{2.41}$$

For the Darcian flow of a compressible fluid through a fracture,

$$\frac{p_i^2 - p_0^2}{2pL} = Q \frac{12\mu}{d^3 w \rho g} \tag{2.42}$$

And

$$d = \left(\frac{12Q\mu}{w\rho g} \frac{2pL}{p_i^2 - p_0^2}\right)^{\frac{1}{3}} \tag{2.43}$$

The expression of k_f can also be written as follows (Kim et al., 2003):

$$k_f = \frac{d^2}{12 f_r} \tag{2.44}$$

where d is mean aperture width; f_r is the surface roughness factor varied from 1.04 to 1.65. Lomize (1951) offered the experimental form:

$$f_r = 1 + 6(\frac{\delta d}{d})^{1.5} \tag{2.45}$$

where δd is a measure of the surface roughness (asperity heights). Walsh and Brace (1984) proposed $f_r = T_{tor}{}^2$, where T_{tor} is a mean fracture tortuosity (ratio of actual to apparent path lengths).

Zimmerman and Bodvarsson (1996) proposed:

$$k_f = \frac{d^2}{12}(1 - \frac{3\sigma_d^2}{2d^2})(1 - 2C_f) \tag{2.46}$$

where σ_d is the standard deviation of the aperture width and C_f is the fractional contact area between two surfaces.

Research on fluid flow in fractures and in fractured porous media has a long history (Barenblatt et al., 1960; Warren and Root, 1963). The research focused on four main aspects of fracture flow: (1) conceptual model development; (2) analytical and numerical solution scheme development; (3) description of fracture hydraulic characteristics in static and deforming media; and (4) development of stochastic methods to describe fracture flow and hydrogeologic parameter distributions.

Several conceptual models describing flow through fractured porous media have been developed. Each model can be categorized according to the storage and flow capabilities of the porous medium and the fracture. The storage characteristics are associated with porosity while the flow characteristics are connected with permeability. There are four main conceptual models: (1) explicit discrete fracture; (2) dual continuum; (3) discrete fracture network; and (4) single equivalent continuum. There are also other models such as multiple-interacting continua model and multiporosity/multipermeability models.

There are also other differences between these methods based on the spatial and temporal scales of integration or averaging of the flow regime. Berkowitz et al. (1988) noted four scales of concerns of the fracture flow: (1) the very near field, where flow takes place in a single fracture

and porous medium exchange is possible. (2) the near field, where flow occurs in a fractured porous medium and each fracture is described in detail; (3) the far field, where flow occurs in two overlapping continua with mass exchanged through coupling parameters; and (4) the very far field, where fracture flow occurs in an equivalent porous medium.

There are already several numerical models including explicit discrete representations of fractures. The discrete-fracture models can explicitly represent the fluid potential gradients and fluxes between fractures and porous media with minimal non-physical parameterization. However, the acquisition of the data can be laborious if there are too many fractures. Besides the computational burden can increase significantly with the increase of the fracture number.

Dual-continuum methods were proposed by Barenblatt et al. (1960) and extended by Warren and Root (1963). Dual-continuum models are based on the idealized flow medium including a primary porosity by deposition and lithification and a secondary porosity by fracturing, jointing or dissolution (see Figure 2.10 and Figure 2.11). Unfractured rock masses account for much of the porosity of the medium but little of the permeability. On the other hand, fractures have high permeability but almost no storage. Hence the porous medium and fractures are viewed as two separate but overlapping continua. Fluid heat transfer between porous media and fractures take place at the interface of fracture-porous medium.

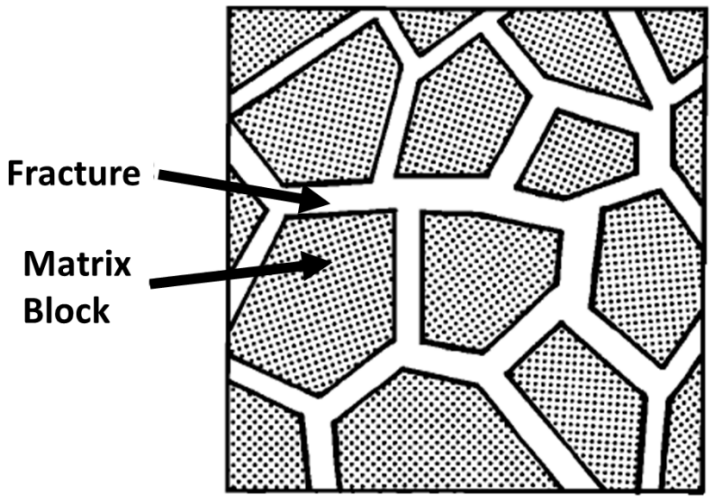

Figure 2.10: Dual-Continuum model (Barenblatt et al., 1960)

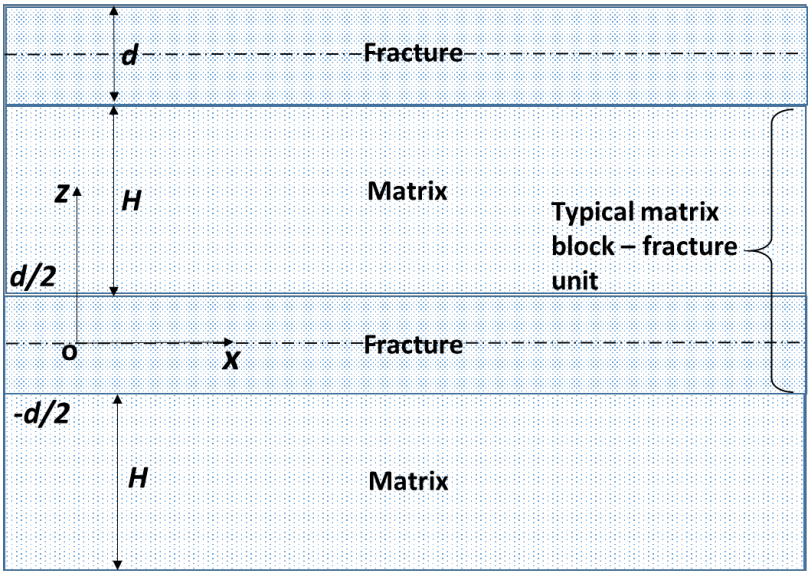

Figure 2.11: Dual-porosity parallel fracture model

Discrete-fracture network models are a class of dual-continuum models in which the porous medium is not represented. All flow is restricted to the fractures. This idealization approach reduces the computational burdens. Fracture "legs" are usually represented with lines or planes in two or three dimensions (Diodato, 1994), as shown in Figure 2.12.

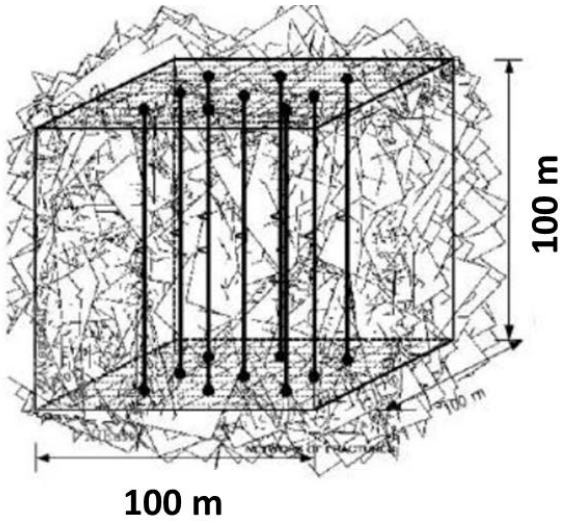

Figure 2.12: Discrete Fracture Network (Diodato, 1994)

In the Single Equivalent Continuum Model, the volume considered is large enough that the permeability is a sum of fracture and porous media permeability. This approximation can

significantly simplify the problem. Pruess et al. (1986) proposed a model for a single equivalent continuum in unsaturated fractured rock where hydraulic conductivity was taken as a sum of hydraulic conductivity from the fracture and porous media. Pruess et al. (1990a,b) found that the approach was unacceptable when the flow velocity and fracture spacings are large and the permeability of the rock matrix is low. General speaking, if the scales of integration are large enough, the single equivalent continuum method will work well.

2.3.2 Fracture Flow Modelling

Martin et al. (2005) proposed a domain decomposition approach for fracture flow modelling. The model consists of two separated subdomains divided by an internal boundary. Each subdomain represents a porous media and the internal boundary represents a fracture. The model is derived through a process of averaging across the fracture, and obtains a flow equation along the fracture that is coupled with flow equations in the porous media through Robin type conditions imposed at the interface.

Romano-Perez & Diaz-Viera (2015) used a Discrete Fracture Model to model the fracture flow where the fracture is treated as an interior boundary. The fracture is usually a very long and narrow domain with high aspect ratio within a very wide porous block of rock. Discretizing the fracture domain explicitly requires a very dense mesh consisting of a huge number of infinitesimally small elements. Discrete fracture model approach basically consists in representing fractures as (n-1) dimensional objects in an n-dimensional domain, i.e., in 2D fractures could be represented by line segments and in 3D by polygons, respectively. The advantage of this approach is in reducing the degrees of freedom and enhancing computational performance particularly for the cases in which the fracture permeability is higher than the surrounding porous medium.

Bakhsh et al. (2016) provided a simple conceptual model to investigate the behaviour of a doublet system. The thermal performance of the system is assessed based on advancement of the cold front in a reservoir. The effect of high permeability induced or pre-existing natural fracture on reservoir thermal breakthrough time and geometry of the heat transfer volume are expected. Numerical simulation was conducted using commercial software, COMSOL

Multiphysics, as shown in Figure 2.13. To avoid high aspect ratio geometry in the model, the fracture is considered as an interior boundary. At boundaries, flow is defined normal instead of tangent to the boundary plane. To govern the velocity field along the fracture, Darcy's law equation must be modified in this boundary condition. The modification is applied to the equation by accounting for fracture thickness:

$$d\frac{\partial}{\partial t}(n_f\rho_{fr}) + \nabla_t \cdot (d\rho_{fr}u) = 0 \quad y,z \in \partial\Omega_f \tag{2.47}$$

$$u = -\frac{k_f}{\mu}\nabla_t p \quad y,z \in \partial\Omega_f \tag{2.48}$$

where, d is the fracture's thickness (m), n_f is the fracture porosity (dimensionless), ρ_{fr} is the fracture density (kg/m^3), u gives the modified Darcy's velocity on the fracture (m/s), k_f is the permeability of the fracture (m^2), μ is the fluid dynamic viscosity (Pa$\cdot$s). To restrict the equations to the fracture's plane, ∇_t, the tangential gradient operator is applied for flow in the fracture.

The Neumann boundary condition is applied for mass flow at the fracture edge intersected with the matrix block and hence, no-flow condition is applied on fracture's edges:

$$n \cdot u = 0 \quad \text{at } \partial^2\Omega_f \text{ fracture edges} \tag{2.49}$$

To calculate heat transfer in the fracture, the heat transport equation in a porous matrix needs to be modified to account for the fracture thickness:

$$d(\rho c)\frac{\partial T}{\partial t} + d(\rho c)u \cdot \nabla_t T + \nabla_t \cdot q_f = n \cdot q' \tag{2.50}$$

$$q_f = -d\lambda\nabla_t T \tag{2.51}$$

$$(\rho c) = (1-n_f)(\rho c)_{fr} + n_f(\rho c)_f \tag{2.52}$$

$$\lambda = (1 - n_f)\lambda_{fr} + n_f \lambda_f \tag{2.53}$$

where, (ρc) is the effective volumetric heat capacity of the fracture-fluid volume at constant pressure ($J/(m^3K)$). The third term in the left hand side of Equation (2.50) represents the conductive heat flux in the fracture-fluid volume where the computational domain is restricted by the tangential gradient and the term on the right gives the heat supply through the fracture walls by conduction.

As the fluid moves faster through the fractures and relatively slower through the surrounding porous media, the temperature field of the domain follows a similar pattern with the fracture plane becoming cooler than the surrounding porous media, as shown in Figure 2.14.

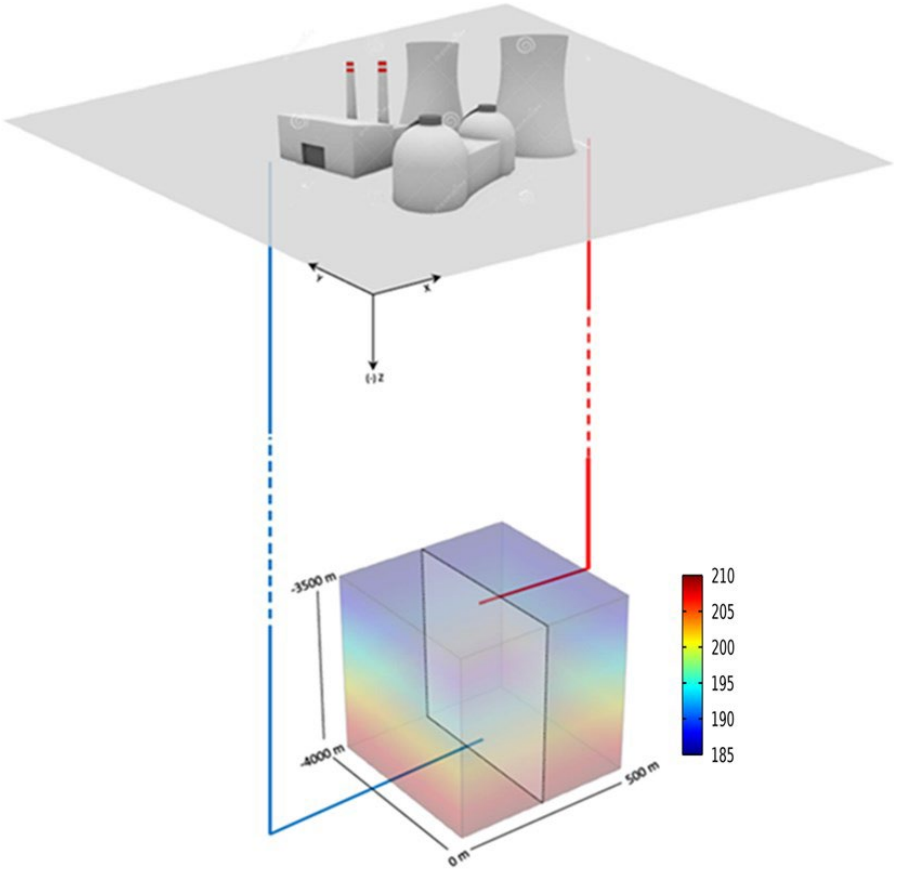

Figure 2.13: scheme of the conceptual fractured sedimentary basin located in a region with temperature gradient of 0.05 Kelvin per meter (Bakhsh et al., 2016)

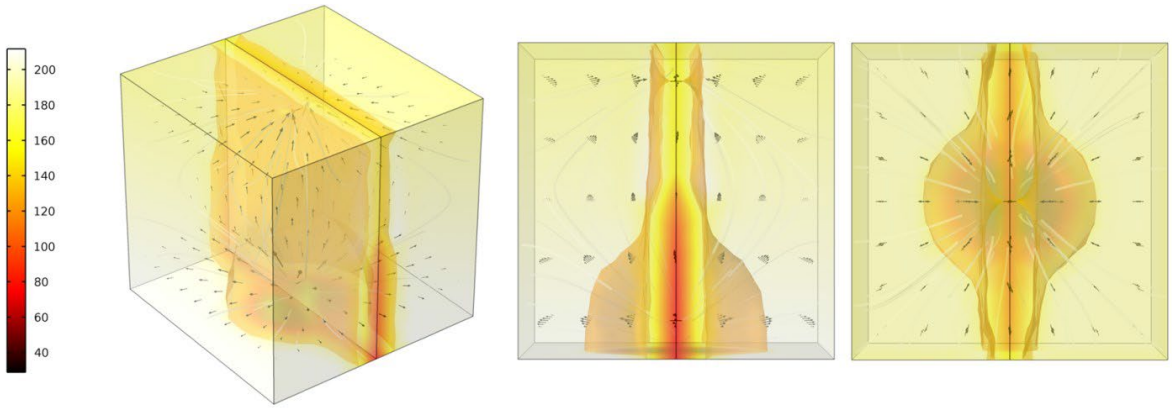

Figure 2.14: Hydraulic and thermal performance of the benchmark reservoir model over 30 years of heat extraction a) isometric view b) side view c) plan view (Bakhsh et al., 2016)

Zhao et al. (2011) developed a hybrid approach combining discrete element method (DEM) for stress-flow simulations and a particle tracking algorithm to systematically investigate the influence of stress on solute transport in fractured rocks for the first time, considering different stress and hydraulic pressure conditions. The flow chart of this approach is shown in Figure 2.15. The numerical results show that stress not only significantly changes the solute residence time through the fractured networks, but also changes the solute travel paths. Matrix diffusion plays a dominant role in solute transport when the hydraulic gradient is small, which is often encountered in practice.

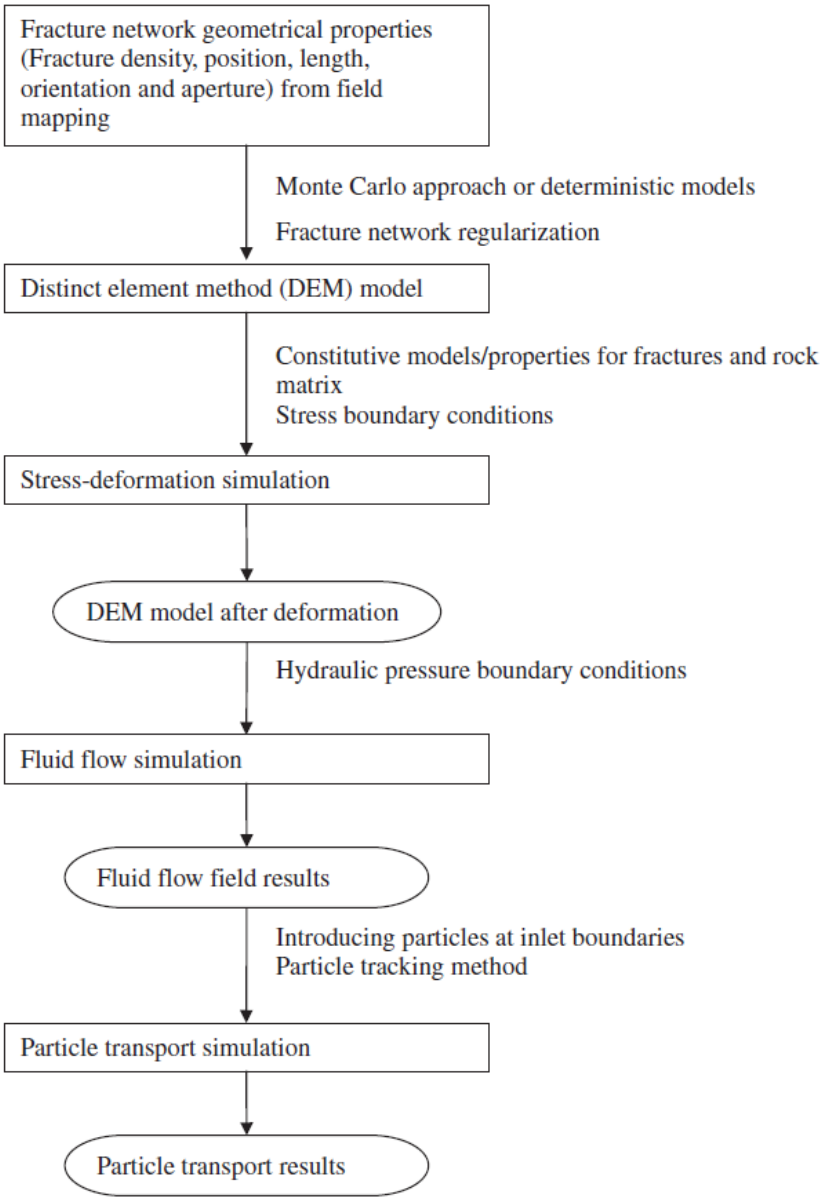

Figure 2.15: Flow chart for coupled stress-flow-transport simulation in fractured rocks (Zhao et al., 2011)

Zou et al. (2015) investigated the effects of wall surface roughness on fluid flow through rock fractures. A wavelet analysis technique was developed to define a mathematical criterion for decomposing the original wall surface roughness profiles of a fracture into a high-frequency (secondary roughness) profile and a low-frequency (primary roughness) profile, in order to examine their impacts on fluid flow, by solving the Navier-Stokes equations without linearization, using a self-developed 2D finite volume method (FVM) code. The results

indicated that the high-frequency secondary roughness is the main cause for dynamic evolution of Eddy flow regions in the fracture flow field, besides the Reynolds number (Re).

Noetinger (2015) proposed an original method allowing transient pressure diffusion in the Discrete Fracture Networks (DFN), as shown in Figure 2.16. The matrix was assumed to be impervious. A systematic approximation scheme was built, allowing the initial DFN by a set of N unknowns located at each identified intersection between fractures. The main assumption was using a quasi steady state hypothesis, stating that the characteristic diffusion time over one single fracture is negligible compared to the characteristic time of the macroscopic problem.

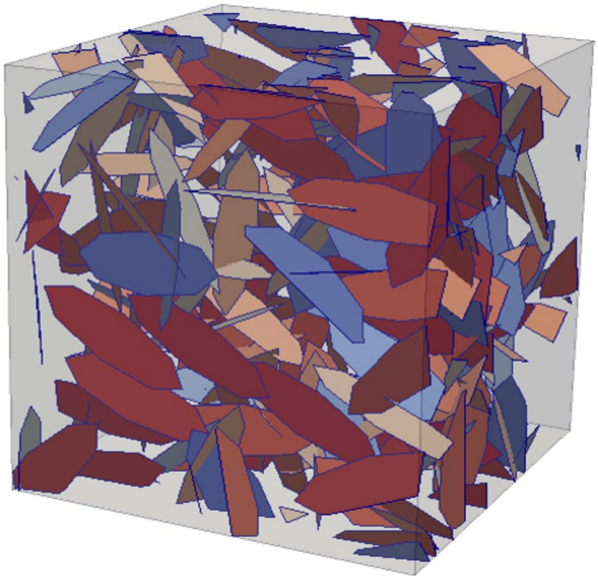

Figure 2.16: 3D network of 2D polygonal fractures in a cubic box (Noetinger, 2015)

Holzbecher et al. (2010) used the commercial software COMSOL to model the fracture flow in a bounded flow field, as shown in Figure 2.17. They used a lower dimensional representation of fracture, i.e. to combine a 1D fracture model with a 2D geometry for low permeable porous medium. This procedure was introduced using the potential and the stream function formulations. The potential values calculated for the fracture in the 1D fracture geometry, are used as boundary conditions in the 2D geometry. For that purpose, they used the COMSOL option to enter “extrusion coupling variables”. Meshing was always made with a drastic refinement near to the fracture. The potential colour plot, streamlines and velocity field with elliptic fracture and two permeable layers are shown in Figure 2.18.

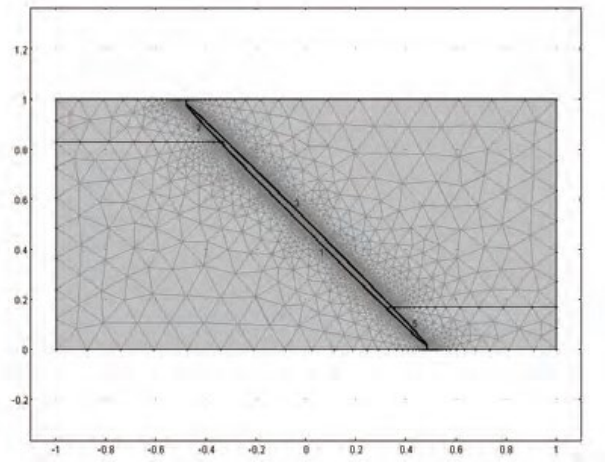

Figure 2.17: Fracture in a bounded flow field (Holzbecher et al., 2010)

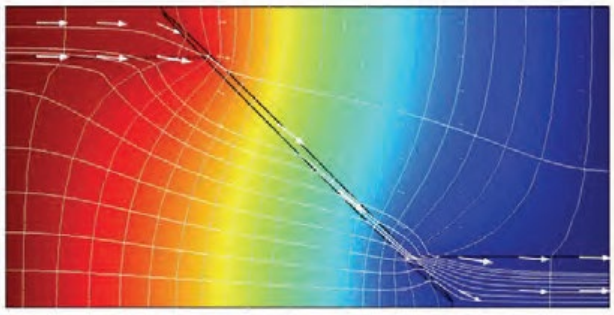

Figure 2.18: Potential colour plot, streamlines and velocity field with elliptic fracture and two permeable layers (Holzbecher et al., 2010)

Wu and Pruess (2000) presented an integral method for analysing transient fluid flow through a fractured medium, which has pressure dependent permeability. Approximate analytical solutions have been obtained for one-dimensional linear and radial flow by an integral-solution technique, in which the density of the fluid, and the porosity and permeability of the formation, are treated as arbitrary functions of pressure. The calculations show that neglect of changes in fracture permeability leads to large errors under the condition of high injection pressure.

Bond et al. (2013) discussed the influence of fracture anisotropy on CO_2 flow. By combining structural geological fracture models with well data and present-day stress information, a permeability tensor can be estimated, leading to significantly improved predictions of CO_2 migration within geological storage sites. To adopt permeability tensors modelled here and to accurately predict the migration anisotropy of injected CO_2 for an active storage site, an

understanding of the interplay of existing tectonic fracture sets with present-day stress is required.

Maryska et al. (2004) conducted numerical simulations of fracture flow with a mixed-hybrid Finite Element Method (FEM) stochastic discrete fracture network model. The fractures are approximated by a network of planar circle disks, which is generated on the basis of statistical data obtained from field measurements. The network is discretized into a mesh consisting of triangular elements placed in three-dimensional space. Geometrical approximations in fracture planes are used, which allow for a significant simplification of the final triangular meshes. Two-dimensional Darcy flow is considered in each fracture. An aperture defining its hydraulic permeability was assigned to each triangle in order to accurately simulate the channelling effect. The lowest order Raviart-Thomas mixed finite element method is applied for the discretization. This method gives quite an accurate velocity field, which is computed directly and satisfies the mass balance on each triangular element. The distribution of the piezometric head in the fracture network is shown in Figure 2.19.

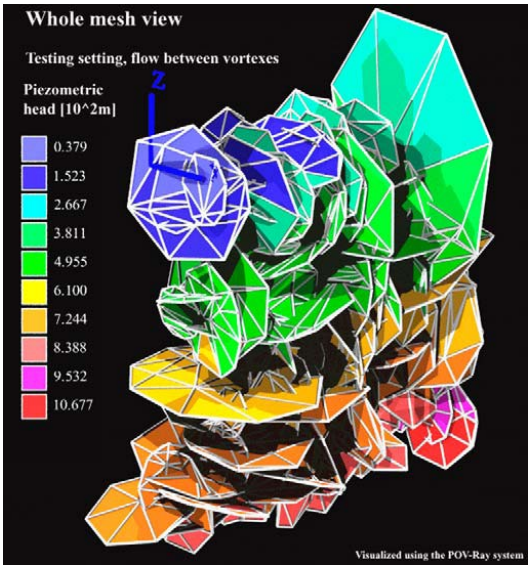

Figure 2.19: Distribution of the piezometric head in the fracture network (Maryska et al., 2004)

Kim et al. (2003) presented numerical computations for single phase flow through three-dimensional digitized rock fractures under varied simulated confining pressures appropriate to midcrustal depths. The computations are performed using a Finite Difference, Lattice Boltzmann method, which simulates Navier-stokes flow. The digitized fracture data sets come

from profile elevations taken on tensile induced fractures in Harcourt granite. Use of the finite difference lattice Boltzmann method allows computation on nonuniform grid spacing, enabling accurate resolution across the aperture width without extensive refinement in the other two directions.

2.3.3 Discussion

In summary, a list of advantages and limitations of different fracture numerical modelling methods is given in Table 2.2.

Table 2.2: Comparisons between different fracture numerical modelling methods

Model	Advantages	Limitations
Explicit Discrete-fracture model	Explicitly represent the fluid potential gradients and fluxes between fractures and porous media.	If there are too many fractures, the acquisition of data can be laborious and the computational burden can be large.
Dual-continuum parallel fracture model	The porous media and fractures are simplified as two separate but overlapping continua.	Because of such simplicity, it is not easy to model one specific fracture in detail.
Discrete-fracture network model	All the fractures in the model are represented in detail and computational burdens are reduced.	The porous media in the model are not represented.
Single Equivalent Continuum model	It is good to model a large scale volume by considering the permeability of the volume	Fractures in the model cannot be represented thus it is not possible to study one

	as a sum of fracture and porous media permeability, which significantly simplifies the problem.	specific fracture in the model.

In terms of the fracture flow problem in the thesis, both fracture and porous media need to be modelled in detail and there is only one fracture in the model. Therefore, the Explicit Discrete-fracture model mentioned above is used in the thesis.

In order to reduce degrees of freedom and enhance computational performance, a technique introduced by Martin et al. (2005), Romano-Perez & Diaz-Viera (2015) and Bakhsh et al. (2016) is applied in the Explicit Discrete-fracture model by treating a fracture as an interior boundary.

2.4 Geothermal Projects and Simulation

2.4.1 Lund (Sweden) Geothermal Heat Pump Project

Satman (2011) discussed the Lund Geothermal Heat Pump Project which is implemented in a confined unconsolidated sandstone reservoir in Scania, the southernmost province in Sweden. After 25 years of heat extraction and reinjection of cold water to the reservoir, the expected cooling was observed. About 550L/s of ground water was extracted from four wells and subsequently reinjected into five wells. 250 GWh of heat energy was produced to the district heating net annually. The distance between the production and injection wells was around 100 metres. The reservoir temperature ranged from 21 to 24 ℃. The injection temperature was 3.5 ~ 5 ℃. The locations of the geothermal wells are shown in Figure 2.20. The production temperatures for all wells from the start of the operation are shown in Figure 2.21. Satman (2011) compared the measured production well temperature with the Gringarten-Sauty solution to obtain some parameters of the doublet system and reservoir, as shown in Figure 2.22. Therefore, the purpose of Figure 2.22 is not to validate the Gringarten-Sauty solution by well

data. In fact, as the extraction rate of Well Sk-2 and the thickness of the aquifer for Well Sk-2 are unknown (only the total amount of water extracted from four wells is known), it is unrealistic to use the well data to validate the Gringarten-Sauty solution.

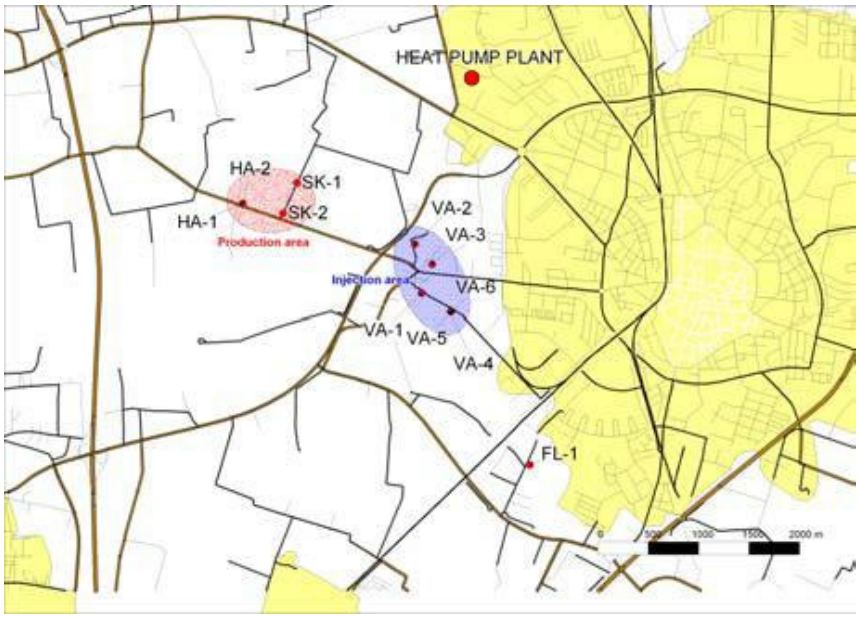

Figure 2.20: Map showing the locations of the geothermal wells west of Lund (Bjelm and Alm, 2010)

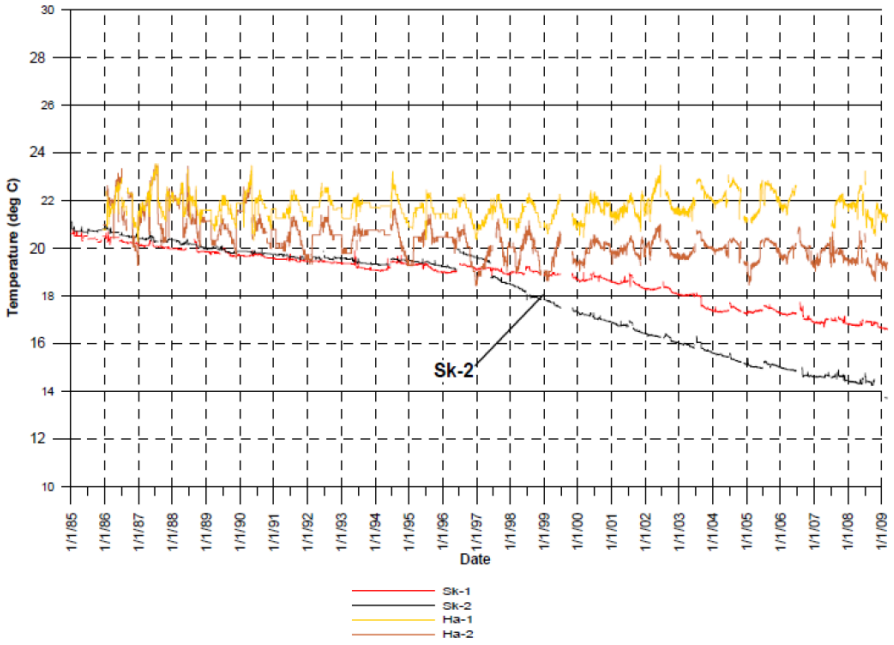

Figure 2.21: Production temperature for the wells since start of operation (Bjelm and Alm, 2010)

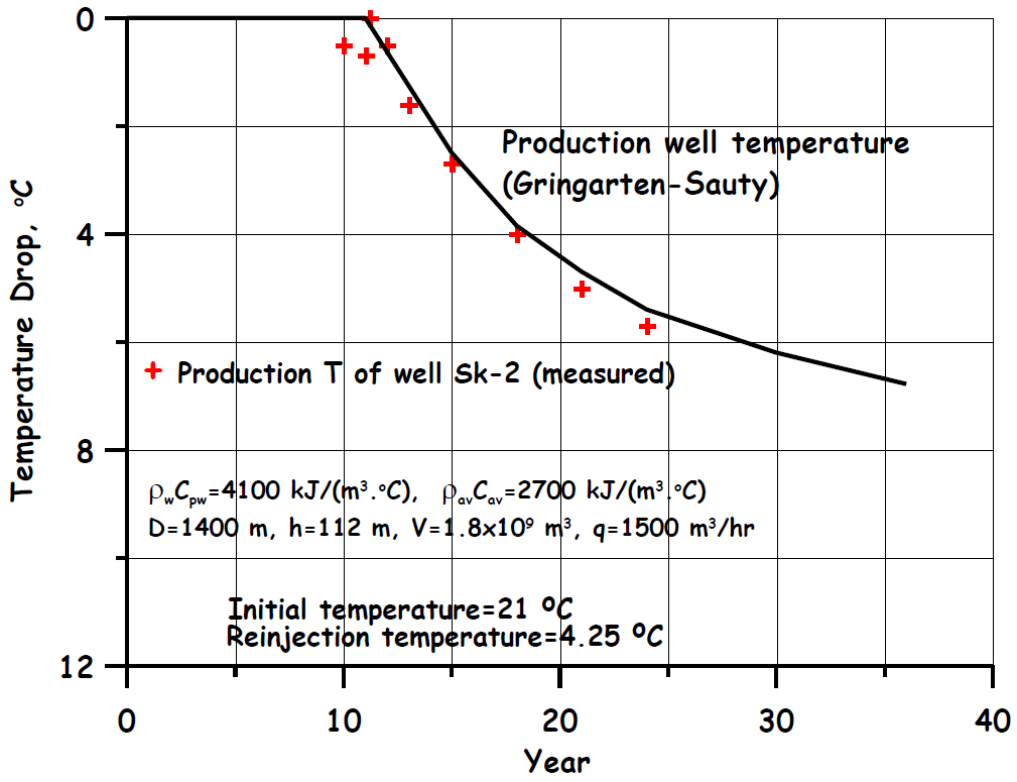

Figure 2.22: Comparison of measured production well temperature versus calculated one (Satman, 2011)

2.4.2 Continental Deep Drillhole (KTB) in Germany

Szalaiova et al. (2015) used the area of the 9.1-km-deep Continental Deep Drillhole (KTB) in Germany as a case study for a geothermal reservoir situated in folded and faulted metamorphic crystalline crust, which is shown in Figure 2.23. A numerical simulation of conductive-advective heat transport was performed with the SHEMAT-Suite code (Clauser, 2003; Rath et al., 2006). The model was based on geological units and fault and fracture distributions obtained from the interpretation of 3-D seismic reflection data. Their model confirmed the previous findings that diffusive heat transport was the dominant process at the KTB site. The modelled and observed temperature data fit well within 0.2 degrees bounds. Although thermal conditions at the site were suitable for geothermal energy production, hydraulic conditions were unfavourable without engineered stimulation.

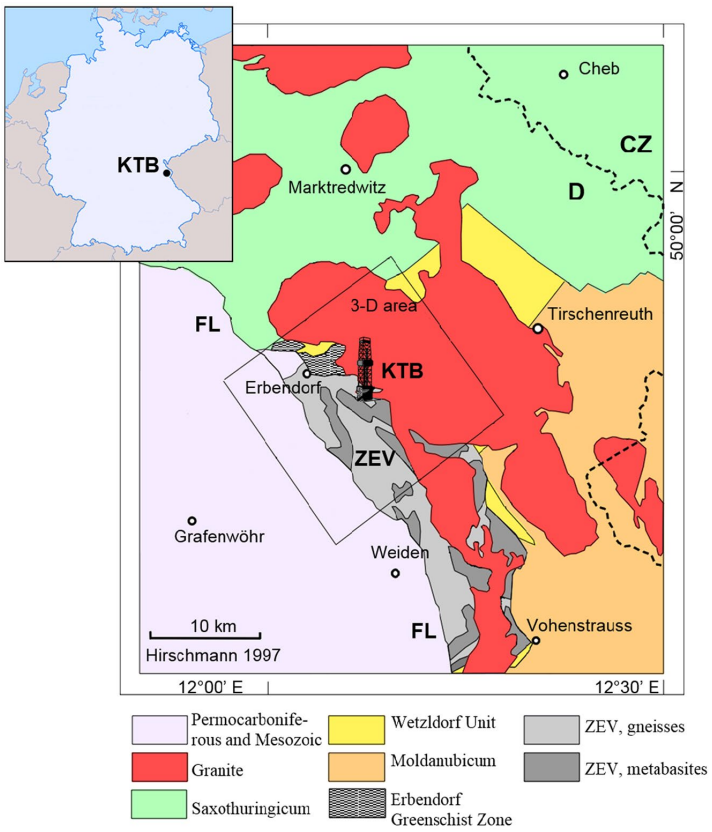

Figure 2.23: Geological map of the area of the KTB drill hole and the area of the 3-D seismic experiment (square) (Szalaiova et al., 2015)

2.4.3 Heat production in a sandstone reservoir in the north-eastern German basin

Vogt et al. (2013) analysed the likelihood of success for heat production strategies in a sand stone reservoir in the north-eastern German basin in a depth of about 2 km by simulating both double and single well configurations, as shown in Figure 2.24. They combined seismic interpretation, numerical modelling, and stochastic estimation of rock properties to predict the transient temperature and pressure variations and their uncertainties in a geothermal reservoir. They used 3D seismic data and stratigraphy data from about 100 wells at 1500 – 2500 m depth for setting up a 3D stratigraphic model. Using 3D inversion of temperature data obtained in the wells, a specific heat flow of 77.7 mWm^{-2} ± 1.2 mWm^{-2} at 6 km depth was obtained, in agreement with a temperature of 87.1 ℃ ± 1.8 K in the Rhaetian sandstone target layer at a depth of ~ 2 km. For different types of potential geothermal well installations inside the

Rhaetian sandstone layer, the probability of success was merely 1.6%. This probability of success is obtained by the ratio of the number of realizations meeting the requirements for temperature and pressure and the total number of realizations in the ensemble. This is (16.3±2.0)% for temperature, (22.8±4.3)% for pressure, and (1.6±1.6)% for both combined.

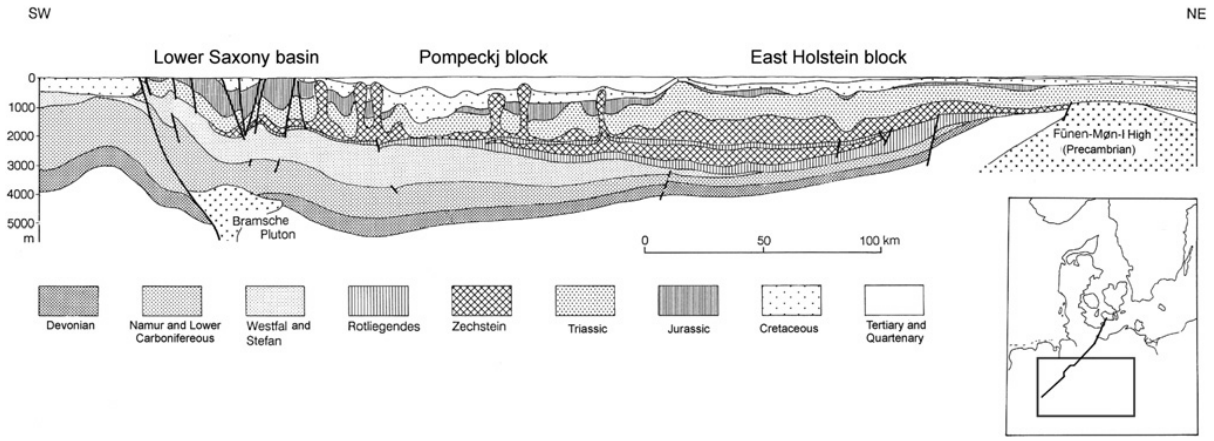

Figure 2.24: Geologic section along the profile shown in the small map of the north-eastern German basin. The box inside the map indicates the target region. (Vogt et al., 2013)

2.4.4 Den Haag Zuidwest (Netherlands) district heating system

Mottaghy et al. (2011) considered a deep geothermal project within the framework of the Den Haag Zuidwest district heating system in the Netherlands, as shown in Figure 2.25. The system was intended to provide heating for 6000 houses with a geothermal power of about 5MWt. The target temperature was about 75 ℃, with a reinjection temperature of 40 ℃ at a flow rate of 150 m^3h^{-1}. The target layer was found at a depth of about 2200 m with an average thickness of 50 m. They set up a detailed 3D numerical reservoir model, with the aim of predicting the evolution of the producer and injector temperatures, and the extent of the cooled area around the injector. The simulation results indicated that no significant thermal breakthrough would be obtained during the system operation. Fluid temperatures of 76.5 ℃ were measured, which is very close to the predicted value.

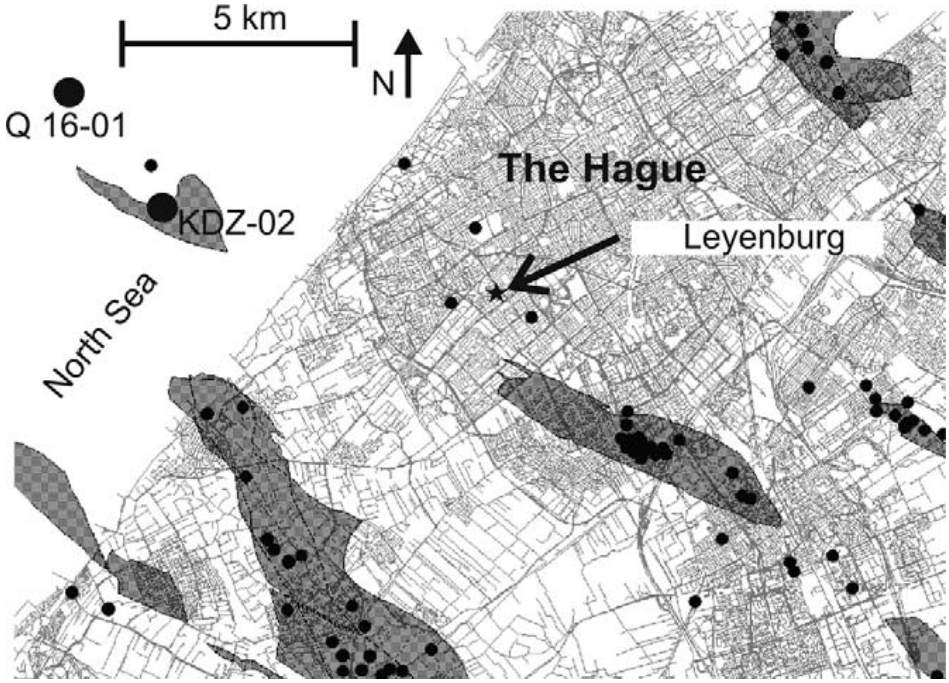

Figure 2.25: Location (Leyenburg) of the geothermal installation and the existing exploration wells (black dots). Two key wells that are used for this study, Q16-01 and KDZ-02, are located offshore. (Mottaghy et al., 2011)

2.4.5 Winnipeg, Manitoba, Canada

Ferguson and Woodbury (2005) examined the factors affecting the magnitude and timing of temperature increases at production wells in groundwater-source cooling applications through numerical modelling and observations at a case study site in Winnipeg, Manitoba, Canada, as shown in Figure 2.26. Generic simulations carried out using typical hydrogeologic parameters for the Carbonate Rock Aquifer suggested that temperature increases of a few degrees would occur at a typical production well only a few years after the start of operation in a given system. The spacing of the wells and pumping rates were found to have a greater effect than material properties in a homogeneous aquifer. The comparison between measured and modelled temperatures at the production well is shown in Figure 2.27. As the measured temperatures are scattered points, it is not possible to match the measured temperatures with the modelled temperatures exactly. However, it can be found in Figure 2.27 that the modelled temperatures match with the trend of the measured temperatures in general. Therefore, the measured temperatures at the production well can validate the numerical models to some extent.

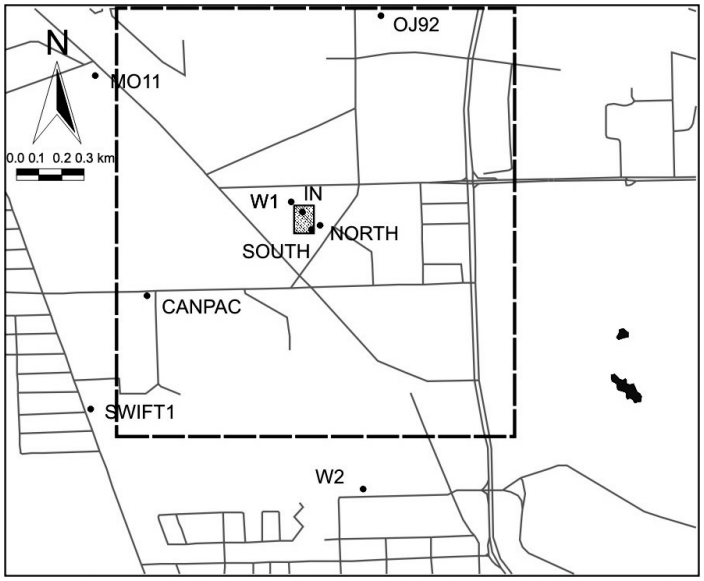

Figure 2.26: Map of the St. Boniface area of Winnipeg, showing the location of observation wells and the property investigated in this study. IN, injection well; SOUTH, south production well; NORTH, north production well. Shaded area around wells IN and SOUTH represents the zone of increased permeability. (Ferguson and Woodbury, 2015)

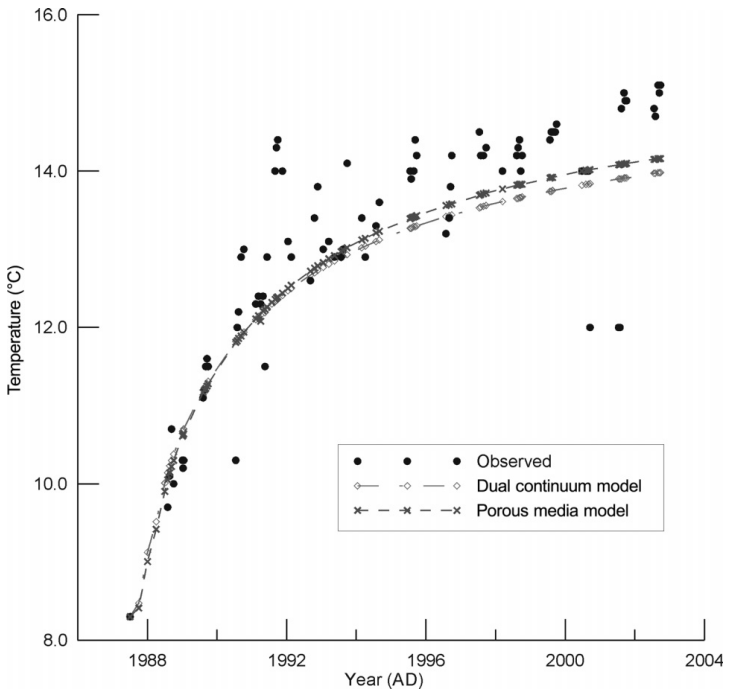

Figure 2.27: Measured and modelled temperature at the south production wells at the industrial site in St. Boniface (Ferguson and Woodbury, 2015)

2.4.6 Soultz-sous-Forets (France) site of the European Hot Dry Rock Program

Sanjuan et al. (2006) discussed the results drawn from tracer tests performed in 2000 – 2005 during hydraulic stimulation operations and a short-term circulation test in wells GPK-2, GPK-3, and GPK-4 at the Soultz-sous-Forets (France) site of the European Hot Dry Rock Program, which is at less than 3900 m depth before the year 2000, and at about 5000 m depth in the period 2000 – 2005, as shown in Figure 2.28. These tests consistently indicated that only low amounts of the injected fresh water were recovered and that the proportion of native brine was relatively high in the produced fluids. The tracer tests gave evidence of a fast and relatively direct hydraulic connection between GPK-3 and GPK-2 (short loop) but also indicated the existence of another larger and slower hydraulic connection between the wells (large loop).

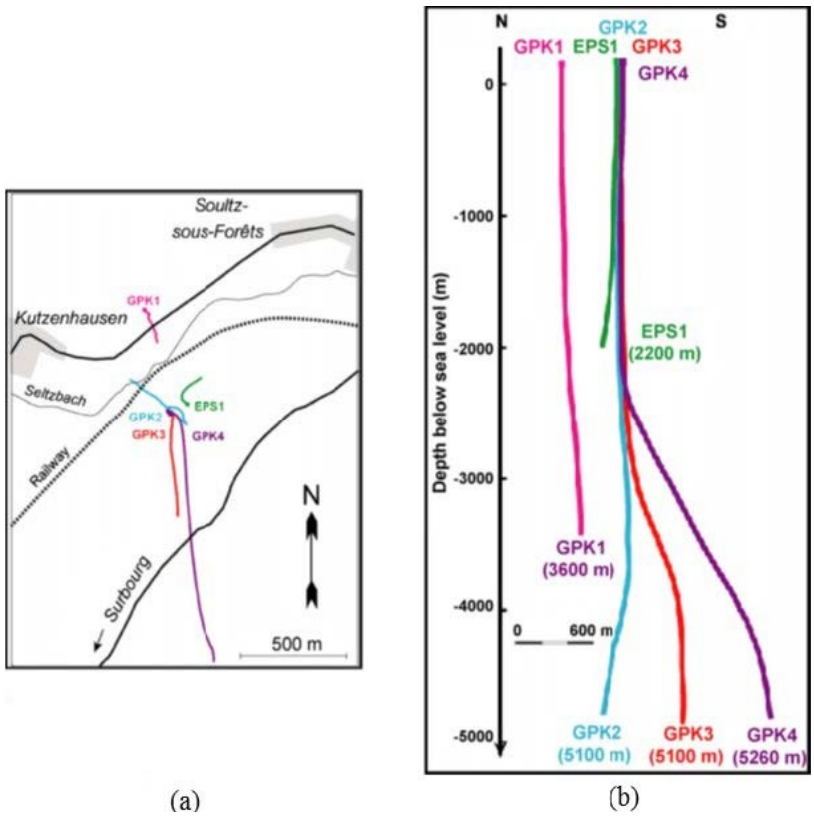

Figure 2.28: (a) Location map and profiles of the geothermal wells (Dezayes et al., 2005); (b) Geological cross-section between the geothermal wells (Gentier et al., 2003; Hooijkaas et al., 2006)

2.4.7 EGS Project in Basel, Switzerland

The EGS project Deep Heat Mining was started to develop a geothermal plant in Basel, Switzerland, as shown in Figure 2.29. In December 2006, an intense hydraulic stimulation into a 5 km granitic target zone was performed that resulted in perceivable induced seismicity above acceptable levels. 12000 m^3 of water was injected at wellhead pressure up to 300 bar within 6 days. The seismic activity, recorded by a sophisticated microseismic monitoring system, increased during the process up to a local event magnitude of M_L 2.7 after which the injection was aborted and the well shut in, as shown in Figure 2.30 (Haring et al., 2008). On 28th March 2017, in consultation with Basel Industrielle Werke (IWB), the Department of Health of the Canton of Basel decided to re-open the borehole (Swiss Seismological Service website).

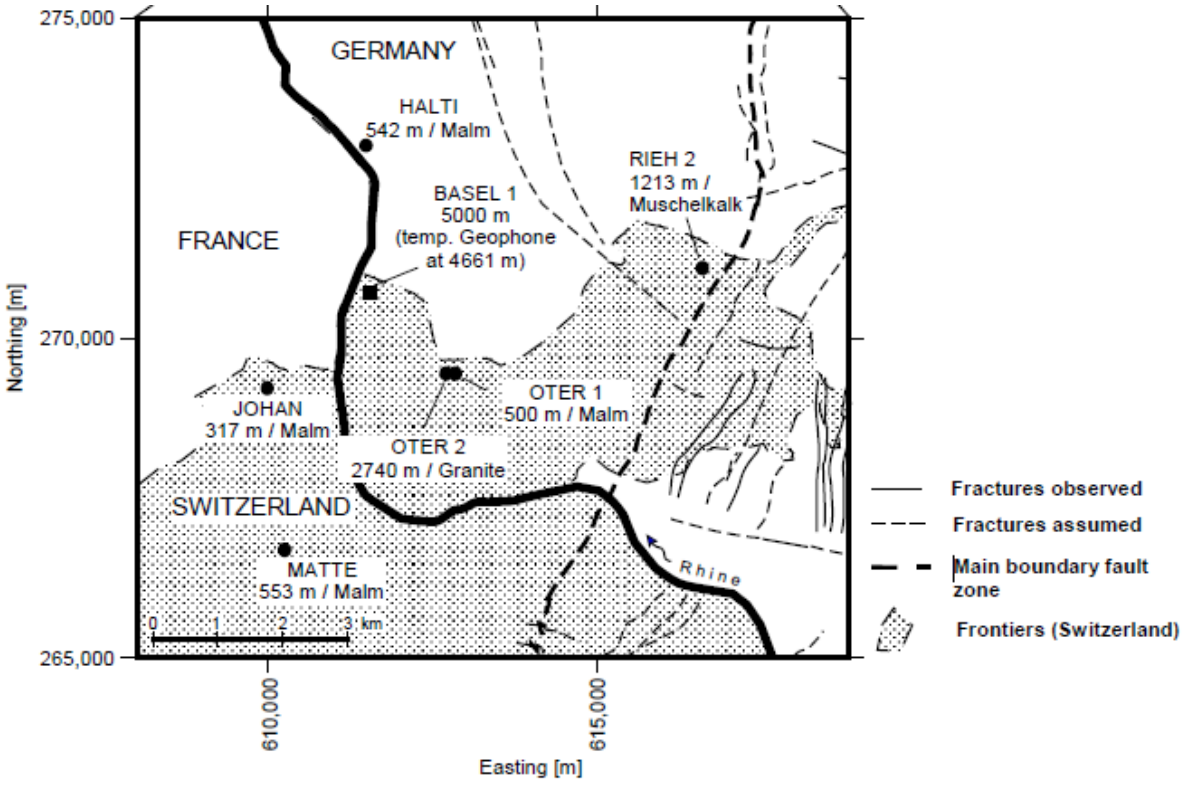

Figure 2.29: Microseismic network; seismic stations marked by black circles; injection well marked by black square (Haring et al., 2008)

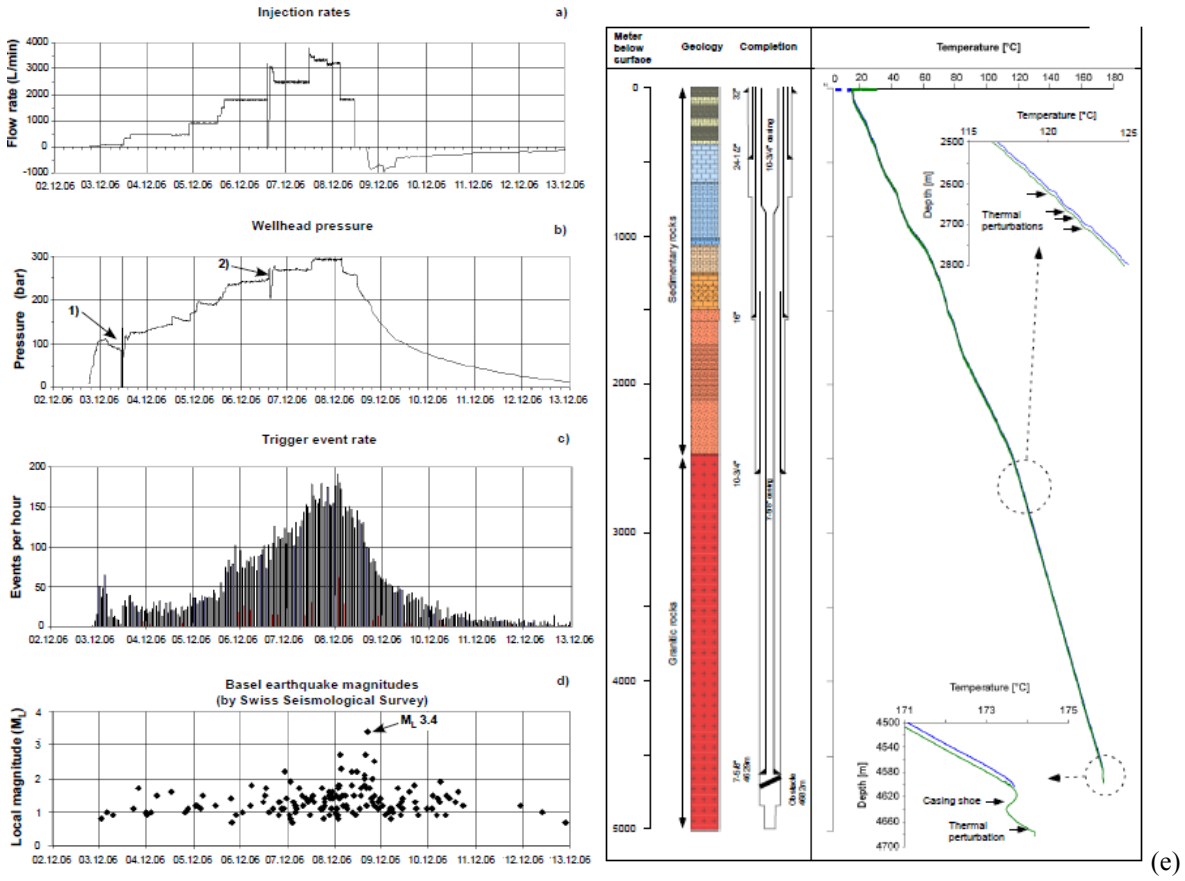

Figure 2.30: (a) injection rates; (b) wellhead pressure; (c) trigger event rate; (d) Basel earthquake magnitude; (e) temperature logs of the injection well (Haring et al., 2008)

2.4.8 Geothermal Projects in the UK

Currently there is only one geothermal system exploited in the UK, which is located in Southampton. The Southampton borehole (put on production in 1987) has supplied hot water at a temperature of 76 ℃ from Triassic (Sherwood) sandstones overlain by a Triassic (Keuper) mudstone seal at a depth of 1.7 km in the Wessex Basin and produced 1.7 MWt (heat) which forms the basis for the Southampton District Energy Scheme that supplies heat and power to a university, hospital and commercial buildings in central Southampton (Gluyas et al., 2018). A summary of deep boreholes drilled in the UK after 2000 is shown in Table 2.3.

Table 2.3: A summary of deep boreholes drilled in the UK after 2000 (Gluyas et al., 2018)

Location	**Completion**	**Well depth (m)**	**Bottom hole temperature (℃)**	**Main aquifer depth (m)**	**Temperature of aquifer (℃)**
Eastgate 1	December 2004	995	46	411	27
Eastgate 2	July 2010	420	-	Not present	No flow
Science Central	July 2011	1821	73	1418.5-1797	No flow

2.4.9 Discussion

Above all, most of the current geothermal projects lack the detailed well temperature data and relevant parameters of reservoir and doublet systems. Besides, due to anisotropy and inconsistence of reservoir and non-uniform injection/extraction rate, it is difficult to determine the accurate average parameters used in the new analytical solutions proposed in the thesis. Therefore, it is inaccurate to use the experimental data to validate the analytical solutions. However, the comparison between the experimental data and the analytical solutions can be achieved to some extent by matching the trend of those data.

Compared to other geothermal projects mentioned in this chapter, the Winnipeg, Manitoba, Canada project has the most detailed well temperature data, reservoir data and doublet system data. Therefore, the Winnipeg, Manitoba, Canada project is selected to compare its experimental data with the new analytical solutions in the thesis.

Chapter 3 Extended Lauwerier Model

As introduced in Chapter 1, deep geothermal energy is clean, sustainable and abundant. Recently deep geothermal energy has become important in the energy supply and it is believed to have a good potential and prospect. During the process of using deep geothermal energy, the temperature distribution in the ground is a basic and significant part of assessing its potential.

A typical doublet scheme consists of one cool water injection well and one hot water extraction well. As long as the temperature distribution in the ground is known and predictable, it is possible to evaluate the temperature of the extracted hot water, the thermal breakthrough around the injection well, the optimum location of the extraction well and the energy that can be extracted from the system.

There are three primary methods for estimating the temperature distribution within the aquifer when Hot Sedimentary Aquifer (HSA) is used for heating: (1) Numerical simulation, in which the temperature distribution can be obtained using numerical software (such as COMSOL or Fluent); (2) Field testing, where the temperature distribution of the aquifer layer can be directly measured. This may be time-consuming and very expensive; (3) Use of an analytical solution, which allows for simple and rapid assessment of a potential geothermal site before conducting complex numerical simulations or field testing (Scott et al., 2005; Kocabas, 2004).

Numerical simulations are commonly used for the evaluation of complex situations, such as irregular geometries, anisotropic properties and complicated boundary conditions. Hence, analytical solutions cannot and should not replace numerical simulations. However, analytical solutions can provide a general overview of the principle effects and a rough estimation of the geothermal potential of a site. In this thesis, a simple engineering analysis method is proposed to estimate the temperature distribution and thermal breakthrough around the injection well so that an optimal location for the hot water extraction well can be evaluated.

This thesis focuses on a case in which there is no regional groundwater flow, so that only the injection well and the extraction well dominate the flow in the aquifer. Heat transport for a

doublet scheme is rather difficult as the flow in the aquifer is the superposition of the radial flow around the injection well and the extraction well.

As stated in Section 2.2, there is no analytical solution up to now that gives the temperature distribution in the aquifer, the temperature at the extraction well or the optimal location of the extraction well if the interaction between two wells is considered. Because of the difficulties encountered in modelling a doublet system, Chapter 3 puts forward an alternative and attractive approach, which uses a single well model to simplify a doublet scheme, on the assumption that the extraction well is far away enough (>1000 m) from the injection well that the interaction between the two wells is negligible. This assumption generally holds true in practice, as the separation of the wells in current typical doublet systems is more than 1000 m (Mijnlieff et al., 2007; Mottaghy et al., 2011; Lopez et al., 2010; Willems et al., 2016). The modification to account for this injection and extraction well interaction issue is proposed in Chapter 5.

3.1 Extended Lauwerier Model

This study extends the Lauwerier model (introduced in Section 2.1.3) and proposes an analytical solution to the transient heat transfer problem with an axisymmetric geometry, as shown in Figure 3.1. The problem involves heat conduction and advection in a homogeneous hot aquifer layer of thickness H [m]. The initial temperature of the aquifer and overburden layers is denoted by T_0 [K]. At time $t = 0$, water with temperature T_w (lower than T_0) is injected into the aquifer layer at a constant rate through the injection well. The lower boundary of the aquifer layer is impermeable and adiabatic, whereas the upper boundary is impermeable and non-adiabatic. Symmetry can be used if both the lower and upper boundaries are non-adiabatic (i.e. heat is supplied from both boundaries). In such a case, the aquifer thickness should be halved to obtain the solution. The solution gives the spatial and temporal temperature distribution around an injection well. This in turn allows us to determine the optimal location of an extraction well, as shown in Figure 3.1. For simplicity, the model assumes that the temperature of the aquifer layer is uniform in the vertical direction.

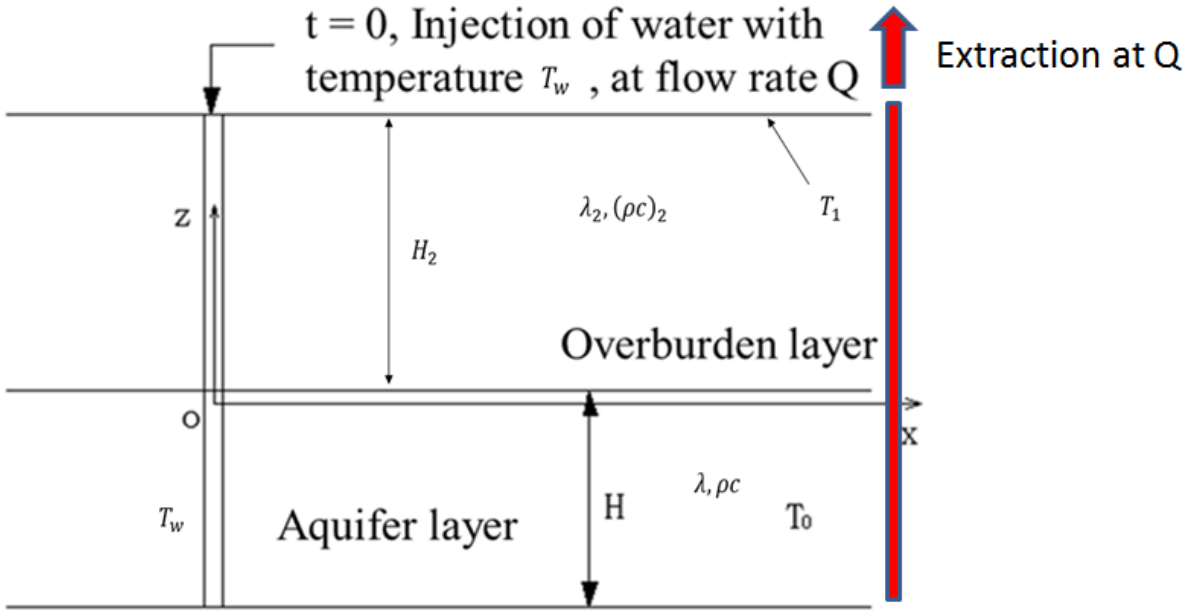

Figure 3.1: The Extended Lauwerier Model

3.2 Convective Heat Transfer Boundary

In the new solution to the axisymmetric problem, it is assumed that heat transfer in the aquifer occurs by both advection (via water movement) and conduction. Along the interface at the boundary between the overburden layer and the aquifer layer, there is a convective heat transfer boundary, with a heat flux of $w_0 = h(T - T_0)$, where h is the convective heat transfer coefficient. The advantage of introducing such a boundary is that the geometry and properties of the whole overburden layer can be compacted into a single coefficient, h, which characterizes the influence of the overburden layer on the aquifer. The method for selecting an appropriate value of h will be discussed in Chapter 4.

3.3 New Analytical Solution

3.3.1 Governing Equations

The basic governing equations of the problem are as follows (Equation (3.1) is the differential equation for heat advection):

$$\frac{1}{r}\frac{\partial}{\partial r}(rD\frac{\partial T}{\partial r})-v\frac{\partial T}{\partial r}=\frac{\partial T}{\partial t}+\frac{w_0}{\rho cH},\ r>0,\ t\geq 0 \tag{3.1}$$

$$v=q\frac{(\rho c)_f}{\rho c},\quad q=\frac{Q}{2\pi rH}\rightarrow v=\frac{2\alpha D}{r}=\frac{\beta}{r},\quad \alpha=\frac{Q}{4\pi nHDR},\quad \beta=\frac{Q}{2\pi H}\cdot\frac{(\rho c)_f}{\rho c}$$

$$\alpha=\frac{\beta}{2D},\quad R=1+\frac{1-n}{n}\frac{(\rho c)_s}{(\rho c)_f}$$

$$w_0=h(T-T_0) \tag{3.2}$$

$$t=0\ T=T_0 \tag{3.3}$$

$$r\rightarrow 0\ T=T_w \tag{3.4}$$

$$r\rightarrow +\infty\ T=T_0 \tag{3.5}$$

where ρ is the density of the aquifer, c is the specific heat capacity of the aquifer, D is the thermal diffusivity of the aquifer, v is the advection rate of the aquifer, w_0 is the heat flux at the interface between the aquifer and overburden layer, H is the aquifer layer thickness, q is the Darcy flow velocity in the aquifer layer, Q is the volumetric injection rate, α is the dimensionless injection rate, R is the delay factor, n is the porosity, h is the convective heat transfer coefficient, T_0 is the initial temperature, T_w is the water temperature, subscript f represents the water phase, subscript s represents the soil, and no subscript represents the average properties.

3.3.2 Derivation of the Solution

Substituting Equation (3.2) into Equation (3.1) yields the following:

$$\frac{\partial^2 T}{\partial r^2}+\frac{1-2\alpha}{r}\frac{\partial T}{\partial r}=\frac{1}{D}\frac{\partial T}{\partial t}+\frac{h}{\rho cHD}(T-T_0) \tag{3.6}$$

Letting $U(r,s)$ be the Laplace transform of $\{T(r,t)-T_0\}$ transforms Equation (3.6) into the following:

$$\frac{d^2U}{dr^2}+\frac{1-2\alpha}{r}\frac{dU}{dr}-(\frac{s}{D}+\frac{h}{\rho cDH})U=0 \tag{3.7}$$

Applying the same Laplace transform to Equation (3.4) produces the following:

$$U(0,s)=\frac{T_w-T_0}{s} \tag{3.8}$$

Similarly, Equation (3.5) becomes the following after the Laplace transform:

$$\lim_{r\to+\infty}U(r,s)=0 \tag{3.9}$$

Substituting $U=r^{\alpha}U_1$ into Equation (3.7) yields the following:

$$r^2\frac{d^2U_1}{dr^2}+r\frac{dU_1}{dr}-[(\frac{s}{D}+\frac{h}{\rho cDH})r^2+\alpha^2]U_1=0 \tag{3.10}$$

Equation (3.10) is the modified Bessel function and has the following solution (M. Abramowits and I.A. Stegun (eds) 1968, section 9.6.1, page 374):

$$U_1=C_1I_{\alpha}(\sqrt{\frac{s}{D}+\frac{h}{\rho cDH}}r)+C_2K_{\alpha}(\sqrt{\frac{s}{D}+\frac{h}{\rho cDH}}r) \tag{3.11}$$

The term I_{α} in Equation (3.11) is the modified Bessel function of the first kind, defined as follows:

$$I_v(z)=(\frac{1}{2}z)^v\sum_{k=0}^{\infty}\frac{(\frac{1}{4}z^2)^k}{k!\Gamma(v+k+1)} \tag{3.12}$$

K_α is the modified Bessel function of the second kind, defined as follows:

$$K_v(z) = \frac{1}{2}\pi \frac{I_{-v}(z) - I_z(z)}{\sin(v\pi)} \tag{3.13}$$

We then obtain the following from $U = r^\alpha U_1$:

$$U = r^\alpha [C_1 I_\alpha (\sqrt{\frac{s}{D} + \frac{h}{\rho cDH}} r) + C_2 K_\alpha (\sqrt{\frac{s}{D} + \frac{h}{\rho cDH}} r)] \tag{3.14}$$

When $r \to +\infty$, $I_\alpha \to +\infty$ and $K_\alpha \to 0$ (M. Abramowits and I.A. Stegun (eds) 1968, Section 9.6.1, page 374), so $C_1 = 0$. Equation (3.14) yields the following equation:

$$U = C_2 r^\alpha K_\alpha (\sqrt{\frac{s}{D} + \frac{h}{\rho cDH}} r) \tag{3.15}$$

The property of K_α is as follows (M. Abramowits and I.A. Stegun (eds) 1968, section 3.6.9, page 375):

$$r \to 0,\ K_\alpha (\sqrt{\frac{s}{D} + \frac{h}{\rho cDH}} r) \approx \frac{1}{2}\Gamma(\alpha)(\frac{1}{2}\sqrt{\frac{s}{D} + \frac{h}{\rho cDH}} r)^{-\alpha} \tag{3.16}$$

where $\Gamma(\alpha)$ is the gamma function, which is defined as $\Gamma(\alpha) = \int_0^\infty x^{\alpha-1} e^{-x} dx$.

The following is obtained from Equation (3.15):

$$C_2 = \frac{(\frac{1}{2})^{\alpha-1}(T_w - T_0)}{\Gamma(\alpha)} \frac{1}{s} (\frac{s}{D} + \frac{h}{\rho cDH})^{\frac{\alpha}{2}} \tag{3.17}$$

Substituting Equation (3.17) into Equation (3.15) yields:

$$U = \frac{(\frac{1}{D})^{\frac{\alpha}{2}}(\frac{1}{2})^{\alpha-1}(T_w - T_0)}{\Gamma(\alpha)} r^{\alpha} \frac{1}{s}(s + \frac{h}{\rho cH})^{\frac{\alpha}{2}} K_{\alpha}(\sqrt{s + \frac{h}{\rho cH}}\, \frac{r}{\sqrt{D}}) \tag{3.18}$$

Let $F(s) = s^{\frac{\alpha}{2}} K_{\alpha}(\sqrt{s}\, \frac{r}{\sqrt{D}})$, we obtain:

$$F[s - (-\frac{h}{\rho cH})] = (s + \frac{h}{\rho cH})^{\frac{\alpha}{2}} K_{\alpha}(\sqrt{s + \frac{h}{\rho cH}}\, \frac{r}{\sqrt{D}}) \tag{3.19}$$

Substituting Equation (3.19) into Equation (3.18) yields the following:

$$U = \frac{(\frac{1}{D})^{\frac{\alpha}{2}}(\frac{1}{2})^{\alpha-1}(T_w - T_0)}{\Gamma(\alpha)} r^{\alpha} \{\frac{1}{s} F[s - (-\frac{h}{\rho cH})]\} \tag{3.20}$$

The nature of the inverse Laplace transforms gives the following (M. Abramowits and I.A. Stegun (eds) 1968, Section 29.2.6, page 1020):

$$L^{-1}\{\frac{1}{s} F[s - (-\frac{h}{\rho cH})]\} = \int_0^t L^{-1}\{F[s - (-\frac{h}{\rho cH})]\} dt \tag{3.21}$$

Applying the inverse Laplace transform to both sides of Equation (3.20) provides:

$$T - T_0 = \frac{(\frac{1}{D})^{\frac{\alpha}{2}}(\frac{1}{2})^{\alpha-1}(T_w - T_0)}{\Gamma(\alpha)} r^{\alpha} L^{-1}\{\frac{1}{s} F[s - (-\frac{h}{\rho cH})]\} \tag{3.22}$$

Substituting Equation (3.21) into Equation (3.22) yields the following:

$$T - T_0 = \frac{(\frac{1}{D})^{\frac{\alpha}{2}}(\frac{1}{2})^{\alpha-1}(T_w - T_0)}{\Gamma(\alpha)} r^{\alpha} \int_0^t L^{-1}\{F[s - (-\frac{h}{\rho cH})]\} dt \tag{3.23}$$

The nature of the inverse Laplace transform gives the following (M. Abramowits and I.A. Stegun (eds) 1968, Section 29.2.12, page 1021):

$$L^{-1}\{F[s-(-\frac{h}{\rho cH})]\} = e^{-\frac{h}{\rho cH}t} L^{-1}\{F(s)\} = e^{-\frac{h}{\rho cH}t} L^{-1}\{s^{\frac{\alpha}{2}} K_{\alpha}[\sqrt{s}(\frac{r}{\sqrt{D}})]\} \tag{3.24}$$

The inverse Laplace transform formula is shown below (V.S. Arpaci 1966, equation 52, page 347),

$$L^{-1}\{s^{\frac{\alpha}{2}} K_{\alpha}[\sqrt{s/b}\cdot x]\} = \frac{x^{\alpha}}{b^{\alpha/2}(2t)^{\alpha+1}} e^{-\frac{x^2}{4bt}} \tag{3.25}$$

Yielding:

$$L^{-1}\{s^{\frac{\alpha}{2}} K_{\alpha}[\sqrt{s}(\frac{r}{\sqrt{D}})]\} = \frac{(\frac{r}{\sqrt{D}})^{\alpha}}{(2t)^{\alpha+1}} e^{-\frac{r^2}{4Dt}} \tag{3.26}$$

Substituting Equation (3.26) into Equation (3.24) produces the following:

$$L^{-1}\{F[s-(-\frac{h}{\rho cH})]\} = e^{-\frac{h}{\rho cH}t} \frac{(\frac{r}{\sqrt{D}})^{\alpha}}{(2t)^{\alpha+1}} e^{-\frac{r^2}{4Dt}} \tag{3.27}$$

Substituting Equation (3.27) into Equation (3.23) yields:

$$T = T_0 + \frac{T_w - T_0}{(4D)^{\alpha}\Gamma(\alpha)} r^{2\alpha} \int_0^t \frac{e^{-(\frac{h}{\rho cH}\tau + \frac{r^2}{4D\tau})}}{\tau^{\alpha+1}} d\tau \tag{3.28}$$

If $\frac{r^2}{4D\tau} = x$, then Equation (3.28) becomes the following:

$$T = T_0 + \frac{T_w - T_0}{\Gamma(\alpha)} \int_{\frac{r^2}{4Dt}}^{\infty} e^{-(x+\frac{hr^2}{4\rho cDH}\frac{1}{x})} x^{\alpha-1} dx \tag{3.29}$$

$$\alpha = \frac{1}{4\pi nR} \cdot \frac{\rho c}{H\lambda} Q\,,\ \beta = \frac{Q}{2\pi H} \cdot \frac{(\rho c)_f}{\rho c}\,,\ R = 1 + \frac{1-n}{n}\frac{(\rho c)_s}{(\rho c)_f}$$

where n is the porosity.

In the dimensionless form, T^* (r^*, t^*) reads:

$$T^* = \frac{1}{\Gamma(\alpha)} \int_{\frac{r^{*2}}{t^*}}^{\infty} e^{-(x+h^* r^{*2}\frac{1}{x})} x^{\alpha-1} dx \tag{3.30}$$

$$T^* = \frac{T - T_0}{T_w - T_0}\,,\ \ r^* = \frac{1}{H} r\,,\ t^* = \frac{4\lambda}{\rho c H^2} t\,,\ h^* = \frac{H}{4\lambda} h\,,\ \alpha = \frac{1}{4\pi nR} \cdot \frac{\rho c}{H\lambda} Q$$

An example of this new analytical solution (Equation (3.29)) is shown in Figure 3.2, which gives the spatial and temporal temperature profiles for a given injection rate of Q = 0.003 m^3/sec and h = 0.17 W/(m^2K). The cold water temperature is 30 degrees.

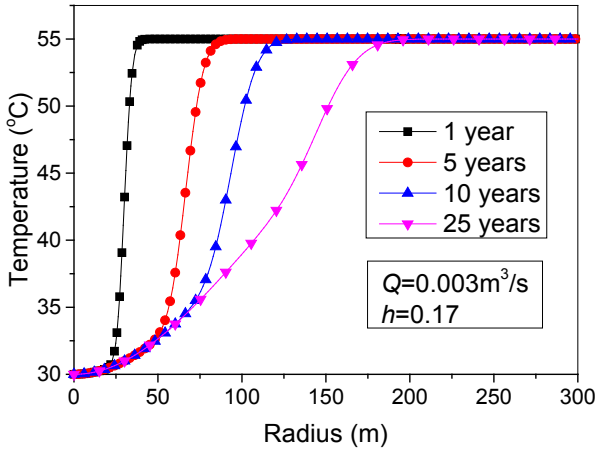

Figure 3.2: Temperature distribution in the aquifer for the new analytical solution

The other input values are given in Table 3.1, which are all typical values in practice.

Table 3.1: Values for parameters used in the figures

$T_0(^\circ\mathrm{C})$	$T_w(^\circ\mathrm{C})$	$H(\mathrm{m})$	$\lambda(\mathrm{W/mK})$	$(\rho c)_f$ (J/m^{3}K)	$(\rho c)_s$ (J/m^{3}K)	n
55	30	50	1.125	1000×4200	2800×830	0.25

3.4 Degeneration and Validation of the New Analytical Solution

3.4.1 Heat Transfer Coefficient *h* = 0

When the heat transfer coefficient in the new analytical solution is $h = 0$, there is no heat exchange at the interface so that the scenarios and boundary conditions of the new analytical solutions and the second piecewise function of Barends axisymmetric solutions (Equation 2.25) are exactly the same. Therefore, they should give the same results if the new analytical solutions are correct. The second piecewise function of Barends axisymmetric solution is given as:

$$T = T_0 + (T_w - T_0)\frac{\Gamma[\alpha,\eta^2]}{\Gamma[\alpha]} \tag{3.31}$$

where $\Gamma[\alpha,\eta^2]$ is defined as:

$$\Gamma[\alpha,\eta^2]=\int_{\frac{r^2}{4Dt}}^{\infty} e^{-x}x^{\alpha-1}\mathrm{d}x \tag{3.32}$$

Substituting Equation (3.32) into Equation (3.31) yields the following:

$$T=T_0+\frac{T_w-T_0}{\Gamma[\alpha]}\int_{\frac{r^2}{4Dt}}^{\infty} e^{-x}x^{\alpha-1}\mathrm{d}x \tag{3.33}$$

Letting $h = 0$ in the new analytical solution (Equation (3.29)) provides the following:

$$T=T_0+\frac{T_w-T_0}{\Gamma[\alpha]}\int_{\frac{r^2}{4Dt}}^{\infty}e^{-x}x^{\alpha-1}\mathrm{d}x \tag{3.34}$$

It can be seen that Equations (3.33) and Equation (3.34) are identical. Therefore, when the heat transfer coefficient $h = 0$, the new analytical solution degenerates into Equation (3.31) (Barends axisymmetric solution).

3.4.2 Thermal Diffusion Coefficient $D = 0$

Assuming a thermal diffusion coefficient of $D = 0$ simplifies the governing equation Eq. (3.1) into a first-order partial differential equation, which is a piecewise function that can be easily solved:

$$T=T_0+(T_w-T_0)e^{-\frac{hr^2}{2\beta\rho cH}},\ r\le\sqrt{2\beta t} \tag{3.35}$$

$$T=T_0,\ r>\sqrt{2\beta t} \tag{3.36}$$

Substituting $\alpha=\frac{\beta}{2D}$ into the new analytical solution, Equation (3.29), and expressing in an equivalent form provides:

$$T=T_0+\frac{T_w-T_0}{\Gamma(\frac{\beta}{2D})}\int_{\frac{r^2}{4Dt}}^{\infty}e^{-(x+\frac{hr^2}{4\rho cDH}\frac{1}{x})}x^{\frac{\beta}{2D}-1}dx \tag{3.37}$$

With respect to Equation (3.37), which is in an equivalent form to Equation (3.29), letting $D = 0$ or $D\to 0$ does not readily convert the equation into Equation (3.35) or Equation (3.36). However, letting D be a minimum value (the normal value of D is approximately 2×10^{-7}, and here, $D=3\times10^{-9}$) yields the piecewise functions of Equation (3.35) and (3.36) illustrated using MAPLE and compared to Equation (3.37) in Figure 3.3.

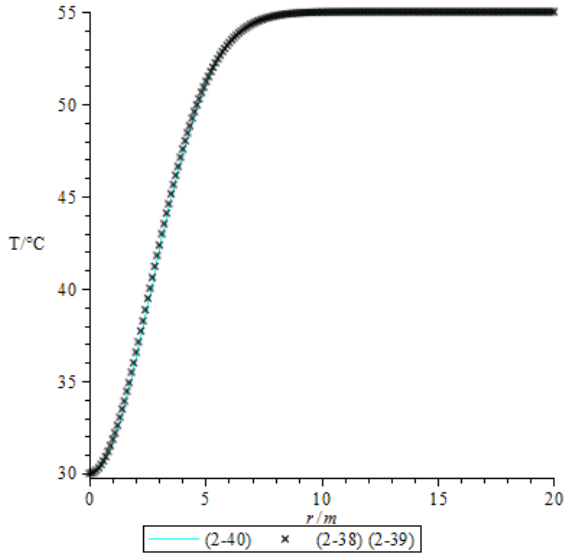

Figure 3.3: Comparison between Equation (3.37) and the piecewise functions (3.35) and (3.36)

Figure 3.3 shows that the curve resulting from Equation (3.37) entirely overlaps that of the piecewise functions of Equation (3.35) and (3.36). Therefore, when the thermal diffusion coefficient D = 0, the new analytical solution degenerates into the piecewise functions of Equation (3.35) and (3.36).

3.4.3 Dimensionless Injection Rate $\alpha = 0.5$

When the dimensionless injection rate $\alpha = 0.5$, Equation (3.1) simplifies into a second-order constant coefficient differential equation without a first-order term, which can be easily solved to obtain the following:

$$T = T_0 + \frac{T_w - T_0}{2\sqrt{\pi}\sqrt{D}} r \int_0^t \frac{e^{-(\frac{h}{\rho cH}\tau + \frac{r^2}{4D\tau})}}{\tau^{1.5}} d\tau \tag{3.38}$$

Letting $\alpha = 0.5$ in the new analytical solution, Equation (3.29) yields:

$$T = T_0 + \frac{T_w - T_0}{2\Gamma(0.5)\sqrt{D}} r \int_0^t \frac{e^{-(\frac{h}{\rho cH}\tau + \frac{r^2}{4D\tau})}}{\tau^{1.5}} d\tau \tag{3.39}$$

It is known from the nature of the gamma function that $\Gamma(0.5) = \sqrt{\pi}$; therefore, Equation (3.39) is identical to Equation (3.38). Thus, when the dimensionless injection rate $\alpha = 0.5$, the new analytical solution degenerates into Equation (3.38).

In summary, the new analytical solution degenerates into the known analytical solutions from the three cases above; therefore, the proposed new analytical solution is assessed to be correct.

3.5 Parameter Impact Analysis

3.5.1 Dimensionless Injection Rate α

Dimensionless injection rate α represents the ratio between heat advection and heat conduction. The effects of varying α, on the new analytical solution are shown in Figure 3.4. The parameter values used in Figure 3.4 are shown in Table 3.1. Time t is 10^8 s ≈ 3.2 years. The heat transfer coefficient $h = 10$ W/(m^{2}K).

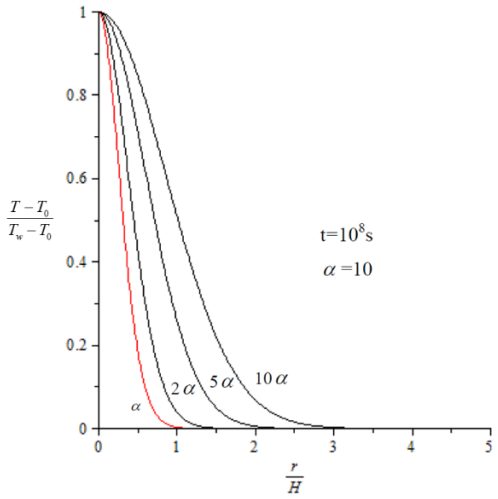

Figure 3.4: Effects of different α

Figure 3.4 shows that the dimensionless injection rate α affects the temperature distribution in the following manner:

(1) The slope of the curve near r = 0 decreases with increasing α, which suggests that the injected cold water affects a larger area around the injection well (the temperature in this region

becomes close to the temperature of the cold water). The dimensionless temperature declines sharply outside of this range. In addition, further data analysis has shown that the gentle slope disappears at small values, and the dimensionless temperature sharply declines from $r = 0$.

(2) For a given injection time, the penetration depth significantly increases with increasing α (temperature-influence area). It was calculated that the penetration depth did not converge by increasing α to a large infinite value; that is, when α is large enough, the temperature of a larger area will be affected. Of course it is impossible for α to be infinite, and the actual value of α has an upper limit corresponding to the maximum volumetric injection rate.

3.5.2 Time *t*

It is apparent that the injection time t is a very important parameter for non-steady state heat transfer problems. It can be deduced directly from the new analytical solution that the dimensionless temperature is a decreasing function of time t. Figure 3.5 shows the temperature distribution after one week, one month, six months, one year, and two years. The parameter values used in Figure 3.5 are shown in Table 3.1. The dimensionless injection rate $\alpha = 6$. The heat transfer coefficient $h = 10$ W/(m^{2}K).

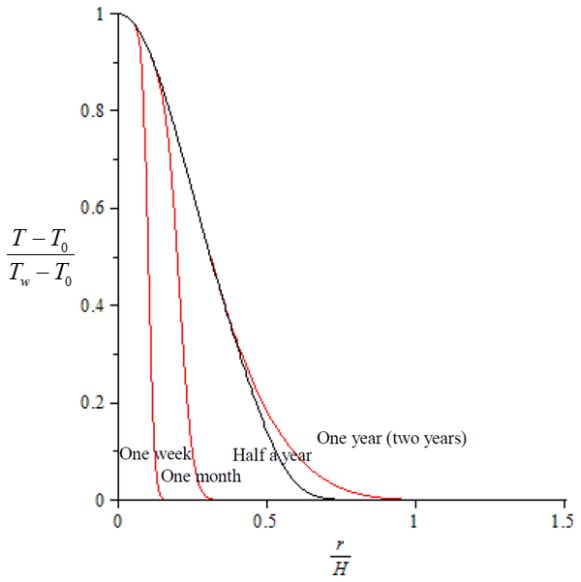

Figure 3.5: The temperature distributions at different time t

In Figure 3.5, the temperature distribution at 1 year coincides with that of 2 years, which indicates that the temperature distribution of the aquifer layer has reached a steady state after 1 year.

It is noted that this observation is very different from the planar symmetric problem. In the planar symmetric problem, this quasi-steady-state does not exist, and the temperature influence sphere continues to increase with time and is not convergent. This quasi-steady state exists in the axisymmetric problem, and time is convergent. Therefore, the magnitude of the changes in the temperature distribution gradually decreases over time. Once a certain time value is reached, the temperature distribution of the aquifer layer remains consistent, as thermal equilibrium is reached; therefore, the injection well can only affect the temperature distribution within a certain radius. The reason for this contrast is the difference in water flow rate, which is constant in the planar symmetric problem, allowing for the thermal advection to continue to affect the surrounding area. However, in the axisymmetric problem, the water flow rate is inversely proportional to the radius; thus, the larger the radius, the slower the flow rate and the weaker the thermal advection effect. Once the coupling effect of thermal advection and conduction in the aquifer layer is reduced to the point where they balance out the heat transfer at the interface between the aquifer and overburden layers, the temperature distribution reaches a steady state.

It also can be seen from Figure 3.5 that the region within a smaller radius reaches a steady state first, where the temperature remains constant, while the temperature in the region within a larger radius continues to change. For increasingly longer periods of time, the steady-state region gradually extends outward. This figure shows that the curve gradually converges with the steady state curve from the inside out, until a steady state is reached.

3.5.3 Heat Transfer Coefficient *h*

The heat transfer coefficient h is a very important parameter in the analytical solution because it is the parameter in the convective heat transfer boundary condition that directly determines the magnitude and conditions of the heat transfer at the interface between the aquifer and overburden layer. The analytical solution indicates that the temperature distribution is a

decreasing function of *h*. The effects of different *h* on the temperature distribution are shown in Figure 3.6 and Figure 3.7. The parameter values used in Figure 3.6 and Figure 3.7 are shown in Table 3.1. The dimensionless injection rate $\alpha = 6$. Time *t* is 10^8 s ≈ 3.2 years.

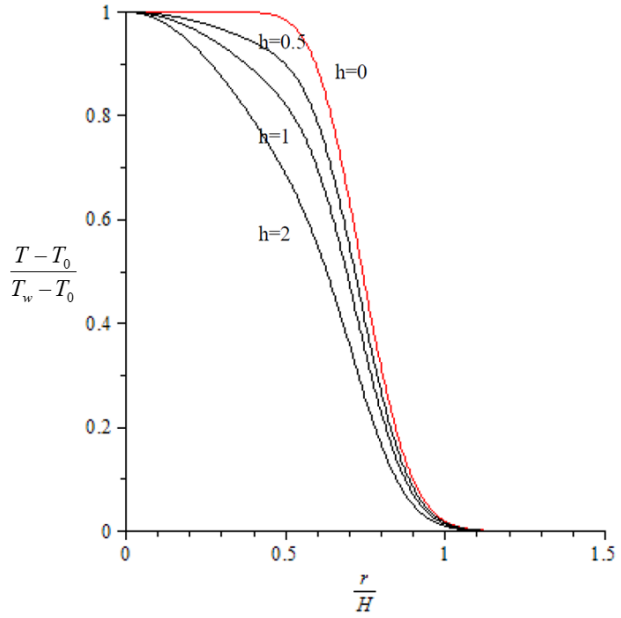

Figure 3.6: Effects of variations in *h* on the temperature distribution (when *h* is small)

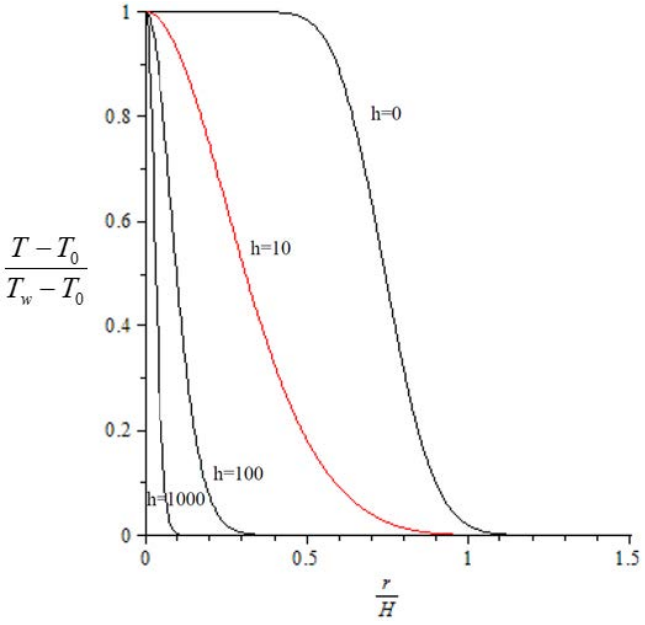

Figure 3.7: Effects of variations in *h* on the temperature distribution (when *h* is large)

Figure 3.6 indicates that the slope near the flat section of the curve increases significantly with increasing *h*. The case when $h = 0$ is special, as this boundary is adiabatic. In this case, a long horizontal segment of the curve lies near the vertical axis, which means that the temperature in this region is the same as the initial water temperature. The reason for this phenomenon is that the boundary is heat-insulating, and the heat in the overburden layer cannot pass into this region, which is directly affected by the cold water. Therefore, the temperature is consistent with the injected water temperature. As *h* increases, the heat from the overburden layer passes into the region, and the temperature difference between the overburden layer and this region is significant. The heat transfer at the interface is proportional to the temperature difference, which is high; therefore, the horizontal segment of the curve is no longer present.

However, the temperature difference between the overburden and aquifer layers is small at large radii (near the penetration depth, which is the extent around the injection well that can be affected by the cold injected water at a certain time). The heat transfer in this region is small due to the small *h*; hence, it is insufficient to have an effect on the penetration depth, which is still primarily determined by heat advection and conduction in the aquifer layer. Therefore, the penetration depth remains constant.

The values of *h* in Figure 3.7 are large, and the slope near the axis increases significantly with increasing *h* while the penetration depth decreases significantly, which is very different from the case for smaller *h*. This can be attributed to the fact that the heat flux $h(T - T_0)$, remains large when *h* is large, even if the temperature difference is small near the penetration depth region, which is sufficient to significantly affect the penetration depth.

3.5.4 Thermal Diffusivity *D*

The thermal diffusivity *D* represents the diffusion rate of heat conduction in the aquifer layer. The proportion of heat conduction in the aquifer layer can also be measured by the dimensionless injection rate α. The following parameter impact analysis of *D* is based on small and large dimensionless injection rate α as shown in Figure 3.8 and Figure 3.9, respectively. The parameter values used in Figure 3.8 and Figure 3.9 are shown in Table 3.1 (except for thermal conductivity λ as λ varies with different thermal diffusivity *D*). Time *t* is

10^8 s ≈ 3.2 years . The heat transfer coefficient $h = 10$ W/(m^{2}K) . The dimensionless injection rate $\alpha = 4$ in Figure 3.8 and $\alpha = 40$ in Figure 3.9.

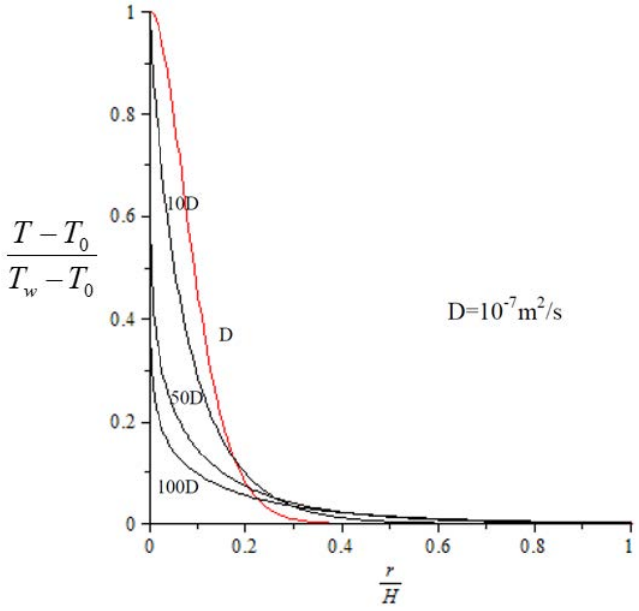

Figure 3.8: Effects of variations in thermal diffusivity on the temperature distribution ($\alpha = 4$)

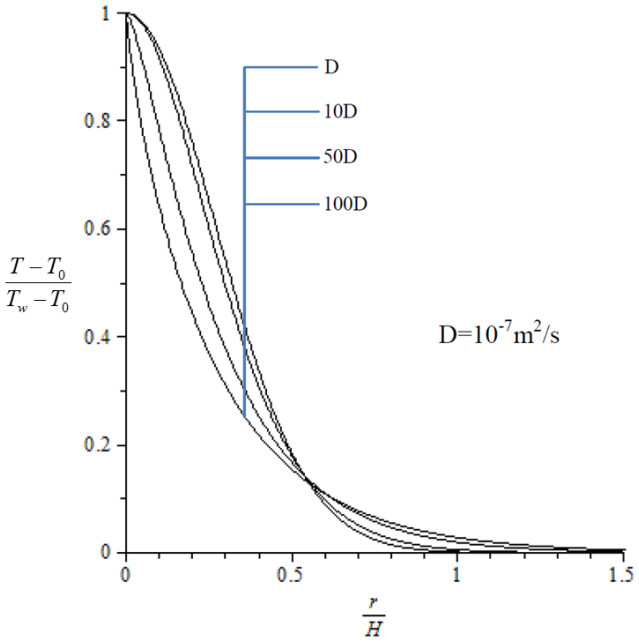

Figure 3.9: Effects of variations in thermal diffusivity on the temperature distribution ($\alpha = 40$, the thermal diffusivities are D, $10D$, $50D$ and $100D$ from left to right)

Figure 3.8 shows that, when α is small, i.e. when the proportion of heat conduction is large, the thermal diffusivity *D* exhibits a significant influence on the temperature distribution. Figure 3.9 shows that, when α is large, *D* exhibits a smaller influence on the temperature distribution. The figures also show that curves with different values of *D* intersect, in contrast to the previous parameter analyses. In other words, the temperature near the injection well increases with the increasing thermal diffusivity *D*; the cold penetration distance also increases with the increasing *D*. The flow velocity near the injection well is so fast that thermal advection plays the dominant role in this area. The temperature of the soil in this region is cooled instantly by the injected cold water, and thus a large temperature difference between this region and its outer region is created. With a greater thermal diffusivity *D*, the amount of heat transferring from the outer region to the region near the injection well is also greater so that the temperature near the injection well increases. However, in the area far away from the injection well, the flow velocity is small thus thermal conduction dominates in this area. With a greater thermal conductivity *D*, the cold front penetrates further and thus the cold penetration distance increases. Therefore, in Figure 3.8 and Figure 3.9, the curves with different values of thermal diffusivity *D* intersect each other.

3.6 Verification of the New Analytical Solution by Numerical Simulations

A commercial software, COMSOL, is used to conduct the numerical simulations of the problem examined in this chapter. An axisymmetric 2D model shown in Figure 3.10 is developed. The cross section of the model is a 200 m × 50 m rectangle. An injection well is located in the axis, namely the left boundary of the rectangle. The left boundary of the model is a temperature boundary equal to the temperature of the injected cold water (30 degrees); the injection rate $Q = 0.001\ \mathrm{m}^3/\mathrm{s}$; the upper and lower boundaries are convective heat transfer boundaries with $h = 5\ \mathrm{W/(m^2K)}$; the right boundary is an outflow boundary. The initial temperature of the model is 55 degrees. The physics used in the model is "Heat Transfer in Porous Media", in which both thermal advection and conduction are considered. Other parameters used in the model are shown in Table 3.1. The mesh consists of 24880 quadratic

triangular elements (the maximum element size is 1 m and the minimum element size is 0.004 m), as shown in Figure 3.10. As the vertical direction temperature in the new analytical solutions is uniform, the vertical thermal conductivity in the COMSOL model is set to 100 times the transverse thermal conductivity to make the vertical direction temperature in the COMSOL model closer to uniform, which matches with the conditions in the new analytical solutions. For the new analytical solutions (1D model), the heat flux from the overburden layer is averaged over the thickness of the aquifer. For the numerical simulations (2D model), the heat flux from the overburden layer firstly transfers to the interface between the aquifer and overburden layer and then continues to transfer to other parts of the aquifer by the vertical thermal conduction of the aquifer. The temperature distribution at 4.8 years for the whole model calculated by COMSOL is shown in

Figure 3.11. It can be seen in the figure that the vertical direction temperature is not completely uniform, because the area near the interface is directly heated by the overburden layer that its temperature is a little higher than that of the centreline. The temperature distributions around the injection well at different times are shown in Figure 3.12. The temperature distributions around the injection well calculated by COMSOL can be compared with the temperature distributions given by the new analytical solutions, validating the new analytical solution.

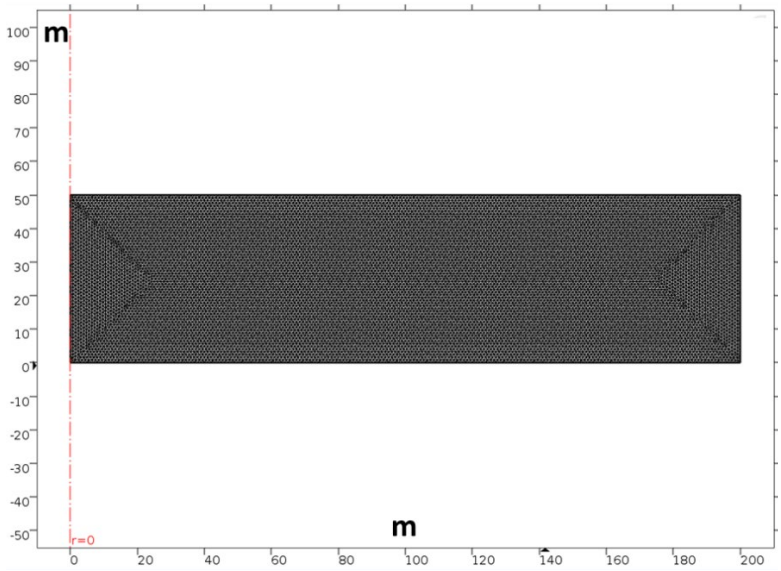

Figure 3.10: Comsol model and mesh

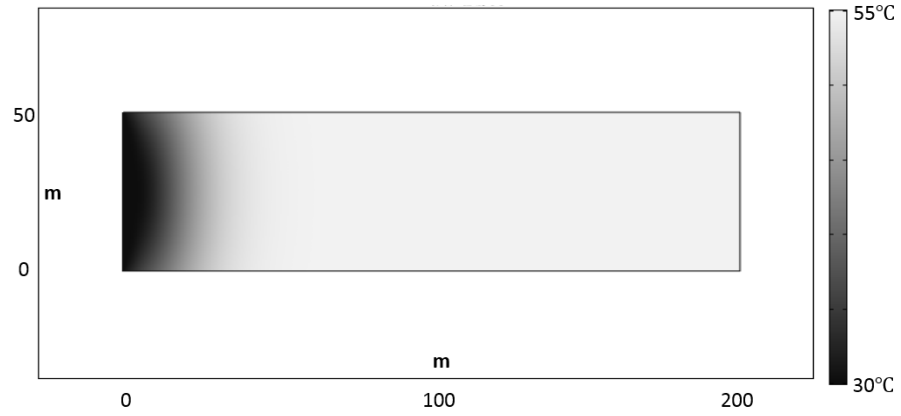

Figure 3.11: Temperature distribution at 4.8 years

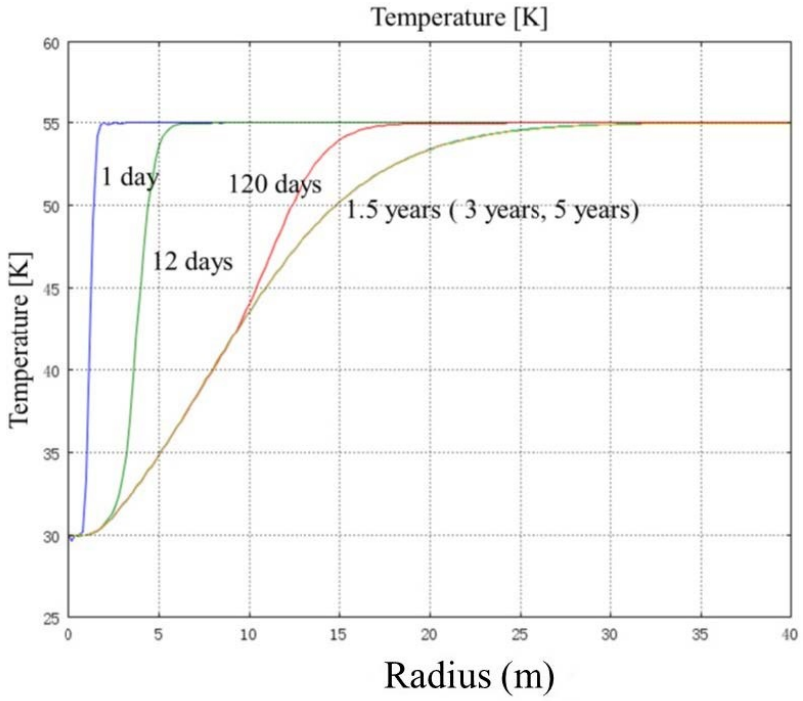

Figure 3.12: Temperature distributions around the injection well at different times

Figure 3.12 shows that the curves for 1.5, 3 and 5 years completely overlap with each other, which once again proves the previous conclusion: the quasi-steady-state solution exists in the axisymmetric problem under the convective heat transfer boundary condition.

The comparisons between the new analytical solutions and COMSOL solutions are shown in Figure 3.13, Figure 3.14 and Figure 3.15. Figure 3.13 considers the case in which both time *t*

and injection rate Q are small. Figure 3.14 considers the case in which time t is small and injection rate Q is large. Figure 3.15 considers the case in which both time t and injection rate Q are large. It can be seen that the new analytical solution agrees with the numerical solution quite well in all these cases. In Figure 3.13, it is noted that there is a tiny fluctuation in the COMSOL solution. The fluctuation is caused by the fact that it is a 2D model and there is heat conduction in the vertical direction.

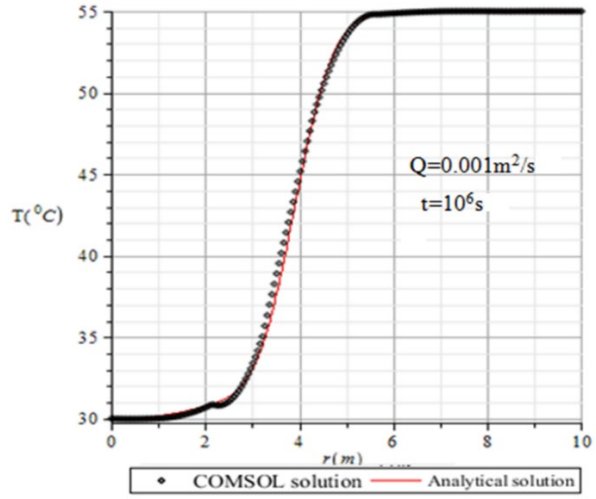

Figure 3.13: Both time t and injection rate Q are small

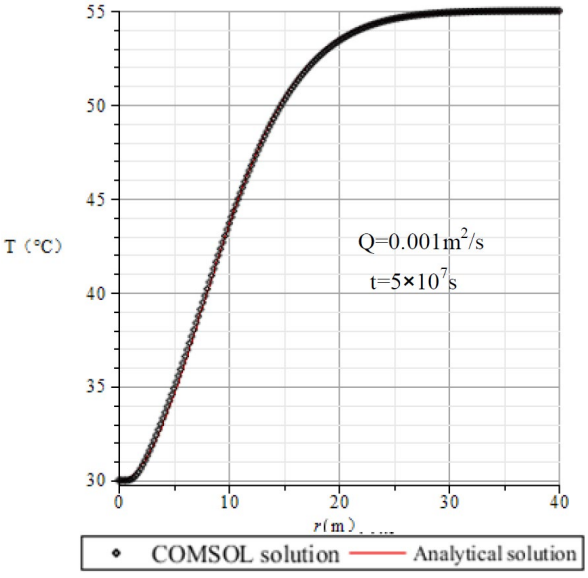

Figure 3.14: Time t is large and injection rate Q is small

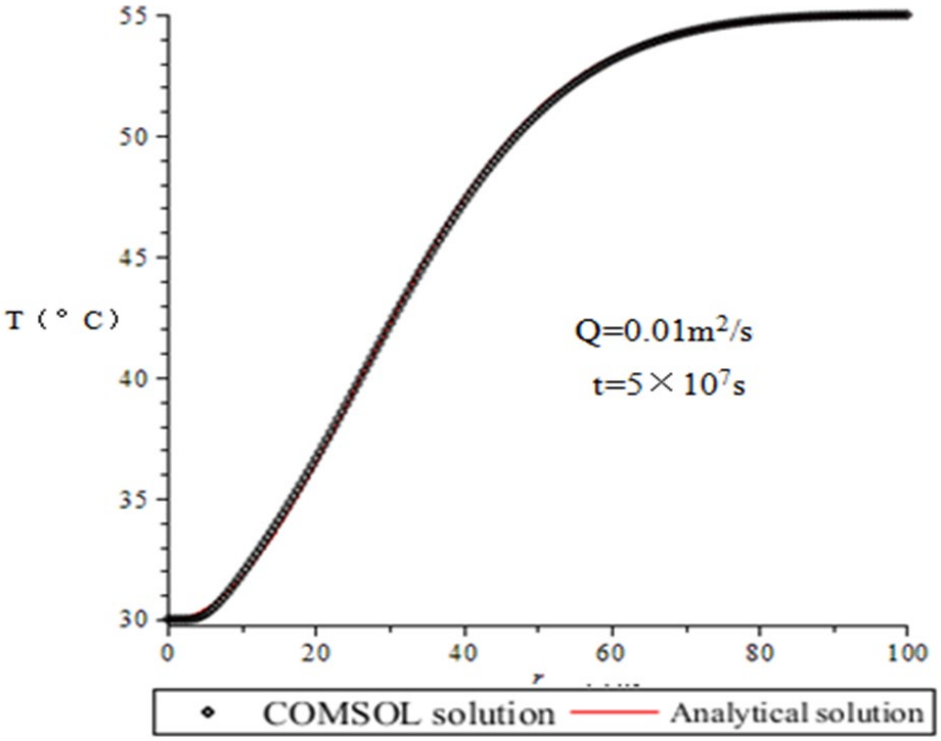

Figure 3.15: Both time t and injection rate Q are large

3.7 Extracted Power

After the temperature distribution of the aquifer at different times is known, it is possible to estimate the time-dependent variation of geothermal energy extracted from the extraction well, which is located at a given distance from the injection well. Considering that the temperature at the extraction well is T, the extracted power P can be estimated using the following equation:

$$P = \rho Q \cdot c(T - T_w) \tag{3.40}$$

Substituting the temperature expression of Equation (3.29), we obtain the following extracted power:

$$P = 2\pi H \rho c \cdot \beta[-(T_w - T_0) + \frac{T_w - T_0}{\Gamma(\frac{\beta}{2D})} \int_{\frac{r^2}{4Dt}}^{\infty} e^{-(x+\frac{hr^2}{4\rho cDH}\frac{1}{x})} x^{\frac{\beta}{2D}-1} dx] \tag{3.41}$$

where $\beta = \frac{Q}{2\pi H} \cdot \frac{(\rho c)_f}{\rho c}$

The above equation is the energy that can be extracted at an extraction well located at a distance r from the injection well at different times. For example, Figure 3.16 and Figure 3.17 show the energy extracted from an extraction well at location r and using a water injection rate Q (at the quasi-steady state conditions), using the parameter set given in Table 3.1. Time t is 25 years which is a typical lifespan of a geothermal system. The heat transfer coefficient between the aquifer and overburden layer is $h = 10$ W/(m^{2}K) . The temperature in the vertical direction of the aquifer is uniform. The interaction between the injection well and extraction well is first neglected.

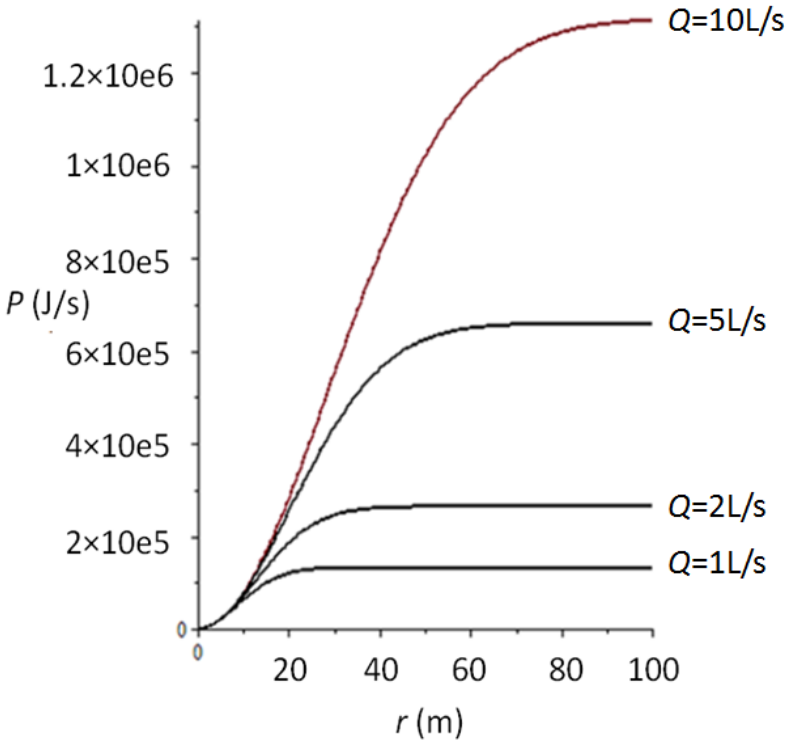

Figure 3.16: Evaluation of extracted energy, $P - r$

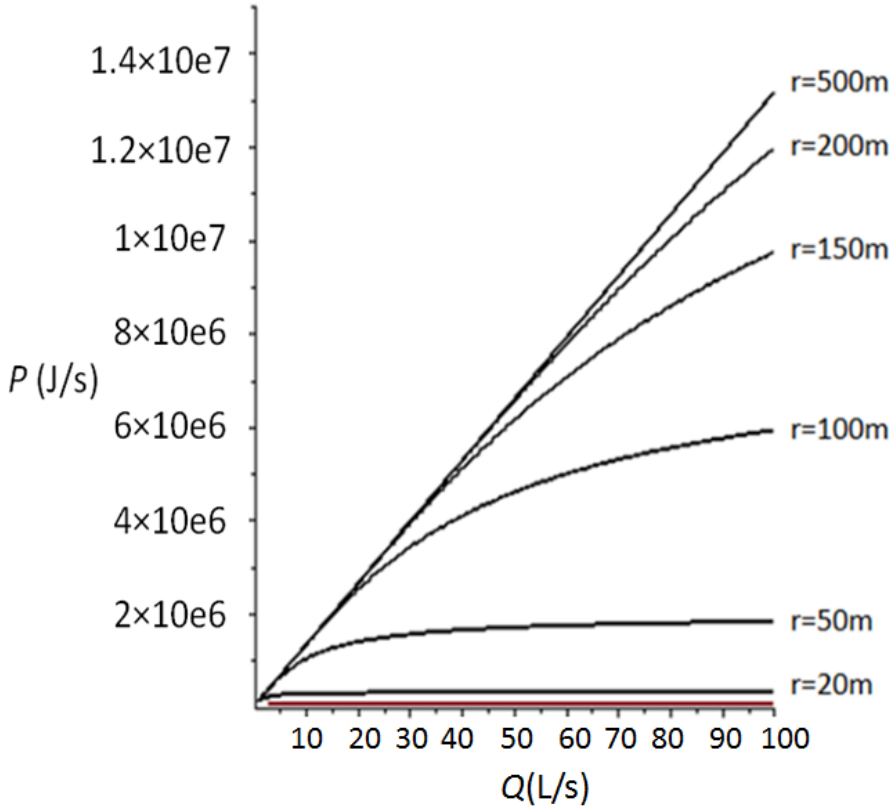

Figure 3.17: Evaluation of extracted energy, $P - Q$

The extraction well should be located beyond the area where the temperature is affected by the injection well at a given injection rate. For example, if the injection rate in Figure 3.16 is 1 L/s, it can be seen from the figure that the distance between the injection well and the extraction well should be greater than 25 m. Also, at a given location of the extraction well, there is an upper limit for the energy even if the injection and extraction rate become very large. For example, if the distance between the injection well and the extraction well in Figure 3.17 is 50 m, it can be seen from the figure that the maximum energy that can be extracted from the extraction well is about 1.5×10^{6} J/s. Hence there is a suitable set of rates and locations in which it is economically viable to extract heat from the ground.

3.8 Summary

This chapter applied a convective heat transfer boundary between the aquifer and overburden layers for the axisymmetric problem based on the Lauwerier model. The new analytical

solution was obtained using Laplace transforms and considers both heat advection and conduction. Besides, the parameter impact analysis was given. A quasi-steady-state solution was found to exist in the axisymmetric problem, while in the planar symmetric problem such steady state does not exist. The analytical solution agrees with the numerical solution. As long as the relevant parameters are obtained, the new analytical solution can intuitively illustrate the temporal and spatial temperature distribution within the aquifer, and therefore allows us to develop a simple engineering analysis method to obtain the temperature distribution in the aquifer. It is possible to determine the location of the extraction well and to evaluate the geothermal potential of the hot water aquifer for a given well geometry.

Chapter 4 Determination of Heat Transfer Coefficient *h*

In Chapter 3, a new analytical solution was deduced using the convective heat transfer boundary condition, $q = h(T - T_0)$. But it neglected the interaction between the injection well and extraction well. In order to use the new analytical solution to assess the actual field conditions, a value for heat transfer coefficient, h needs to be defined for a given set of conditions. In this chapter, we will discuss how to determine the value of heat transfer coefficient h from the geometry and thermal properties of the reservoir.

4.1 Methodology

The value of h should be a function of the geometry and thermal properties of the reservoir as well as the injection rate. In this study, a series of finite element analyses was conducted to develop a relationship between the dimensionless coefficient, h^* and the other dimensionless reservoir thermal properties. First, the time-dependent temperature distribution of the aquifer was calculated, and then the results were compared to the results given by the analytical solution. An appropriate value for the dimensionless coefficient, h^*, was determined by matching the two.

4.2 Finite Element Analysis of the Model with the Overburden Layer

The model is axisymmetric with respect to the injection well, as shown in Figure 4.1. The physics used in the model are “Heat Transfer in Porous Media” and “Heat transfer in Solids”. The upper layer is the overburden layer and the lower one is the aquifer layer. The thickness of the overburden layer is 950 m, whereas that of the aquifer layer is 50 m. The radius of the

well is 0.1 m and the radius of the outer boundary is 400 m. The surface of the overburden layer is regarded as a temperature boundary whose temperature is the same as the ambient temperature. Generally, the geothermal temperature increases linearly with the depth in the ground. Hence, it is assumed in the model that the initial temperature in the overburden layer is proportional to the depth. The lower boundary of the aquifer is thermally insulated and impermeable.

The heat transfer at the interface between the overburden layer and the aquifer is by heat conduction. For the purpose of accuracy, the model mesh uses 358,242 quadratic triangular elements. Finer elements are used near the well, with a minimum element size of 0.1 m. Sensitivity analysis was conducted to ensure that the outer boundary has a negligible effect on the results within the typical 25 years lifetime of the operation.

The temperature distribution of the whole model at a time of 32 years ($\approx 10^9$ sec) for Q = 0.001 m^3/s is shown in Figure 4.1, using the parameter set given in Table 3.1. Figure 4.2 shows the temperature distributions in the aquifer layer at four different times (3.2 years, 6.4 years, 16 years and 32 years). The temperature reduction around the injection well propagates outwards over time, with a radius of influence of approximately 150 m after 32 years.

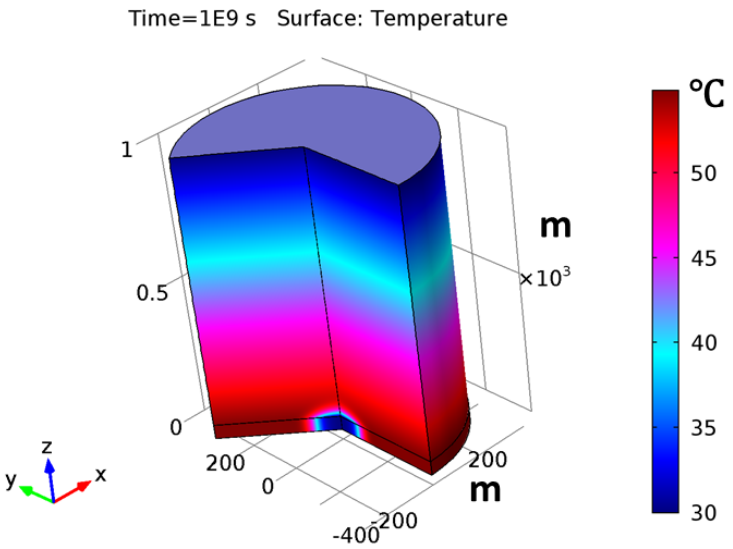

Figure 4.1: Temperature of the whole model

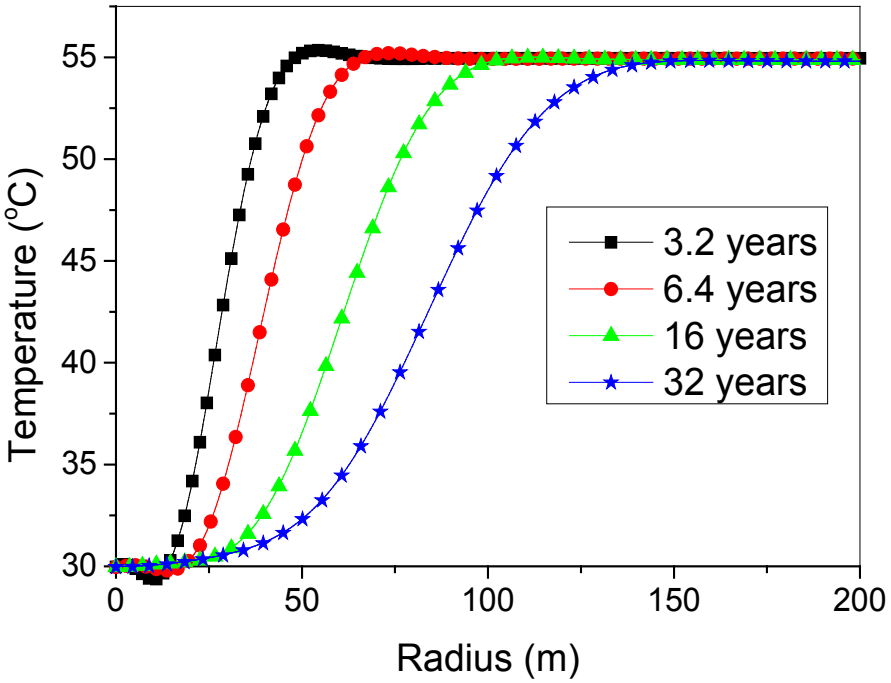

Figure 4.2: Temperature distribution in the aquifer layer at different times

4.3 Dimensionless Parameters

For a given aquifer condition of thickness H and conductivity λ , the heat transfer coefficient, h, can be normalised by the following dimensionless form:

$$h^* = \frac{H}{4\lambda} h \tag{4.1}$$

Inspection of the governing equations (Eqs. (3.1) ~ (3.5)) suggests that the numerical solutions for different cases are influenced by the dimensionless injection rate, α, and the dimensionless thickness and thermal parameters of the overburden layer (thickness H_2 and conductivity λ_2). As the specific heat capacity of the overburden layer, c_2, is not generally subjected to a wide degree of variability in geological environments (Schon, 1996; Ferguson et al., 2005), c_2 is not included in the normalization process.

$$\text{Dimensionless thickness: } H^* = \frac{H_2}{H} \tag{4.2}$$

$$\text{Dimensionless thermal conductivity: } \lambda^* = \frac{\lambda_2}{\lambda} \tag{4.3}$$

$$\text{Dimensionless injection rate: } \alpha = \frac{1}{4\pi nR} \cdot \frac{\rho c}{H\lambda} Q \tag{4.4}$$

As the thickness of the overburden layer is normally much greater than the thickness of the aquifer layer, it was found that the heat transfer coefficient, h^*, does not depend on the thickness of the overburden layer (Equation (4.2)). This is shown in Figure 4.3 for two different cases (the aquifer layer H = 50 m, the overburden layer H_2 = 200 m and 500 m at 1, 10 and 25 years).

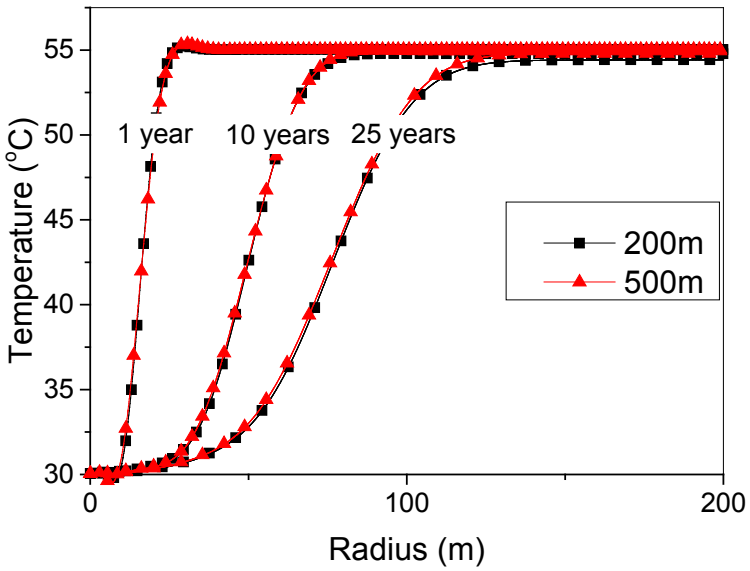

Figure 4.3: Influence of the thickness of the overburden layer

Therefore, it is assumed that $h^* = f(\alpha, \lambda^*)$. In practice, the water injection rate is normally around 0.03 m^3/s. In this study, the range of water injection rate is set to be 0.0001~0.1 m^3/sec and the corresponding dimensionless injection rate, α, is 0.6 ~ 600 (H = 50 m, λ =

1.125 W/(m·K), ρc = 2830 kJ/(m^3·K), n = 0.25 and R = 2.66). The values are all typical values used in practice. The thermal conductivity of the overburden layer can be greater or smaller than that of the aquifer layer. In this study, the dimensionless thermal conductivity of the overburden layer, λ^*, was varied between 0.1 and 10.

Using the new analytical solution, the effect of h^* on the temperature profile after 25 years of operation is shown in Figure 4.4. The input parameters are the same as those shown in Chapter 3. The value of h^* can be adjusted to match the numerical results. As the dimensionless heat transfer coefficient, h^*, characterises the heat exchange at the interface, a larger value of h^* means that more heat transfers from the overburden layer to the aquifer, and hence the radius of the cold influence is smaller. As the dimensionless coefficient, h^* increases, the temperature at any location increases and the temperature gradient around the well becomes larger.

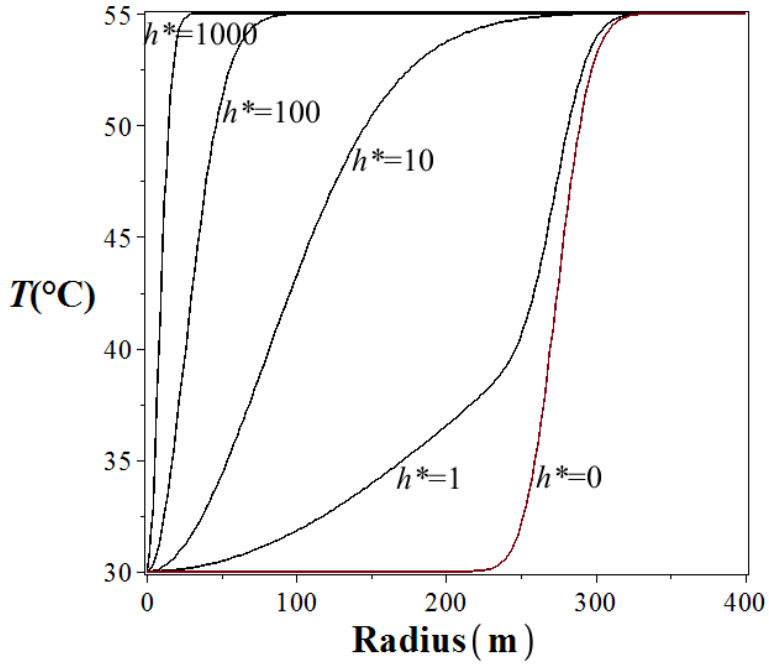

Figure 4.4: The location of the heat front against various values for the dimensionless coefficient h^*

4.4 Curve Fitting Exercise

As the analytical solution developed in Chapter 3 is a transient one, a series of specific times must be chosen in order to match the two solutions to find the optimal equivalent value for the

dimensionless coefficient, h^*. Assuming that the typical lifespan of a geothermal system is 25 years, an emphasis was made in this study to match the spatial temperature profiles between the analytical solution and the numerical results over a period of up to 25 years, in order to evaluate the optimal value of h^*, as shown in Figure 4.5. This is for the case of $\lambda^*=2$ and α = 17.83 (Q = 0.003 m^3/sec), using the other parameters as defined in Table 3.1. It can be seen that the two solutions cannot be matched exactly at 25 years and other years for both the near-well section and the breakthrough section. In this study, more emphasis is made on finding a good match at the breakthrough section, which is more important in geothermal evaluation and system design. In this case, the best equivalent h^* is evaluated to be 1.7. If the emphasis is made to match the near well section, the best equivalent h^* would be 0.6 as show in Figure 4.6.

Figure 4.7 shows the match for different times when the dimensionless injection rate is α = 5.94 (Q = 0.001 m^3/sec) for the case of $\lambda^*=1$ and using the other parameters as defined in Table 3.1. In this case, the two solutions match very well at the breakthrough section over different times, so h^* = 1.2 is the best equivalent heat transfer coefficient.

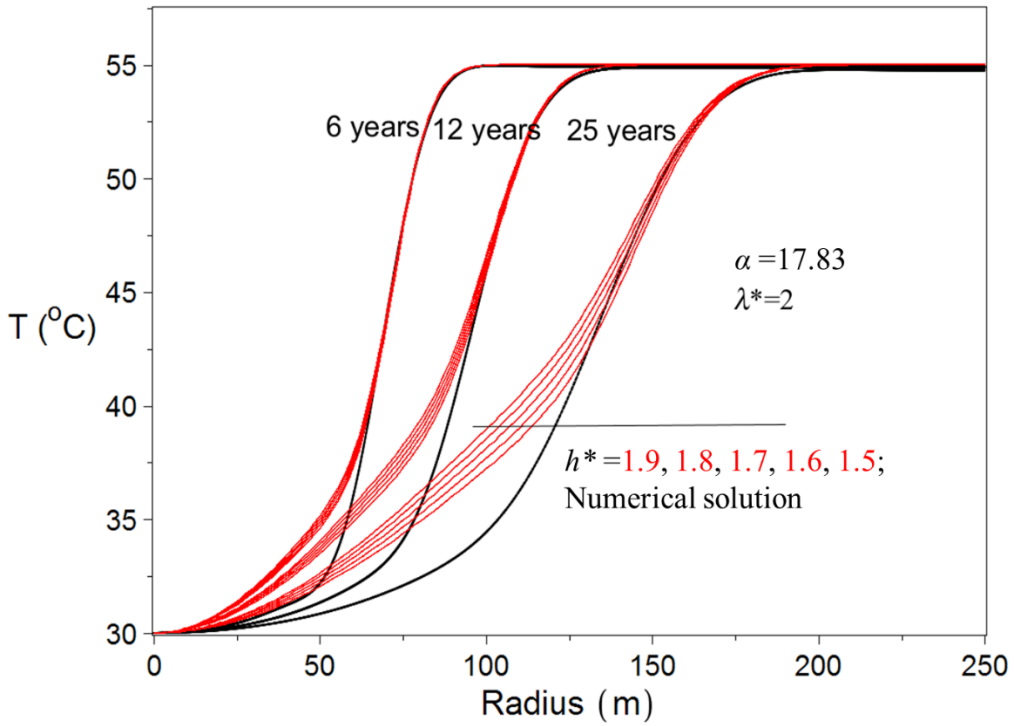

Figure 4.5: Comparison between numerical solutions and analytical solutions with different values of h^*

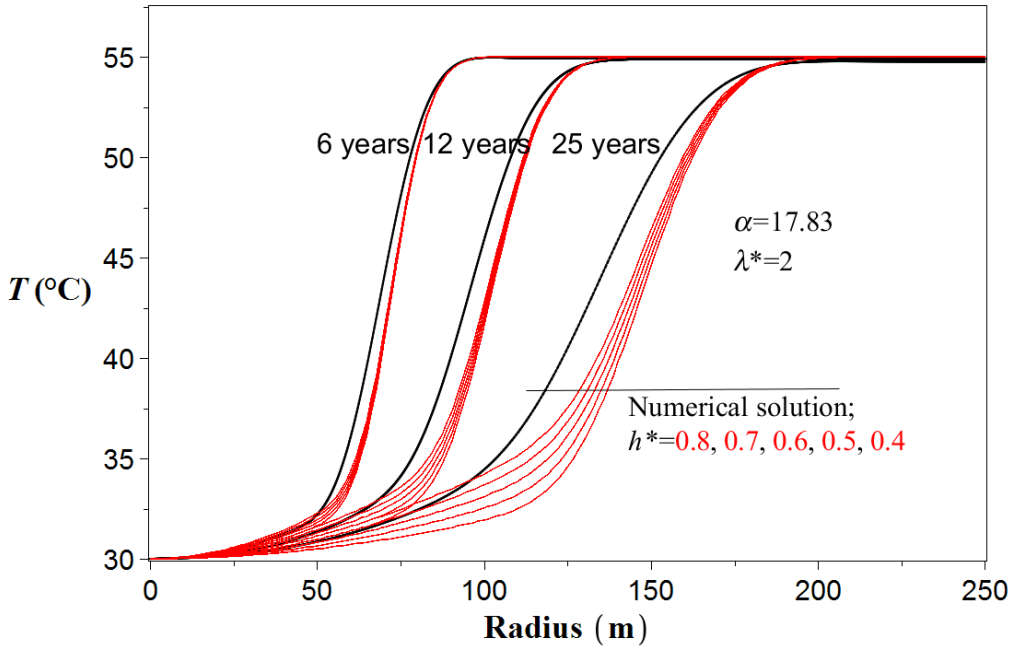

Figure 4.6: Another set of comparisons between the numerical and analytical solutions with different values of h^*, based on the near-well section

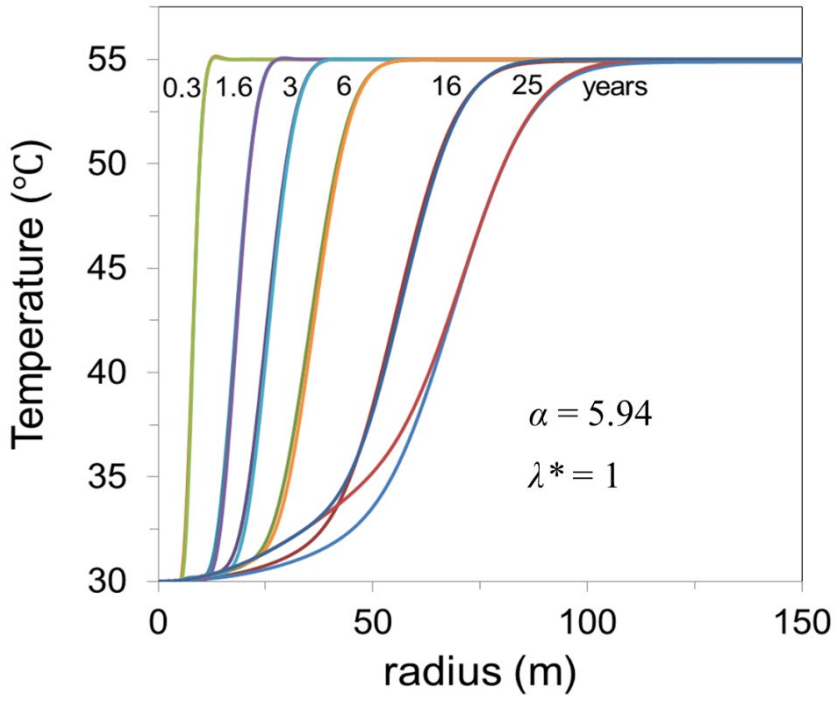

Figure 4.7: Comparison between the numerical solutions and analytical solutions ($h^* = 1.2$) at different times

4.5 Expression of h^* as a Function of α and λ^*

Figure 4.8 shows how the curve-fitted h^* varies with λ^* and α. The data analysis results show that the trend of h^* varying with α for $1 \leqslant \lambda^* \leq 10$ (when the thermal conductivity of the overburden layer is greater than that of the aquifer layer) is different from that of $0.1 \leq \lambda^* < 1$ (when the thermal conductivity of the overburden layer is smaller than that of the aquifer layer). The physical explanation of the difference is that the overburden layer acts as a heat conduit in the former and a heat barrier in the latter.

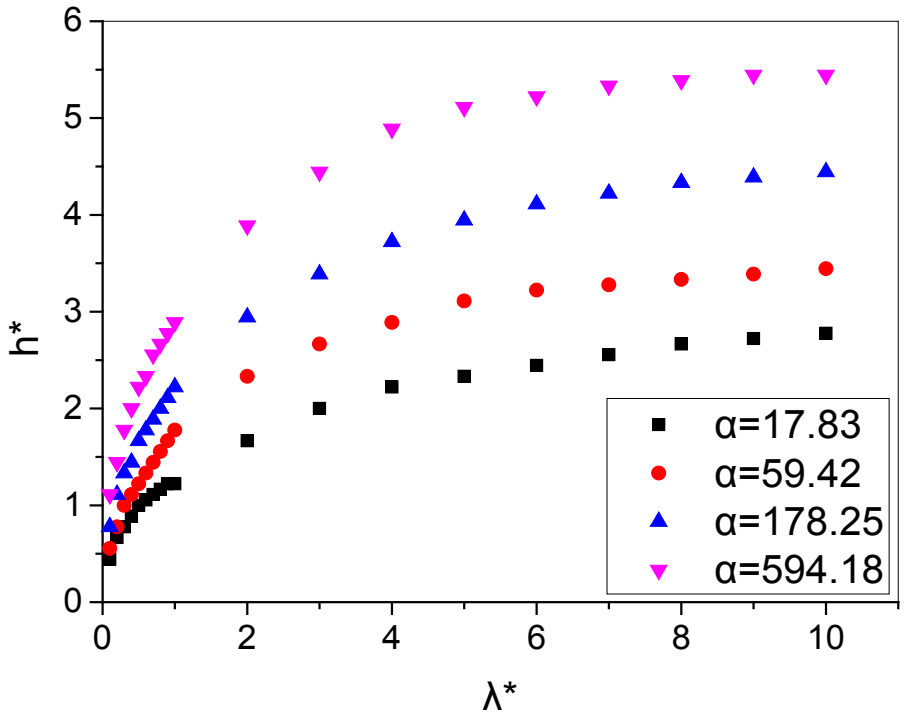

Figure 4.8: How the optimal h^* varies with λ^* and α

4.5.1 $1 \leqslant \lambda^* \leq 10$ ($\lambda_{overburden} > \lambda_{aquifer}$) – Heat Conduit Overburden Layer Case

The trend line of h^* against α for $1 \leqslant \lambda^* \leq 10$ is shown in Figure 4.9. The results show that for a given value of λ^*, the expression of h^* has a form of $h^* = c\alpha^d$. Further data analysis shows

that the coefficient, c, and the exponent, d, are both functions of λ^*. The trend line of c against λ^* is shown in Figure 4.10, and the trend line of d against λ^* is shown in Figure 4.11.

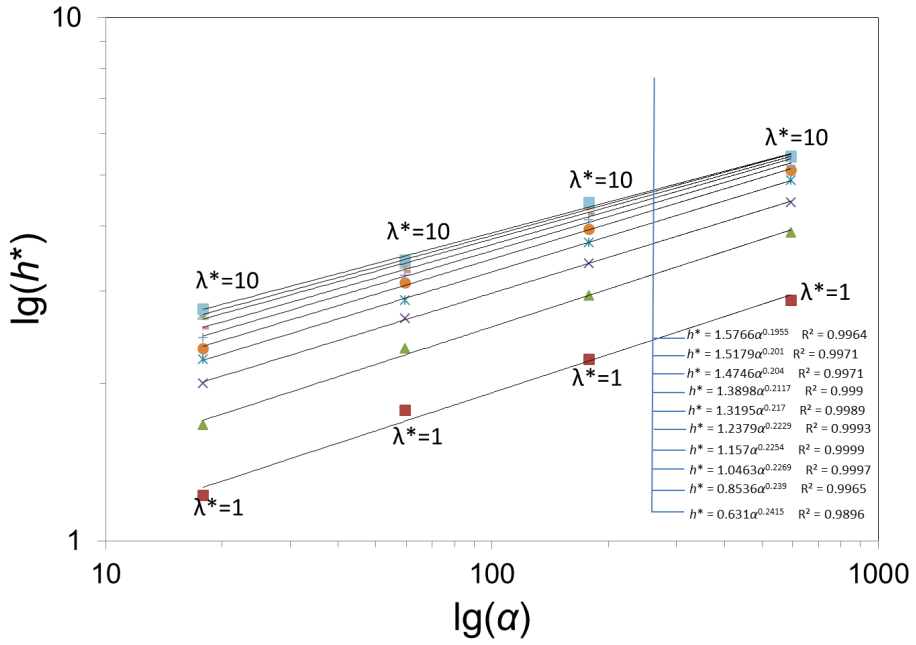

Figure 4.9: The trend line of h^* against α for $1 \leq \lambda^* \leq 10$

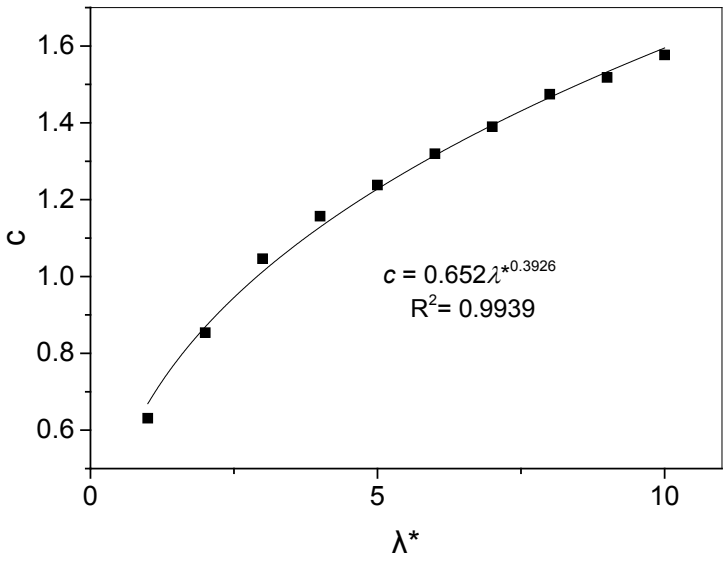

Figure 4.10: The trend line of c against λ^* for $1 \leq \lambda^* \leq 10$

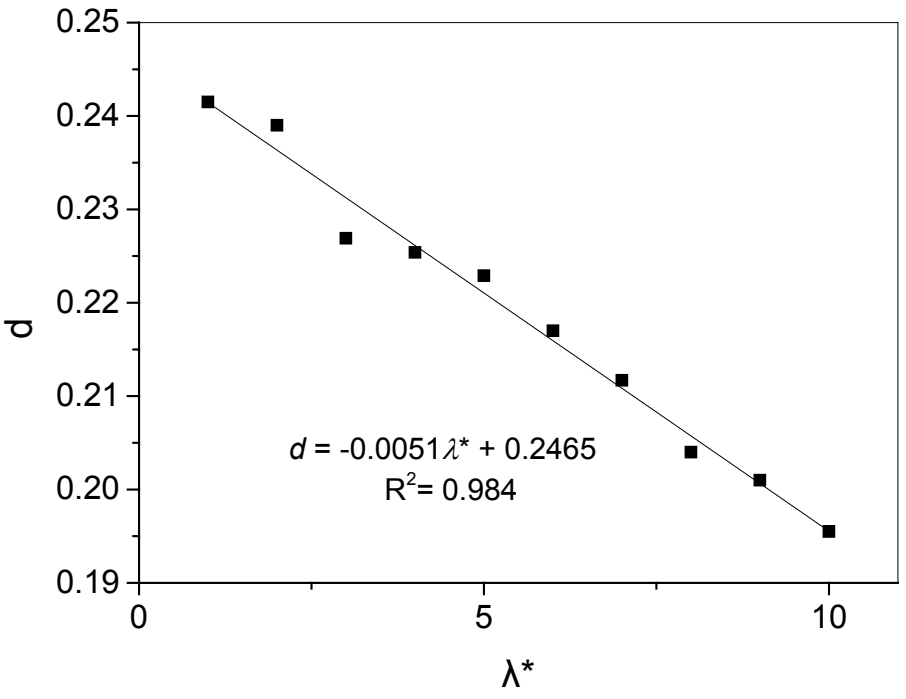

Figure 4.11: The trend line of d against λ^* for $1 \le \lambda^* \le 10$

In summary, for $1 \le \lambda^* \le 10$, the following empirical expression of h^* is proposed for values of α ranging from 0.6 to 600.

$$h^* = 0.652\lambda^{*0.3926}\,\alpha^{0.2465-0.0051\lambda^*},\quad 1 \le \lambda^* \le 10,\quad 0.6 \le \alpha \le 600 \tag{4.5}$$

In Equation (4.5), as the index of λ^* is greater than that of α, h^* is more sensitive to the value of λ^*. However, as the range of α is much greater than that of λ^* in practice, h^* is greatly influenced by α. The term $\lambda^{*0.3926}$ indicates that the value of h^* increases with λ^* as the heat flux between the aquifer and the overburden layer increases. The term $\alpha^{0.2465-0.0051\lambda^*}$ indicates that the value of h^* increases with the increasing α and the contribution of α to h^* slightly decreases with the increasing λ^*. As α represents the ratio between thermal advection and conduction, an increase in overburden layer conductivity increases the conductivity process around the interface between the aquifer and overburden layer. Thus the contribution of α to h^* decreases with an increase in λ^*, especially when λ^* is large.

4.5.2 $0.1 \leq \lambda^* < 1$ ($\lambda_{overburden} < \lambda_{aquifer}$) – Heat Barrier Overburden Layer Case

Figure 4.12 shows curve fitted equations of h^* against λ^* for different values of α. The expression for h^* has a form of $h^* = m\lambda^{*n}$ for a given value of α. It is found that the coefficient, m, and the exponent, n, are both functions of α. As the dimensionless heat transfer coefficient h^* characterises the heat exchange at the interface, the dimensionless injection rate α has an influence on heat conduction, i.e. the term λ^{*n}, so that the exponent n is a function of α. The trend line of m against α is shown in Figure 4.13.

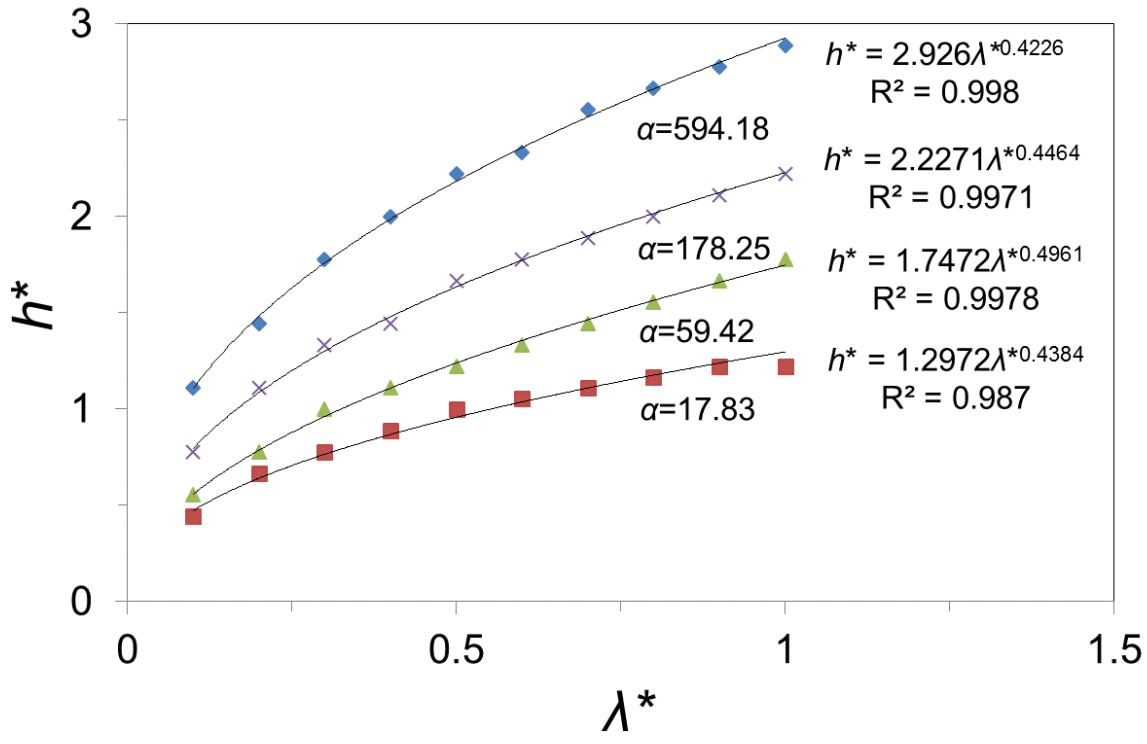

Figure 4.12: The trend line of h^* against λ^* for different values of α

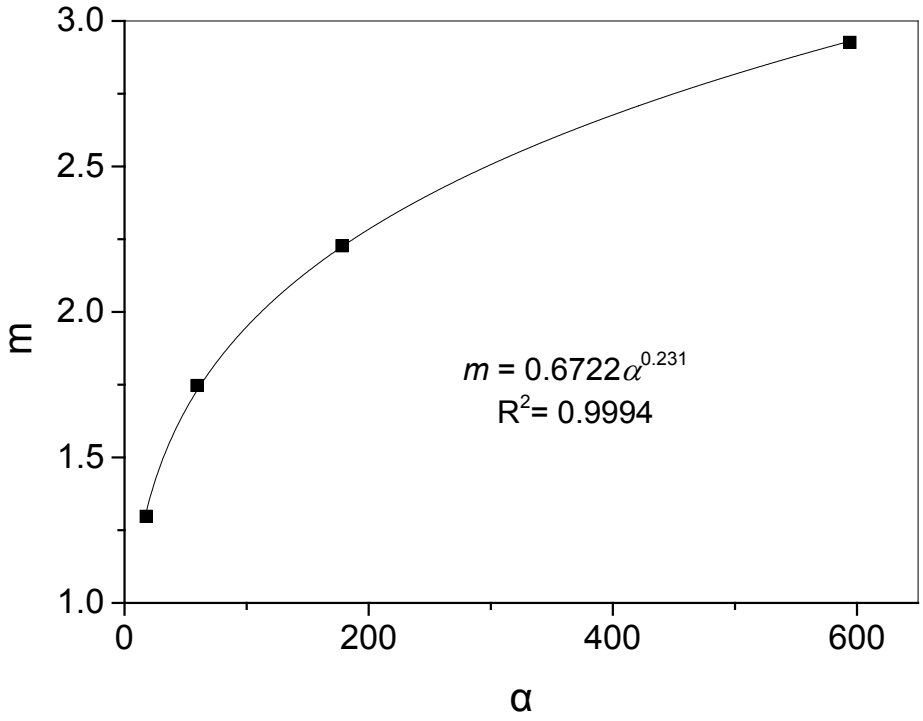

Figure 4.13: The trend line of m against α

The exponent n varies with α, ranging between 0.4 and 0.5. However, for values of λ^* between 0.1 and 1, the average exponent of $n = 0.45$ was used for simplicity. As shown below, the maximum error in h^* from this simplification was estimated to be 0.1 when the maximum value of m (2.926) is assigned:

$$\Delta h^*_{\max} = 2.926 \times 0.1^{0.45} - 2.926 \times 0.1^{0.4961} = 0.1$$

As shown in Section 4.4, the accuracy of h^* in the curve fitting is ± 0.1. Hence, this error in h^*, which is introduced by using the h^* function to summarise the raw data in Figure 4.8, is within the accuracy of the proposed curve fitting method.

In summary, for $0.1 \leq \lambda^* < 1$, the following empirical expression of h^* is proposed for values of α ranging from 0.6 to 600.

$$h^* = 0.6722\alpha^{0.231}\lambda^{*0.45}, \quad 0.1 \le \lambda^* < 1, \quad 0.6 \le \alpha \le 600 \tag{4.6}$$

In Equation (4.6), as the index of λ^* is greater than that of α, h^* is more sensitive to the value of λ^*. However, as the range of α is much greater than that of λ^* in practice, h^* is greatly influenced by α. The term $\lambda^{*0.45}$ indicates that the value of h^* increases with the increasing λ^* as the heat flux between the aquifer and the overburden layer increases. The intrinsic reason why we can use $n = 0.45$ for simplicity and the maximum error in h^* from this simplification is small (0.1), is that the influence of heat advection α on the heat conduction term λ^{*n} is small. The term $\alpha^{0.231}$ indicates that the value of h^* increases with the increasing α and the contribution of α to h^* is not affected by λ^* which is different from that of Equation (4.5). The explanation is that, because λ^* is small in this case, the change of λ^* will not affect the contribution of α significantly.

4.6 Error Analysis of the Derived Equations

The h^* expressions given by Equation (4.5) and Equation (4.6) can be useful in engineering practice when they are used in conjunction with the proposed analytical solution. For a given injection rate, Q, and the thermal conductivity values of the aquifer and the overburden layers, the dimensionless injection rate, α, and the dimensionless overburden layer thermal conductivity, λ^*, can be computed and substituted into the proposed h^* expression to evaluate the dimensionless coefficient, h^* or coefficient h. Once the coefficient, h, is known, Equation (3.30) is used to estimate the temperature distribution in the aquifer with time, which in turn can be used to determine the location of the extraction well and to evaluate the extracted energy using Equation (3.41). The calculation can be done for different values of Q to conduct a back-of-the-envelope evaluation of the geothermal potential of a site.

When the analytical solution is used, any error associated with the curve fitting exercises needs to be quantified. The case shown in Figure 4.5 can be taken as an example with an error analysis of the derived empirical equations (Equation (4.5) and Equation (4.6)), assuming that the curve fitted value is the ground truth ($h^* = 1.7$ in this case). The dimensionless injection rate is $\alpha = 17.83$ and the dimensionless thermal conductivity of overburden layer is $\lambda^* = 2$. The other

parameters are given in Table 3.1. Substituting these values in Equation (4.5) gives the following h^* value:

$$h^* = 0.652\lambda^{*0.3926}\,\alpha^{0.2465-0.0051\lambda^*} = 0.652*2^{0.3926}17.8254^{0.2465-0.0051*2} = 1.69$$

The error is $\Delta h^* = 1.69 - 1.7 = -0.01$, which is within the accuracy of the curve fitting ($\Delta h^* = \pm 0.1$) when the analytical solution was fitted to the FE results.

Similar exercises can be done for other sets of input parameters and the results are shown in Figure 4.14. The range of error values is $\Delta h^* = \pm 0.11$ at the maximum. Again these values are considered to be within the range of the accuracy of the curve fitting exercise ($\Delta h^* = \pm 0.1$). Therefore, the overall error in h^* is approximately $\Delta h^* = \pm 0.2$, which should be considered when sensitivity analysis is done using the proposed analytical solution.

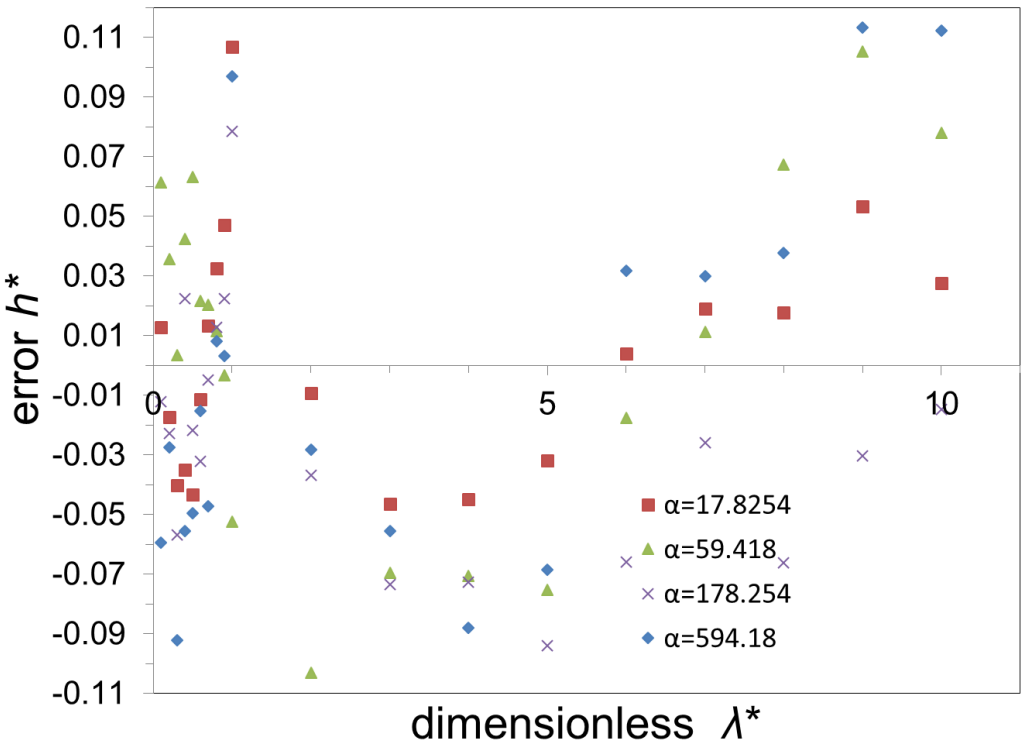

Figure 4.14: Error in estimating h^*

4.7 Summary

The new analytical solution uses the convective heat transfer coefficient, h, from the overlying boundary. This boundary condition at the interface not only reflects the actual heat transfer process at the interface, but also models the heat transfer process in the overburden layer. In this study, it is proposed that the dimensionless equivalent heat transfer coefficient is expressed as a function of the dimensionless injection rate and the dimensionless thermal conductivity of the overburden layer. A series of FE simulations were conducted, and the analytical model was curve fitted to the FE results to evaluate the values of the dimensionless equivalent heat transfer coefficient. Based on the results of the curve fitting exercise, two empirical equations (Equation (4.5) and Equation (4.6)) were proposed for typical HSA cases. Applying the analytical solution coupled with these empirical equations and along with proper error estimates, it is possible to conduct a simple and rapid evaluation of the geothermal potential of a particular site. For example, after obtaining relevant parameters of a site, we can first calculate the dimensionless injection rate α and dimensionless thermal conductivity of the overburden layer λ^*. By substituting α and λ^* into Equation (4.5) or Equation (4.6), we can obtain the dimensionless heat transfer coefficient h^*. Then, by substituting h^* into Equation (3.30), we can obtain the temperature distribution of the site and the optimal location of the extraction well. Finally, by substituting h^* into Equation (3.41), it is possible to estimate the amount of energy that can be extracted from the site.

Chapter 5 Revised Analytical Solution Considering Interaction

In this chapter, the interaction effect between the injection well and the extraction well of a geothermal doublet system is evaluated and quantified based on Lauwerier's model that considers heat transfer by advection and conduction in the aquifer as well as convective heat transfer from the overburden layer where a heat transfer coefficient is applied. The discussion of the interaction effect is divided into two cases. In the first case, the distance between the injection well and the extraction well is larger than the critical distance so that the temperature of water at the extraction well will keep equal to the initial temperature of the aquifer during the typical life span of the system. The revised analytical solution that gives the spatial and temporal temperature distribution in the aquifer is obtained. With this revised solution, the optimal location of the extraction well can be determined. In the second case, the distance between the two wells is smaller than the critical distance so that the temperature of water at the extraction well will start to decrease during the life span of the system. The relation between the temperature of the extracted water and time is also obtained. With this expression of the temperature of the extracted water, the amount of the extracted geothermal energy varying with time can also be evaluated. Finally, the revised analytical solution is compared with the experimental data and the numerical solutions and they match with each other well.

5.1 Methodology

A Finite Element Analysis software COMSOL is used to build the model including both the injection well and extraction well and then analyze the interaction effect. This COMSOL model is a fluid flow and heat transfer fully coupling model so that it is able to effectively evaluate the interaction effect of two wells in terms of heat transfer. The temperature distribution along the line connecting two wells considering interaction effect can be given by the numerical model. The analytical solution will be compared with the numerical temperature distribution

and then the parameters in the analytical solution are varied so as to fit the numerical solution. Hence a revised analytical solution can be obtained. As a result, the interaction effect is included in the analytical solution via this approach.

5.2 COMSOL Model

The model is a 2D square with one injection well and one extraction well as shown in Figure 5.1. The physics used in the model are "Heat Transfer in Porous Media" and "Darcy's Law". The units of the horizontal axis and the vertical axis are [m]. The scale of the model needs to be adapted according to the injection and extraction rate (it is 3000 m * 3000 m for Q = 10 L/s). Generally, the scale of the model increases with increasing injection and extraction rate. The thickness of the aquifer layer H = 50 m (though it is a 2D model, a thickness H can still be assigned to the model in COMSOL which means that the temperature along the thickness H is constant). The thickness of the aquifer H is an essential input parameter in the heat transfer calculation. The radius of the two wells is both 0.5 meters. The distance between the two wells is 1000 m in this case. A constant flow rate (Q = 10 L/s in this case) is applied to the surface of the circumferential boundaries of the injection well and extraction well. The temperature of the surface of the injection well is constant (30 degrees in this case). The outer boundary conditions of the square mesh model are thermal insulated boundary and 0 pressure boundary (the relative hydraulic pressure on this boundary is 0). The initial temperature of the model is 55 degrees. An out-of-plane heat flux boundary is $w_0 = h(T - T_0)$, where h is the convective heat transfer coefficient. The value of h can be determined using Equation (4.5) and Equation (4.6) in Chapter 4, which is perpendicular to the 2D square mesh model and is applied to reflect the convective heat transfer boundary in the analytical solution. This 2D model effectively characterizes the 3D model comprising the aquifer and the overburden layer: (1) the aquifer is represented by the 2D square mesh with a virtual thickness of H = 50 m, which ensures that the temperature along the thickness is exactly constant. (2) the overburden layer is represented by the out-of-plane heat flux boundary and the properties of the overburden layer are simplified into the equivalent heat transfer coefficient h, as discussed in Chapter 4. With these settings, the parameters, boundary and initial conditions, etc. are exactly the same as that of the

analytical solution except for the interaction. Therefore, the interaction effect is the only controlled variable when the numerical solution is compared to the analytical solution. For the purpose of good accuracy, the model is meshed with 179,888 quadratic triangular elements. Finer elements are used near the well with a minimum element size of 0.05 m. Sensitivity analysis was conducted to ensure that the outer boundary has negligible effect on the results within a typical life span of the operation (i.e. 25 years).

Using the values in Table 3.1, the temperature distribution for the numerical model at a time of 25 years (≈7.9×10^8 sec) for the Q = 10 L/s case is shown in Figure 5.2. The temperature distributions from the injection well to the extraction well at four different times (1 year, 5 years, 10 years and 25 years) are shown in Figure 5.3.

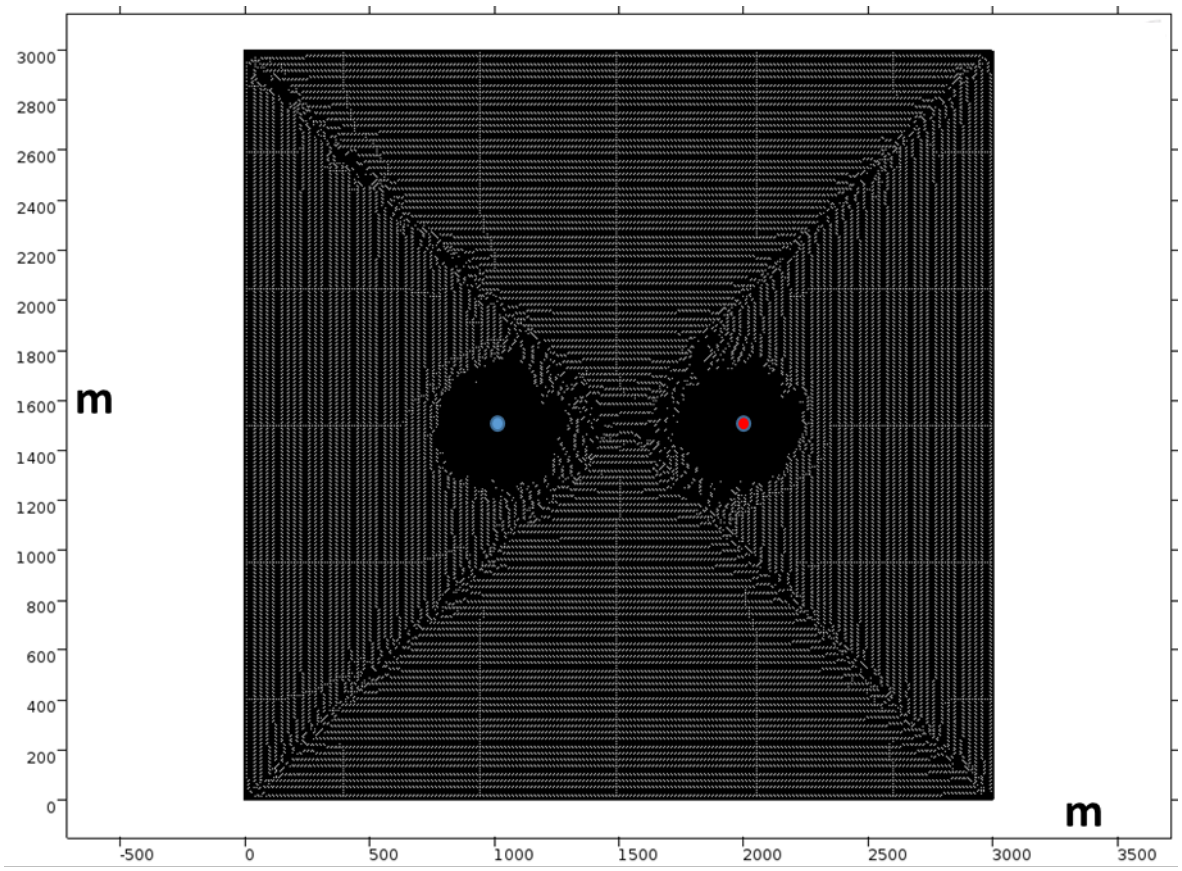

Figure 5.1: 2D square mesh model

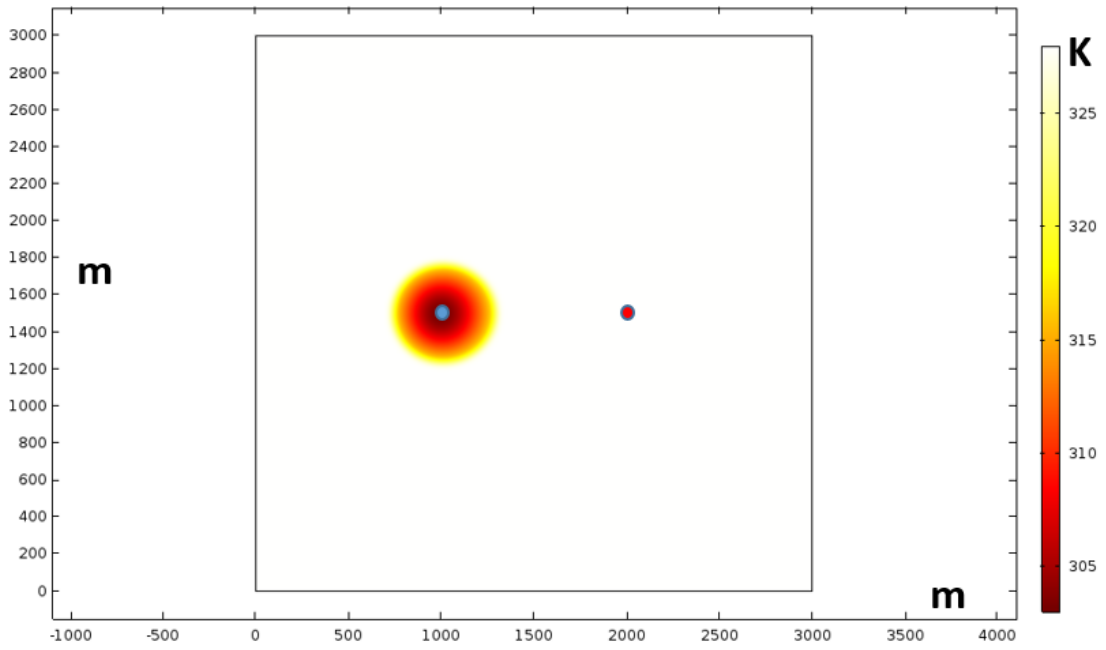

Figure 5.2: Temperature distribution of the model at 25 years

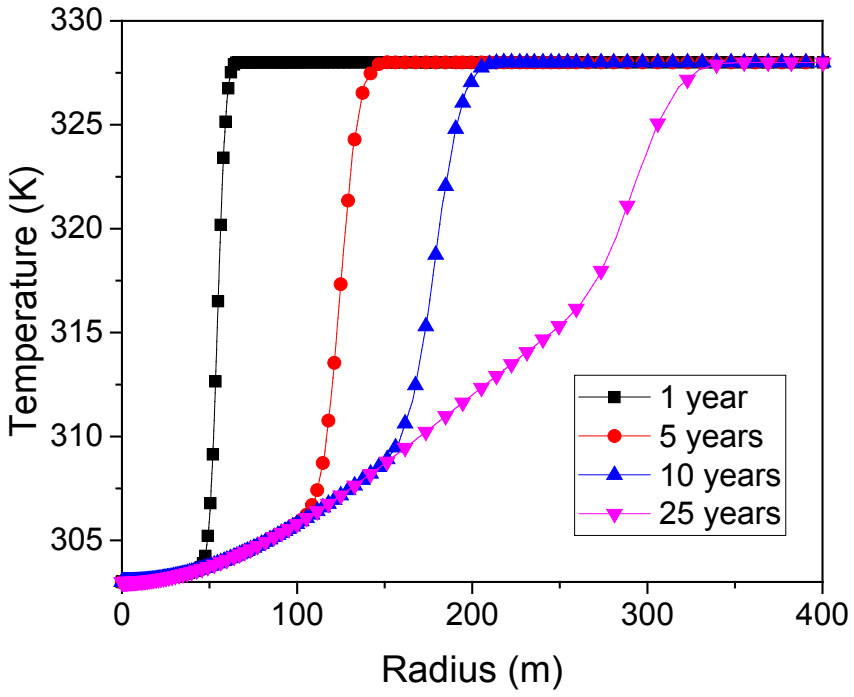

Figure 5.3: Temperature distributions between two wells for different times

5.3 Critical Distance between Two Wells

The critical distance between the injection well and the extraction well is the minimal distance that the temperature of the extracted water at the end of the life span of the system (i.e., 25 years) is still equal to the initial temperature of the aquifer. In other words, the system can achieve the maximum efficiency during the life span if the distance is greater than the critical distance. The respective critical distance L_c for different injection rate can be obtained by varying the distance between two wells in the numerical model until the temperature at the extraction well equals the initial temperature of the aquifer which is 55 degrees in this case.

According to some preliminary analysis, the critical distance L_c is closely related to the heat breakthrough distance given by the analytical solution. The heat breakthrough distance L_b is the extent that the temperature of the injected water can influence without the extraction well, as shown in Figure 5.4. With the increasing distance from the injection well, the temperature of the aquifer infinitely approaches (but never equals) the initial temperature. As a result, the heat breakthrough distance L_b is defined as the distance when the temperature of the aquifer T_b satisfies a threshold of $\frac{T_b - T_0}{T_w - T_0} = 1\%$. This threshold (percentage) should be adequately small to ensure that the temperature change at the heat breakthrough distance L_b is small. On the other hand, if this threshold is too small, the corresponding L_b will be very large, which indicates that the distance between two wells will be greater and the cost for pipelines and surface facilities will increase largely. Therefore, a threshold of 1% is a reasonable choice. The relation between the dimensionless heat breakthrough distance L_b^* ($L_b^* = \frac{L_b}{H}$) and the dimensionless injection rate α (see Equation (3.30)) is shown in Figure 5.5, where H is the thickness of aquifer.

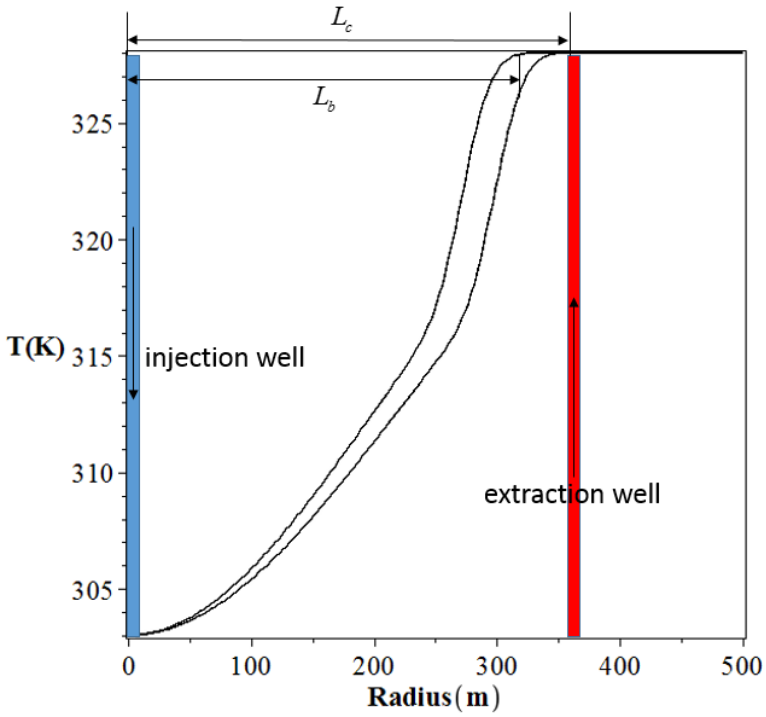

Figure 5.4: Critical distance L_c and heat breakthrough distance L_b

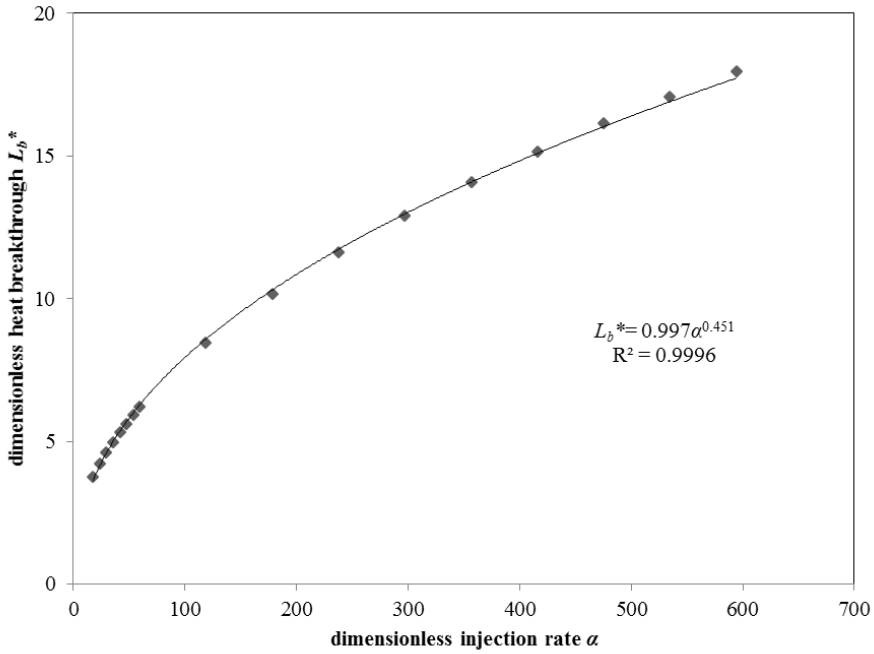

Figure 5.5: Dimensionless heat breakthrough against the dimensionless injection rate

From Figure 5.5, the expression of the dimensionless heat breakthrough distance L_b* is as follows:

$$L_b^* = 0.997\alpha^{0.451},\ 0.6 \le \alpha \le 600 \tag{5.1}$$

The relationship between the dimensionless critical distance L_c* ($L_c^* = \frac{L_c}{H}$, H is the thickness of aquifer) and the dimensionless heat breakthrough distance L_b* is shown in Figure 5.6.

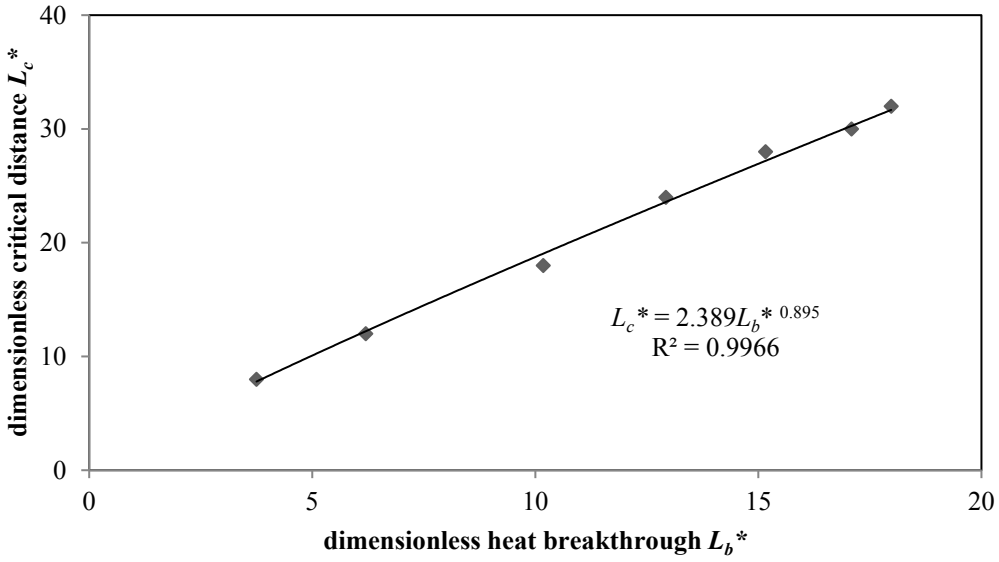

Figure 5.6: relationship between the dimensionless critical distance and the dimensionless heat breakthrough

From Figure 5.6, the expression of the dimensionless critical distance L_c* is as follows:

$$L_c^* = 2.389 L_b^{*0.895} \tag{5.2}$$

Substituting Equation (5.1) into Equation (5.2), the expression of the dimensionless critical distance L_c^* in terms of the dimensionless injection rate α is as follows:

$$L_c^* = 2.383\alpha^{0.404},\ 0.6 \le \alpha \le 600 \tag{5.3}$$

Equation (5.3) can be very useful in engineering practice as it gives the best location of the extraction well, taking account of the heat flux at the interface between the aquifer and the overburden layer which other currently available solutions neglect.

Taking the model in Figure 5.2 as an example, the injection rate Q = 10 L/s, thus $\alpha = 59.4$.

$$L_c^* = 2.383\alpha^{0.404} = 2.383 \times 59.4^{0.404} = 12.41$$

Hence the critical distance $L_c = H \cdot L_c^* = 50 \times 12.41 = 620$ m. So the optimal well distance for the model is around 600 m. The actual well distance in the model $L = 1000$ m is so large that it is not economical.

If the injection rate Q = 60 L/s, thus $\alpha = 356.4$.

$$L_c^* = 2.383\alpha^{0.404} = 2.383 \times 356.4^{0.404} = 25.59$$

Hence the critical distance $L_c = H \cdot L_c^* = 50 \times 25.59 = 1280$ m. So the optimal well distance for the model is around 1300 m. The actual well distance in the model $L = 1000$ m is so small that it is not efficient.

5.4 Curve Fitting Exercise

The revised analytical solution considers an efficient geothermal system that the extraction well is far away enough from the injection well so that the temperature of the extracted water always equals the initial temperature of aquifer during the life span. In other words, the temperature of the extracted water does not decrease with time during the life span. During the process of evaluating the interaction effect to deduce the revised analytical solution, the distance between two wells should be greater than the critical distance to ensure that the temperature of the extracted water keeps constant during the life span, namely $L \geq L_c$ should be satisfied.

As both the numerical and analytical solutions are transient, a series of specific times must be chosen in order to match between these two solutions to find the revised analytical solution.

Since the typical life span of a geothermal system is 25 years, the emphasis is made to match the spatial temperature profiles between the numerical and analytical results up to 25 years. After some trials, it is found that the analytical solutions can match with the numerical solutions well by increasing the injection rate Q in the analytical solution to a larger value Q'. Apparently, Q' is related to the injection rate Q and the distance between the two wells L, namely $Q' = f(Q, L)$. When the distance L is very large, $Q' = Q$. For example, in Figure 5.7, Q' is equal to 0.011 m^3/s for an injection rate Q = 0.01 m^3/s and distance L = 900 m. By comparing the analytical solutions with the numerical solutions applying different Q and L values, the corresponding value of Q' can be determined with this curve fitting exercise. Finally, the revised analytical solution considering the interaction effect can be obtained by replacing the injection rate Q in the analytical solution with $Q' = f(Q, L)$.

In the dimensionless form, it reads $\alpha' = f(\alpha, L^*)$, where $\alpha' = \frac{1}{4\pi nR} \cdot \frac{\rho c}{H\lambda} Q'$, $L^* = \frac{L}{H}$.

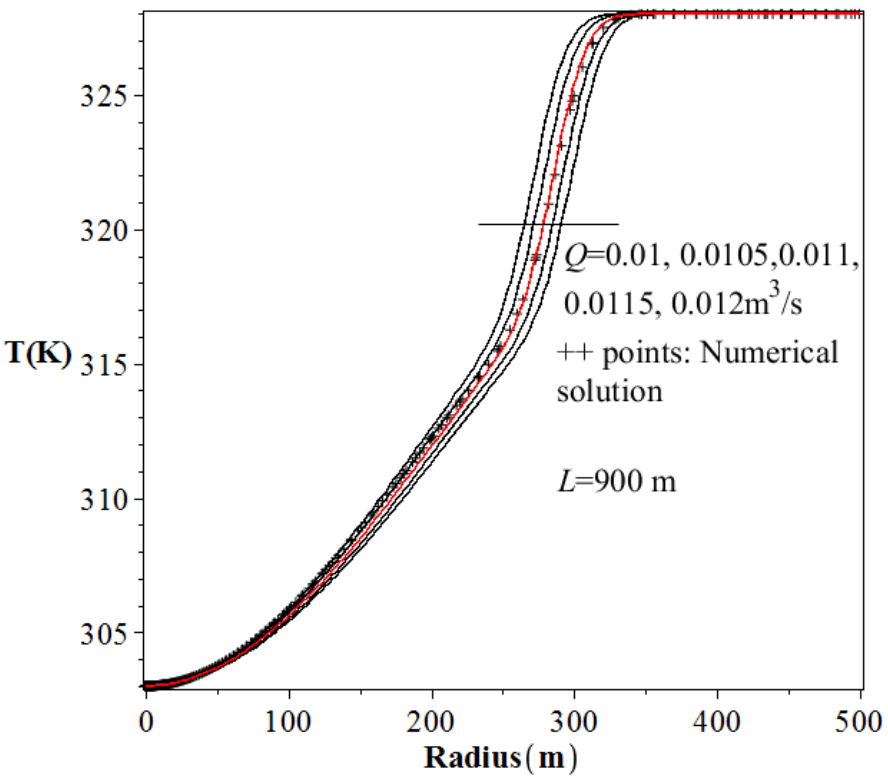

Figure 5.7: An example of the curve fitting

5.5 Revised Analytical Solution

Repeating the curve fitting exercise in Section 5.4 for different injection rates Q and different well distances L, the respective revised injection rate Q' is obtained. As Q' approaches Q, let

$$Q' = Q + Q'' \tag{5.4}$$

In the dimensionless form, Equation (5.4) can be written as:

$$\alpha' = \alpha + \alpha'' \tag{5.5}$$

where $\alpha'' = \frac{1}{4\pi nR} \cdot \frac{\rho c}{H\lambda} Q''$

α'' against different α and L^* is shown in Figure 5.8 (the unit of Q is m^3/s).

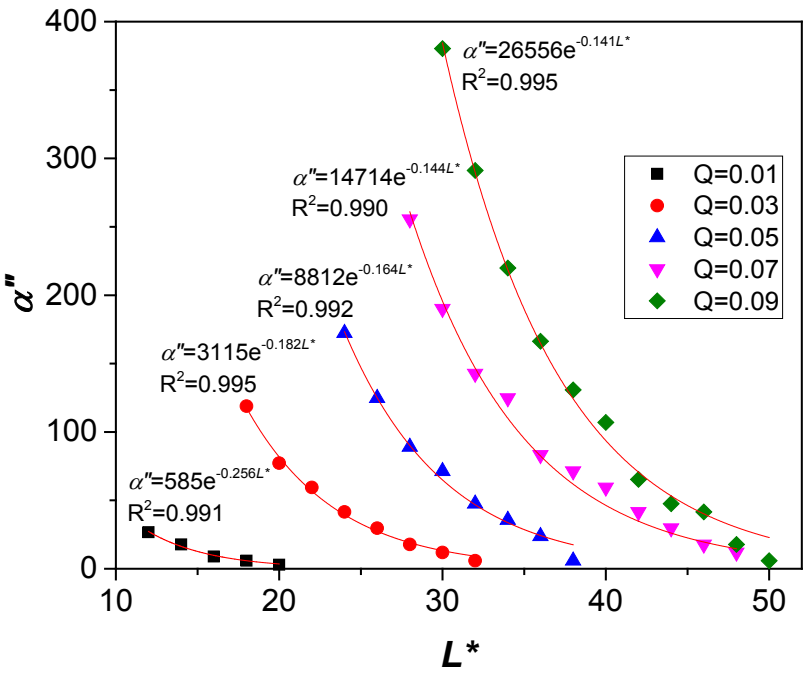

Figure 5.8: α'' against different α and L^*

From Figure 5.8, it is known that α'' has the following form:

$$\alpha'' = m\mathrm{e}^{-nL^*} \tag{5.6}$$

where m and n are the functions of α.

The expressions of m and n are shown in Figure 5.9 and Figure 5.10.

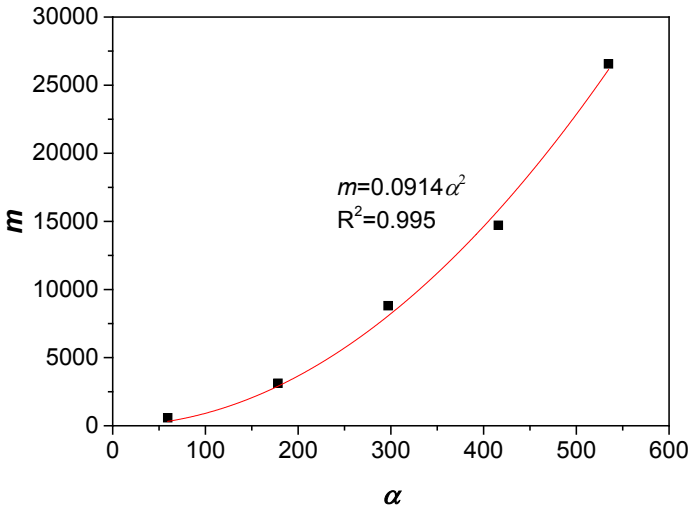

Figure 5.9: Expression of m

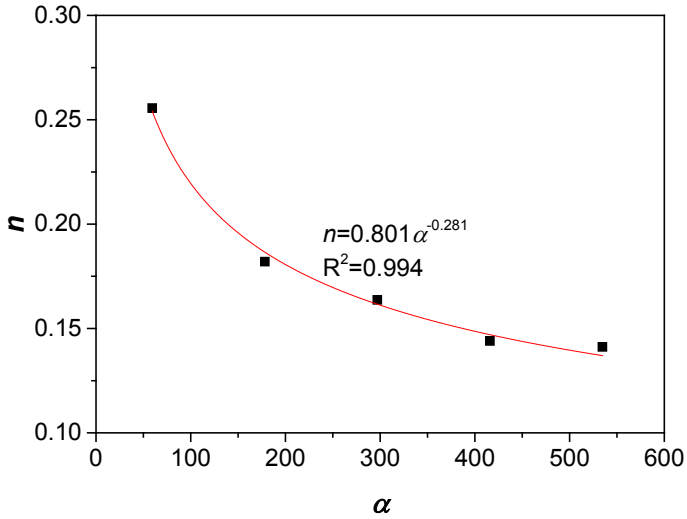

Figure 5.10: Expression of n

From Figure 5.9 and Figure 5.10, the expression of *m* and *n* are as follows:

$$m = 0.0914\alpha^2 \tag{5.7}$$

$$n = 0.801\alpha^{-0.281} \tag{5.8}$$

Substituting Equation (5.7) and Equation (5.8) into Equation (5.5) and Equation (5.6), the expression of the dimensionless revised injection rate α' is as follows:

$$\alpha' = \alpha + 0.0914\alpha^2 \, \mathrm{e}^{-0.801\alpha^{-0.281}L^*}, \; 0.6 \le \alpha \le 600 \tag{5.9}$$

As mentioned in Section 5.4, the temperature distribution in the aquifer for a doublet scheme has the same form of analytical solution as that of a single injection well scheme, which is written as follows:

$$T^* = \frac{1}{\Gamma(\alpha')} \int_{\frac{r^{*2}}{t^*}}^{\infty} e^{-(x + h^* r^{*2} \cdot \frac{1}{x})} x^{\alpha'-1} dx \tag{5.10}$$

where α' can be obtained from Equation (5.9).

It can be seen from Eqs. (5.9) and (5.10) that when the well distance *L* is large, α' approaches α so that the revised analytical solution Equation (5.10) approaches the analytical solution Equation (3.30). It also proves the validity of the single well model in Chapter 3 which uses a single well model to simplify a doublet scheme, on the assumption that the extraction well is far away enough from the injection well that the interaction between the two wells is negligible.

5.6 Temperature of Extracted Water

5.6.1 Extraction Well

For an extraction-only scheme without an injection well, the extraction process does not decrease the temperature of the aquifer but only the water pressure of the aquifer. Thus both

the temperatures of the extracted water and the aquifer are constant and equal. However, for a doublet scheme with an injection well and an extraction well, the temperature of the extracted water may be affected by the injected cold water. As discussed in Section 5.3, this influence depends on the distance between the two wells. If the distance between the two wells is greater than the critical distance, namely $L \geq L_c$, then during the life span of the geothermal system (25 years), the temperature of the extracted water will not be affected by the injected cold water and will be invariably equal to the initial temperature of the aquifer which is 55 degrees in this case.

On the contrary, if $L < L_c$, at a certain moment of the life span, the aquifer in the vicinity of the extraction well can be cooled by the injected cold water. Thus the temperature of the extracted water begins to decrease against time. With the assumption of the instant thermal equilibrium between the water and matrix in the aquifer, the temperature of the extracted water is equal to the temperature of the aquifer at the extraction well. Therefore, the temperature of the extracted water can be represented by the temperature of Point A in Figure 5.11.

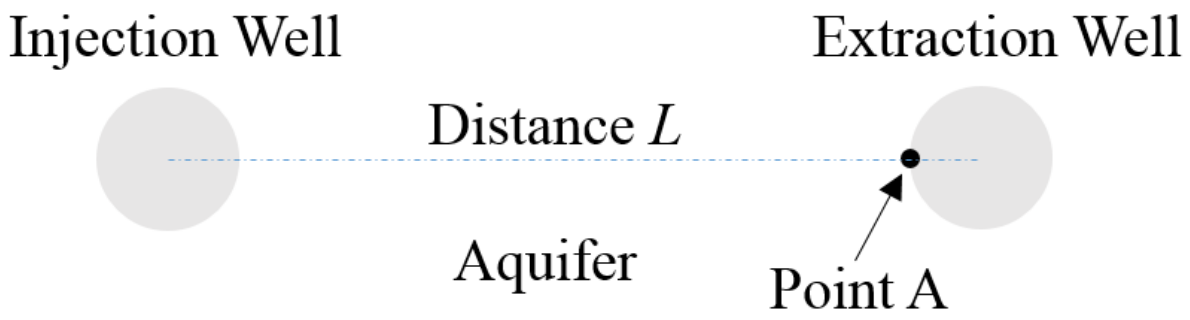

Figure 5.11: Plan view of a doublet scheme

5.6.2 Temperature of Extracted Water by COMSOL

The temperature of the extracted water against time can be obtained numerically by COMSOL. The COMSOL model used is exactly the same as that described in Section 5.2. The temperature change with time at Point A, which is also the temperature of the extracted water, as shown in Figure 5.12 and Figure 5.13. It can be seen from Figure 5.12 that, for a given injection rate and varied well distances (less than the critical distance for this injection rate, which is 600 m in this case), the temperature of the extracted water stays constant (equal to the temperature of the

aquifer) for some time at the beginning of the life span, and then it decreases sharply to a steady state, the temperature of which is greater than the injected cold water temperature. For a larger well distance (less than the critical distance), the time for the beginning constant temperature is longer and the steady-state temperature is also higher. When the well distance increases to the critical distance, the temperature of the extracted water is constant during the life span. Similarly, it can be seen from Figure 5.13 that, for a given well distance and varied injection rates (whose corresponding critical distances are all greater than this given well distance), the temperature of the extracted water stays constant (equal to the temperature of the aquifer) for some time at the beginning of the life span, and then it decreases sharply to a steady state, the temperature of which is greater than the injected cold water temperature. For a larger injection rate, the time for the beginning constant temperature is shorter and the steady-state temperature is also lower. When the injection rate decreases to a certain value whose corresponding critical distance is equal to the well distance, the temperature of the extracted water is constant during the life span.

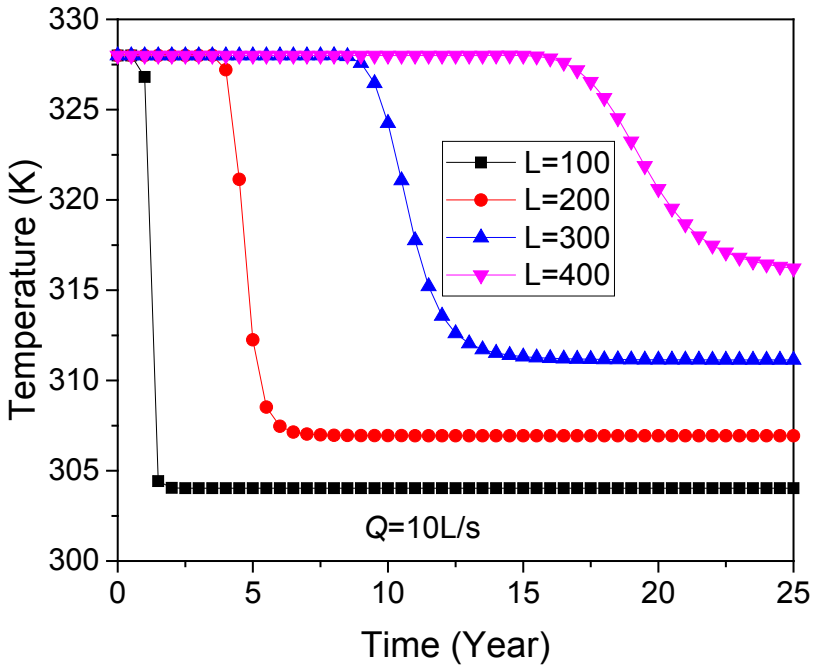

Figure 5.12: Temperature of the extracted water against time with different well distance *L*

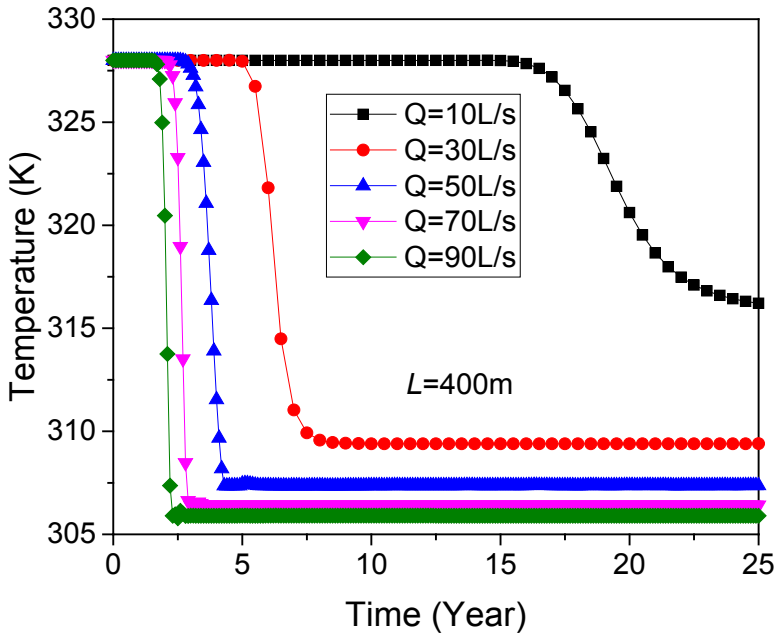

Figure 5.13: Temperature of the extracted water against time with different injection rate Q

5.6.3 Temperature of Extracted Water against Time

As discussed in Chapter 3, if the interaction between the injection well and extraction well is negligible, the temperature of extracted water against time is as follows (substituting $r^* = L^*$ into the analytical solution Equation (3.30)):

$$T^* = \frac{1}{\Gamma(\alpha)} \int_{\frac{(L^*)^2}{t^*}}^{\infty} e^{-(x+h^*(L^*)^2\frac{1}{x})} x^{\alpha-1} dx \tag{5.11}$$

where L^* is the dimensionless distance between the injection well and extraction well.

After some trial and error analysis (for injection rate Q = 1~100 L/s, well distance L = 1~2000 m and time t = 1~25 years), it is found that the temperature of extracted water against time considering the interaction between the injection well and extraction well can still be expressed using Equation (5.11) by multiplying the dimensionless well distance L^* by a reduction factor γ:

$$T^* = \frac{1}{\Gamma(\alpha)} \int_{\frac{(\gamma L^*)^2}{t^*}}^{\infty} e^{-(x+h^*(\gamma L^*)^2 \cdot \frac{1}{x})} x^{\alpha-1} dx \tag{5.12}$$

Equation (5.12) indicates that the interaction between the injection well and extraction well, in effect, shortens the well distance thus lowers the temperature of extracted water.

As the typical life span of a geothermal system is 25 years, the temperature of the extracted water at 25 years is of our interest and concern: it represents the final state of the geothermal system and the influence of the cold injected water on the aquifer. The temperature of the extracted water at 25 years against different well distances is shown as a "cross" in Figure 5.14, which is obtained numerically using COMSOL simulations.

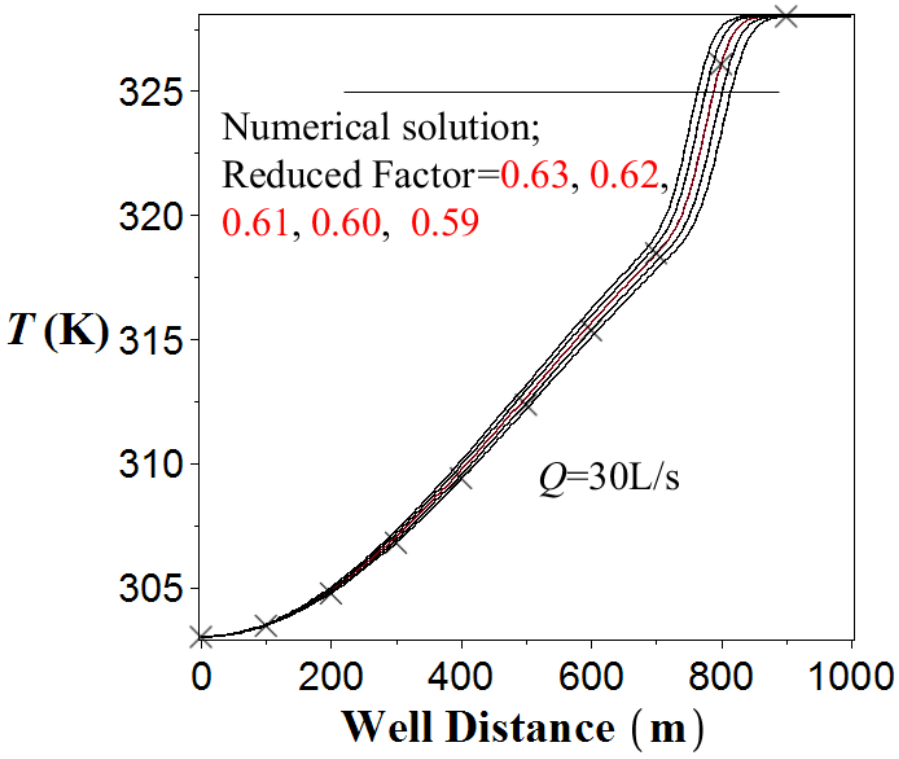

Figure 5.14: Temperature of the extracted water at 25 years against different well distance and curve fitting

Using the curve fitting exercise introduced in Section 5.4 again, the best reduction factor γ is found to be 0.61, see Figure 5.14. Repeating this curve fitting exercise for different injection rates Q, well distances L and time t, it is found that the reduction factors γ are so close that let $\gamma = 0.61$, as shown in Figure 5.15 and Figure 5.16.

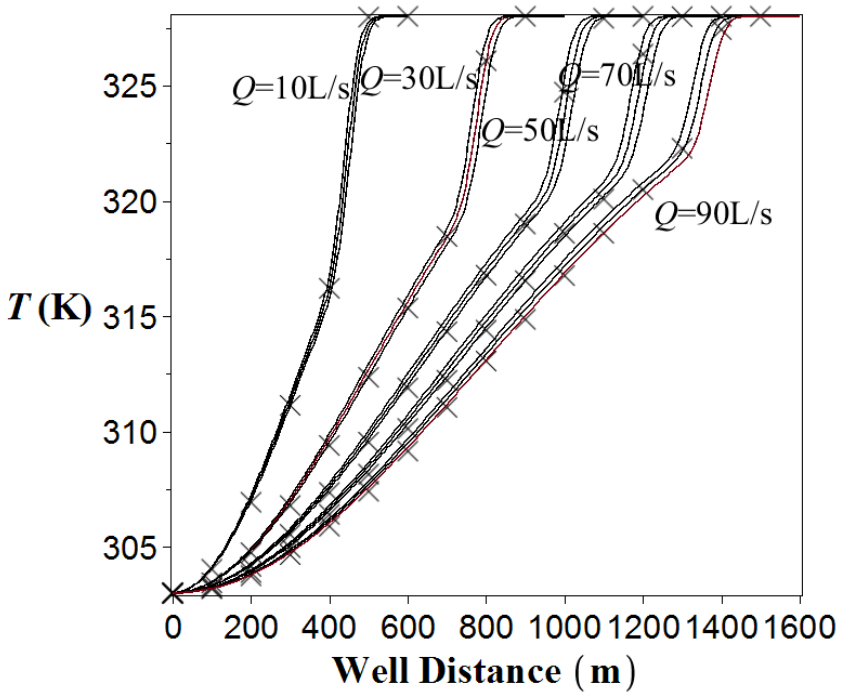

Figure 5.15: Curve fitting exercise for different injection rates Q and different well distances L using reduction factor $\gamma = 0.61$

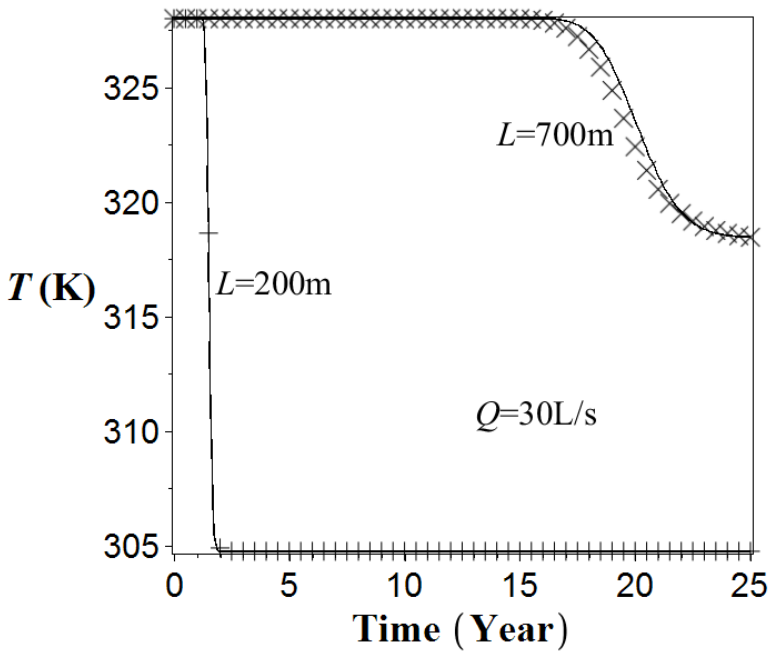

Figure 5.16: Curve fitting exercise for different time t and different well distances L using reduction factor $\gamma = 0.61$

Substituting $\gamma = 0.61$ into Equation (5.12), the expression of the temperature of the extracted water against time is as follows:

$$T^* = \frac{1}{\Gamma(\alpha)} \int_{\frac{(0.61L^*)^2}{t^*}}^{\infty} e^{-(x+h^*(0.61L^*)^2 \cdot \frac{1}{x})} x^{\alpha-1} dx \tag{5.13}$$

With the revised analytical solution Equation (5.13), the temperature of extracted water against time can be obtained as long as the injection rate, well distance and other input parameters are known.

5.7 Comparison between the Revised Analytical Solution and Experimental Data

In practice, it is difficult and laborious to obtain the experimental data about the temperature distribution between the injection well and the extraction well thus such experimental data are quite rare and limited. However, during the life span of a geothermal doublet system, it is always necessary to monitor the temperature of the extracted water so that the efficiency of the doublet system can be evaluated. As a result, the experimental data about the temperature of the extracted water against time are abundant and of good quality. In this chapter, the performance of the revised analytical solution for the temperature of the extracted water (Equation (5.13)) is examined by the experimental data of the temperature of the extracted water of a field test conducted by Ferguson and Woodbury (2005).

5.7.1 Case and Comparisons

An industrial site in the St. Boniface area of Winnipeg, Manitoba is chosen for the comparison, primarily due to the relatively complete extraction well temperature records (Ferguson and Woodbury, 2005), which has been introduced in Section 2.4. The plan view of the site is shown in Figure 5.17.

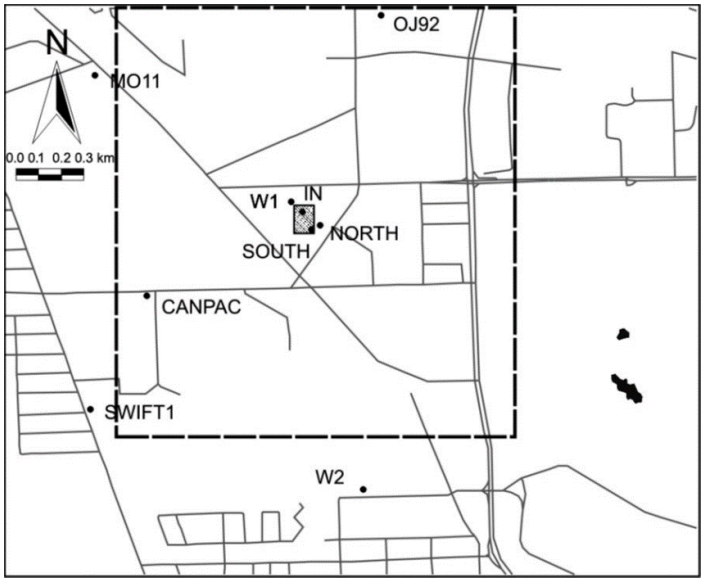

Figure 5.17: Map of the St. Boniface area of Winnipeg, showing the location of observation wells and the property investigated in this study. IN, injection well; SOUTH, south extraction well; NORTH, north extraction well. Shaded area around wells IN and SOUTH represents the zone of increased permeability. (Ferguson and Woodbury, 2005)

The doublet system consists of the injection well and the south extraction well as shown in Figure 5.18.

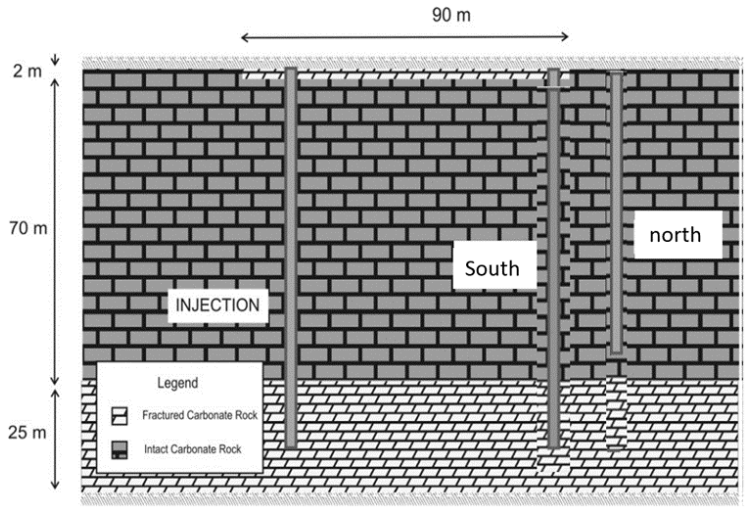

Figure 5.18: The doublet system consists of the injection well and the south extraction well

The extraction rate of the observed data is $Q = 2.6$ L/s. This continuous extraction rate involves a volume of water equal to that which would be used in 1 week if the maximum instantaneous

rate licensed by Manitoba Water Branch were to be used 8 hours per day for 5 days per week. The distance between the injection well and the extraction well is $L = 70$ m for observed. The thickness of the aquifer is 90 m and hence the dimensionless injection rate is $\alpha = 4.8$. It is noted that the lower boundary of the aquifer is also thermal permeable and hence $H = 90/2 = 45$ m is used for Equation (5.13) because of symmetry. The thermal conductivity of the soil is $\lambda_s = 2.4$ W/(m·K) for observed. The heat capacity of the soil is $(\rho c)_s = 2800 \cdot 1200$ J/(m^{3}K). The porosity of the rock is $n = 0.1$. The initial temperature of the aquifer is $T_0 = 8.3$ °C. The temperature of the injected hot water is $T_w = 16$ °C.

Substituting these parameters into Equation (5.13), the comparison among the revised analytical solution, experimental data and the numerical solutions (numerical solutions used in that paper) for the temperature of the extracted water is shown in Figure 5.19. The black dots are the measured temperature of the water at the south extraction well from 1988 to 2004. These dots fluctuate as the actual temperature of the injected water and the injection rates are variable during the operation of the system. The black lines are the temperature of the water at the south extraction well by the numerical simulations in the paper (Ferguson and Woodbury, 2005).

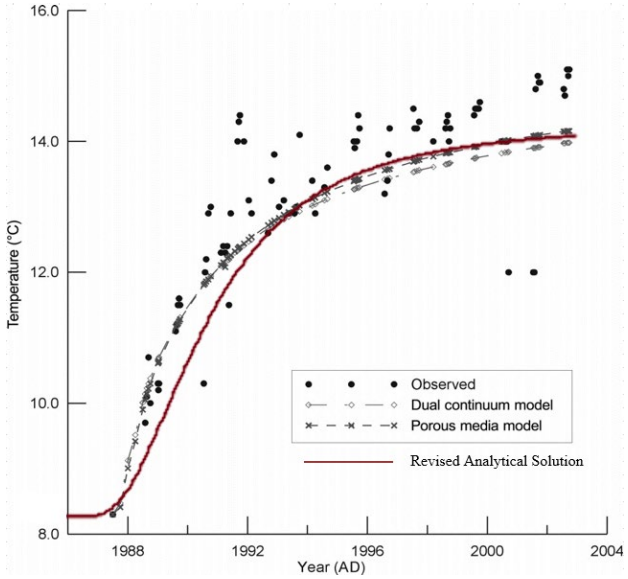

Figure 5.19: Comparison among the revised analytical solution, the experimental data and the numerical solutions

It can be seen from the figure that the revised analytical solution matches with general trends of the experimental data well. The difference between the revised analytical solution and the experimental data is mainly a result of variable injection temperatures and injection rates that exist in the system but are not captured in the revised analytical solution. The heterogeneities of aquifer geometry and material properties also contribute to this difference.

5.7.2 Parametric Analysis

5.7.2.1 Injection Rate *Q*

As the injection rate *Q* is the basic parameter that can be altered in the design of a doublet system, it is important to see how the injection rate *Q* affects the doublet system via a sensitivity analysis. The comparison among the revised analytical solution for different injection rates, experimental data and the numerical solutions (numerical solutions used in that paper) for the temperature of the extracted water is shown in Figure 5.20.

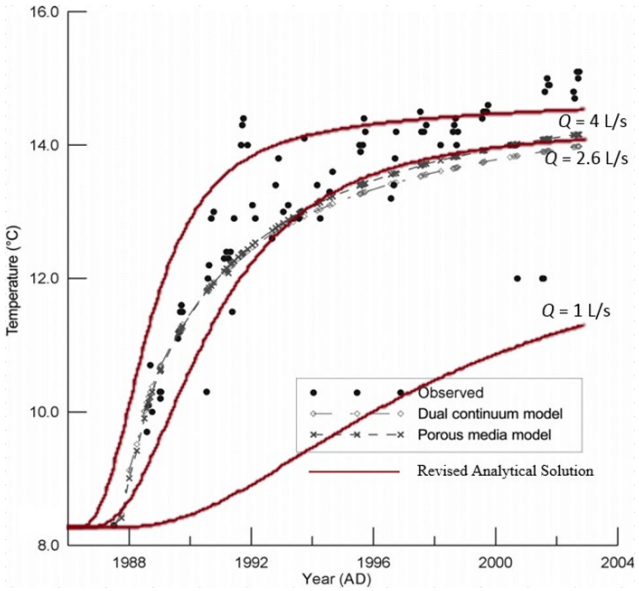

Figure 5.20: The comparison among the revised analytical solution for different injection rate, experimental data and the numerical solutions

It can be seen from the figure that the temperature of the extracted water is very sensitive to the value of the injection/extraction rate. The temperature of the extracted water increases with the increasing injection/extraction rate: when the rate is small, the temperature of the extracted

water is close to the initial temperature of the aquifer; when the rate is large, the temperature of the extracted water will be finally close to the temperature of the injected hot water. The thermal breakthrough time decreases with the increasing injection/extraction rate: when the injection rate is large, the temperature of the extracted water will start to rise in a very short time.

5.7.2.2 Thermal Conductivity λ

Thermal conductivity is an important input material parameter in both the analytical solutions and numerical simulations. The aquifer is actually heterogeneous in practice so it causes errors when a single constant thermal conductivity is assigned to the aquifer. Besides, there are also some errors in measuring the thermal conductivity by experiment. Therefore, it is important to conduct a sensitivity analysis in terms of the thermal conductivity. The values of thermal conductivity selected in the sensitivity analysis are within the range of the typical values of thermal conductivity. The comparison among the revised analytical solution for different thermal conductivity, experimental data and the numerical solutions (numerical solutions used in that paper) for the temperature of the extracted water is shown in Figure 5.21.

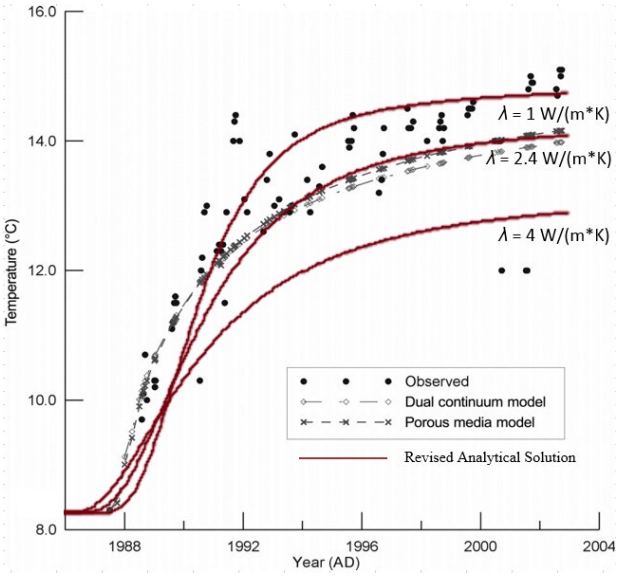

Figure 5.21: The comparison among the revised analytical solution for different thermal conductivity, experimental data and the numerical solutions

It can be seen from the figure that the temperature of the extracted water is sensitive to the value of the thermal conductivity. The temperature of the extracted water decreases with the increasing thermal conductivity. When the thermal conductivity is large, the surrounding cold aquifer can better cool the area affected by the injected hot water so that the temperature of the extracted water will be lower.

5.7.2.3 Well Distance *L*

As the well distance *L* is another basic parameter that can be altered in the design of a doublet system, it is important to see how the well distance *L* affects the doublet system via a sensitivity analysis. The comparison among the revised analytical solution for different well distance, experimental data and the numerical solutions (numerical solutions used in that paper) for the temperature of the extracted water is shown in Figure 5.22.

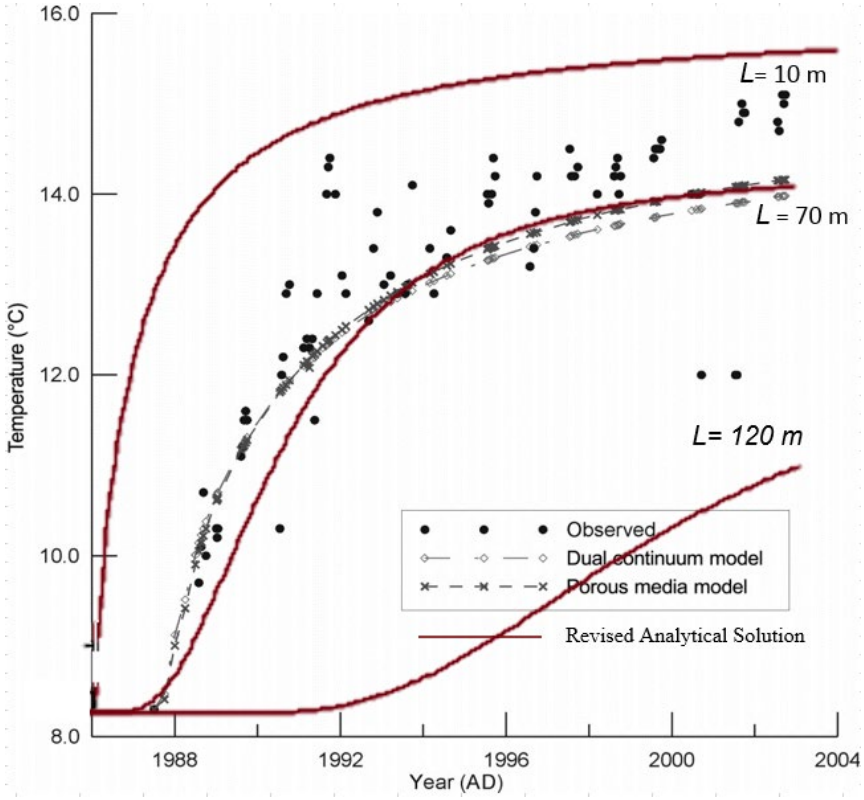

Figure 5.22: The comparison among the revised analytical solution for different well distance, experimental data and the numerical solutions

It can be seen from the figure that the temperature of the extracted water is extremely sensitive to the well distance. The temperature of the extracted water decreases with the increasing well distance: when the well distance is small, the temperature of the extracted water will start to rise in a very short time and finally be close to the temperature of the injected hot water; when the well distance is large, the temperature of the extracted water will start to rise after a long time and finally be close to the initial temperature of the aquifer.

5.8 Summary

This chapter extends the analytical solution for a single injection well to a doublet scheme by considering the interaction effect between the injection well and the extraction well. The expression of the critical distance between two wells is obtained so that the best location of the extraction well can be determined. For the case that the well distance is greater than the critical distance, the revised analytical solution gives the spatial and temporal temperature distribution in the aquifer for a doublet scheme. For the case when the well distance is smaller than the critical distance, another revised analytical solution is proposed to give the temperature of the extracted water against different time, injection rate and well distance. The revised analytical solution is compared with the experimental data and the numerical solutions and they match with each other well which can validate the revised analytical solution to some extent and show the usefulness of the analytical solution in practice. According to parametric analysis, injection rate Q and well distance L are the most critical parameters to the temperature of the extracted water, as injection rate Q determines the flow rate and temperature distribution of the aquifer and well distance L determines the location of the extraction well.

Chapter 6 Fracture Flow

In Chapters 3 to 5, an engineering analysis method was proposed to analyse a typical deep geothermal system: a doublet system with one injection well and one extraction well, without fractures or faults in the model. However, some fractures or faults are often encountered in the targeted aquifer. Generally speaking, the fractures will act as conduits or barriers in terms of heat transfer and fluid flow, influencing the performance of the doublet system. Therefore, in certain scenarios, it may be necessary to evaluate the effects of fractures on the performance of a doublet system, such as the temperature distribution and the temperature of the extracted water. This issue is considered in this chapter.

6.1 Two Kinds of Fracture Models

In order to evaluate the effects of a fracture on the performance of a doublet system, the fracture needs to be explicitly modelled in the doublet model. There are primarily two ways to model a fracture in COMSOL. One approach is to consider the fracture as a domain and explicitly and directly model the fracture, as shown in Figure 6.1. The model is a 1500 m * 1500 m 2D square with one injection well and one extraction well. The physics used in the model are "Heat Transfer in Porous Media" and "Darcy's Law". The units of the horizontal axis and the vertical axis are [m]. The thickness of the aquifer layer H = 50 m (though it is a 2D model, a thickness H can still be assigned to the model in COMSOL which means that the temperature along the thickness H is constant). The thickness of the aquifer H is an essential input parameter in the heat transfer calculation. The radius of the two wells is both 0.5 meters. The distance between the two wells is 600 m in this case. A constant flow rate (Q = 10 L/s in this case) is applied to the surface of the circumferential boundaries of the injection well and extraction well. The temperature of the surface of the injection well is constant (30 degrees in this case). The outer boundary conditions of the square mesh model are 0 pressure boundary (the relative hydraulic pressure on this boundary is 0) and thermal insulated boundary. The error of assigning the thermal insulated boundary is quite small because there is water flowing across this boundary

and thermal advection effect is much stronger than the thermal conduction. The initial temperature of the model is 55 degrees. An out-of-plane heat flux boundary is $w_0 = h(T - T_0)$, where h is the convective heat transfer coefficient. The value of h can be determined using Equation (4.5) and Equation (4.6) in Chapter 4, which is perpendicular to the 2D square mesh model and is applied to reflect the convective heat transfer boundary in the analytical solution.

The area bounded by the inclined double lines represents the fracture. The inclination of the fracture is 34 degrees and the fracture thickness is 1 m. In other words, the fracture in the domain model has a geometric width with physical properties, such as density, permeability, thermal conductivity, etc. The physical properties of the porous media and fracture are shown in Table 6.1 and Table 6.2. The fracture is usually a very long and narrow domain with a very high aspect ratio within a very wide porous media. Discretizing the fracture domain explicitly requires a very dense mesh consisting of a large number of infinitesimally small elements.

The other approach, which is the approach used in this study, is to model the fracture as an interior boundary, as shown in Figure 6.2. The physics used in the model are “Heat Transfer in Porous Media” and “Darcy’s Law”. The boundary conditions and physical properties are the same as that in the domain model. The inclined line represents the fracture (the inclination is 34 degrees too). The fracture is a line with physical properties, such as density, permeability, thermal conductivity, etc. The advantage of this approach is in reducing the degrees of freedom and enhancing computational performance.

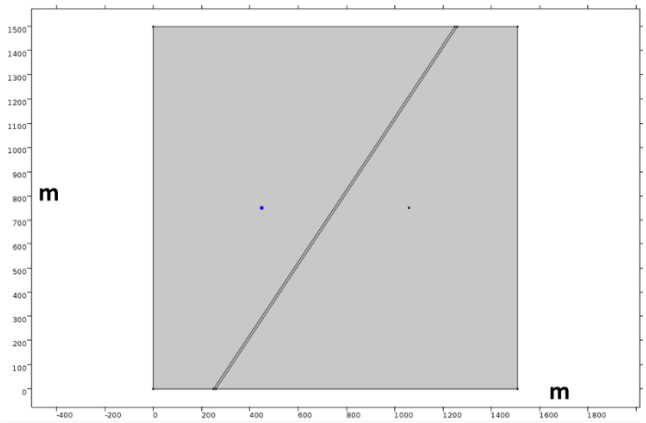

Figure 6.1: Domain model

Table 6.1: Properties of the porous media

Property	**Value**	**Unit**
Density	2800	kg/m^3
Permeability	1.00E-09	m^2
Porosity	0.25	1
Thermal conductivity	1.3	W/(mK)
Heat capacity at constant pressure	830	J/(kgK)

Table 6.2: Properties of the fracture

Property	**Value**	**Unit**
Density	2800	kg/m^3
Permeability	1.00E-06	m^2
Porosity	0.5	1
Thermal conductivity	3	W/(mK)
Heat capacity at constant pressure	830	J/(kgK)

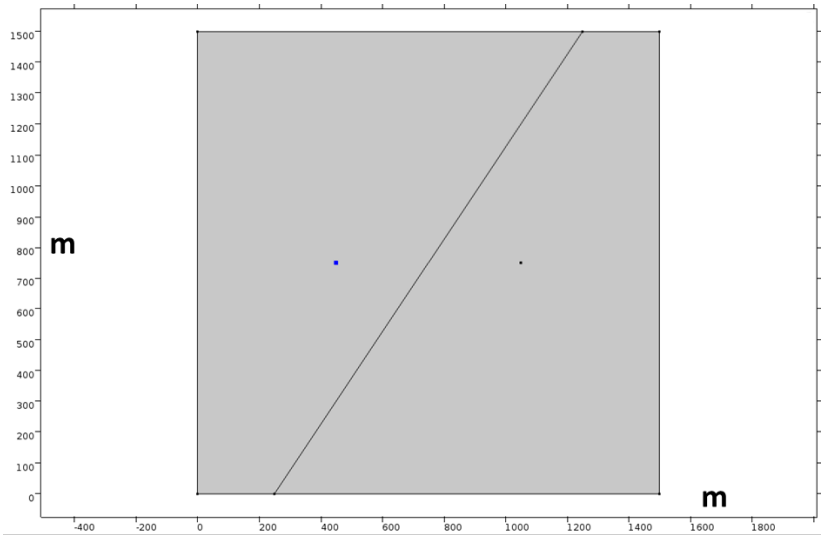

Figure 6.2: Line model

The contours of Darcy's velocity of aquifer for the two cases (the domain model and line model) are the same, as they overlap with each other, as shown in Figure 6.3. The computed Darcy's velocity profiles between the injection well and the extraction well of the two cases are shown in Figure 6.4. It can be seen that the velocity around the injection well and the extraction well is large (6.4×10^{-5} m/s) but the velocity at the mid-point is small (1.5×10^{-7} m/s).

The two curves almost overlap with each other. The only difference is that there is a small hump at the location of the fracture in the domain model that represents the water velocity in the fracture (4.8×10^{-6} m/s) while there is no such hump at the location of the fracture in the line model. The reason for this difference is that the fracture in the domain model has a geometric width but the fracture in the line model is only a line. The curve of the line model goes smoothly at the location of the fracture and the velocity in the fracture for the line model is not shown explicitly in the figure. The Darcy's velocity in the fracture for the line model can be obtained separately.

The Darcy's velocity profiles along the fracture in the domain model and the line model are the same, as shown in Figure 6.5. The velocity along the fracture firstly goes down close to zero and then goes up to the peak (4.8×10^{-6} m/s), which is equal to the velocity in the fracture in Figure 6.4, at the mid-point of the two wells. It can be seen in Figure 6.3 that the velocity along the fracture changes the direction at two points where the velocity along the fracture is zero because the velocity field is continuous. The velocity is symmetric with respect to the mid-point of the two wells because of the symmetry of the doublet system.

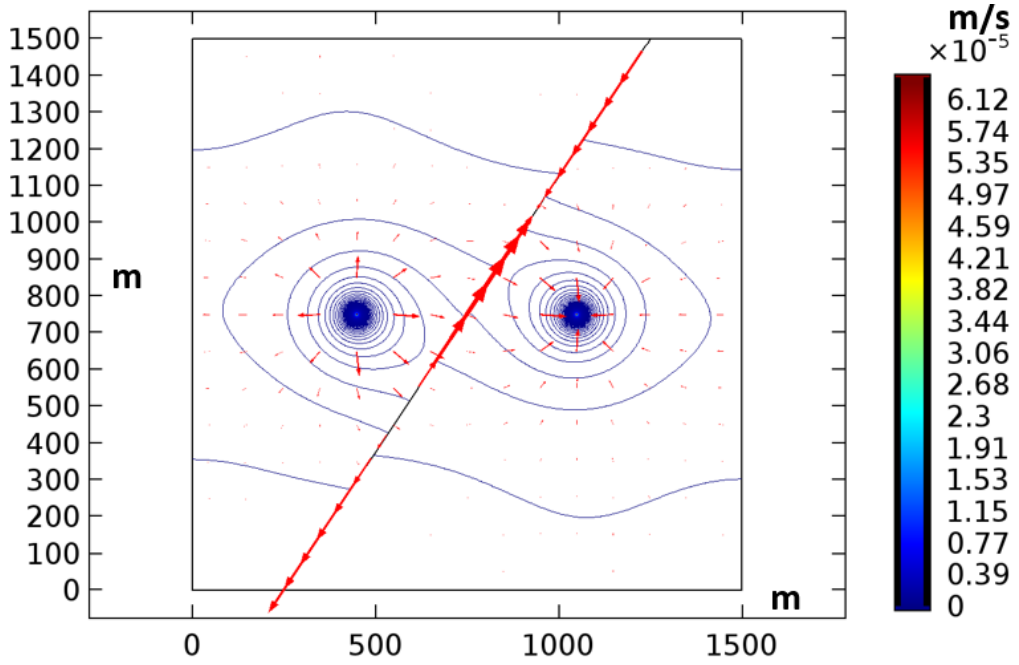

Figure 6.3: Contours of Darcy's velocity for the two cases

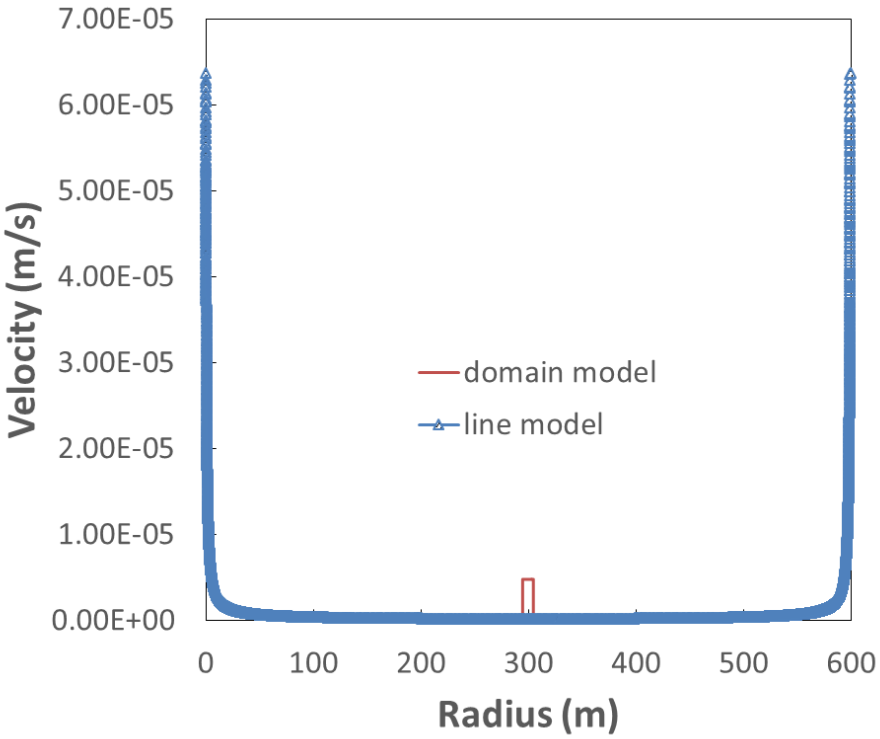

Figure 6.4: Velocity of the water between the injection well and the extraction well in both models

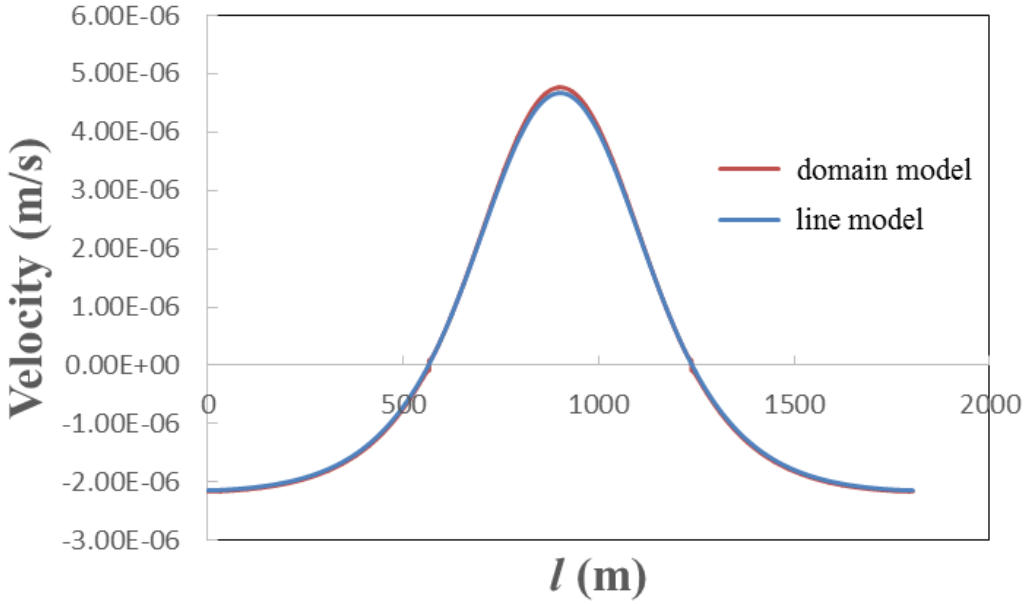

Figure 6.5: Velocity of the water along the fracture in both models

The temperature contours at 25 years for the line model and the domain model are the same, as they overlap with each other, as shown in Figure 6.6.

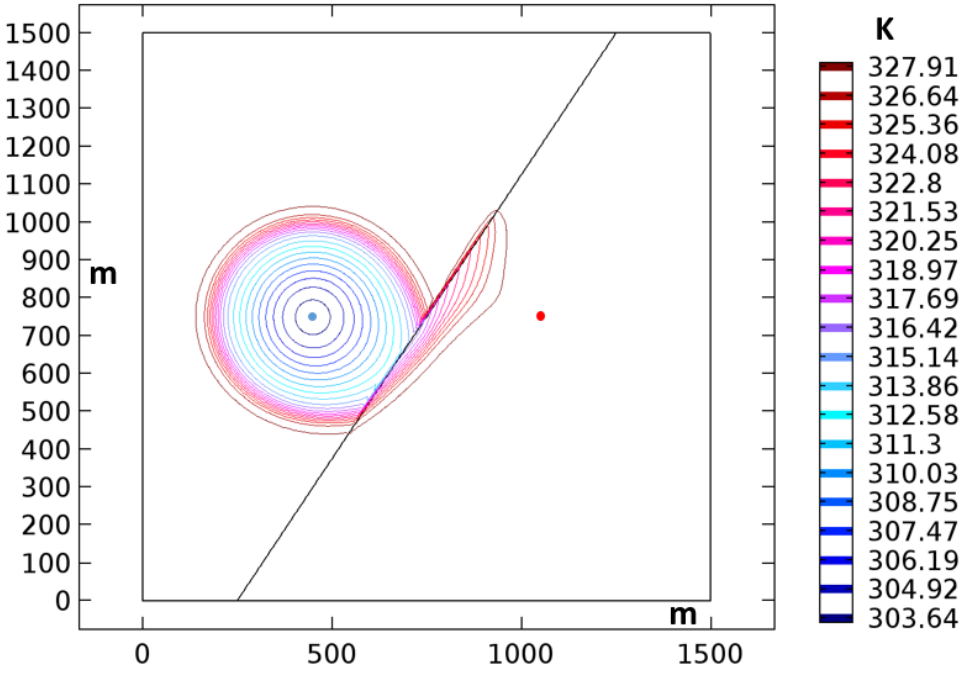

Figure 6.6: Temperature contours at 25 years for the line model and domain model

6.2 Line Model for Fracture Flow Simulation

The line model for a fracture flow simulation is available in COMSOL. In this study, a line representing the fracture was added to the original 2D model introduced in Section 5.2 (see Figure 6.2). The model is a 2D square with one injection well and one extraction well. The scale of the model needs to be adapted according to the injection and extraction rate (it is 3000 m * 3000 m for Q = 10 L/s). Generally, the scale of the model increases with the increasing injection and extraction rate. The radius of the two wells is both 0.5 meters. The constant flow rate Q is applied to the surface of the injection well and the extraction well. The temperature of the surface of the injection well is constant (30 degrees). The outer boundary conditions for the square are thermal insulated boundary and 0 pressure boundary. The initial temperature of the model is 55 degrees. An out-of-plane heat flux boundary ($w_0 = h(T - T_0)$, h is the convective heat transfer coefficient. The value of h can be determined using Equation (4.5) and

Equation (4.6) in Chapter 4. It reflects the convective heat transfer boundary in the analytical solution. The relevant parameters for the porous media and the fracture are applied, as shown in Table 6.1 and Table 6.2. The distance between the two wells is 100 m and the width of the fracture is 1 m in this case.

The pressure distribution and the streamlines, under the influence of the fracture, are shown in Figure 6.7. Both pressure distribution and streamlines are significantly affected by the fracture. They are rotated by a certain angle, which is roughly equal to the angle A of the fracture in this case, because the permeability of the fracture is much larger than that of the porous media (1000 times) so that the streamlines are perpendicular to the fracture. As a result, the pressure distribution and the streamlines are rotated by a certain angle close to the angle of the fracture.

The temperature distribution of the fracture case is shown in Figure 6.8. As the temperature distribution is directly related to the pressure distribution, the contours of the temperature are also rotated by a certain angle close to the angle of the fracture. Besides, as the water is flowing in the fracture, the contours of the temperature in the vicinity of the fracture are stretched in the same direction as the Darcy's velocity in the fracture.

The temperatures of the extracted water with and without fracture are shown in Figure 6.9. The temperatures of the extracted water against time with and without the existence of the fracture are nearly the same, as the angle of the fracture, A, is small in this case. When the angle of the fracture is small, both the water velocity and water travel distance along the fracture are small. As a result, the influence of the water travelling along the fracture on the heat breakthrough distance of the doublet system is small. Therefore, the temperatures of the extracted water against time with and without the existence of the fracture are nearly the same. Hence, the effect of fracture on geothermal energy performance is small in this case. However, the performance will be influenced by the geometry of the fault as shown in the next section.

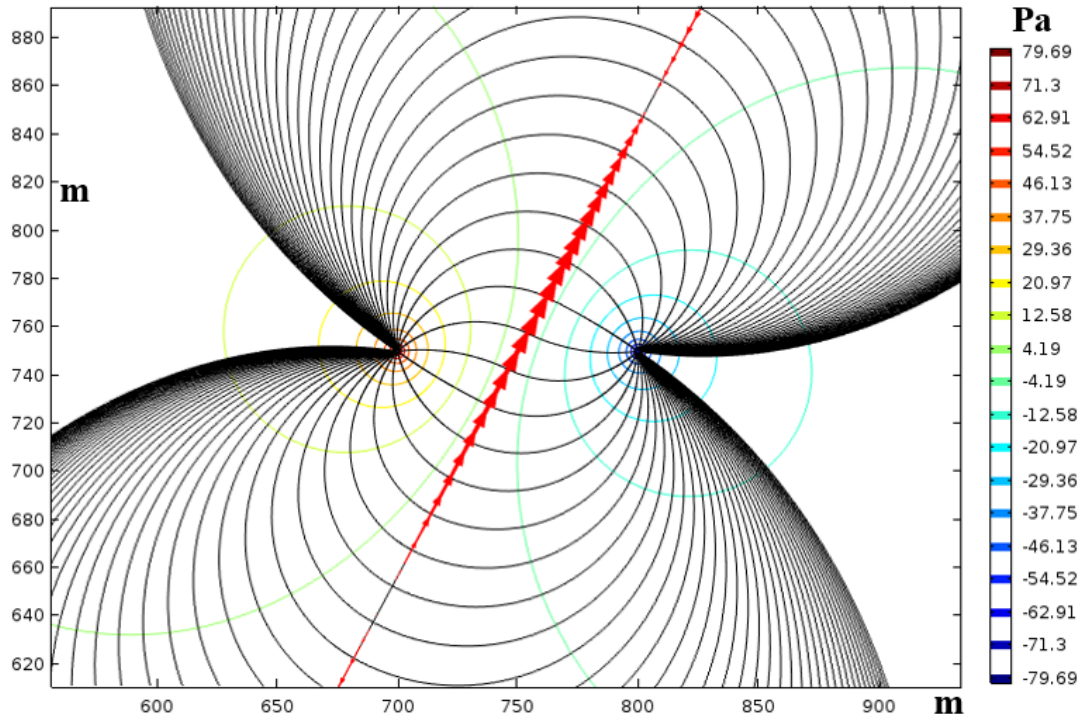

Figure 6.7: Pressure distribution and streamlines at 25 years

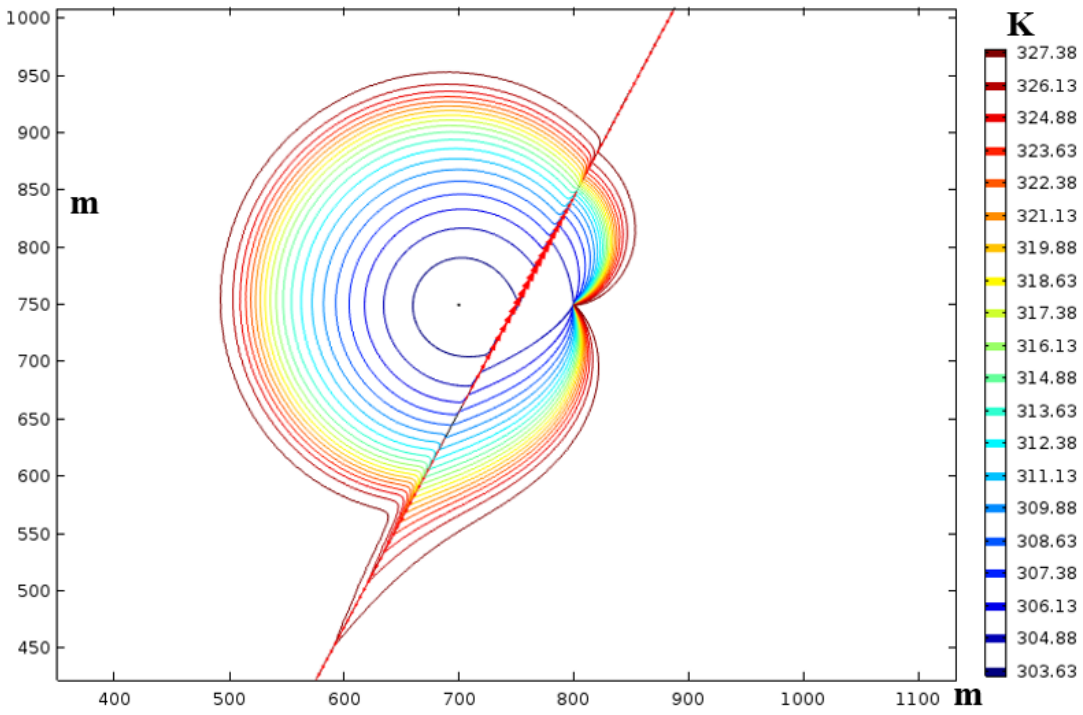

Figure 6.8: Temperature distribution at 25 years with the fracture

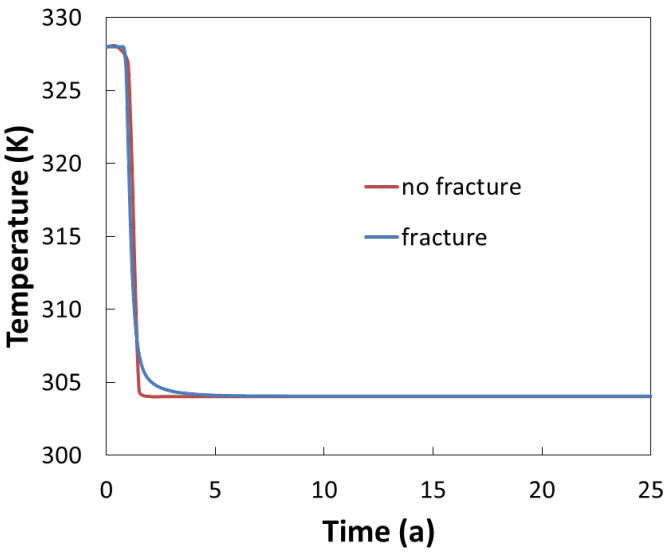

Figure 6.9: Temperature of the extracted water with and without the fracture

6.3 Effect of Fracture Positions

The performance of a doublet system is affected by the position of the fracture. The position of the fracture can be expressed as the coordinate of the mid-point of the fracture (x, y), and the angle of the fracture A, as shown in Figure 6.10.

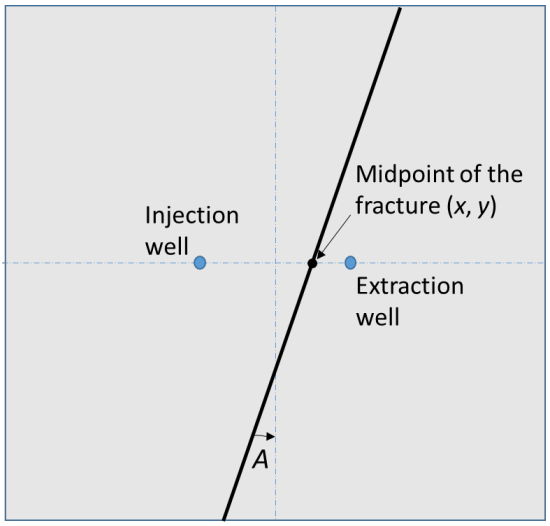

Figure 6.10: Position of the fracture

6.3.1 Fracture at the Symmetry Axis

When a fracture is located at the symmetry axis of the two wells, the mid-point of the fracture overlaps with the mid-point between the injection well and the extraction well. The angle of the fracture $A = 0$. The pressure distribution and streamlines are shown in Figure 6.11.

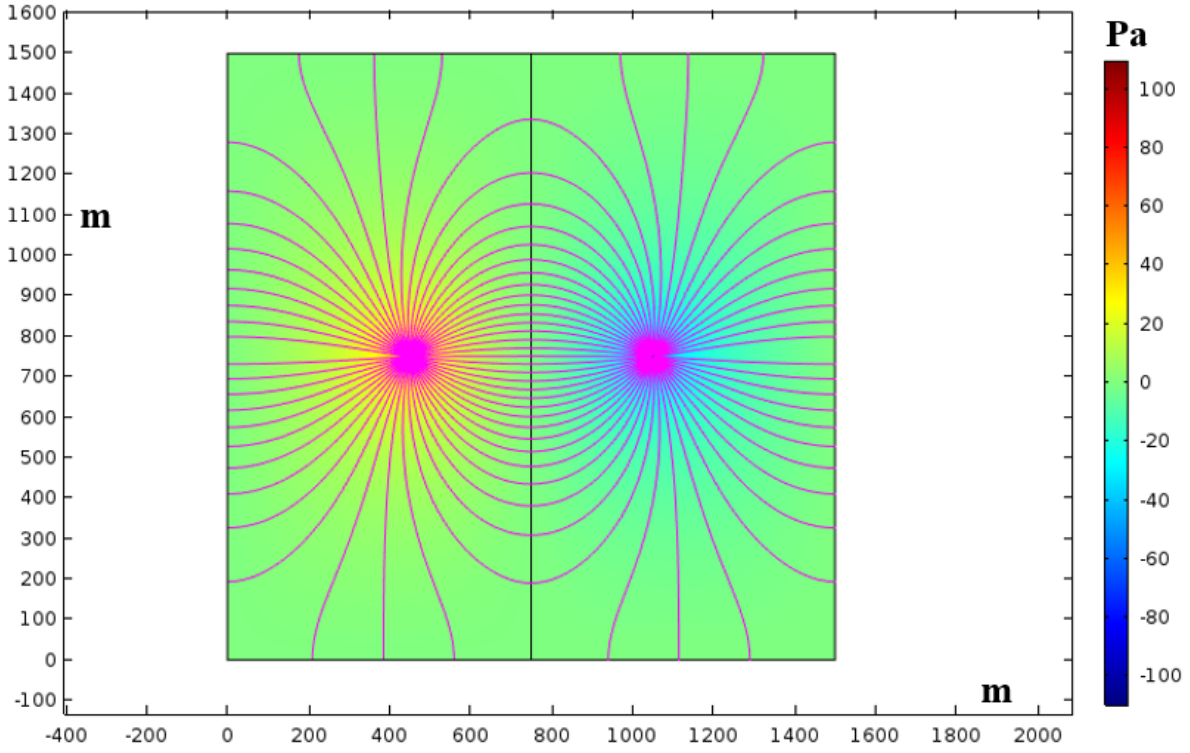

Figure 6.11: Pressure distribution and streamlines with the fracture

This case is a special one that the fracture will have no influence on the whole doublet system. The pressure distribution and temperature distribution of the whole model are exactly the same as the one without the fracture. The temperature distributions along the two wells at 25 years with and without the fracture are shown in Figure 6.12. The temperature of the extracted water against time with and without the fracture is shown in Figure 6.13. They completely overlap with each other because the streamlines are all perpendicular to the symmetry axis of the two wells. When the fracture is located at the symmetry axis, the water still flows perpendicularly across the fracture but not along the fracture just like the case without the fracture. Therefore, the existence of the fracture will have no effect on the streamlines and heat transfer.

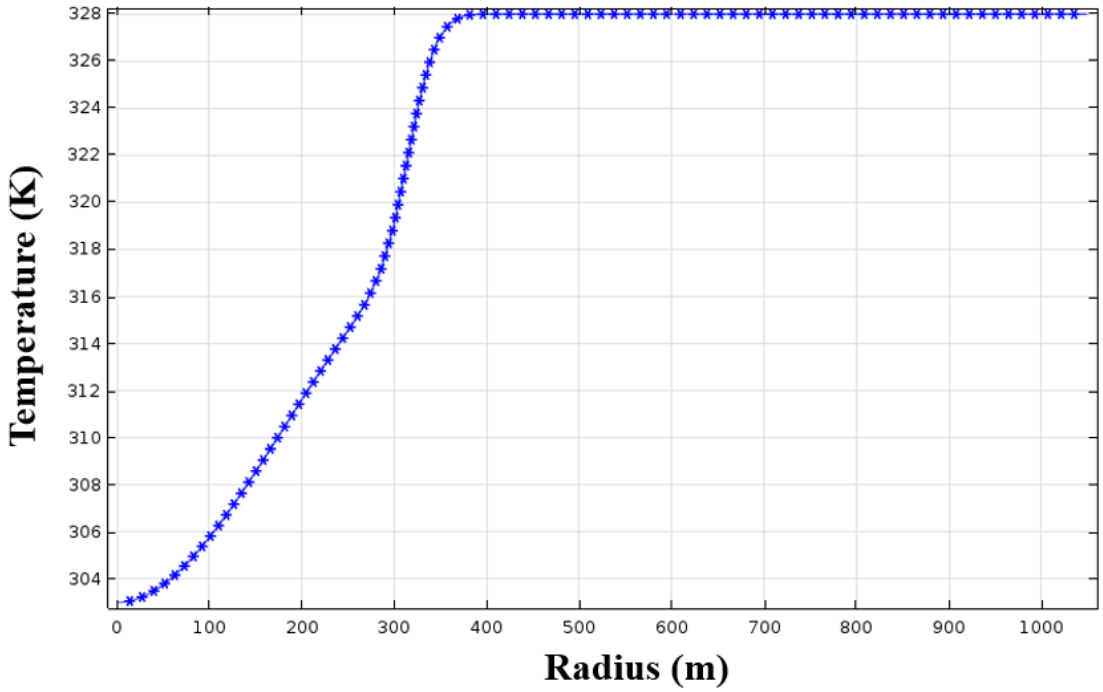

Figure 6.12: Temperature distributions along the two wells at 25 years with (line) and without (asterisk) the fracture

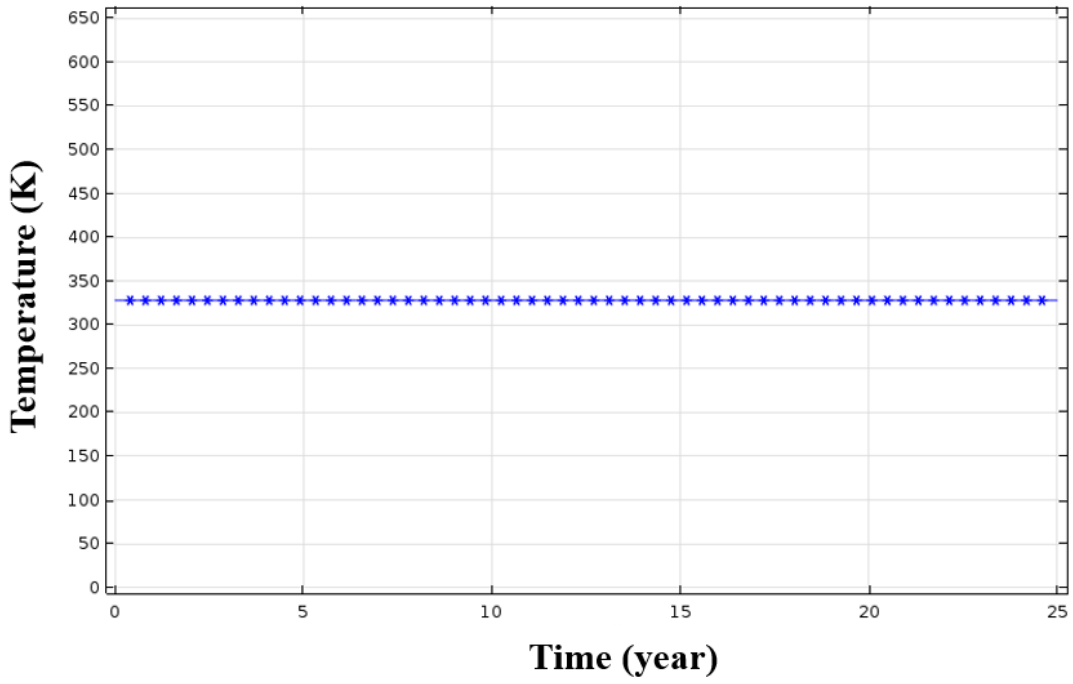

Figure 6.13: Temperature of the extracted water against time with (line) and without (asterisk) the fracture

6.3.2 Effect of the Mid-point Coordinate of Fracture

The position of the fracture can be expressed as the coordinate of the mid-point of the fracture (x, y), and the angle of the fracture A. Therefore, these two parameters can be varied to examine how the position of the fracture affects the doublet system performance. In this section, the angle A of the fracture is kept constant (let $A = \pi / 4$) but the fracture position is shifted left or right from the mid-point between the injection and extraction wells to evaluate the effect of the mid-point coordinate (x, y) of the fracture on the doublet system performance. The distance between the injection and extraction wells should be equal to or greater than the critical distance (See Section 5.3), which is 600 m for the injection rate $Q = 0.01$ m^3/s in this case. By doing so, the temperature of the extracted water is constant during the life span of the system. In other words, the temperature of the extracted water will not decrease during the life span of the system in spite of the existence of the cold injection well so that a good thermal efficiency will be achieved. The geometry, boundary conditions and properties of the porous media and fracture are the same as that in Section 6.1.

Figure 6.14 shows the temperature distribution at 25 years when the fracture is shifted 200 m left from the midpoint. As the fracture is close to the injection well, the temperature of the water is still lower than the initial temperature of the aquifer when the injected water arrives at the fracture. Given the permeability of the fracture is much higher than that of the porous media, the arrived cold water flows along the fracture rapidly. The cold water flowing in the fracture cools the surrounding porous media so that a long and narrow low-temperature area around the fracture can be seen in the figure. Meanwhile, the cold water flowing in the fracture also gets heated and it leaves the fracture and continuously be heated by the porous media and comes out from the extraction well. As the angle A of the fracture is not large enough in this case, the influence of the fracture on the double system is limited; that is, the temperature of the extracted water does not decrease after 25 years of operation. Therefore, it is still an efficient doublet system even though the fracture exists.

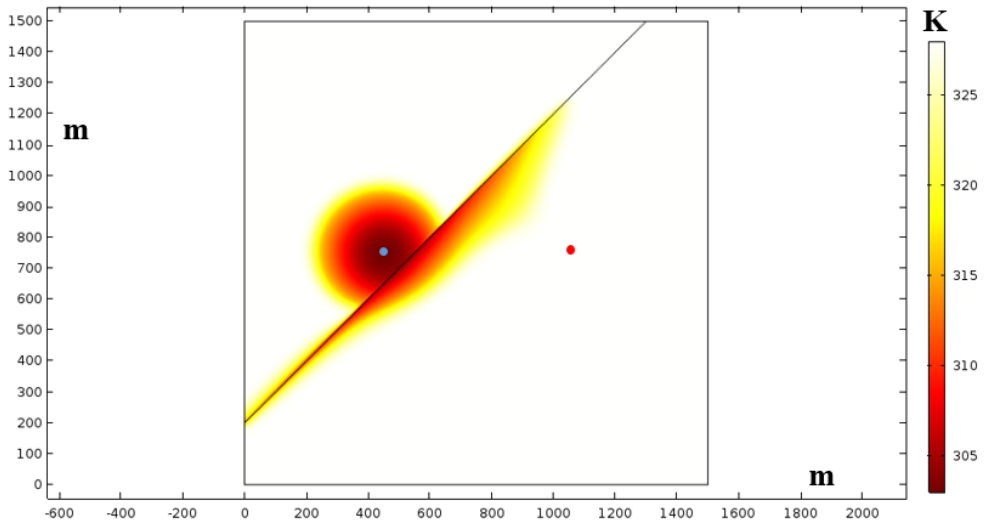

Figure 6.14: Temperature distribution when the fracture is shifted 200 m left

Figure 6.15 shows the temperature distribution at 25 years when the fracture is located 200 m right from the mid-point. As the fracture is far away from the injection well, the temperature of the injected water is already equal to the initial temperature of the aquifer when it arrives at the fracture. In other words, the temperature of the water flowing in the fracture is equal to the temperature of the surrounding area so that there is no low-temperature area around the fracture. The temperature of the extracted water does not decrease at 25 years so it is still an efficient doublet system.

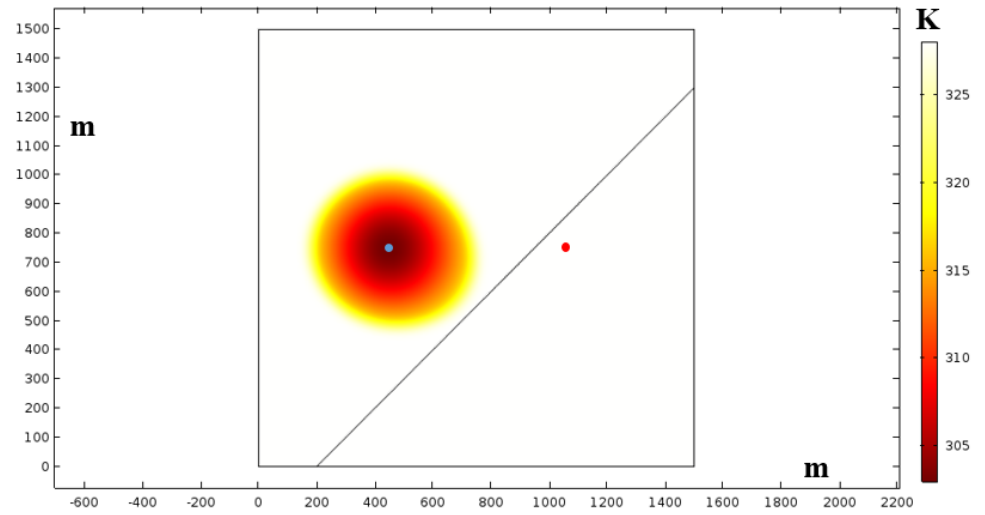

Figure 6.15: Temperature distribution when the fracture is shifted 200 right

Figure 6.16 shows the temperature distribution at 25 years when the fracture is located 400 m left from the midpoint. The fracture is no longer between the injection and extraction wells and is on the left side of the injection well. Some injected water proceeds to the fracture, flows along the fracture, leaves the fracture and finally arrives at the extraction well. When the angle *A* of the fracture is small, the time it takes for this flow path is longer than that of the direct flow path connecting the injection well and the extraction well. And therefore the influence of the fracture is little. Again, as the fracture is close to the injection well, the temperature of the water is still lower than the initial temperature of the aquifer when the injected water arrives at the fracture. The cold water flowing in the fracture cools the surrounding porous media so that a long and narrow low-temperature area around the fracture can be seen in the figure. It is also an efficient doublet system during its life span.

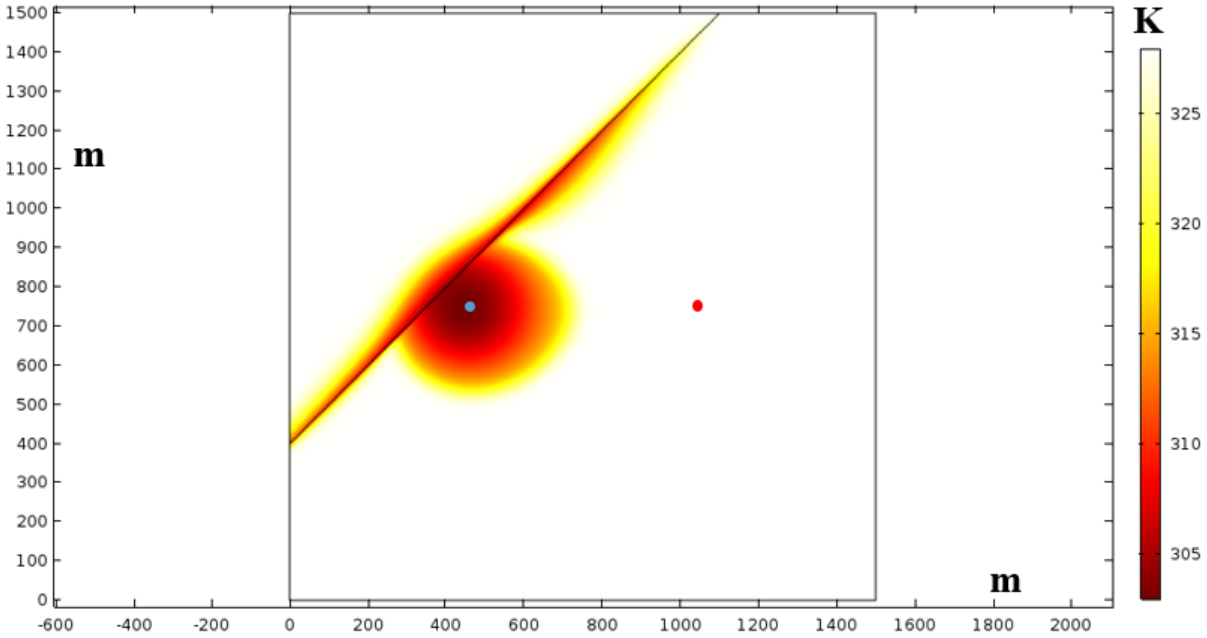

Figure 6.16: Temperature distribution when the fracture is shifted 400 m left

Figure 6.17 shows the temperature distribution at 25 years of operation when the fracture is located 400 m right of the midpoint. The fracture is no longer between the injection and extraction wells and is on the right side of the extraction well. In this case, as the fracture is far away from the injection well and there is no low-temperature area around the fracture. The time it takes for the flow path passing through the fracture is longer than that of the direct flow path connecting the injection well and the extraction well. Therefore, the effect of the fracture

on the system performance is limited and this doublet system is still efficient at the end of its life span.

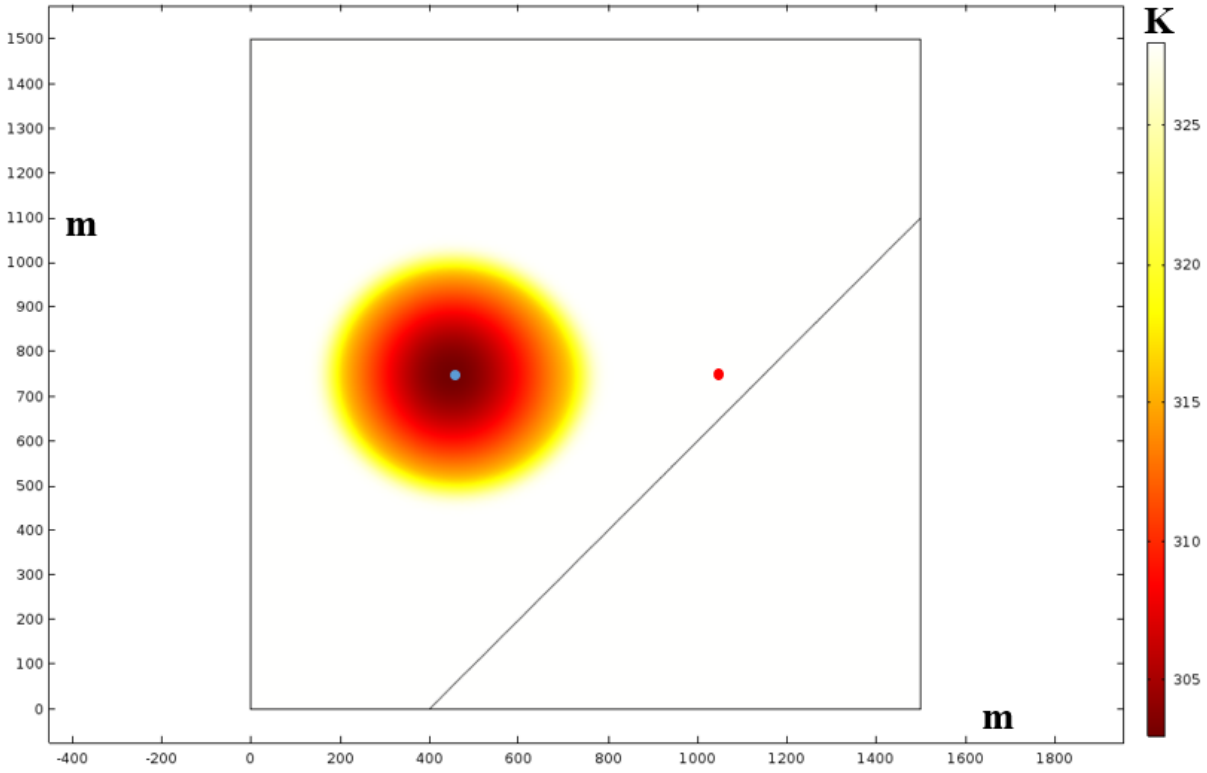

Figure 6.17: Temperature distribution when the fracture is shifted 400 m right

From the figures above, the temperature distribution for the case when the fracture is shifted left from the midpoint is different from that when the fracture is shifted right. In other words, these two scenarios are not symmetric. In addition, the fracture has greater influences on the doublet system performance when it is shifted to the left from the midpoint. If the fracture is close to the injection well, large amount of cold water flows in the fracture so that the area around the fracture is cooled down by the injected cold water. If the fracture is far away from the injection well, the amount of water flowing in the fracture is little and its temperature is close to the initial temperature of the aquifer. The cooling effect around the fracture is not apparent.

Repeating this procedure, the temperature distributions along the two wells at 25 years for different fracture positions as shown in Figure 6.18 can be examined. Note that when the fracture is shifted left, the negative sign is used; when the fracture is shifted right, the positive

sign is used; when the fracture is at the mid-point, it is 0. In this case, when the fracture is located at – 300 m, the fracture passes through the injection well; when the fracture is located at + 300 m, the fracture passes through the extraction well.

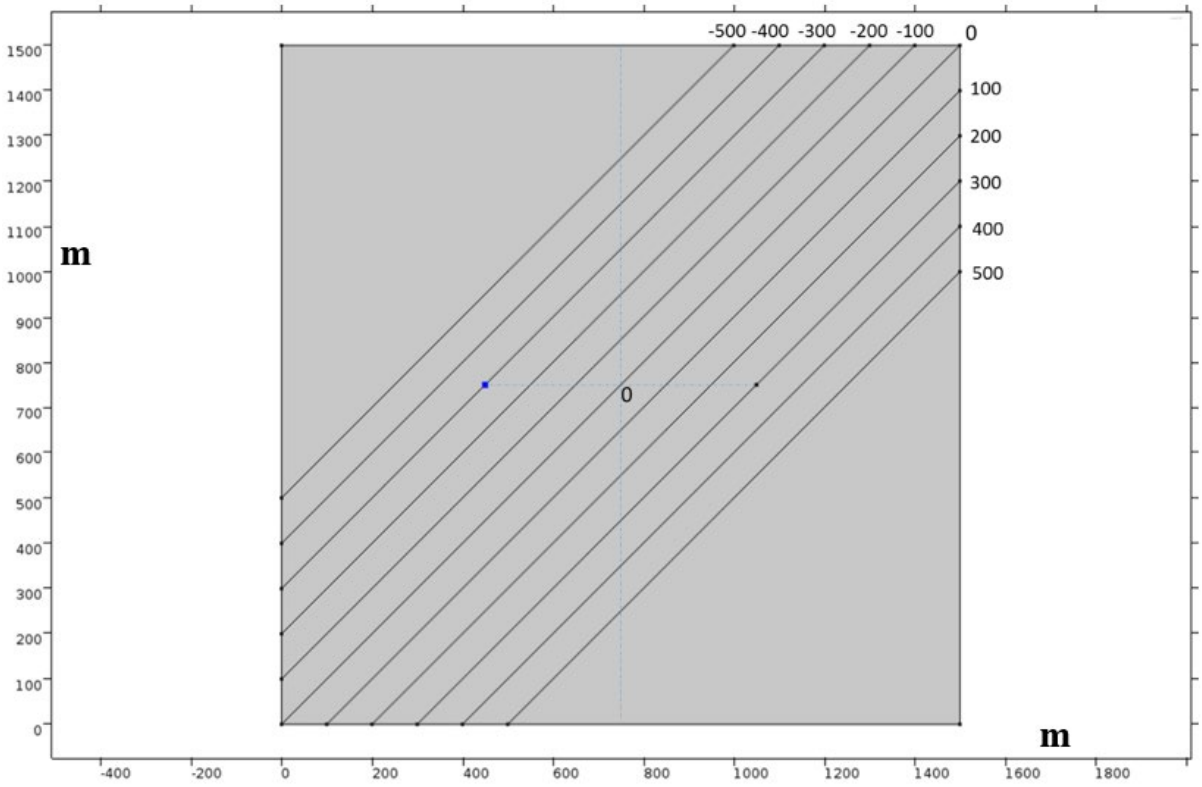

Figure 6.18: Different fracture positions

CASE (1) - The fracture is on the left of the injection well, namely the fracture is located at - 500, - 400 and - 300.

The temperature distributions along the two wells at 25 years for the fracture position - 500, - 400, - 300 and the model without a fracture are shown in Figure 6.19. Compared with the case without a fracture, the curves with the fracture are all on the left of the curve without a fracture. In other words, the heat breakthrough distance for the fracture's position - 500, - 400, - 300 is smaller than that of the case without a fracture. Therefore, when the fracture is on the left of the injection well, it will have a deceleration effect on the doublet system performance: the heat breakthrough distance becomes smaller. In addition, as the order of the heat breakthrough distance is $L_b(-300) < L_b(-400) < L_b(-500)$, the deceleration effect is the greatest when the

fracture is at the injection well and the deceleration effect becomes weaker when the fracture is shifted left from the injection well.

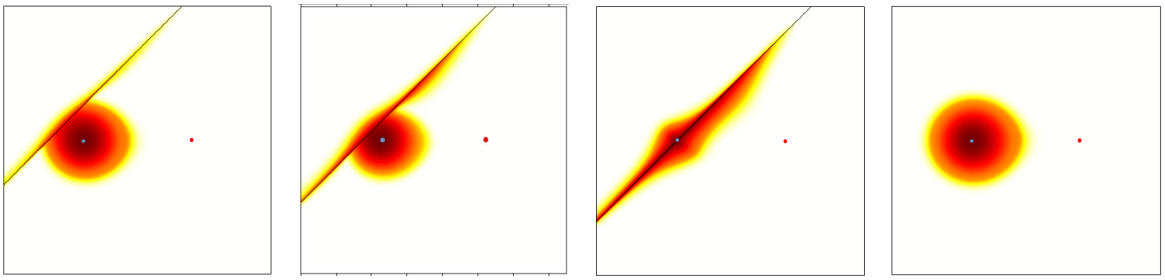

(a) -500 (b) -400 (c) -300 (d) Without fracture

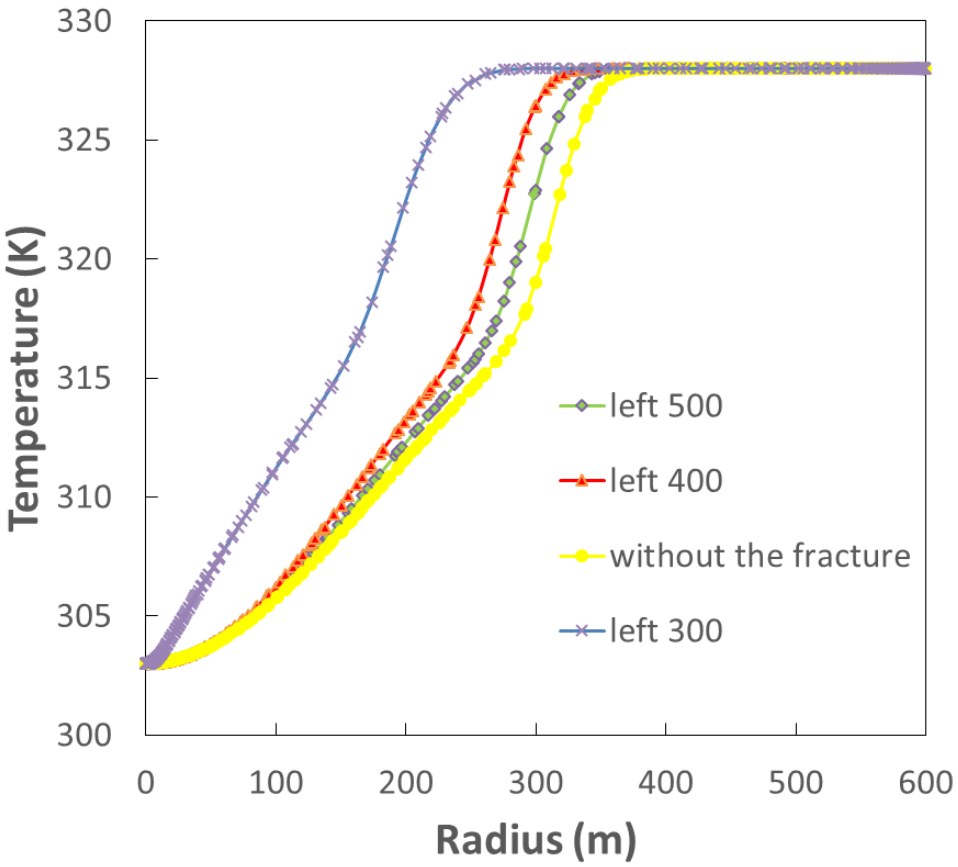

(e) Temperature distributions along the two wells at 25 years

Figure 6.19: Temperature contours and temperature distributions along the two wells at 25 years when the fracture is on the left of the fracture

The reason why the fracture through the injection well has the greatest deceleration effects on the temperature distribution along the two wells will be explained in the next Case (2). When the fracture is shifted further left from the injection well, the fracture is further away from the doublet system so that the deceleration effect of the fracture becomes weaker.

CASE (2) - The fracture is located between the injection well and the mid-point, namely the fracture is at - 300, -200, -100, 0.

The temperature distributions along the two wells at 25 years for the fracture position - 300, - 200, - 100, 0 and the model without a fracture are shown in Figure 6.20. It can be seen from the figure that, the heat breakthrough distance L_b, has the following relationship:

$$L_b(-300) < L_b(-200) < L_b(\text{no fracture}) < L_b(-100) < L_b(0)$$

As $L_b(\text{no fracture}) < L_b(-100) < L_b(0)$, the fracture at these positions has an acceleration effect on the heat breakthrough distance. In other words, the fracture accelerates the cold front towards the extraction well and thus increases the cold front accordingly.

In conclusion, the deceleration effect of the fracture becomes weaker when the fracture is shifted right from the injection well. Then the deceleration effect of the fracture becomes zero at a certain point between the injection well and the mid-point. After this point, the fracture gives the acceleration effect. Then this acceleration effect increases when the fracture is shifted right from that point. Finally, when the fracture is located at the mid-point, the acceleration effect of the fracture becomes the greatest.

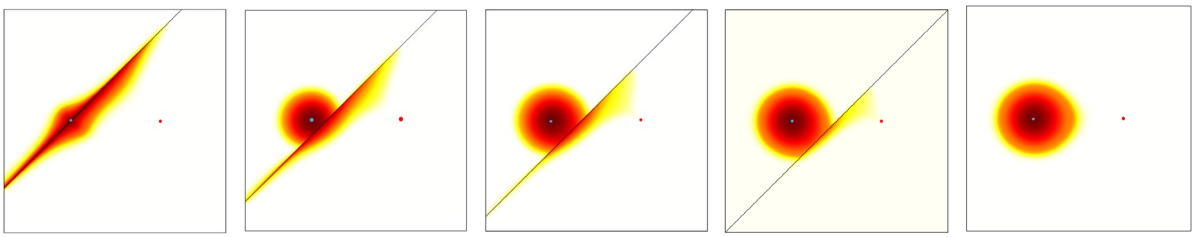

(a) -300 (b) -200 (c) -100 (d) Mid-point (e) Without fracture

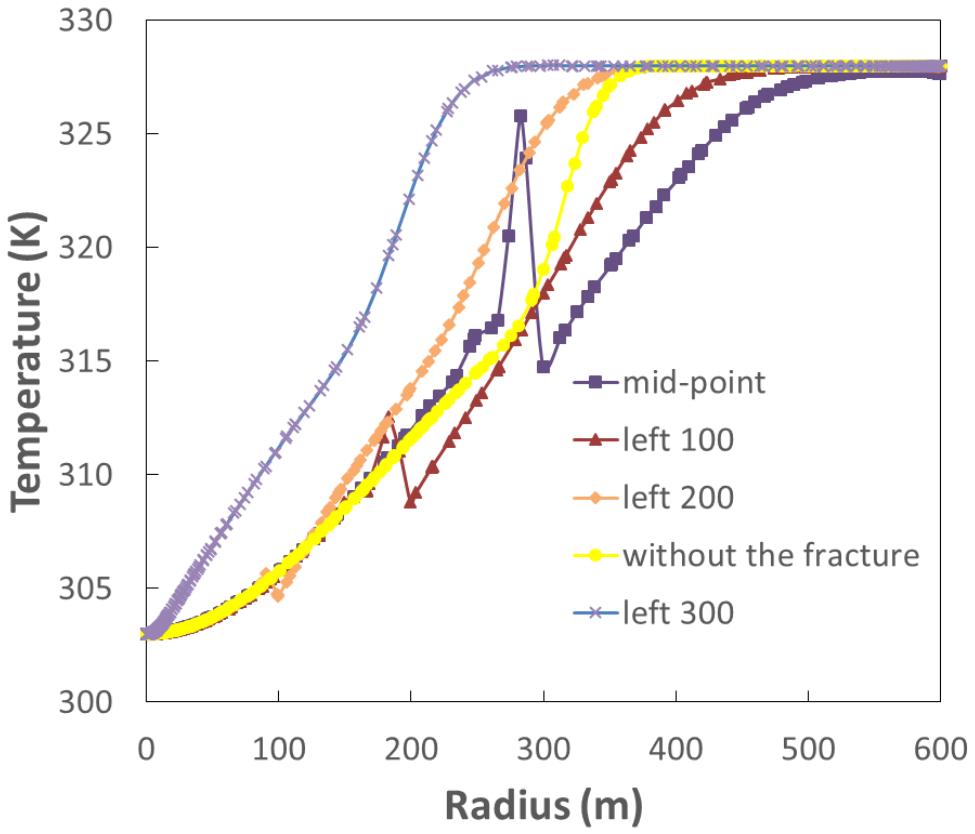

(f) Temperature distributions along the two wells at 25 years

Figure 6.20: Temperature contours and temperature distributions along the two wells at 25 years when the fracture is between the injection well and the mid-point

The reason why the mid-point fracture has the greatest acceleration effect on the temperature distribution along two wells is shown in Figure 6.21. The yellow arrows give the flow path when the fracture is at the mid-point while the red arrows give the path when the fracture is shifted left. The zone between two fractures is considered and the velocities along the yellow arrows and red arrows are examined. For the flow in the fracture, the time it takes to travel in the fracture is much shorter than that in the porous media as the permeability of the fracture is much higher than that of the porous media. Hence the comparison of the velocity in the porous media is made. The velocity along the purple arrow equals to that of the yellow arrows because the velocity field (magnitude) of the doublet system is central symmetric in terms of the midpoint of the two wells and the purple arrow is central symmetric to the yellow arrow so that their velocities are equal. However, the velocity along the purple arrow is greater than that of

the red arrow according to the properties of the velocity field of a doublet system that a point which is closer to the injection (extraction) well and horizontal axis has a higher velocity. Therefore, the velocity along the yellow arrows is greater than that of the red arrows. As a result, the time it takes for the yellow path is shorter than that of the red path. Hence the mid-point fracture has a greater acceleration effect than the fracture shifted to the left.

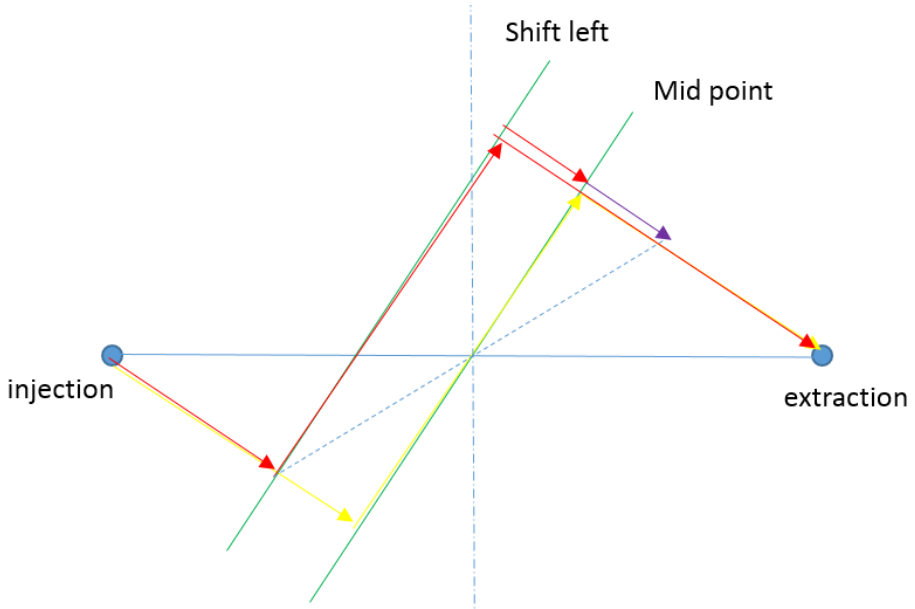

Figure 6.21: Explanation for the mid-point fracture

Similar to the explanation made using Figure 6.21, the reason why the fracture through the injection well has the greatest deceleration effect on the temperature distribution along two wells is shown in Figure 6.22. The yellow arrows are the flow paths when the fracture is through the injection well while the red arrows are the paths when the fracture is shifted right from the injection well. Again the zone between two fractures is considered and the velocities along the yellow arrows and red arrows are examined. For the flow in the fracture, the time it takes to travel in the fracture is much shorter than that in the porous media as the permeability of the fracture is much higher than that of the porous media. The velocity along the purple arrow is smaller than that of the red arrow because the red arrow is closer to the injection well and the horizontal axis than the purple arrow. Therefore, the velocity along the yellow arrows is smaller than that of the red arrows. As a result, the time it takes for the yellow path is longer

than that of the red path. The fracture through the injection well has a greater deceleration effect than the fracture shifted right from the injection well.

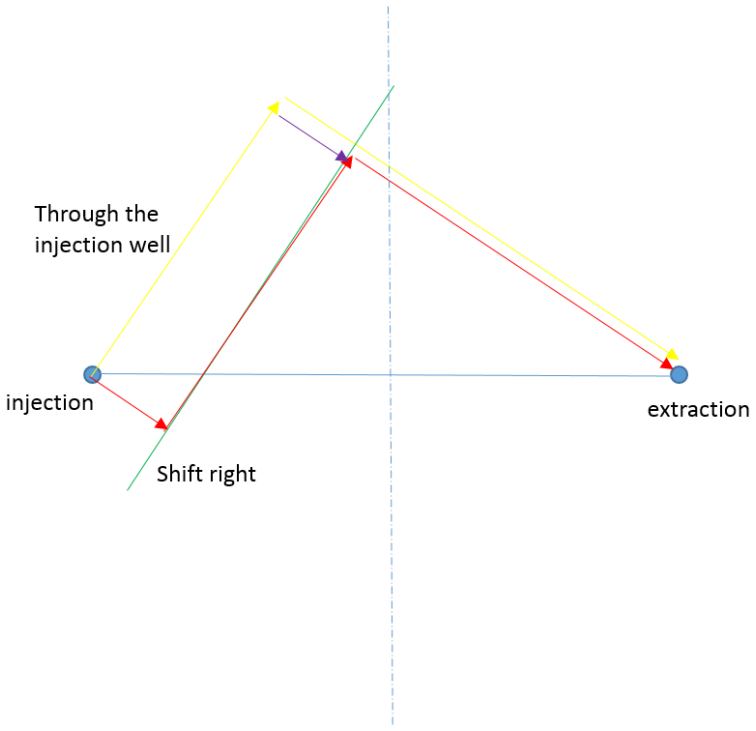

Figure 6.22: Explanation for the fracture through the injection well

CASE (3) - The fracture is located between the mid-point and the extraction well, namely the fracture is at 0, 100, 200, 300.

The temperature distributions along the two wells at 25 years for the fracture position 0, 100, 200, 300 and the model without a fracture are shown in Figure 6.23. The heat breakthrough distance L_b, has the following relationships:

$$L_b(300) < L_b(200) < L_b(\text{no fracture}) < L_b(100) < L_b(0)$$

The acceleration effect of the fracture becomes weaker when the fracture is shifted right from the mid-point. Then the acceleration effect of the fracture becomes zero at a certain point between the mid-point and the extraction well. The deceleration effect of the fracture increases when the fracture is shifted right from that point. Finally, when the fracture is located at the extraction well, the deceleration effect of the fracture becomes the greatest. The reason why

the fracture at the extraction well has the greatest deceleration effect on the temperature distribution along two wells is similar to the explanation made using Figure 6.22.

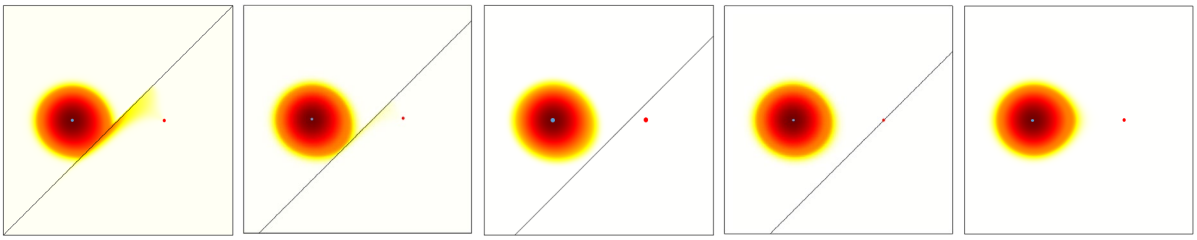

(a) Mid-point (b) +100 (c) +200 (d) +300 (e) Without fracture

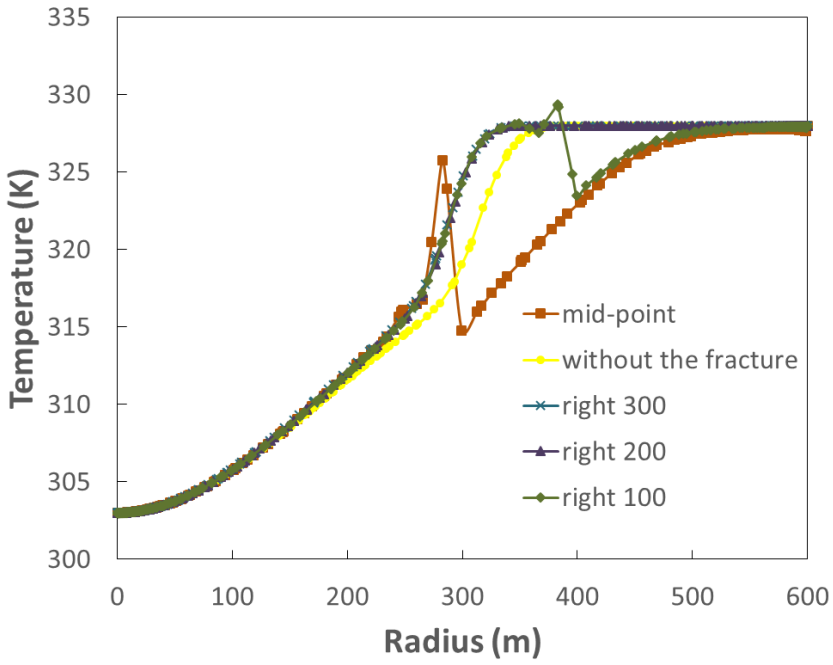

(f) Temperature distributions along the two wells

Figure 6.23: Temperature contours and temperature distributions along the two wells at 25 years when the fracture is between the mid-point and the extraction well

CASE (4) - The fracture is on the right of the extraction well, namely the fracture is located at 300, 400 and 500.

The temperature distributions along the two wells at 25 years for the fracture position 300, 400, 500 and the model without a fracture are shown in Figure 6.24. The heat breakthrough distance L_b has the following relationships:

$$L_b(300) < L_b(400) < L_b(500) < L_b(\text{no fracture})$$

The deceleration effect of the fracture becomes weaker when the fracture is shifted right from the extraction well. When the fracture is shifted further right from the extraction well, the fracture is further away from the doublet system so that the deceleration effect of the fracture becomes weaker.

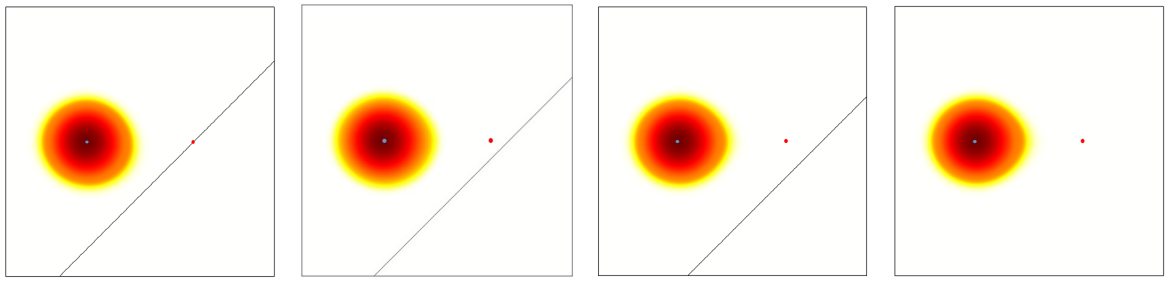

(a) +300 (b) +400 (c) +500 (d) Without fracture

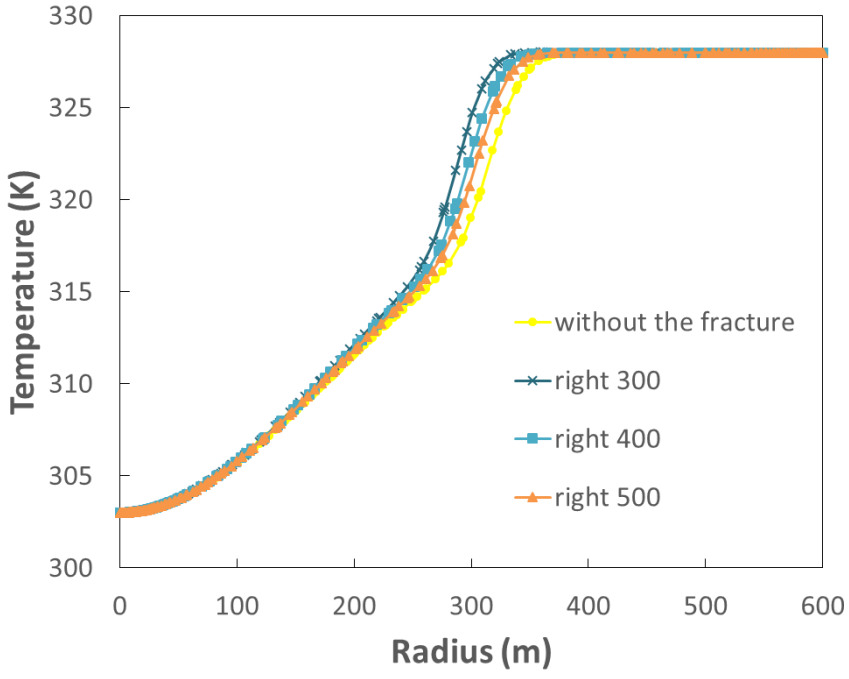

(e) Temperature distributions along the two wells

Figure 6.24: Temperature contours and temperature distributions along the two wells at 25 years when the fracture is on the right of the extraction well

According to the discussion above, the deceleration effect of the fracture becomes the greatest when the fracture is located at the injection well and the extraction well. The deceleration effects of the fracture at the injection well and the extraction well are compared in Figure 6.25. The deceleration effect of the fracture at the injection well is greater than the deceleration effect of the fracture at the extraction well. This is because when the fracture is at the injection well, large amount of the injected cold water flows in the fracture and travel in a roundabout way to the extraction well. Therefore, the deceleration effect of the fracture at the injection well is greater than the deceleration effect of the fracture at the extraction well.

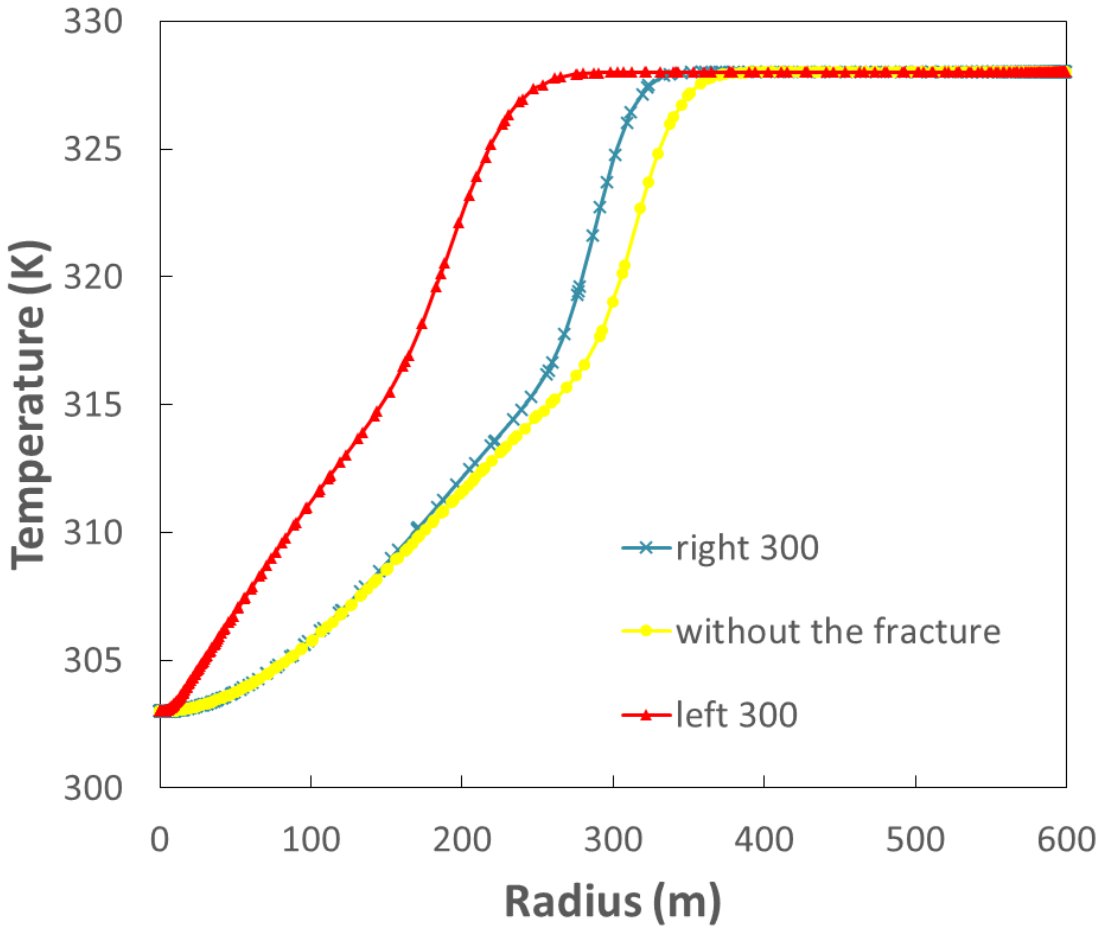

Figure 6.25: Comparison between the deceleration effect at the injection well and the extraction well

In summary, the influence of fracture position on the temperature distributions along the two wells are shown in Figure 6.26. The acceleration or deceleration effect of the fracture is

characterised by $(L_b - L_{b,no}) / L_{b,no}$, where L_b is the heat breakthrough distance with the fracture and $L_{b,no}$ is the heat breakthrough distance without the fracture. The positive sign is the acceleration effect while the negative sign is the deceleration effect. Generally speaking, the fracture that is far away from the mid-point between the two wells acts as barriers, decelerating the cold front towards the extraction well. It decreases the heat breakthrough distance, even though the permeability of the fracture is much greater than that of the porous media, which is quite counterintuitive.

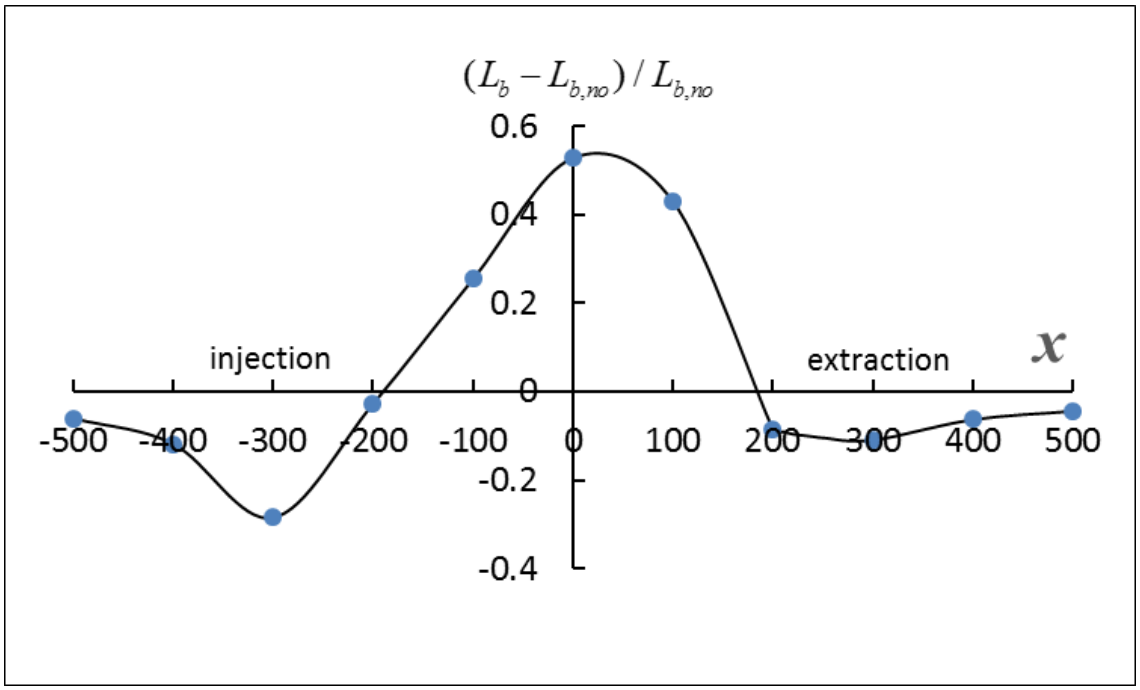

Figure 6.26: Influences of the fracture positions on the temperature distribution

Note that the premise of the above conclusion is that the angle of the fracture A is not so large. If the angle of the fracture A is very large, the deceleration effect becomes the acceleration effect (See Section 6.4.2). The value of the critical angle for this case will be discussed in Section 6.5.7.

6.4 Effect of Fracture Angle

6.4.1 Acceleration Effect

In Section 6.3.2, the effect of the mid-point coordinate of the fracture on the system performance was examined. As the mid-point fracture has the greatest acceleration effect on the doublet system, the effect of angle A of the mid-point fracture is examined to ensure that the most critical case is considered.

In Section 6.3.1, it was concluded that the fracture has no effect on the doublet system at all when the angle of the mid-point fracture $A = 0$. Next, an extreme case when the angle A is large (78.7 degrees) is considered here. The pressure distribution and streamlines for this case are shown in Figure 6.27. The temperature distribution at 25 years is shown in Figure 6.28. The temperature distributions along the two wells for 0.5, 1, 2, 5 and 25 years are shown in Figure 6.29. The temperature of the extracted water against time is shown in Figure 6.30.

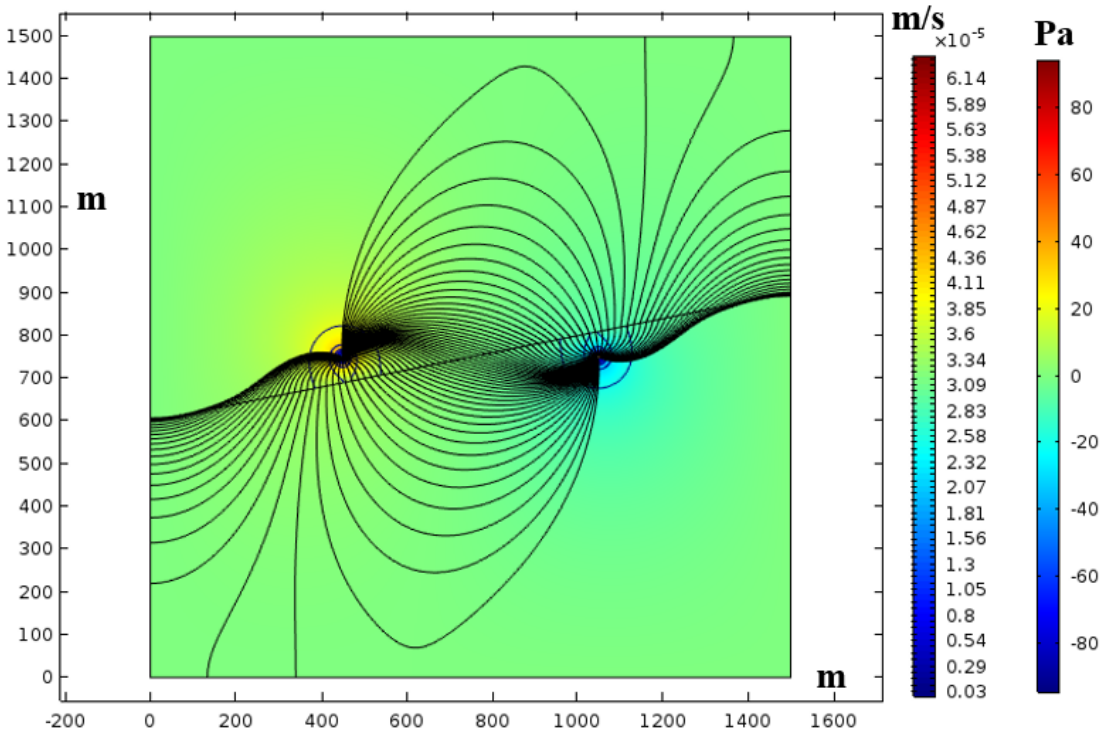

Figure 6.27: Pressure distribution and streamlines for $A = 78.7$ degrees

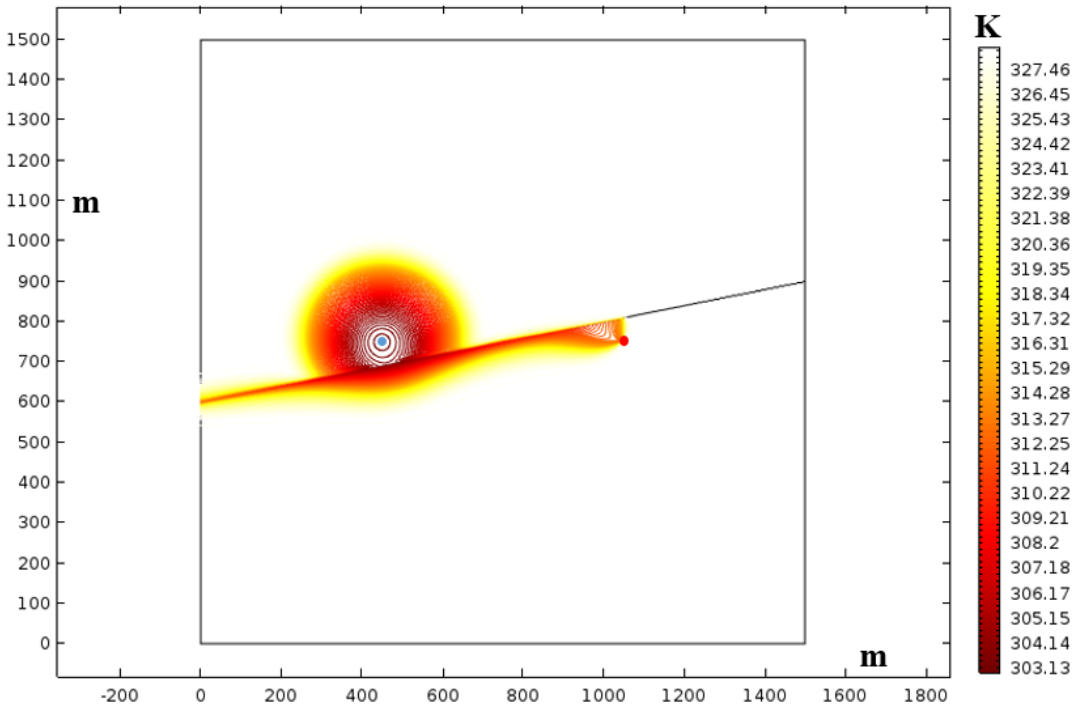

Figure 6.28: Temperature distribution at 25 years for $A = 78.7$ degrees

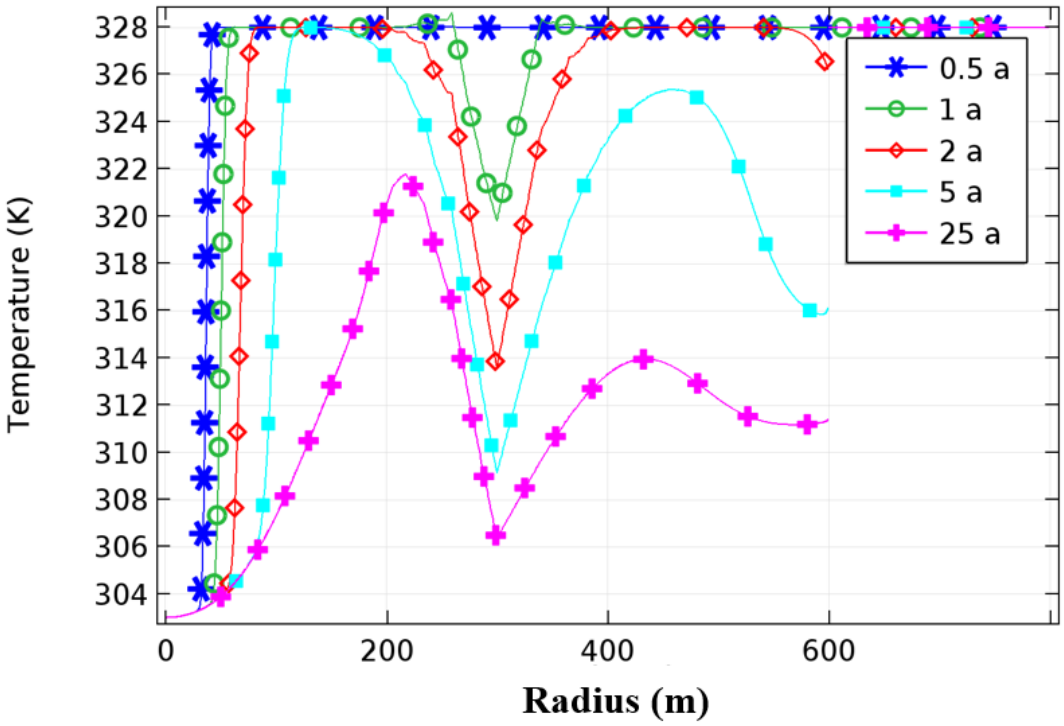

Figure 6.29: Transient temperature distribution at 0.5, 1, 2, 5 and 25 years

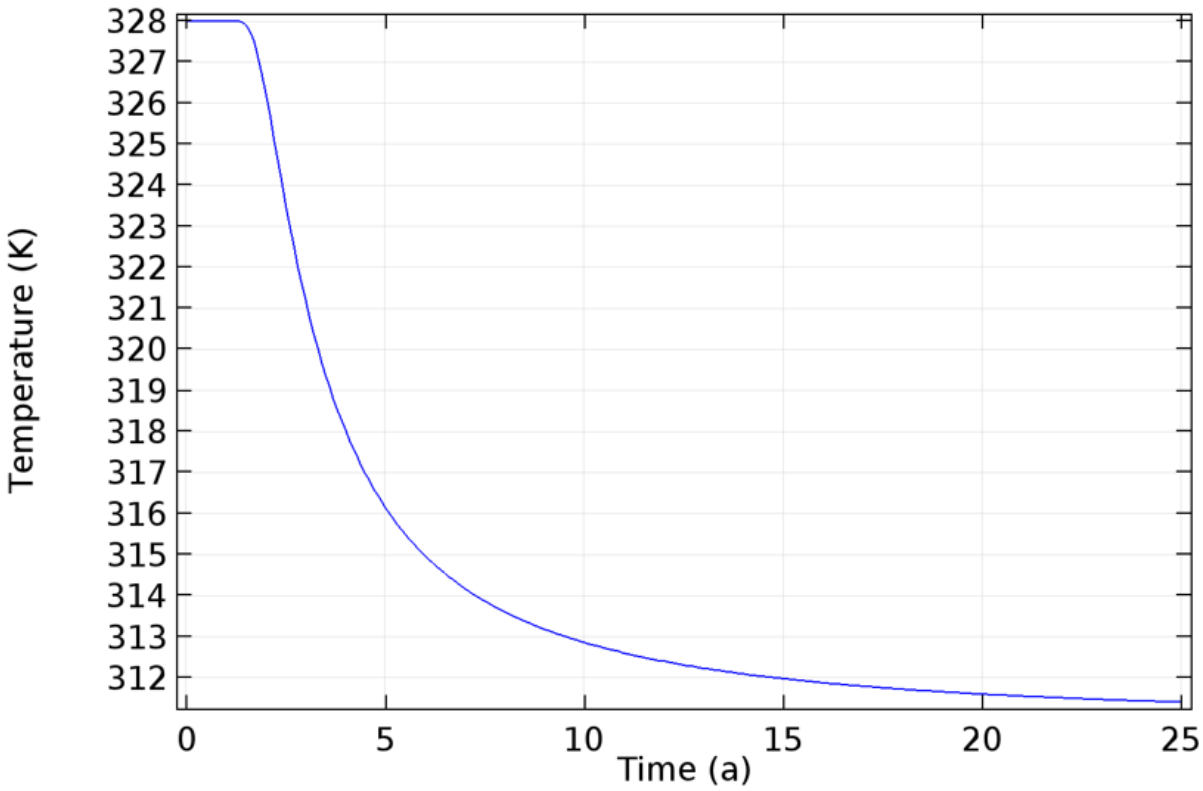

Figure 6.30: Temperature of the extracted water

As shown in Figure 6.29, at the early time (0.5 years) of the doublet system, the cold injected water travelling through the fracture has not yet arrived at the mid-point of the two wells. The temperature around the injection well is only cooled by the injected cold water through the porous media. When the cold injected water travelling through the fracture arrives at the mid-point of the two wells (1 year), the area around the mid-point is cooled by the cold injected water through the fracture which looks like a V-shape notch on the curve. When the cold injected water travelling through the fracture then through the porous media arrives at the extraction well, the temperature of the extracted water begins to decrease (2 years). In other words, the doublet system is no longer efficient at the moment.

The temperature of the extracted water decreases continually until the end of the life span of the doublet system (25 years). The temperature of the extracted water at 25 years can be obtained either from Figure 6.29 or Figure 6.30 which is about 311.5 K. Hence, when the angle A of the fracture is large, the effect of the fracture will be so large that the temperature of the

extracted water begins to decrease during the life span of the doublet system. The acceleration effect of the fracture increases with the increasing angle A of the fracture.

The explanation for this conclusion is quite straight-forward. When the angle A of the fracture becomes larger, the fastest flow path between the injection well and the extraction well will include a longer section of the fracture and a shorter section of the porous media. As a result, the time for the injected water to travel from the injection well to the extraction well will be shorter. Therefore, the temperature of the extracted water is cooled down by the injected cold water during the life span of the doublet system.

6.4.2 Deceleration Effect

As described in Section 6.3.2, the deceleration effect of the fracture is the greatest when the fracture is located at the injection well. The maximum deceleration effect takes place when the fracture is located at the injection well and the angle of the fracture is $A = 0$. The streamlines and the temperature distribution at 25 years are shown in Figure 6.31 and Figure 6.32, respectively.

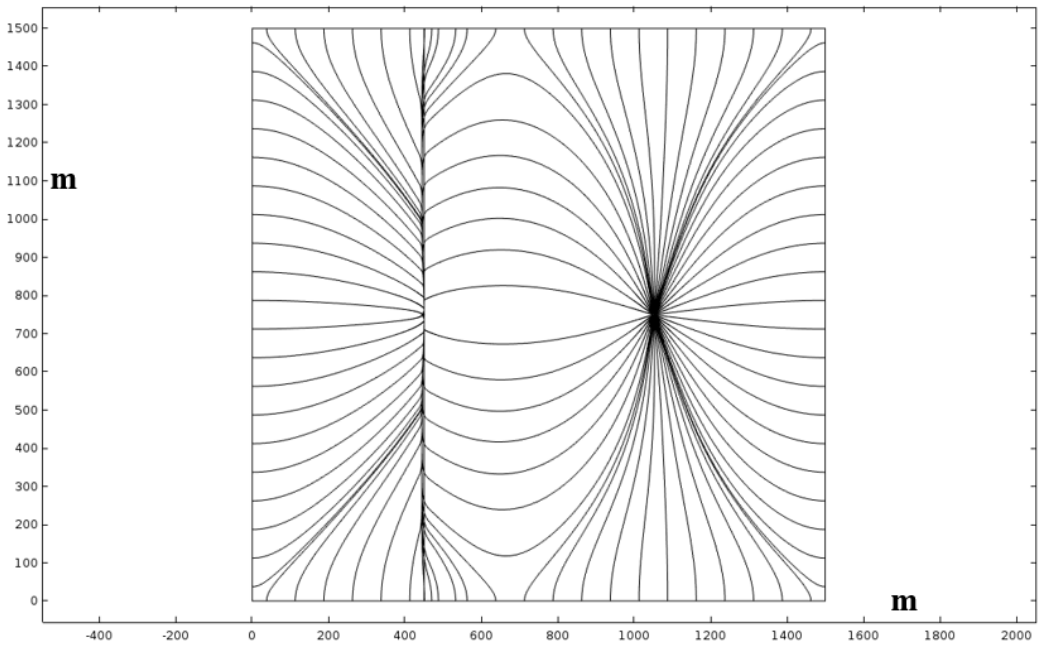

Figure 6.31: Streamlines for the maximum deceleration effect

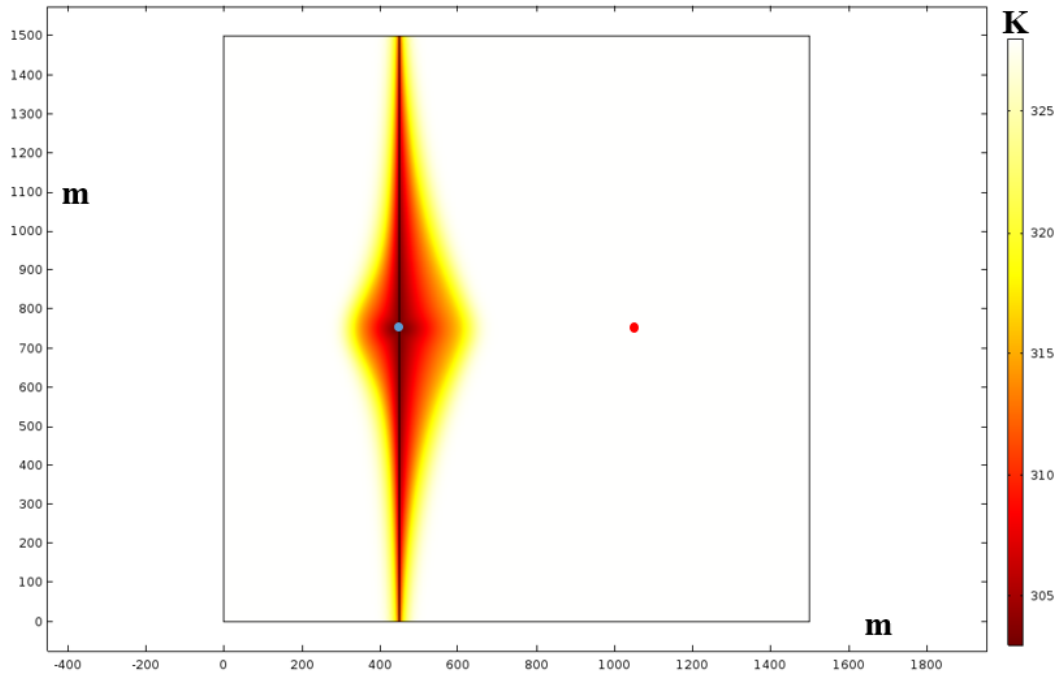

Figure 6.32: Temperature distribution at 25 years for the maximum deceleration effect

It can be seen in Figure 6.31 that the shape of the streamlines on the right of the fracture does not change and the streamlines are not rotated as the angle of the fracture $A = 0$. The streamlines are cut vertically by the fracture. As shown in Figure 6.32, the fracture is through the injection well and hence the majority of the cold injected water flows through the fracture that is perpendicular to the injection well - extraction well direction so that the water in the fracture does not flow towards the extraction well. This in turn makes the deceleration effect maximum. The temperature distribution along the two wells at 25 years for $A = 0$ and $A = \pi / 4$, is shown in Figure 6.33. It can be found that the deceleration effect for $A = 0$ is greater than that for $A = \pi / 4$ in Section 6.3.2.

The maximum deceleration effect of the fracture takes place when the fracture is located at the injection well and the angle of the fracture $A = 0$. The deceleration effect of the fracture decreases with the increasing angle of the fracture A. If the angle of the fracture A is large enough, the deceleration effect will vanish and then will be replaced by the acceleration effect (consider the extreme case in which the fracture is horizontal). The critical angle at which the deceleration effect turns into the acceleration effect will be discussed in Section 6.5.7.

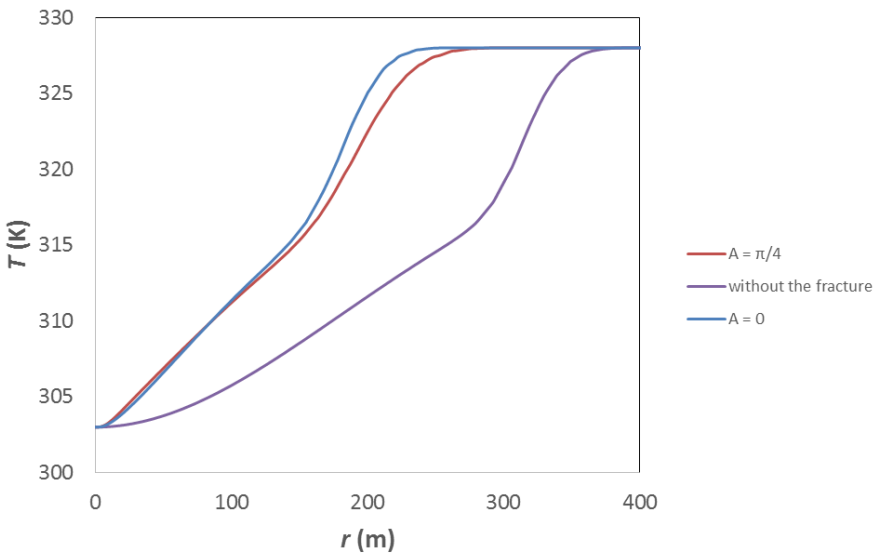

Figure 6.33: The temperature distribution along two wells at 25 years for $A = 0$ and $A = \pi / 4$

6.5 Critical Angle Governing the System Performance

As described in Section 6.4, the acceleration effect of the fracture on the doublet system performance increases with the angle A of the fracture. When the angle of the fracture A = 0 and the fracture is located at the mid-point between the two wells, the acceleration effect of the fracture is zero and the temperature distribution along the two wells is not affected by the fracture. The temperature of the extracted water keeps constant during the life span of the system when the distance between the two wells is equal to or greater than the critical distance. The temperature of the extracted water decreases due to the acceleration effect of the fracture when the angle of the fracture increases to a certain degree. To make the case most unfavourable, the distance between the two wells is considered to be equal to the critical distance L_c.

6.5.1 Critical Distance between the Two Wells

As discussed in Section 5.3, the temperature of the extracted water is constant during 25 years, when the distance between the two wells is more than the critical distance. The expression of the critical distance is as follows:

$$L_c^* = 2.383\alpha^{0.404},\ 0.6 \le \alpha \le 600$$

where α is the dimensionless injection rate.

In the following analysis, the distance between the two wells is assigned as the critical distance and then the angle of the fracture is varied.

6.5.2 Thermal Conductivity of Fracture

A preliminary parametric study shows that, for the practical values of the thermal conductivity of the fracture and the porous media, the thermal conductivity λ_f of the fracture has limited influence on the temperature distribution along the two wells and the temperature of the extracted water against time, as shown in Figure 6.34 and Figure 6.35. In this figure, λ_s is the thermal conductivity of the porous media. It is noted that there is a temperature jump at the extraction well because the temperature on the right side of the extraction well is equal to the initial temperature of aquifer.

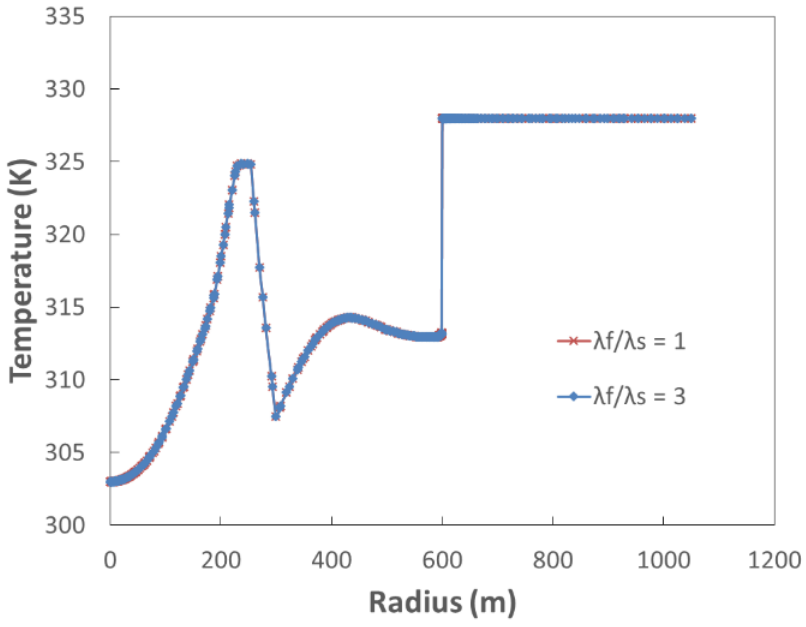

Figure 6.34: Temperature distribution along two wells at 25 years for different thermal conductivity of the fracture

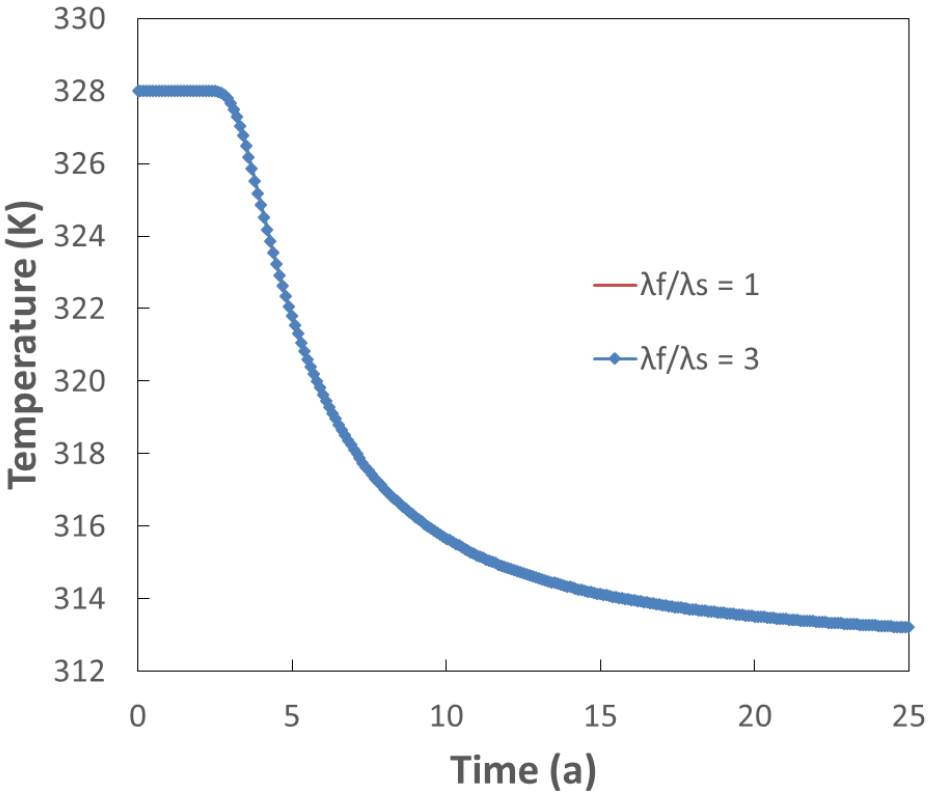

Figure 6.35: Temperature of the extracted water against time for different thermal conductivity of the fracture

In Figure 6.34 and Figure 6.35, the two curves exactly match with each other. As the permeability of the fracture is very large and hence the flow velocity in the fracture is also very large. The heat transfer by advection is much larger than that by conduction and the influence of the thermal conductivity of the fracture is very little. Therefore, in the following numerical simulations, $\lambda_f / \lambda_s = 1$ is assumed.

6.5.3 Porosity of Fracture

A preliminary parametric study shows that the porosity of the fracture has limited influence on the temperature distribution along the two wells, as shown in Figure 6.36. The two curves exactly match with each other. The water velocity in the fracture is dominated by the permeability of the fracture. The contribution of the porosity to the velocity is already included in the permeability. Therefore, the porosity of the fracture has limited influence on the water velocity in the fracture thus limited influence on the temperature distribution.

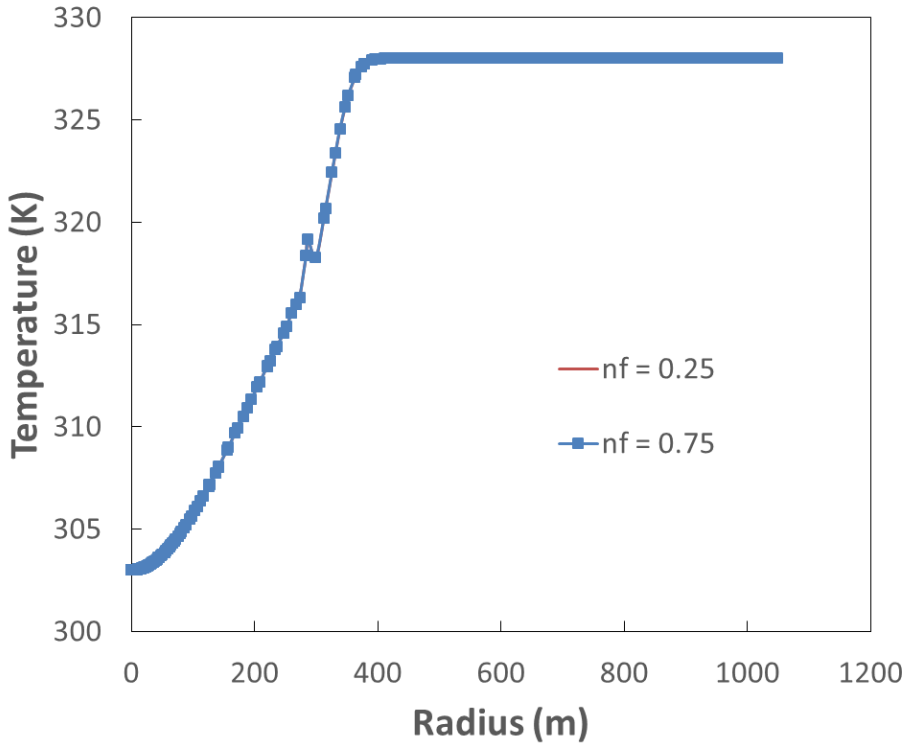

Figure 6.36: Temperature distribution along two wells at 25 years for different porosity of the fracture

Therefore, in the following numerical simulations, $n_f / n_s = 1$ is assumed.

6.5.4 Permeability of Fracture and Porous Media

A preliminary parametric study shows that, with the same $(k_f - k_s)/k_s$ (the permeability of the fracture k_f and that of the porous media k_s), the temperature distribution along the two wells at 25 years and the temperature of the extracted water against time are the same, as shown in Figure 6.37 and Figure 6.38. The unit for k_f and k_s is [m^2]. In practice, the permeability of the fracture k_f is much larger than that of the porous media k_s. Therefore, generally, we have $\frac{k_f - k_s}{k_s} \approx \frac{k_f}{k_s}$. The geometry and boundary conditions in this case are the same as that in Section 6.3 except that the angle of the fracture is very large in this case. As a result, the acceleration effect of the fracture is so large that the temperature of the extracted water decreases during the life span and the doublet system is no longer efficient.

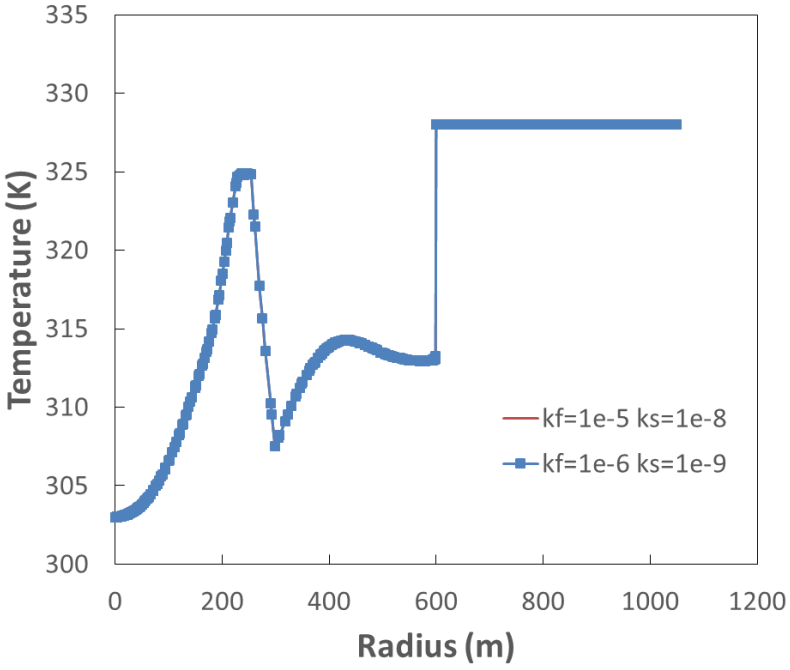

Figure 6.37: Temperature distribution along two wells at 25 years with different k_f and k_s

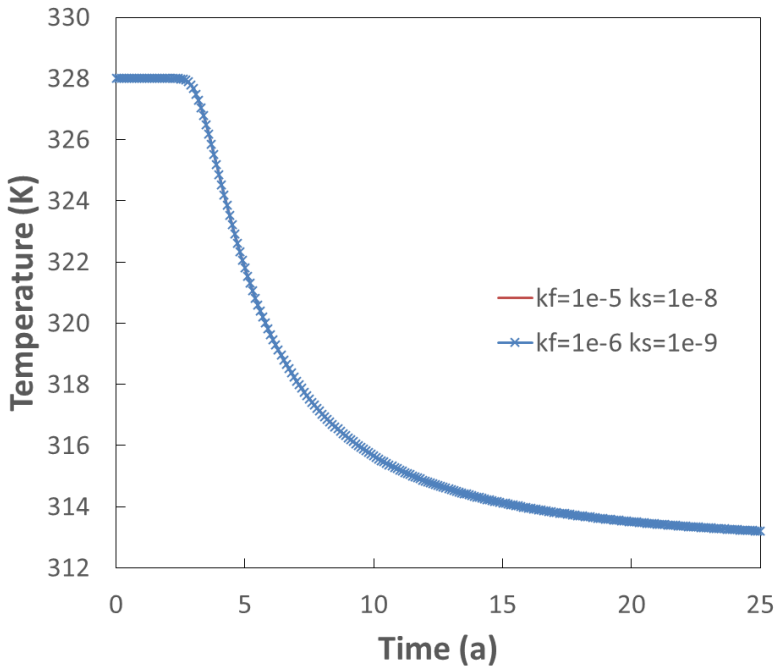

Figure 6.38: Temperature of the extracted water against time with different k_f and k_s

For both curves, $(k_f - k_s)/k_s = 1000$, the two curves exactly match with each other in the above figures. The temperature distribution along the two wells at 25 years and the temperature of the extracted water against time are related to $(k_f - k_s)/k_s$. The curves are the same for the same $(k_f - k_s)/k_s$ and k_s values do not affect the temperature distributions. Considering a case without a fracture firstly, as the injection rate is specified, the k_s values do not affect the velocity field and temperature distributions of the model but only the pressure field of the model. Then a fracture is added to the model. The velocity field and temperature distributions are affected by the fracture and are related to $(k_f - k_s)/k_s$. If the permeability of the fracture and porous media is the same $(k_f = k_s)$, $(k_f - k_s)/k_s = 0$ so the fracture has no influence on the velocity field and temperature distributions. Therefore, in the following numerical simulations, $k_s = 10^{-9}\,\mathrm{m}^2$ is used and k_f values are varied.

6.5.5 Thickness of Fracture

The temperature distribution along the two wells at 25 years and the temperature of the extracted water against time for different permeability values k_f and thicknesses d of the fracture are shown in Figure 6.39 and Figure 6.40. The unit for the permeability k_f is [m^2] and the unit for the thickness d is [m]. The geometry and boundary conditions in this case are the same as that in Section 6.3 except that the angle of the fracture is very large in this case and the values of the permeability of the fracture k_f and thickness of the fracture d are varied. As a result, the acceleration effect of the fracture is so large that the temperature of the extracted water decreases during the life span and the doublet system is no longer efficient.

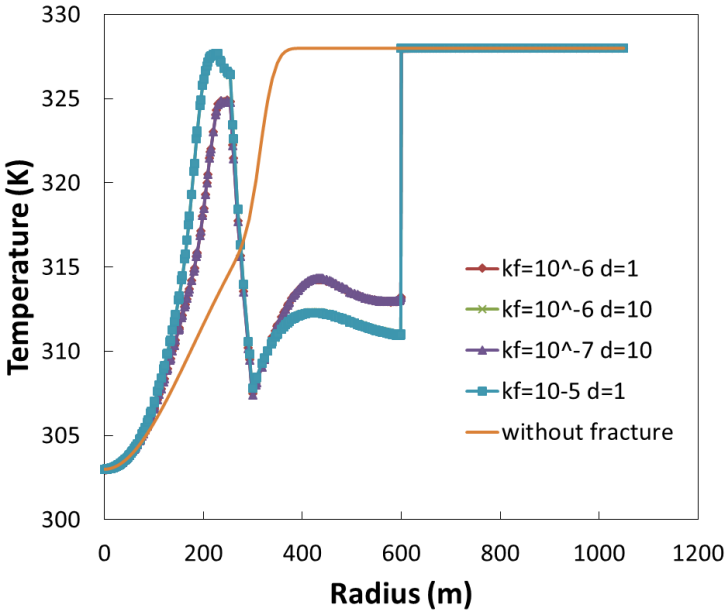

Figure 6.39: Temperature distribution along two wells at 25 years for different permeability and thickness of the fracture

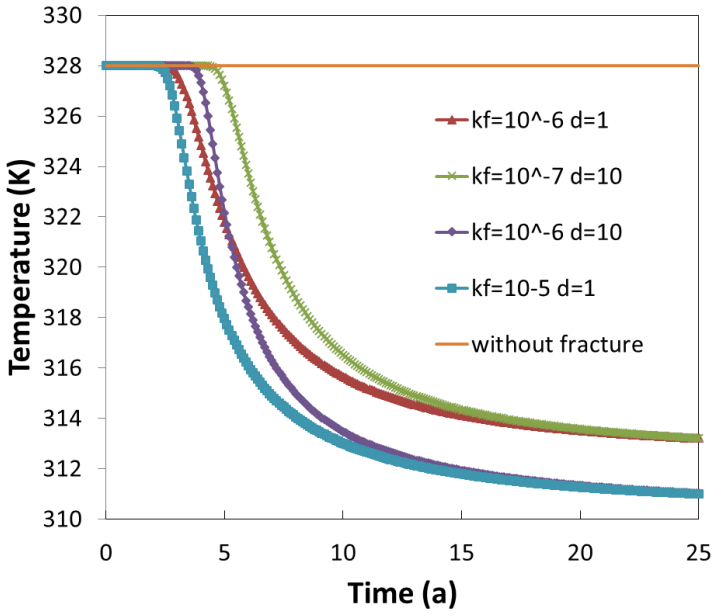

Figure 6.40: Temperature of the extracted water against time for different permeability and thickness of the fracture

From Figure 6.39, it can be seen that the temperature distribution along the two wells at 25 years is the same with the same value of $(k_f - k_s)d$. The peak of the curve for

$(k_f - k_s)d = 10^{-5}\,\mathrm{m}^3$ is lower than that for $(k_f - k_s)d = 10^{-6}\,\mathrm{m}^3$. This is because, with a larger $(k_f - k_s)d$, a greater amount of cold water flows through the fracture so that the amount of cold water flowing directly towards the extraction well from the injection well through the porous media is less. Therefore, the cooling effect along the two wells on the left of the fracture is weak and thus the peak of the curve is lower with a larger $(k_f - k_s)d$. As a greater amount of cold water flows through the fracture with a larger $(k_f - k_s)d$, the acceleration effect of the fracture is greater and the temperature at the extraction well is lower with a larger $(k_f - k_s)d$.

The temperature of the extracted water at 25 years is also the same with the same value of $(k_f - k_s)d$, as shown in Figure 6.40. In addition, with the same $(k_f - k_s)d$, if the permeability of the fracture k_f is larger, the cold water travels faster through the fracture. As a result, the time when the temperature of the extracted water begins to decrease is shorter for a larger k_f.

In summary, the controlling parameter for the fracture is $(k_f - k_s)d$. The dimensionless form of this parameter is $\dfrac{(k_f - k_s)d}{k_s H}$, where H is the thickness of the aquifer.

6.5.6 Case 1: Critical Angle θ when Fracture is at Mid-point

The critical angle θ of the fracture is that, at this angle, the temperature of the extracted water will not decrease during the life span of the doublet system. In the following analysis, the critical angle θ is defined as the largest angle that satisfies:

$$\frac{T_e - T_0}{T_w - T_0} < 1\% \tag{6.1}$$

where T_e is the temperature of the extracted water at 25 years, T_w is the temperature of the injected water and T_0 is the initial temperature of the aquifer.

The critical angle θ of the fracture is not only related to the properties of the fracture, but also related to the dimensionless injection rate α. Actually, the critical angle θ decreases with the

increasing $\frac{(k_f - k_s)d}{k_s H}$ and the increasing α. As $\frac{(k_f - k_s)d}{k_s H}$ and α increase, there is more injected cold water travelling through the fracture and the critical angle θ must be smaller to shorten the water travel distance along the fracture so that the temperature of the extracted water will not decrease during the life span. The dimensionless form of the critical angle θ can be expressed as:

$$\theta = f\left(\frac{(k_f - k_s)d}{k_s H}, \alpha\right) \tag{6.2}$$

The method of finding the expression of the critical angle θ is shown in Figure 6.41. The fracture is located at the mid-point when the acceleration effect of the fracture is the greatest. The angle A of the fracture is increased until Equation (6.1) does not hold and the angle A of the fracture that satisfies Equation (6.1) is evaluated as the critical angle θ of the fracture. For different values of the dimensionless fracture property $\frac{(k_f - k_s)d}{k_s H}$ and the dimensionless injection rate α, the corresponding critical angle θ can be obtained. When $k_f - k_s = 0$, the fracture has the same property as the porous media that the fracture will not affect the doublet system and hence the critical angle of the fracture becomes $\theta = 90^\circ$.

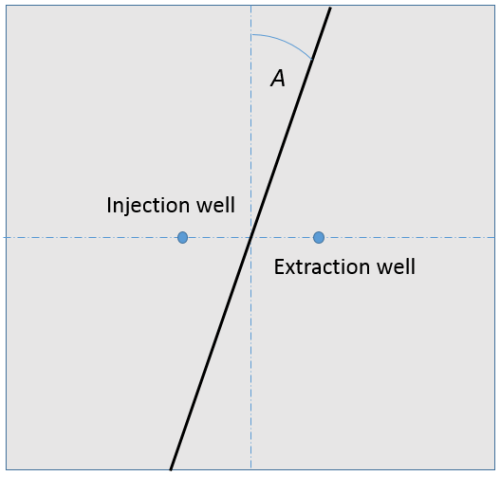

Figure 6.41: Method of finding the expression of the critical angle

For example, the following case is considered: the injection rate $Q = 0.01\ \mathrm{m}^3/\mathrm{s}$, the property of the fracture $(k_f - k_s)d = 10^{-6}\mathrm{m}^3$, the dimensionless injection rate $\alpha = 59.4$ and the dimensionless fracture property $\frac{(k_f - k_s)d}{k_s H} = 20$.

Firstly, the angle of the fracture $A = 45^\circ$ is tried. The temperature distribution along the two wells at 25 years and the temperature of the extracted water against time for $A = 45^\circ$ are shown in Figure 6.42 and Figure 6.43. It can be seen from Figure 6.42 that the fracture has an acceleration effect on the temperature distribution. It can be seen from Figure 6.43 that the temperature of the extracted water at 25 years for $A = 45^\circ$, $\frac{T_e - T_0}{T_w - T_0} = 0.76\% < 1\%$ so $A = 45^\circ$ is not larger than the critical angle.

Then the angle of the fracture A is increased and $A = 46^\circ$ is tried. It can be seen from Figure 6.44 that the temperature of the extracted water at 25 years for $A = 46^\circ$, $\frac{T_e - T_0}{T_w - T_0} = 2.0\% > 1\%$ so $A = 46^\circ$ is larger than the critical angle. Therefore, the critical angle θ of the fracture for the given dimensionless fracture property $\frac{(k_f - k_s)d}{k_s H} = 20$ and the dimensionless injection rate $\alpha = 59.4$ is 45 degrees.

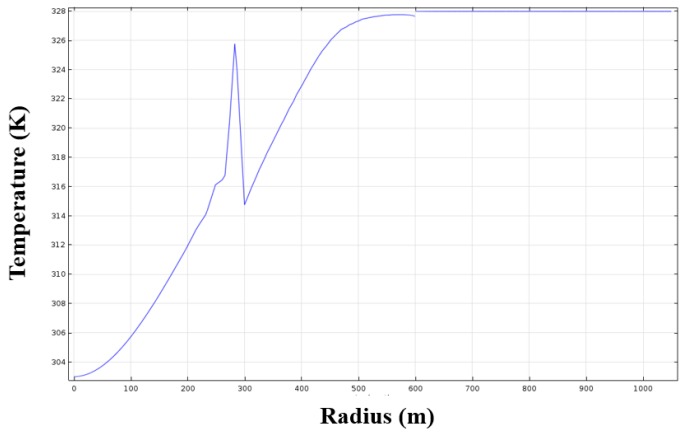

Figure 6.42: Temperature distribution along two wells at 25 years for A = 45 degrees

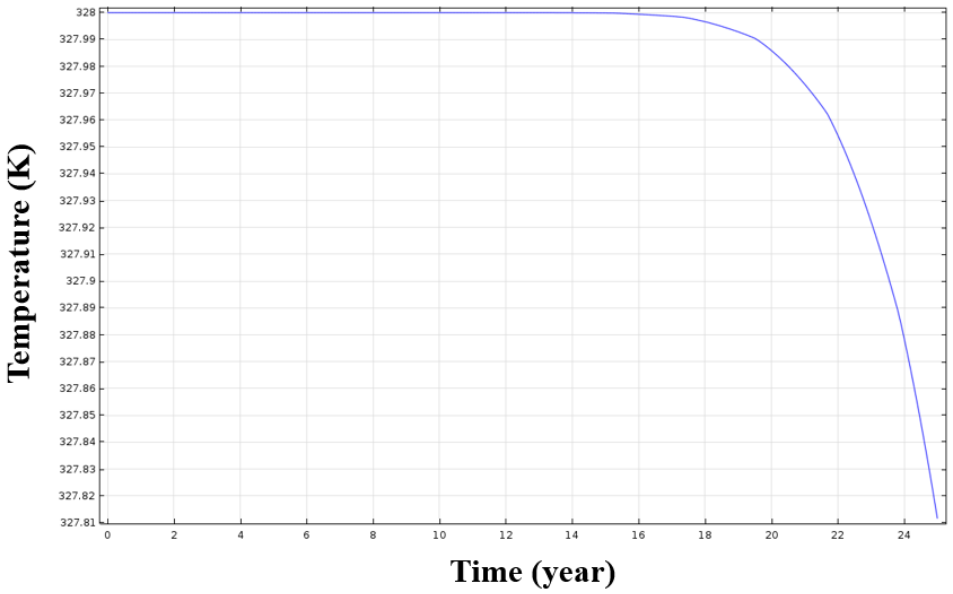

Figure 6.43: Temperature of the extracted water against time for A = 45 degrees

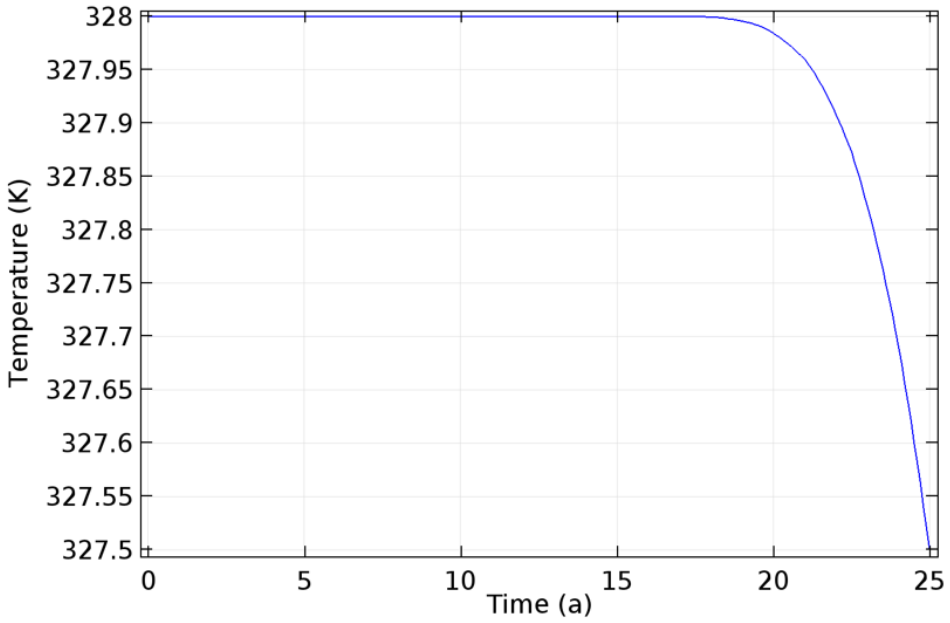

Figure 6.44: Temperature of the extracted water against time for A = 46 degrees

By conducting a series of analysis, the relationship between the critical angle of the fracture θ and the dimensionless injection rate α and the dimensionless fracture property $\frac{(k_f - k_s)d}{k_s H}$ is shown in Figure 6.45 (the corresponding α for Q = 10, 30, 50, 70 and 90 L/s are α = 59.4, 178.2, 297, 415.8 and 534.6).

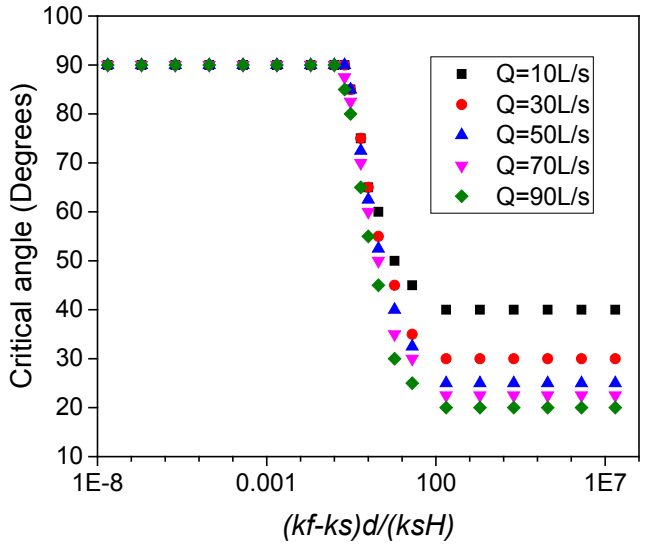

Figure 6.45: Critical angle for different dimensionless injection rates and fracture properties

It can be seen from Figure 6.45 that the critical angle of the fracture θ decreases with the increasing dimensionless fracture property and also decreases with the increasing dimensionless injection rate α. When the dimensionless fracture property is small, namely $\frac{(k_f - k_s)d}{k_s H} < 10^{-5}$, the critical angle of the fracture $\theta = 90^{\circ}$ which indicates that the temperature of the extracted water will not decrease during the life time of the doublet system for any angle of the fracture A as long as the dimensionless fracture property is very small. When the dimensionless fracture property is large ($\frac{(k_f - k_s)d}{k_s H} > 100$), the critical angle of the fracture is equal to a lower-bound value θ_c which indicates that the temperature of the extracted water will not decrease during the life time of the doublet system for any dimensionless fracture property as long as the angle of the fracture is $A \le \theta_c$. The value of θ_c decreases with the increasing dimensionless injection rate α.

By trial and error, it was found that, for a given dimensionless injection rate α, the critical angle of the fracture θ can be expressed with respect to the logarithm of the dimensionless fracture property, $\lg\frac{(k_f - k_s)d}{k_s H}$, using the Boltzmann function as follows:

$$\theta = A_2 + \frac{A_1 - A_2}{1 + \mathrm{e}^{\frac{k-k_0}{b}}} \tag{6.3}$$

where $k = \lg\dfrac{(k_f - k_s)d}{k_s H}$; A_1, A_2, k_0 and b are the parameters for the Boltzmann function.

According to the upper and lower bounds of the critical angle θ shown in Figure 6.45, $A_1 = 90^\circ$ and $A_2 = \theta_c$. The curve fittings using the Boltzmann function are shown in Figure 6.46.

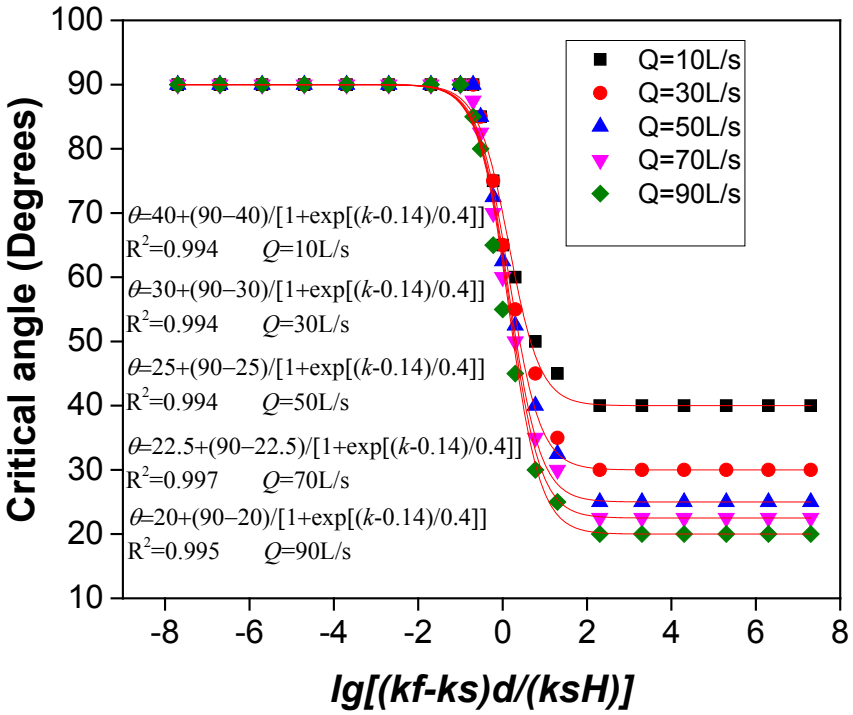

Figure 6.46: Curve fitting for different dimensionless injection rate α

It can be known from Figure 6.46 that the expression of the critical angle θ has the following form:

$$\theta = \theta_c + \frac{90 - \theta_c}{1 + e^{\frac{k-0.14}{0.4}}} \tag{6.4}$$

where $k = \lg\frac{(k_f - k_s)d}{k_s H}$; θ_c is a function of the dimensionless injection rate α.

The relation between θ_c and the dimensionless injection rate α is shown in Figure 6.47. The expression of θ_c is as follows:

$$\theta_c = -9.09 \ln \alpha + 77.08 \tag{6.5}$$

where α is the dimensionless injection rate.

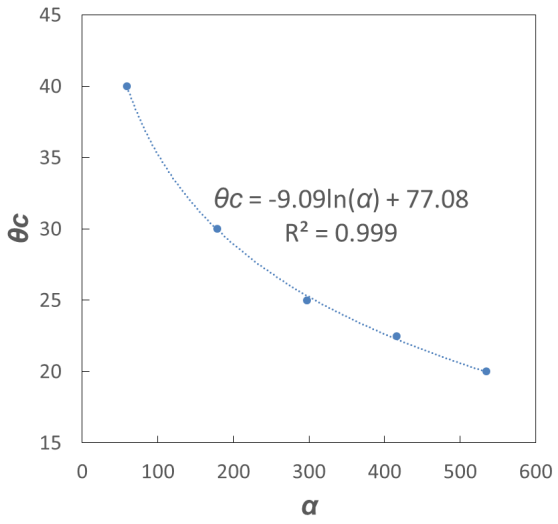

Figure 6.47: The relation between θ_c and the dimensionless injection rate α

Therefore, the expression of the critical angle θ of the fracture in terms of the dimensionless injection rate α and the dimensionless fracture property $\frac{(k_f - k_s)d}{k_s H}$ is proposed:

$$\theta_{mid} = \theta_{c,mid} + \frac{90 - \theta_{c,mid}}{1 + e^{\frac{k-0.14}{0.4}}} \tag{6.6}$$

where $k = \lg\frac{(k_f - k_s)d}{k_s H}$; $\theta_{c,mid} = -9.09 \ln \alpha + 77.08$; α is the dimensionless injection rate and $0.6 \le \alpha \le 600$.

Equation (6.6) can be useful in practice. It gives the most critical case that the temperature of the extracted water will not be affected by the fracture so that the doublet system is thermal efficient during its life span. In other words, given the cold water injection rate and the angle and properties of the fracture, it is possible to decide whether the doublet system is still efficient during its life time with the existence of the fracture in the system or not. In addition, given the cold water injection rate and the angle of the fracture, the maximum value of the fracture permeability that will keep the doublet system efficient during its life time can be evaluated.

6.5.7 Case 2: Critical Angle θ when Fracture is at Injection Well or Extraction Well

Following the procedures described in Section 6.5.6, when the fracture is located at the injection well, the curve fitting using the Boltzmann function is shown in Figure 6.48.

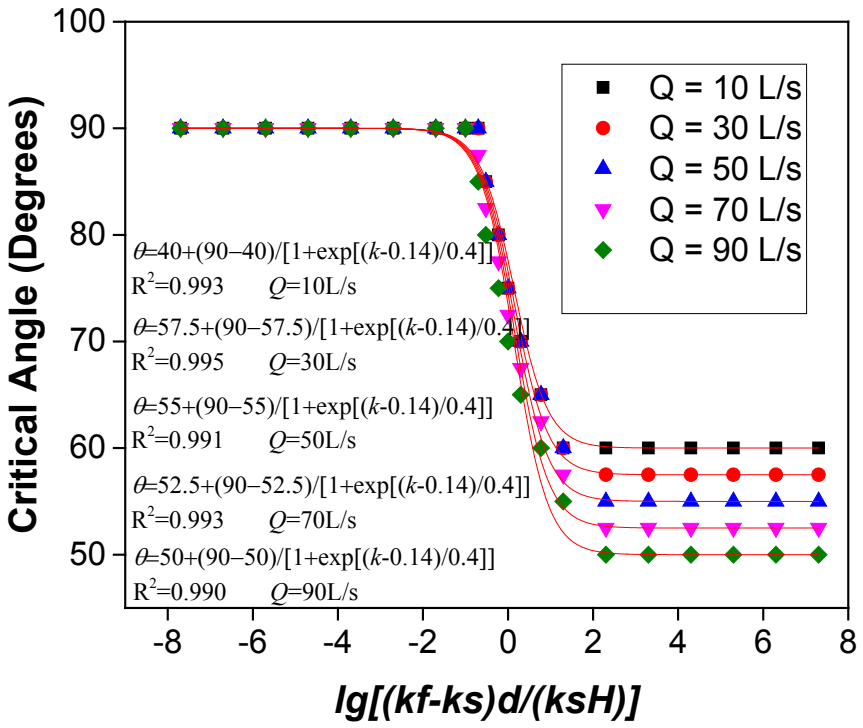

Figure 6.48: Curve fitting for the case that the fracture is located at the injection well

It can be seen from Figure 6.48 that the expression of the critical angle θ has the same form as Equation (6.4), but with different values of θ_c, as follows:

$$\theta = \theta_c + \frac{90 - \theta_c}{1 + e^{\frac{k-0.14}{0.4}}} \tag{6.7}$$

where $k = \lg \frac{(k_f - k_s)d}{k_s H}$; θ_c is a function of the dimensionless injection rate α.

The relation between θ_c and the dimensionless injection rate α is shown in Figure 6.49. The expression of θ_c is as follows:

$$\theta_c = -0.021\alpha + 61.25 \tag{6.8}$$

where α is the dimensionless injection rate.

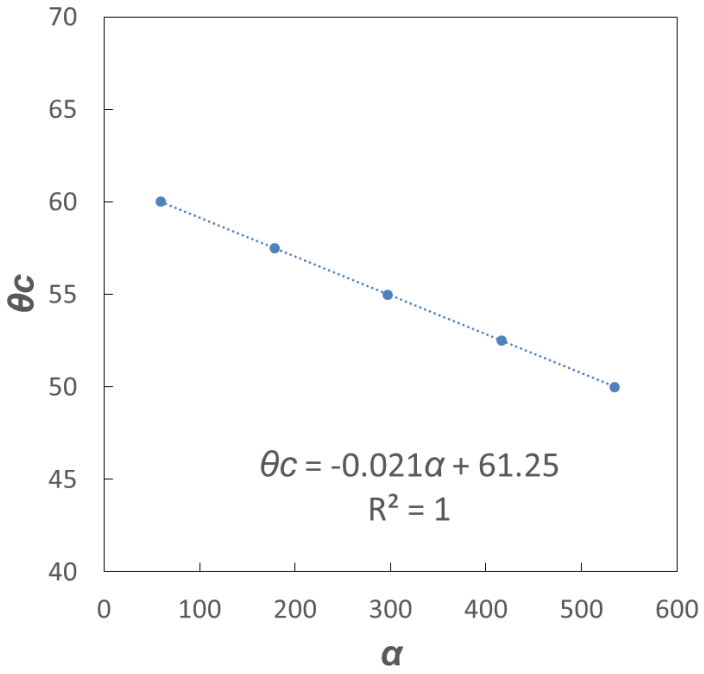

Figure 6.49: The relation between θ_c and the dimensionless injection rate α

Therefore, the expression of the critical angle θ of the fracture in terms of the dimensionless injection rate α and the dimensionless fracture property $\frac{(k_f - k_s)d}{k_s H}$ is as follows:

$$\theta_{in} = \theta_{c,in} + \frac{90 - \theta_{c,in}}{1 + e^{\frac{k-0.14}{0.4}}} \tag{6.9}$$

where $k = \lg\frac{(k_f - k_s)d}{k_s H}$; $\theta_{c,in} = -0.021\alpha + 61.25$; α is the dimensionless injection rate and $0.6 \le \alpha \le 600$.

Similarly, when the fracture is located at the extraction well, the expression of the critical angle θ of the fracture in terms of the dimensionless injection rate α and the dimensionless fracture property $\frac{(k_f - k_s)d}{k_s H}$ is as follows:

$$\theta_{ex} = \theta_{c,ex} + \frac{90 - \theta_{c,ex}}{1 + e^{\frac{k-0.14}{0.4}}} \tag{6.10}$$

where $k = \lg\frac{(k_f - k_s)d}{k_s H}$; $\theta_{c,ex} = -0.011\alpha + 55.63$; α is the dimensionless injection rate and $0.6 \le \alpha \le 600$.

Equation (6.9) and Equation (6.10) are also the critical angles for the fracture at the injection well and the extraction well respectively at which angle the deceleration effect of the fracture turns into the acceleration effect.

6.6 Critical Angle for Any Position of Fracture

Based on the discussion given in Section 6.5, especially the results in Section 6.5.6 and Section 6.5.7, now it is possible to evaluate the critical angle for any position of the fracture. A fracture

can either be between the two wells or not between the two wells. These two cases are discussed separately.

6.6.1 Case 1: Fracture between Two Wells

The illustration for the fracture between the two wells is shown in Figure 6.50.

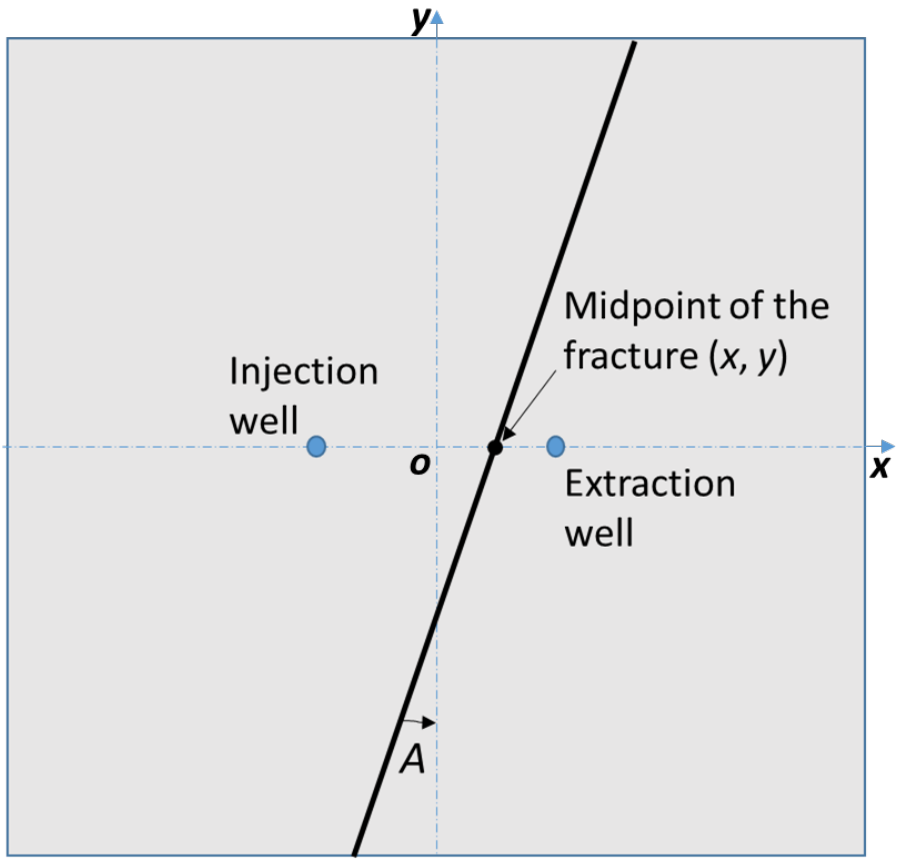

Figure 6.50: The fracture between the two wells

If the fracture is between the injection well and the origin *O*, the results of a series of parametric simulation show that the critical angle θ is approximately a linear function of the *x* coordinate of the fracture, as shown in Figure 6.51.

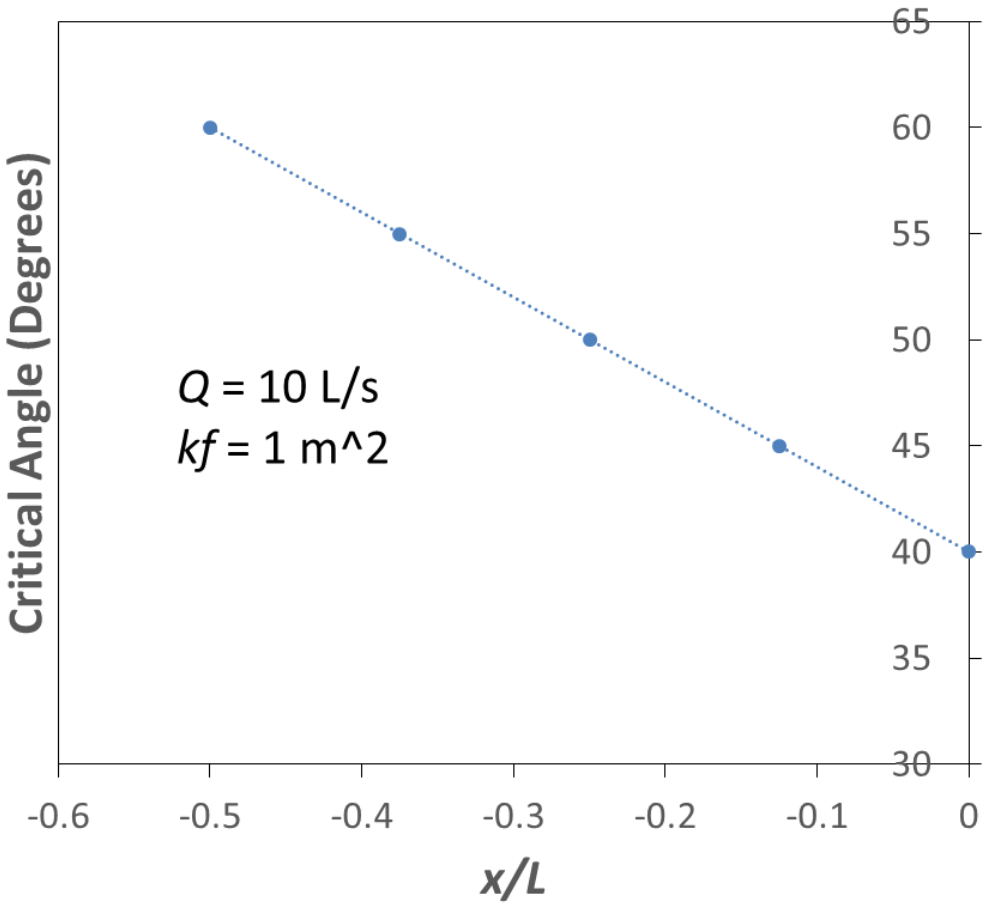

Figure 6.51: The relationship between the critical angle and the *x* coordinate of the fracture

Therefore, the critical angle for the fracture between the injection well and the origin can be expressed using the interpolation method, as shown by the following equation.

$$\theta = \frac{-x}{0.5L}\theta_{in} + (1 + \frac{x}{0.5L})\theta_{mid}, \quad -0.5 \le x / L \le 0 \tag{6.11}$$

where the expression of θ_{in} is given by Equation (6.9) and the expression of θ_{mid} is given by Equation (6.6).

Similarly, if the fracture is between the origin and the extraction well, the critical angle for the fracture can be expressed as follows:

$$\theta = \frac{x}{0.5L}\theta_{ex} + (1 - \frac{x}{0.5L})\theta_{mid},\ 0 \le x/L \le 0.5 \tag{6.12}$$

where the expression of θ_{ex} is given by Equation (6.10) and the expression of θ_{mid} is given by Equation (6.6).

In summary, the critical angle for the fracture between the two wells can be expressed as follows:

$$\theta = \begin{cases} \frac{-x}{0.5L}\theta_{in} + (1 + \frac{x}{0.5L})\theta_{mid}, & -0.5 \le x/L \le 0 \\ \frac{x}{0.5L}\theta_{ex} + (1 - \frac{x}{0.5L})\theta_{mid}, & 0 \le x/L \le 0.5 \end{cases} \tag{6.13}$$

where

$$\theta_{in} = \theta_{c,in} + \frac{90 - \theta_{c,in}}{1 + e^{\frac{k-0.14}{0.4}}},\ \theta_{c,in} = -0.021\alpha + 61.25;$$

$$\theta_{ex} = \theta_{c,ex} + \frac{90 - \theta_{c,ex}}{1 + e^{\frac{k-0.14}{0.4}}},\ \theta_{c,ex} = -0.011\alpha + 55.63;$$

$$\theta_{mid} = \theta_{c,mid} + \frac{90 - \theta_{c,mid}}{1 + e^{\frac{k-0.14}{0.4}}},\ \theta_{c,mid} = -9.09\ln\alpha + 77.08;$$

$$k = \lg\frac{(k_f - k_s)d}{k_s H},\ 0.6 \le \alpha \le 600$$

6.6.2 Case 2: Fracture not between Two Wells

The illustration of the case in which the fracture is not between the two wells (the two wells are on the same side of the fracture) is shown in Figure 6.52.

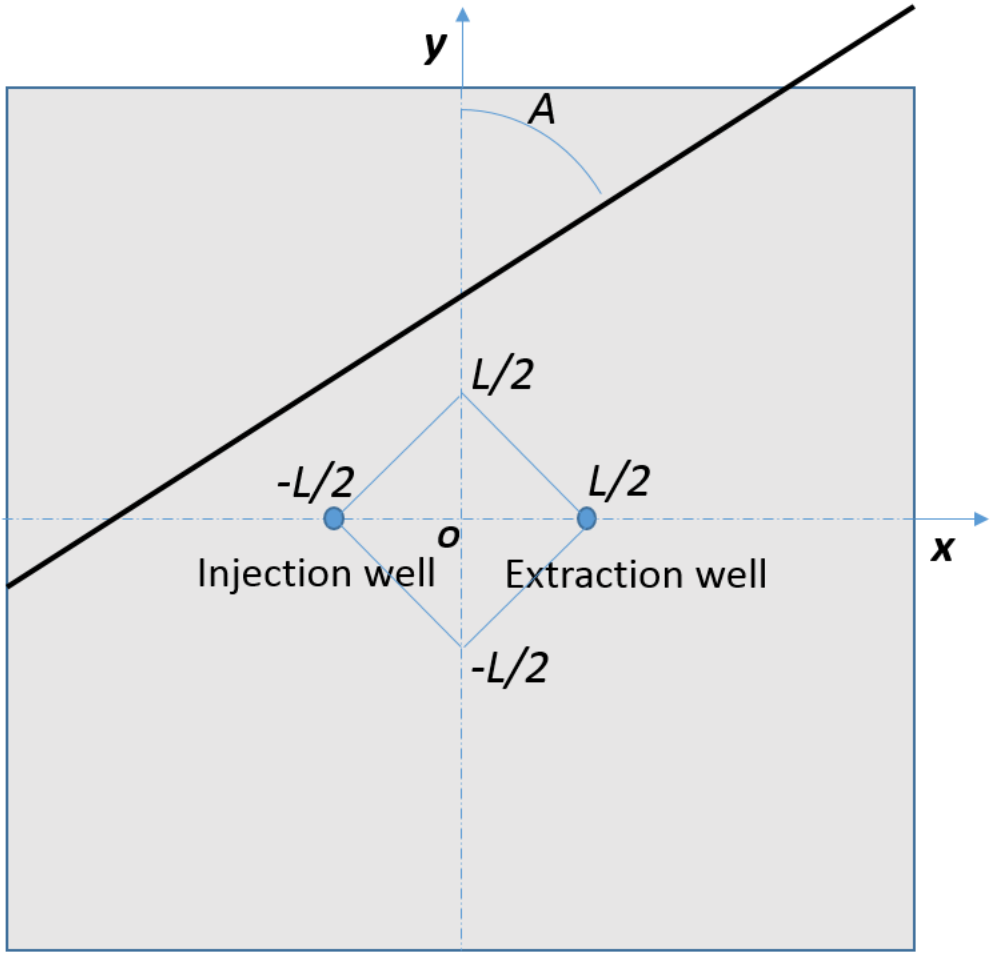

Figure 6.52: The fracture is not between the two wells

The mid-point of the fracture which moves along the symmetry axis of the two wells is considered. When the fracture passes through (0, L/2), the temperature of the extracted water at 25 years is still equal to the initial temperature of the aquifer for any angle A of the fracture, any fracture property $\frac{(k_f - k_s)d}{k_s H}$ and any dimensionless injection rate α, as shown in Figure 6.53. It is noted that the critical angle θ_{in} and θ_{ex} are $\theta_{in} \geq 50^\circ$, $\theta_{ex} \geq 50^\circ$ (see Equation (6.9) and Equation (6.10)). For the case that the fracture passes through (0, L/2) and the fracture is not between the two wells, the most critical scenario is when the fracture passes through the injection well or the extraction well. Then the angle A of the fracture is $A = 45^\circ < \theta_{in}, \theta_{ex}$. Therefore, the fracture will not affect the temperature of the extracted water during the life span of the doublet system.

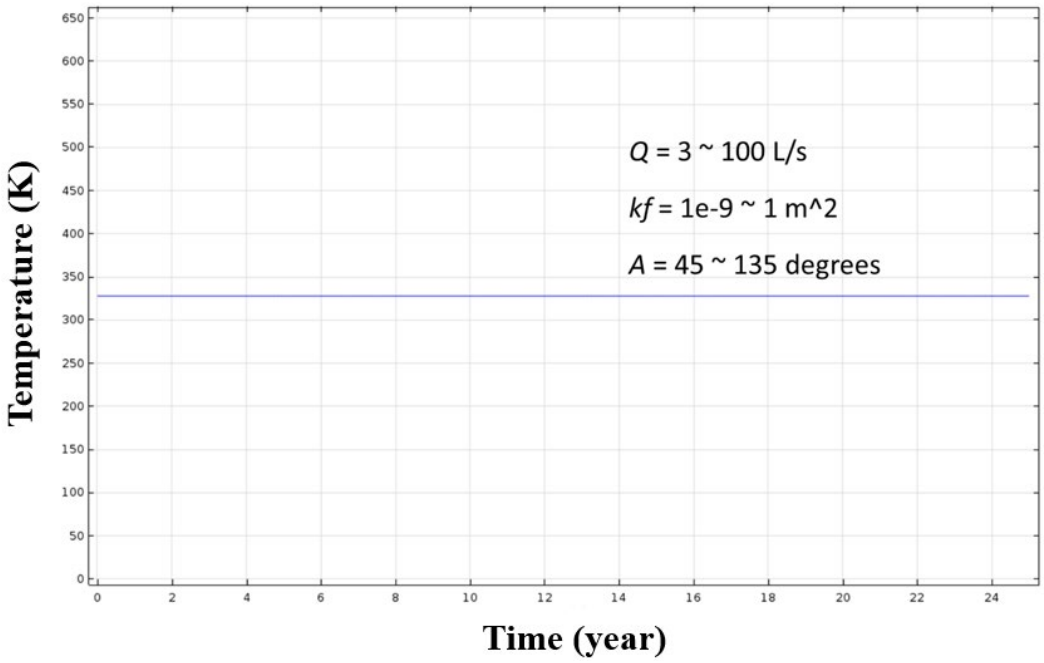

Figure 6.53: The temperature of the extracted water at 25 years when the fracture passes through (0, *L*/2)

Because of the symmetry of the doublet system, the case in which the fracture passes through (0, -*L*/2) is exactly the same.

In summary, if the fracture does not pass through the small square bounded by (-*L*/2, 0), (0, -*L*/2), (*L*/2, 0) and (0, *L*/2) as shown in Figure 6.52, the fracture will have no influence on the temperature of the extracted water. In other words, the critical angles θ of the fracture for all these cases are $\theta = 90^{\circ}$.

When the mid-point of the fracture is between the origin and (0, *L*/2), namely the *y* coordinate of the fracture $0 < y < L/2$, the most critical scenario of the fracture having the greatest influences on the temperature of the extracted water is still when the fracture passes through the injection well or the extraction well. Therefore, if the angle of the fracture $A \le \theta_{in}$ or $A \le \theta_{ex}$, the fracture will have no influence on the temperature of the extracted water. If the angle of the fracture $A > \theta_{in}$ or $A > \theta_{ex}$, the temperature of the extracted water will decrease at 25 years because of the influences of the fracture. Given the injection rate α and the position and angle of the fracture, the maximum permeability of the fracture that will not decrease the temperature of the extracted water can be obtained using Equation (6.9) and (6.10). Because of

the symmetry of the doublet system, the case in which the fracture is between the origin and (0, - L/2) is exactly the same.

Above all, the critical angle θ for any position of the fracture is summarised in Figure 6.54.

Position	Critical Angle
Fracture totally in the green zone	$\theta = 90^{\circ}$
Fracture through the red solid line	$\frac{-x}{0.5L}\theta_{in} + (1 + \frac{x}{0.5L})\theta_{mid}$
Fracture through the green dash dot line	$\frac{x}{0.5L}\theta_{ex} + (1 - \frac{x}{0.5L})\theta_{mid}$
Fracture only through the blue dash line	$A \le \theta_{in}$ or θ_{ex}, $\theta = 90^{\circ}$ $A > \theta_{in}$ or θ_{ex}, inefficient system

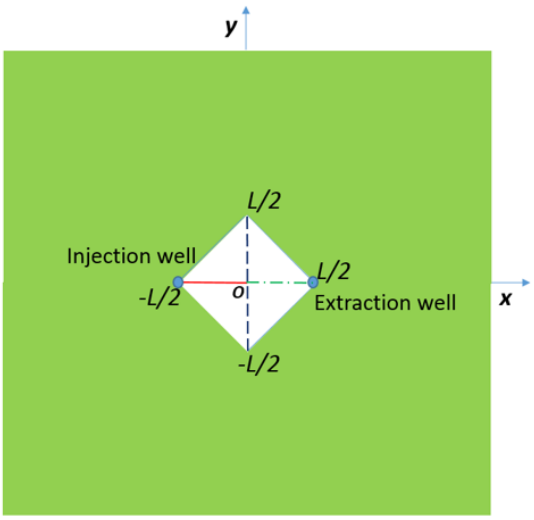

Figure 6.54: Summary of critical angle for any position of the fracture

6.7 Summary

In this chapter, a simulation result of the line model of the fracture is compared to that of the equivalent domain model of the fracture to ensure the validity of the line model which is computationally efficient. A series of line model simulations were then conducted to evaluate the influences of the fracture on the doublet system performance. Results show that the existence of fracture has an acceleration effect or a deceleration effect on the system performance depending on the position of the fracture. The effect of fracture properties such as thermal conductivity, porosity, permeability and thickness on the system performance was examined. In particular, the angle of the fracture critical to the doublet system performance was examined. Using the results of the simulations, a series of mathematical expressions to evaluate the critical angle for any position of the fracture in the doublet system are proposed. All the work in this chapter has been validated by numerical simulations and will be validated by the laboratory or field data in the future work.

Chapter 7 Conclusions and Recommendations for Future Research

7.1 Introduction

This thesis proposes an engineering analysis method to analyse a typical deep geothermal system: a doublet system with one injection well and one extraction well. An analytical solution of the temperature distribution around an injection well is developed considering the effect of the overburden layer on the temperature distribution inside the aquifer layer.

The interaction between the injection well and extraction well is first neglected. An equivalent heat transfer coefficient, which is used to characterize the effect of the overburden layer on the aquifer layer in the analytical solution, is evaluated from a series of finite element simulations for various geological conditions. An empirical expression that links heat transfer coefficient to various physical and geometric properties of the aquifer is developed.

Next a revised analytical solution of temperature distribution and extracted temperature of a geothermal system that takes into consideration the interaction between injection well and extraction well is developed. Then the revised analytical solution is compared with the experimental data from the Winnipeg case and they match with each other well.

Finally the effect of a natural fault/fracture that exists in the aquifer on the performance of a doublet system, namely the temperature distribution and extracted temperature, is evaluated. The position and angle of the fault/fracture are varied to examine the effect of fracture on system performance. Based on the results of a large number of parametric analysis, a series of mathematical expressions to obtain the critical angle for any position of the fracture in the doublet system are proposed.

7.2 Conclusions

7.2.1 New Analytical Solution

A convective heat transfer boundary between the aquifer and overburden layers is applied for the axisymmetric problem based on the Lauwerier model for the first time. Then a new analytical solution was deduced using a series of Laplace transforms. Compared with other relevant analytical solutions, this new analytical solution comprehensively includes heat conduction and heat advection in the aquifer and the heat flux between the aquifer and overburden layer. The degeneration analysis was conducted and it validated the new analytical solution. The parameter impact analysis was made and it was found that the heat breakthrough distance (i) increases with the increasing injection rate, (ii) increases with the increasing thermal diffusivity and (iii) decreases with the increasing heat transfer coefficient. The temperature around the injection well (i) decreases with the increasing injection rate, (ii) increases with the increasing heat transfer coefficient and (iii) increases with the increasing thermal diffusivity.

A quasi-steady-state solution was found to exist in the axisymmetric problem, while in the planar symmetric problem such steady states do not exist. The analytical solution also agrees with the numerical solution. As long as the relevant parameters are obtained, the new analytical solution can intuitively illustrate the temporal and spatial temperature distribution within the aquifer, and therefore allows us to develop a simple engineering analysis method to obtain the temperature distribution in the aquifer. It can be used to determine the location of the extraction well and to evaluate the extracted geothermal power of the hot water aquifer. It was found that there was an upper limit for the extracted power at a given location of the extraction well.

7.2.2 Determination of the Heat Transfer Coefficient

The new analytical solution uses the convective heat transfer coefficient, h, from the overlying boundary. This boundary condition at the interface does not only reflect the actual heat transfer process at the interface, but also models the heat transfer process in the overburden layer. In this study, it is shown that the dimensionless equivalent heat transfer coefficient is expressed

as a function of the dimensionless injection rate and the dimensionless thermal conductivity of the overburden layer so that the new analytical solution effectively incorporates the properties of the overburden layer. It was found that the thickness of the overburden layer has little influence on the temperature distribution in the aquifer. A series of FE simulations were conducted, and the analytical model was curve fitted to the FE results to evaluate the values of the dimensionless equivalent heat transfer coefficient. Based on the results of the curve fitting exercise, two empirical equations (Equation (4.5) and Equation (4.6)) were proposed for typical cases. Applying the analytical solution coupled with these empirical equations and along with proper error estimates, it is possible to conduct a simple and rapid evaluation of the geothermal potential of a particular site.

7.2.3 Revised Analytical Solution Considering Well Interaction

The revised analytical solution in this study is novel as there is no other analytical or semi analytical solution for the doublet system considering the heat conduction and heat advection in the aquifer and the heat flux between the aquifer and overburden layer. The revised analytical solution extended the analytical solution for a single injection well to a doublet scheme by considering the interaction effect between the injection well and the extraction well. The expression of the critical distance between the two wells is obtained so that the best location of the extraction well in a doublet system can be determined.

The spatial and temporal temperature distribution in the aquifer for a doublet scheme can be given by the revised analytical solution when the well distance is greater than the critical distance. It was found that it is valid to use a single well model to simplify a doublet scheme when the extraction well is far away from the injection well. The temperature of the extracted water against different time, injection rates and well distances can be obtained via the revised analytical solution. It was also found that the temperature of the extracted water stays constant for some time at the beginning and then it decreases sharply to a steady state. The revised analytical solution was compared with the experimental data and the numerical solutions. It was found that they matched with each other well which can validate the analytical solution to some extent and show the usefulness of the analytical solution in practice. The discrepancies between the revised analytical solution and the experimental data result from variable injection

temperatures, injection rates and heterogeneities of aquifer geometry and material properties. In addition, by parameter analyses, it was found that the temperature of the extracted water is very sensitive to the injection/extraction rate, thermal conductivity and well distance.

7.2.4 Fracture Flow

By comparing the line model with the domain model, it was found that the line model is valid and computationally efficient. The water velocity in the fracture firstly goes down close to zero and then goes up to the peak. It was found that the pressure distribution, streamlines and temperature distributions in the doublet system were rotated by the fracture and the contours of the temperature in the vicinity of the fracture are stretched in the direction of the fluid flow. The fracture has no influence on the doublet system when the fracture is located at the symmetry axis. The acceleration effect of the fracture is greatest when the fracture is located at the midpoint of the two wells. When the fracture is shifted towards the injection (extraction) well, the acceleration effect decreases and then becomes the deceleration effect. The deceleration effect of the fracture is the greatest when the fracture is located at the injection (extraction) well. The acceleration effect increases with the increasing angle of the fracture and the deceleration effect decreases with the increasing angle of the fracture and then the deceleration effect is replaced by the acceleration effect.

The temperature distribution along the two wells at 25 years is the same with the same value of $(k_f - k_s)d$ and the time when the temperature of the extracted water begins to decrease is shorter for a larger fracture permeability. The thermal conductivity and the porosity of the fracture has little influence on the temperature distribution of the doublet system.

The expressions of the critical angle for any position of the fracture in the doublet system are obtained. The critical angle of the fracture decreases with the increasing dimensionless fracture property and also decreases with the increasing dimensionless injection rate. When the dimensionless fracture property is small, the temperature of the extracted water does not decrease during the life span of the doublet system for any angle of the fracture. When the angle of the fracture is small, the temperature of the extracted water does not decrease during the life span of the doublet system for any dimensionless fracture property. Equipped with these

expressions, it is possible to decide whether the doublet system is still efficient during its life span once the cold water injection rate and the geometry and properties of the fracture are given.

7.3 Recommendations for Future Work

(1) Although the expression of the heat transfer coefficient h in this thesis has already included the most important factors, it is also possible to include other less important factors, such as the heat capacity values of the aquifer and overburden layer, the temperature gradient of the overburden layer, in the empirical equation to find the appropriate heat transfer coefficient h to make the proposed engineering analysis more accurate and more versatile.

(2) In this thesis, only one fracture/fault is added to the doublet system to evaluate the influence of the fracture on the doublet system. Based on the findings of one fracture, it is interesting to add more fractures to the doublet system and examine the interaction between these fractures.

(3) In practice, a geothermal system often has several injection wells and several extraction wells other than a doublet with one injection well and one extraction well. Therefore, it is useful in practice to extend the conclusions and findings for a doublet system to a more general scenario.

(4) The temperature change when the water is pumped passing through the overburden layer can be considered in the future work. As the water from a deeper layer is generally hotter than the shallower layer, the heat of the extracted water will dissipate in the overburden layer thus make the geothermal system inefficient. Therefore, it is useful to quantify this heat loss.

References

Australian Geothermal Energy Association (AGEA) and Australian Geothermal Energy Group (AGEG) (2010). Australian Code for Reporting of Exploration Results, Geothermal Resources and Geothermal Reserves. The Geothermal Reporting Code Second Edition.

Bakhsh, K. J., Nakagawa, M., Arshad, M., & Dunnington, L. (2016). Modeling Thermal Breakthrough in Sedimentary Geothermal System, Using COMSOL Multiphysics. *PROCEEDINGS, 41st Workshop on Geothermal Reservoir Engineering Stanford University, Stanford, California, February 22-24, 2016*, SGP-TR-209.

Bandos, T. V., Álvaro Montero, Fernández, E., Santander, J. L. G., Isidro, J. M., & Pérez, J., et al. (2009). Finite line-source model for borehole heat exchangers: effect of vertical temperature variations. *Geothermics*, 38(2), 263-270.

Bandyopadhyay, G., Gosnold, W., & Mann, M. (2008). Analytical and semi-analytical solutions for short-time transient response ground heat exchangers. *Energy and Buildings, 40*(10), 1816-1824.

Banks, D. (2008). An introduction to thermogeology: ground source heating and cooling. *Blackwell*, Oxford.

Banks, D. (2012). An introduction to thermogeology: ground source heating and cooling, (2nd edition). *Wiley-Blackwell,* Oxford.

Barenblatt, G. I., Zheltov, I. P., & Kochina, I. N. (1960). Basic concepts in the theory of seepage of homogeneous liquids in fissured rocks [strata]. *Journal of Applied Mathematics & Mechanics, 24*(5), 1286-1303.

Barends, F. (2010). Complete Solution for Transient Heat Transport in Porous Media, Following Lauwerier. In *SPE Annual Technical Conference and Exhibition*. Society of Petroleum Engineers.

Barker, J. (2010). Modelling doublets and double porosity. *Quarterly Journal of Engineering Geology and Hydrogeology*, 43(3): 259-268.

Barker, J.A., Downing, R.A., Gray, D.A., Findley, J., Kellaway, G.A., Parker, R.H. and Rollin, K.E. (2000). Hydrogeothermal studies in the United Kingdom. *Quarterly Journal of Engineering Geology and Hydrogeology*, 33.

Batchelor, T., Curtis, R. and Ledingham, P. (2010). Country Update for the United Kingdom. Proceedings of the World Geothermal Congress, Bali.

Berkowitz, B., Bear, J., & Braester, C. (1988). Continuum models for contaminant transport in fractured porous formations. *Water Resources Research, 24*(8), 1225–1236.

Bjelm, L., & Alm, P. G. (2010). Reservoir Cooling After 25 Years of Heat Production in the Lund Geothermal Heat Pump Project. *WORLD GEOTHERMAL CONGRESS, 2010*.

Bodvarsson, G. (1972). Thermal problems in the siting of reinjection wells. *Geothermics*, 1(2): 63-66.

Bödvarsson, G. S., & Tsang, C. F. (1982). Injection and thermal breakthrough in fractured geothermal reservoirs. *Journal of Geophysical Research Solid Earth, 87*(B2), 1031–1048.

Bond, C. E., Wightman, R., & Ringrose, P. S. (2013). The influence of fracture anisotropy on CO2 flow. *Geophysical Research Letters, 40*(7), 1284–1289.

Brandl, H. (2006). Energy foundations and other thermo-active ground structures. *Géotechnique*, 56(2), 81-122.

British Geological Survey. http://www.bgs.ac.uk/research/energy/geothermal

Busby, J. (2010). Geothermal prospects in the United Kingdom. Proceedings of the World Geothermal Congress.

Carslaw, H. S., Jaeger, J. C. (1959). Conduction of Heat in Solids, (2nd edition). *Oxford University Press*, Oxford.

Cheshire East Council (2013). Cheshire East Energy Planning: Review of Geothermal Potential in Cheshire East.

Claesson, J., Dunand, A. (1983). Heat extraction from the ground by horizontal pipes: a mathematical analysis. *Swedish Council for Building Research*, Stockholm.

Clauser, C. (2003). Numerical simulation of reactive flow in hot aquifers using SHEMAT/Processing Shemat*, Springer-Verlag*, 331 p.

Clyde, C. G., & Madabhushi, G. V. (1983). Spacing of wells for heat pumps. *Journal of Water Resources Planning and Management*, *109*(3), 203-212.

De Marsily, G. (1986). Quantitative hydrogeology: groundwater hydrology for engineers. *Academic Press*, Orlando, FL: 277-283.

De Moel, M., Bach, P. M., Bouazza, A., Singh, R. M., & Sun, J. O. (2010). Technological advances and applications of geothermal energy pile foundations and their feasibility in Australia. *Renewable and Sustainable Energy Reviews*, *14*(9), 2683-2696.

Deerman, J. D., Kavanaugh, S. P. (1991). Simulation of Vertical U-tube Ground Coupled Heat Pump Systems using the Cylindrical Heat Source Solution. *ASHRAE Transactions*, 97(1): 287-295.

Department for Energy and Climate Change (DECC) (2010a). National Renewable Energy Action Plan.

Dezayes, Ch., Chevremont, Ph., Tourli`ere, B., Homeier, G., Genter, A. (2005). Geological study of the GPK-4 HFR borehole and correlation with the GPK-3 borehole. Final Report BRGM/RP-53697-FR, Soultz-sous-Forets, France, 94 pp.

Diodato, D. M. (1994). A compendium of fracture flow models, 1994. *Office of Scientific & Technical Information Technical Reports*.

Domenico, P. A. and Schwartz, F. W. (1990). *Physical and chemical hydrogeology (Vol. 44)*. Wiley, New York, 824.

European Commission (2009). Directive 2009/28/EC of the European Parliament and the Council of 23 April 2009 on the promotion of the use of energy from renewable sources and amending and subsequently repealing Directives 2001/77/EC and 2003/30/EC.

European Geothermal Energy Council (EGEC) (2009). Geothermal Heat Pumps-Ground Source Heat Pumps.

Ferguson, G., & Woodbury, A. D. (2005). Thermal sustainability of groundwater-source cooling in Winnipeg, Manitoba. *Canadian Geotechnical Journal, 42*(5), 1290-1301.

Gentier, S., Genter, A., Sanjuan, B., Dezayes, C., Hosni, A., Courrioux, G., Schwartz, S., Feybesse, J.L., Guillou-Frottier, L., Nicol, N., Stein, G., Quinquis, J. P., Braibant, G., Brach, M., Foucher, J.C., Crouzet, C., Besse, A., Izac, J.L. (2003). Hot Dry Rock Energy Project, Soultz-sous-Forets. BRGM Contribution: 04/2002-03/2003 (2nd year report), BRGM/RP-52338-FR, 57 pp.

Global Data (2012). Geothermal Power - Global Market Size, Technology Analysis, Regulations and Key Country Analysis to 2020.

Gluyas, J.G., et al. (2018). Keeping warm: a review of deep geothermal potential of the UK. *Proceedings of the Institution of Mechanical Engineers Part A: Journal of Power and Energy*, 232(1), pp. 115-126.

Gringarten, A. C. (1978). Reservoir lifetime and heat recovery factor in geothermal aquifers used for urban heating. *Pure and Applied Geophysics*, 117(1–2): 297-308.

Gringarten, A. C., & Sauty, J. P. (1975). Theoretical study of heat extraction from aquifers with uniform regional flow. *Journal of Geophysical Research, 80*(80), 4956-4962.

GT Energy (2011). Deep Geothermal Energy: GT Energy Projects. GEOELEC Workshop.

Häring, M. O., Schanz, U., Ladner, F., & Dyer, B. C. (2008). Characterisation of the Basel 1 enhanced geothermal system. *Geothermics, 37*(5), 469-495.

Hart, D. P., Couvillion, R. (1986). *Earth-coupled heat transfer.* National Water Well Association, Dublin.

Holzbecher, E., Wong, L. W., & Litz, M. (2010). Modelling Flow through Fractures in Porous Media. *Proceedings of the COMSOL Conference 2010 Paris.*

Hooijkaas, G. R., Genter, A., & Dezayes, C. (2006). Deep-seated geology of the granite intrusions at the Soultz EGS site based on data from 5 km-deep boreholes. *Geothermics, 35*(5), 484-506.

Huyakorn, P. S., Lester, B. H., & Faust, C. R. (1983). Finite element techniques for modeling groundwater flow in fractured aquifers. *Water Resources Research, 19*(4), 1019–1035.

Ingersoll, L. R., Zobel, O. J., Ingersoll, A. C. (1954). Heat conduction with engineering, geological and other applications. *Madison University of Wisconsin Press*, Madison.

Kavanaugh, S. P. (1985). Simulation and experimental verification of vertical ground-coupled heat pump systems. *Doctoral Thesis*, Oklahoma State University, Stillwater.

Kim, I., Lindquist, W. B., & Durham, W. B. (2003). Fracture flow simulation using a finite-difference lattice Boltzmann method. *Physical Review E Statistical Nonlinear & Soft Matter Physics, 67*(4 Pt 2), 046708.

Lamarche, L. (2011). Analytical g-function for inclined boreholes in ground-source heat pump systems. *Geothermics*, 40(4): 241-249.

Lauwerier, H. A. (1955). The transport of heat in an oil layer caused by the injection of hot fluid. *Applied Scientific Research, Section A*, *5*(2-3), 145-150.

Li, M., Lai, A. C. K. (2013). Analytical model for short-time responses of ground heat exchangers with U-shaped tubes: Model development and validation. *Applied Energy*, 104(C): 510-516.

Lippmann, M. J., & Tsang, C. F. (2010). Ground-water use for cooling: associated aquifer temperature changes. *Ground Water, 18*(5), 452-458.

Lomize, G. M. (1951). *Flow in fractured media* (in Russian), p. 127. Gosenergoizdat, Moscow.

Lund, J. W., Freeston, D. H. & Boyd, T. L. (2011). Direct utilization of geothermal energy 2010 worldwide review. *Geothermics, 40*(3), 159-180.

Marcotte, D., Pasquier, P. (2009). The effect of borehole inclination on fluid and ground temperature for GLHE systems. *Geothermics*, 38(4): 392–398.

Martin, V., Jaffré, J., & Roberts, J. (2005). Modeling fractures and barriers as interfaces for flow in porous media. *SIAM*, 26, 1667–1691.

Maryška, J., Severýn, O., & Vohralík, M. (2005). Numerical simulation of fracture flow with a mixed-hybrid FEM stochastic discrete fracture network model. *Computational Geosciences, 8*(3), 217-234.

Massachusetts Institute of Technology (MIT) (2006). The Future of Geothermal Energy - Impact of Enhanced Geothermal Systems (EGS) in the United States in the 21st Century", MIT/US Department of Energy.

Mei, V. C., Baxter, V. D. (1986). Performance of a ground-coupled heat pump with multiple dissimilar U-tube coils in series. *ASHRAE transactions*, 92(2A): 30-42.

Mottaghy, D., Pechnig, R., & Vogt, C. (2011). The geothermal project Den Haag: 3D numerical models for temperature prediction and reservoir simulation. *Geothermics, 40*(3), 199-210.

Noetinger, B., & Jarrige, N. (2015). A quasi steady state method for solving transient Darcy flow in complex 3D fractured networks. *Journal of Computational Physics, 283*(1), 205-223.

Ogata, A., & Banks, R. B. (1961). *A solution of the differential equation of longitudinal dispersion in porous media* (No. 411-A).

Pruess, K., Wang, J. S. Y., & Tsang, Y. W. (1986). Effective Continuum Approximation for Modeling Fluid Flow in Fractured Porous Tuff, report SAN F86-7000, Sandia National Laboratories, Albuquerque, N.M.

Pruess, K., Wang, J. S. Y., & Tsang, Y. W. (1990a). On Thermohydrologic Conditions Near High-Level Nuclear Wastes Emplaced in Partially Saturated Fractured Tuff: 1. Simulation

Studies with Explicit Consideration of Fracture Effects. *Water Resources Research, 26*(6):1235–1248.

Pruess, K., Wang, J. S. Y., & Tsang, Y. W. (1990b). On Thermohydrologic Conditions Near High-Level Nuclear Wastes Emplaced in Partially Saturated Fractured Tuff: 2. Effective Continuum Approximation. *Water Resources Research, 26*(6):1249–1261.

Ranjith, P. G., & Viete, D. R. (2011). Applicability of the 'cubic law' for non-Darcian fracture flow. *Journal of Petroleum Science & Engineering,78*(2), 321–327.

Rath, V., Wolf, A., & Bücker, H. M. (2006). Joint three-dimensional inversion of coupled groundwater flow and heat transfer based on automatic differentiation: sensitivity calculation, verification, and synthetic examples. *Geophysical Journal of the Royal Astronomical Society, 167*(1), 453–466.

Romano-Perez, C. A., & Diaz-Viera, M. A. (2015). A Comparison of Discrete Fracture Models for Single Phase Flow in Porous Media by COMSOL. *Comsol Conference*.

Rose, P., Hickman, J., McCulloch, J., et al. (2012). Final Report: Creation of an Enhanced Geothermal System through Hydraulic and Thermal Stimulation. Geothermal Technologies Program, U. S. Dept. of Energy.

Rybach, L. & Sanner, B. (2000). Ground-source heat pump systems: the European experience. *Geo-Heat Center Bulletin*, 21, No. 1, 16-26.

Sanjuan, B., Pinault, J. L., Rose, P., Gérard, A., Brach, M., & Braibant, G., et al. (2006). Tracer testing of the geothermal heat exchanger at Soultz-sous-Forêts (France) between 2000 and 2005. *Geothermics, 35*(5–6), 622-653.

Satman, A. (2011). Sustainability of geothermal doublets. *PROCEEDINGS, Thirty-Sixth Workshop on Geothermal Reservoir Engineering Stanford University, Stanford, California, January 31 - February 2, 2011*, SGP-TR-191.

SKM (2012). Geothermal Energy Potential in Great Britain and Northern Ireland. Sinclair Knight Merz: London.

Swiss Seismological Service. www.seismo.ethz.ch/en/earthquakes/monitoring/geothermal-energy-basel/Project-Description/

Szalaiová, E., Rabbel, W., Marquart, G., & Vogt, C. (2015). Geothermal modelling of faulted metamorphic crystalline crust: a new model of the continental deep drilling site KTB (Germany). *Geophysical Journal International, 203*(2), 1039-1053.

Tan, H., Cheng, X., & Guo, H. (2012). Closed Solutions for Transient Heat Transport in Geological Media: New Development, Comparisons, and Validations. *Transport in porous media*, *93*(3), 737-752.

Vogt, C., Iwanowski-Strahser, K., Marquart, G., Arnold, J., Mottaghy, D., & Pechnig, R., et al. (2013). Modeling contribution to risk assessment of thermal production power for geothermal reservoirs. *Renewable Energy, 53*(9), 230-241.

Walsh, J. B., & Brace, W. F. (1984). The effect of pressure on porosity and the transport properties of rock. *Journal of Geophysical Research Solid Earth, 89*(B11), 9425–9431.

Warren, J. E., & Root, P. J. (1963). The behavior of naturally fractured reservoirs. *Society of Petroleum Engineers Journal, 3*(3), 245-255.

Witherspoon, P. A., Wang, J. S. Y., Iwai, K., & Gale, J. E. (1979). Validity of cubic law for fluid flow in a deformable rock fracture. *Water Resources Research, 16*(6), 1016-1024.

Wu, Y. S., & Pruess, K. (2000). Integral solutions for transient fluid flow through a porous medium with pressure-dependent permeability. *International Journal of Rock Mechanics & Mining Sciences, 37*(1–2), 51-61.

Zeng, H. Y., Diao, N. R., & Fang, Z. H. (2002). A finite line‐source model for boreholes in geothermal heat exchangers. *Heat Transfer—Asian Research*, *31*(7), 558-567.

Zhao, Z., Jing, L., Neretnieks, I., & Moreno, L. (2011). Numerical modeling of stress effects on solute transport in fractured rocks. *Computers & Geotechnics, 38*(2), 113-126.

Zimmermann, G., & Reinicke, A. (2010). Hydraulic stimulation of a deep sandstone reservoir to develop an enhanced geothermal system: laboratory and field experiments. *Geothermics, 39*(1), 70-77.

Zimmerman, R. W., & Bodvarsson, G. S. (1996). Hydraulic conductivity of rock fractures. *Transport in Porous Media, 23*(1), 1-30.

Zou, L., Jing, L., & Cvetkovic, V. (2015). Roughness decomposition and nonlinear fluid flow in a single rock fracture. *International Journal of Rock Mechanics & Mining Sciences, 75*, 102-118.